Experimenteel-numerieke evaluatie van de weerstand tegen stabiele scheuruitbreiding en de rekcapaciteit van biaxiaal belaste pijpleidingen

Experimental-Numerical Evaluation of Ductile Tearing Resistance and Tensile Strain Capacity of Biaxially Loaded Pipelines

Matthias Verstraete

Promotor: prof. dr. ir. W. De Waele
Proefschrift ingediend tot het behalen van de graad van
Doctor in de Ingenieurswetenschappen: Werktuigkunde-Elektrotechniek

Vakgroep Mechanische Constructie en Productie
Voorzitter: prof. dr. ir. P. De Baets
Faculteit Ingenieurswetenschappen en Architectuur
Academiejaar 2013 - 2014

UNIVERSITEIT GENT

ISBN 978-90-8578-640-5
NUR 978, 950
Wettelijk depot: D/2013/10.500/73

Supervisor

prof. dr. ir. W. De Waele

Ghent University
Faculty of Engineering and Architecture
Department of Mechanical Construction and Production

Examination Committee

prof. P. De Baets (Chairman)
prof. S. Claessens
prof. W. De Waele
prof. R. Denys
prof. N. Gubeljak
dr. S. Hertelé

Research Institute

Ghent University
Department of Mechanical Construction and Production
Soete Laboratory
Technologiepark 903
B-9052 Zwijnaarde
Belgium

Tel. +32 9 331 04 72
Fax +32 9 331 04 90
Mail Matthias.Verstraete@UGent.be

www.SoeteLaboratory.UGent.be

"If I have seen any further,
it's by standing on the shoulders of giants"

Isaac Newton

Acknowledgements

First, I would like to thank my supervisor Prof. Wim De Waele for providing me the chance of doing research at Soete Laboratory. The numerous discussions, critical reflections and support in writing my IWT project proposal, papers and this dissertation are truly acknowledged. In addition, I would like to thank Prof. Rudi Denys, for sharing his professional network and CWP experience.

I also like to express my gratitude to the Agency for Innovation by Science and Technology (IWT), who made this work possible through grants n° SB-091512 and SB-093512.

Team work makes the dream work. Therefore I would like to express my sincere thanks to all people that have contributed to the results presented in this dissertation. Performing experimental research cannot be based on an individual effort only. On the contrary, it requires days (sometimes nights) of preparation, discussions and testing. Therefore, I would like to explicitly thank:

- *The master students Koen Van Minnebruggen, Dries Van Puyvelde, Jens Maelfait, Matthias Cauwelier, Joeri Van Iseghem and Nick Geldof whom I was honored to guide during the past years. Without their devotion to SENT testing, the number of (not always as) successful tests would have been clearly more limited. Cooperating with these people was a true enrichment for my period at Soete Laboratory. Not only because they challenged me to come up with answers for their scientific questions; they also provided me joy and enthusiasm at work.*
- *Hans Van Severen, Julien De Meyer and Johan Vandenbossche, the technicians from our lab, who were not only present for Saint Eligius and the yearly barbeque, but as well for preparing all test specimens.*
- *Tony Lefevre, who introduced me in the world of testing and took care of lots of the preparation work.*
- *Wouter Ost, the man who kept all machines running and helped to modify the ESH test rigs for SENT testing.*
- *Johan De Clercq and Hans Van Severen, for (dis)mounting the clamps to the test rig.*
- *Chris Bonne, for the assembly of the clip gauges and the numerous small interventions when it came to electronic equipment.*

- *Anja, Gert, Filip, Yves, Kathleen and Michel from the Belgian Welding Institute, for their availability whenever I encountered difficulties in their labs.*

A special thanks also goes to these people that created an enjoyable atmosphere in the laboratory for doing research. First and foremost, I would like to thank Stijn Hertelé. Sharing four years in the same office introduced a lot of joy, discussion, challenges and… friendship in work! Second, I would like to thank Jeroen Van Wittenberghe, Timothy Galle, Koen Van Minnebruggen and Nahuel Micone for sharing the office with me. Third, I would like to thank all other colleagues, Yeczain Perez, Vanessa Rodriguez, Jan De Pauw, Georgette D'Hondt, Josiane Yde, Felicia Jula, Gusztav Fekete, Reza Hojjati Talemi, Matyas Ando, Patric Neis, Mohsen Safaei, Hanan Al Ali, Diego Belato Rosado, Diego Sarzosa Burgos, Saosometh Chhith, Tan Dat Nguyen, Zamaan Sadeghi, Yue Tongyan, Rudy Desmet, Jonathan Vancoillie and Jacob Sukumaran who created an extraordinary environment for doing research, with great team buildings and pleasant support.

Research however not only takes place between the walls of the laboratory. Therefore, I would like to thank a number of people for their remote support and the numerous discussions. In particular I would thank:

- *Dr. Bill Tyson from CANMET MTL for discussing various SENT test procedures and the possibility for cooperating in the round robin on SENT testing.*
- *Dr. Gery Wilkowski from EMC² for sharing his experience in potential drop testing. His guidance was inevitable for selecting suitable test apparatus and interpreting the test results.*

In addition, I would like to thank Erling Østby, Aida Nonn, Timothy 'Dash' Weeks and Duncan Wang for the interesting discussions during various conferences.

Mens sana in corpore sano, a healthy mind in a healthy body. Therefore I would like to thank Eddy Merckx. Not only did he inspire me as he is the greatest cyclist ever, the time I spent on his bikes also introduced a welcomed source of motivation and brain relaxation.

As life is not only about research, I also want to thank my friends. I enjoyed our nights in the pubs, our trips, … and hope there are many more to come! Though, I want to apologize for the times I have skipped our 'meetings'!

Finally, my uppermost gratitude goes to my family; my parents Etienne and Marianne, for facilitating years of studies; my sister Julie; my parents in law Roos and Jean-Luc; and certainly my wife Barbara for the self-confidence she brings me, her enthusiasm, her adventurous spirit and her unconditional support.

Matthias Verstraete
November 2013

Summary

For the construction of gas and oil transportation pipelines, different pipe sections are welded together. The connecting girth welds are a potential weakest link as these might contain defects related to the welding process. To assess the criticality of these defects, several (some of them standardized) assessment procedures are available. Within this dissertation, the focus is on strain based defect assessment procedures. These procedures estimate the defect tolerance as function of the required deformation (strain) in the pipe. This approach gained interest given the harsh environments in which newly developed gas and oil fields are located (e.g. arctic regions, areas prone to landslides, …). However, a number of particularities arise when applying these defect assessment procedures. Two main issues have been considered in this dissertation.

The first relates to the material's ductile tearing resistance, which is a crucial parameter in most strain based defect assessment procedures. For ductile materials, this tearing resistance expresses the material's resistance to (ductile) crack extension as function of the load that is transferred to the crack. The latter is in this dissertation expressed by means of the crack tip opening displacement (CTOD). However, the procedures that are currently available in standards only allow an overly conservative evaluation of this tearing resistance. Hence, a first aim of this dissertation is to present a well validated test method for the evaluation of the tearing resistance with a limited degree of conservatism with respect to pressurized pipes.

On the other hand, one of the strain based defect assessment procedures, developed at Ghent University, is based on historical curved wide plate (CWP) test data. A CWP test consists of an artificially notched pipe section with limited width (e.g. 300 mm), extracted along the pipes longitudinal direction, that is loaded in tension. However, the uniaxial loading in CWP tests contrast the biaxial loading (pressure + axial tension) in transportation pipelines. It has been reported that this biaxial loading has the potential to reduce the deformation capacity relative to the uniaxially loaded situation. Therefore, the second aim of this work is to quantify the difference in deformation capacity between pressurized pipes and CWP specimens.

For the evaluation of the ductile tearing resistance, preference has been given to SENT testing. This comprises a tensile test on a notched square specimen that is extracted along the pipe's longitudinal direction. This test was selected as the magnitude of the crack tip stress fields, referred to as the crack tip constraint, conservatively approximates the one in pressurized pipes. To measure the tearing resistance during SENT testing, a number of experimental methods have first been implemented. These can be divided in methods that evaluate the ductile crack extension and those that evaluate the CTOD. For the measurement of the crack extension, the unloading compliance (UC) and direct current potential drop (DCPD) methods have been implemented. Based on the results of several series of tests, comprising both welded and non-welded specimens, the equivalence between both measurement methods has been demonstrated. To that extent, the accuracy of both methods with respect to the evaluation of the ductile crack extension at the end of the test has been studied for all tests. For the evaluation of the CTOD, the double clip gauge method and the δ_5 method have been compared. At low deformation levels, both yield similar results. In contrast, at higher deformation levels the δ_5 method results in slightly lower CTOD values.

Based on these well validated measurement methods, the tearing resistance has been evaluated for a series of (welded) specimens. For these tests, it has been observed that the extraction position of the specimen along the pipe's circumferential direction (o'clock position) does not influence the tearing resistance. Contrary, a dependency on the initial notch depth and notch orientation has been observed. These dependencies are related to a constraint difference and weld metal heterogeneity respectively. These observations have led to the formulation of guidelines for the evaluation of the tearing resistance.

Focusing on the quantification of the strain capacity of pressurized pipes relative to the strain capacity of CWP specimens, preference is given to a numerical approach. By implementation of the tangency approach, also used for the development of several strain based defect assessment procedures, the tensile strain capacity has been obtained from finite element simulations.

Amongst others, the tearing resistance is required as input parameter for the tangency approach. Preferably, the same tearing resistance curve is used for CWP and pipe specimens. However, this tearing resistance depends on the crack tip constraint. Hence, such approach can only be justified if the difference in constraint between (pressurized) pipes and CWP specimens is limited. To evaluate this constraint difference, the numerically obtained crack tip stress fields have been compared for a series of welded and non-welded configurations. This revealed a minor (out-of-plane) constraint difference, attributed to internal pressure. In combination with results published in literature, this difference has been neglected.

Based on an extensive set of simulations, the relative strain capacity has subsequently been evaluated. This relative strain capacity is primarily influenced by the crack size, the strength mismatch level and the weld misalignment. In contrast, for the investigated configurations, the relative strain capacity is not influenced by the material's uniform elongation and tearing resistance. Eventually, this set of simulations resulted in the formulation of a pressure correction function. This function allows conservatively evaluating the tensile strain capacity of pressurized pipes from CWP test results. It is however acknowledged that the degree of conservatism might in some cases hamper the application of this pressure correction function. In addition, application of this analytical equation is strictly limited to the simulated configurations. Therefore, a second level pressure correction approach is proposed. In this case, the relative strain capacity is determined from a set of simulations considering project specific material and geometrical properties.

In conclusion, the presented work first presents a well validated methodology for the evaluation of the ductile tearing resistance using SENT specimens. Second, by considering the proposed pressure correction in combination with the strain based defect assessment procedure previously developed at Ghent University, the tensile strain capacity of pressurized pipes can conservatively be calculated.

Samenvatting

(Dutch summary)

Voor het aanleggen van pijpleidingen die olie en gas transporteren dienen verschillende buissecties met elkaar verbonden te worden. Deze verbindingen gebeuren typisch door middel van omtrekslassen. Echter, deze lassen vormen vaak een zwakke schakel in dit netwerk van pijpleidingen, aangezien ze fouten kunnen bevatten als gevolg van het lasproces. Om de toelaatbaarheid van deze fouten te bepalen, zonder de integriteit van de buis te beïnvloeden, zijn verschillende al dan niet gestandaardiseerde procedures beschikbaar. Binnen het kader van dit werk wordt enkel gekeken naar rekgebaseerde procedures. Deze beschouwen de vervorming in de buis als ontwerpscriterium, resulterend in een verband tussen de. maximale vervorming (rekcapaciteit) van de buis en de maximaal toelaatbare foutgrootte. Gelet op de recente ontwikkelingen inzake de ontginning van olie en gas is de aandacht voor een dergelijke aanpak sterk toegenomen (bv. voor toepassingen rond de Noordpool of in gebieden waar grondverschuivingen voorkomen). Deze aanpak brengt echter een aantal problemen met zich mee. Twee van de voornaamste vormen het onderwerp van dit werk.

Het eerste probleem heeft betrekking tot de weerstand tegen stabiele scheuruitbreiding van het materiaal waar de fout zich bevindt. Dit is een bepalende factor voor nogal wat rekgebaseerde procedures. Voor ductiele materialen drukt deze het verband uit tussen de (stabiele) scheurgroei en de belasting op de scheur. Deze belasting wordt binnen dit werk beschreven op basis van de opening ter hoogte van de scheurtip (CTOD). Het probleem is dat de methodes die momenteel beschreven staan in standaarden behoorlijk conservatief zijn met betrekking tot de evaluatie van deze weerstand tegen stabiele scheuruitbreiding. Daarom zal binnen dit werk in de eerste plaats aandacht besteed worden aan het ontwikkelen van een methode die toelaat om de weerstand tegen stabiele scheuruitbreiding te bepalen, met een beperkte graad van conservativiteit ten opzichte van buisleidingen onder druk.

Ten tweede dient opgemerkt dat een van deze rekgebaseerde procedures ontwikkeld werd aan de Universiteit Gent. Deze procedure is gebaseerd op beschikbare resultaten van uniaxiale trekproeven op gekromde brede platen (CWP). Deze platen bevatten centraal een artificiële fout en worden in de langsrichting uit een pijpleiding gebrand. De uniaxiale belastingstoestand contrasteert echter met de biaxiale belastingstoestand waaraan de pijpleidingen in realiteit blootgesteld kunnen worden. Deze biaxiale belastingstoestand is een gevolg van de axiale vervorming in combinatie met de inwendige druk die aanwezig is in de pijpleiding. In de literatuur

staat beschreven dat deze biaxiale belastingstoestand aanleiding kan geven tot een significante verlaging van de rekcapaciteit. Daarom zal binnen dit werk aandacht besteed worden aan het kwantificeren van het verband tussen de rekcapaciteit van buizen onder druk en CWP-proefstukken.

Met betrekking tot het bepalen van de weerstand tegen stabiele scheuruitbreiding, wordt gekozen voor een trekproef op een gekerfde proefstaaf met vierkante doorsnede (SENT). Dit type proef werd op basis van een literatuurstudie geselecteerd aangezien de spanningstoestand rond de scheurtip, meer bepaald de triaxialiteit ervan, in grote mate vergelijkbaar is met deze in buizen onder druk. Om de weerstand tegen stabiele scheuruitbreiding te bepalen, werden ten eerste een aantal meetmethodes geïmplementeerd. Hierbij kan onderscheid gemaakt worden tussen deze methodes die toelaten om de scheuruitbreiding te begroten en deze die toelaten de CTOD te meten. Wat het meten van de scheuruitbreiding betreft werden de ontladingscompliante (UC) methode en de gelijkstroom spanningsval (DCPD) methode geïmplementeerd. Op basis van een uitgebreide reeks SENT-proeven, kan worden aangenomen dat beide methodes gelijkwaardig zijn. Zo zijn ze beide in staat om op nagenoeg even nauwkeurige wijze de scheuruitbreiding op het einde van de proef te voorspellen. Wat het meten van de CTOD betreft, werd een methode op basis van twee verplaatsingsmeters vergeleken met de δ_5-methode. Zolang de vervorming beperkt blijft, geven beide methodes aanleiding tot eenzelfde meetresultaat. Naarmate deze vervorming toeneemt, wordt echter duidelijk dat de δ_5-methode ietwat lagere waarden genereert.

Op basis van deze gevalideerde meetmethodes werd de weerstand tegen stabiele scheuruitbreiding geëvalueerd voor een reeks (gelaste) proefstukken. Op basis van de testresultaten kan worden geconcludeerd dat de uitnamepositie met betrekking tot de omtreksrichting van de buis geen invloed heeft op de weerstand tegen stabiele scheuruitbreiding. Anderzijds werd vastgesteld dat zowel de initiële scheurdiepte, alsook de oriëntatie van de scheur een uitgesproken invloed heeft op de weerstand tegen stabiele scheuruitbreiding. Dit wordt toegewezen aan een verschil in triaxialiteit voor de afhankelijkheid van de scheurdiepte, en aan het uitgesproken heterogene karakter van een las voor de oriëntatie. Finaal werden op basis van deze waarnemingen richtlijnen opgesteld voor de bepaling van de weerstand tegen stabiele scheuruitbreiding.

Voor het kwantificeren van het verband tussen de rekcapaciteit van buizen onder druk en CWP-proefstukken, werd de voorkeur gegeven aan een numerieke studie. Op basis van eindige elementen analyses kan de vervormingscapaciteit gesimuleerd worden. Dit gebeurde binnen dit werk volgens methodes beschreven in diverse (gestandaardiseerde) rekgebaseerde procedures.

Een van de parameters die hiertoe dient ingegeven te worden is de weerstand tegen stabiele scheuruitbreiding. Bij voorkeur wordt eenzelfde curve gebruikt voor de simulaties van CWP-proefstukken als voor de simulaties van buizen onder druk. De weerstand tegen stabiele scheuruitbreiding hangt evenwel sterk af van de triaxiliteit van de spanningstoestand aan de scheurtip. Om een dergelijke aanpak te rechtvaardigen diende aangetoond te worden dat de graad van triaxiliteit vergelijkbaar is tussen beide. Hiertoe werden de gesimuleerde spanningsvelden uitgebreid met elkaar vergeleken. Uit die vergelijking blijkt dat er een minimiem verschil is tussen beide, gerelateerd aan de aanwezigheid van de inwendige druk. Op basis van literatuurgegevens kon echter geconcludeerd worden dat dit verschil verwaarloosbaar is.

Vervolgens werd een uitgebreide reeks simulaties uitgevoerd, waarbij de relatieve rekcapaciteit (CWP-proeven relatief ten opzichte van buizen onder druk) bestudeerd werd. Hieruit blijkt dat deze relatieve rekcapaciteit voornamelijk bepaald wordt door de foutgrootte, het sterkteverschil tussen het lasmetaal en het basismateriaal in de buis en de mogelijke uitlijningsfout tussen beide gelaste buizen. Daartegenover staat dat, binnen het grenzen van het onderzochte, de relatieve rekcapaciteit niet beïnvloed wordt door de verlengingscapaciteit van het materiaal en de weerstand tegen stabiele scheuruitbreiding. Op basis van deze resultaten werd finaal een analytische druk correctie formule voorgesteld die toelaat om op conservatieve wijze de rekcapaciteit van buizen onder druk te schatten op basis van het resultaat van een CWP-proef. Hierbij dienen echter twee kanttekeningen gemaakt. In de eerste plaats is de conservativiteit mogelijks behoorlijk groot, wat het gebruik van deze analytische vergelijking ontmoedigt. Ten tweede kan deze vergelijking enkel gebruikt worden binnen de grenzen van het onderzochte. Daarom werd een alternatieve mogelijkheid toegevoegd die toelaat om de relatieve rekcapaciteit op een projectspecifieke wijze te bepalen door gebruik te maken van extra eindige elementen simulaties.

Er kan geconcludeerd worden dat dit werk vooreerst een gevalideerde methode voor het bepalen van de weerstand tegen stabiele scheuruitbreiding aanreikt. Daarnaast kan de rekcapaciteit voor buizen onder druk op veilige wijze afgeschat worden. Dit door gebruik te maken van de voorgestelde drukcorrectie in combinatie met de rekgebaseerde procedure die eerder ontwikkeld werd aan de Universiteit Gent.

Contents

Chapter 1- Research Context and Motivation

Chapter 2 – Research Approach from Full- to Sub-Scale

Chapter 3 – Evaluation of Ductile Crack Extension

Chapter 4 – Evaluation of Crack Driving Force

Chapter 5 – Tearing Resistance: Sources of Variation

Chapter 6 – Evaluation of Deformation and Strain Patterns

Chapter 7 – Comparison of Constraint in CWP Specimens and (Pressurized) Pipes

Chapter 8 – Comparison of Tensile Strain Capacity in CWP Specimens and (Pressurized) Pipes

Chapter 9 – Conclusions and Outlook for Future Research

Appendix A – Experimental Work: Overview of Test Specimens

Appendix B – Statistical Analysis of Relative Strain Capacity

Appendix C – Accuracy and Precision

Appendix D – Modified Boundary Layer (MBL) Model

Symbols and Acronyms

Symbols

a	defect depth
a_0	initial defect depth
a_1, a_2	curve fitting parameter
$\hat{a}_1$, $\hat{a}_2$	curve fitting parameter
A_2	constraint parameter
b	ligament thickness
b_0	initial ligament thickness
B	thickness
B_e	effective thickness
B_N	net thickness
c	half defect length
c_0, c_k	curve fitting parameter
C	compliance
C_d	correction factor for decreasing influence of weld strength mismatch with increasing crack size
C_m	electrical conductance
C_{mm}	correction factor for weld strength mismatch variability
$\mathrm{CTOD}_{\mathrm{ini}}$	CTOD at initiation
d_F	offset between remote and ligament force
D	pipe diameter
$D_{meas;1}$	distance between measurement pins for V
$D_{meas;2}$	distance between crack and first measurement pin for V_{ref}
$D_{meas;3}$	distance between measurement pins for V_{ref}
D_{pin}	pin distance
D_{stab}	stabilization distance
e	misalignment
E	Young's modulus
$f_{ij}(\theta)$	angular function
F	force
F_{max}	maximum force
F_{res}	resulting force in ligament
h	stress triaxiality parameter
h_1	height of lower clip gauge

h_2	height of upper clip gauge
H	daylight grip length
I_a	current flowing through ligament
I_l	current leaking through test rig
I_n	integration constant
I_s	current delivered by power source
J	J-integral
K_I	mode I stress intensity factor
L	length of prismatic section
L_{tot}	total length
M_{res}	resulting bending moment
MM_{YS}	yield strength mismatch
MM_{FS}	flow strength mismatch
MM_{TS}	tensile strength mismatch
n	Ramberg-Osgood strain hardening exponent
N	batch size
p	internal pressure
P_m	limit load for SENT specimens
Q	constraint parameter
Q_m	constraint parameter
r	distance ahead of the crack tip
$\bar{r}$	normalized distance ahead of the crack tip
r_0	notch tip radius
r_i	fitting coefficient
R_m	tensile strength
$R_{p;0.2}$	stress corresponding to plastic strain of 0.2%
$R_{t;0.5}$	stress corresponding to total strain of 0.5%
s_{cr}	straightness of crack front
STD	standard deviation
t	wall thickness
T	constraint parameter (T-stress)
T_i	traction vector
u_i	displacement vector
uEL	uniform elongation
V	potential drop across crack
V_1	displacement measured using lower clip gauge
V_2	displacement measured using upper clip gauge
V_{ref}	reference potential drop measured remote from crack
w	strain energy density
W	height of specimen (for SENT) half width of specimen (for CWP/MWP)
x_k	parameter
$\bar{x}_k$	average value of x_k
$\boldsymbol{X}$	linear combination of parameters x_k
Y/T	yield-to-tensile ratio

α	dimensionless Ramberg-Osgood parameter
Γ	contour
$\delta_1,\ \delta_2$	curve fitting parameters for CTOD resistance curve
δ_5	CTOD measured using two point located 5 mm apart, across the crack tip
δ_{90}	CTOD evaluated using double clip gauge and 90° intercept definition
δ_{CDF}	crack driving force
δ_{ij}	Kronecker delta
$\delta_{macrograph}$	CTOD measured from macrograph
δ_{mat}	tearing resistance
δ_s	scatter on tearing resistance curve
Δa	amount of ductile crack extension
Δa_{9p}	measured crack extension using nine points average method
Δa_b	crack extension attributed to blunting
Δa_{macro}	crack extension measured on macrograph
$\Delta a_{t,uc\,/\,pd}$	totally predicted crack extension using unloading compliance / potential drop method (blunting included)
$\Delta a_{uc\,/\,pd}$	predicted crack extension using unloading compliance / potential drop method (blunting excluded)
ΔQ	variation of Q-parameter
ε	true strain
$\varepsilon_{collapse}$	critical strain before failure through collapse
ε_{crack}	critical strain before failure through unstable ductile crack extension
ε_{design}	design strain
ε_{ij}	strain in ij-direction
ε_{max}	tensile strain capacity
$\varepsilon_{max;up}$	tensile strain capacity for unpressurized pipe
$\varepsilon_{max;pp}$	tensile strain capacity for pressurized pipe
$\varepsilon_{max;CWP}$	tensile strain capacity for CWP
ε_{remote}	remote strain
$\zeta_{CWP;up}$	relative strain capacity between CWP specimens and unpressurized pipes
$\zeta_{pp;CWP}$	relative strain capacity between pressurized pipes and CWP specimens
$\zeta_{pp;up}$	relative strain capacity between pressurized and unpressurized pipes
η_p	dimensionless constant
θ	angle perpendicular to the crack
κ	curvature
ν	Poisson coefficient
ξ	set of all variable parameters
σ	true stress

σ_0	yield strength
σ_{design}	design stress
σ_e	Von Mises equivalent stress
σ_{ij}	stress in ij-direction
$\tilde{\sigma}_{ij}(n,\theta)$	dimensionless functions
σ_{FS}	flow strength
σ_m	hydrostatic stress
σ_{max}	maximum applied tensile stress (tensile stress capacity)
σ_{TS}	tensile strength
σ_{hoop}	hoop stress
$\sigma_{\theta\theta}$	crack tip openings stress
φ	angle parallel to the crack
ψ	variability
ω	set of relative strain capacities

Acronyms

ACPD	alternating current potential drop
API	American Petroleum Institute
ASTM	American Society for Testing and Materials
BM	base metal
BP	British Petroleum
CCT	center crack tension
CMOD	crack mouth opening displacement
CRES	Center for Reliable Energy Systems
CSA	Canadian Standards Association
CT	compact tension
CTOD	crack tip opening displacement
CWP	curved wide plate
DCPD	direct current potential drop
DENT	double edge notch tension
DIC	digital image correlation
DNV	Det Norske Veritas
ECA	engineering critical assessment
EPFM	elastic-plastic fracture mechanics
FAD	failure assessment diagram
FE	finite element
FEA	finite element analysis
GKSS	Gesellschaft für Kernenergieverwertung in Schiffbau und Schiffahrt
GMAW	gas metal arc welding
HAZ	heat affected zone
HRR	Hutchinson-Rice-Rosengren
ID	inner diameter

ISO	International Organisation for Standardization
LEFM	linear elastic fracture mechanics
LVDT	linear variable differential transducer
MBL	modified boundary layer
MWP	medium wide plate
OD	outer diameter
PD	potential drop
SB-FAD	strain based failure assessment diagram
SEM	scanning electron microscope
SENB	single edge notch bending
SENT	single edge notch tension
SMAW	shielded metal arc welding
SSY	small scale yielding
TT	through thickness
UC	unloading compliance
UGent	Ghent University
WM	weld metal
WMC	weld metal center

Chapter 1

–

Research Context and Motivation

1.1 Defect assessment of pipeline girth welds

1.1.1. Girth weld defects

The construction of gas and oil transportation pipelines implies great costs. Roughly 10% of the total project costs are related to girth welding [1.1], required to connect the different pipe sections. These circumferential girth welds might contain defects and hence constitute a potential weakest link. Several defect types can be identified, for example lack of fusion, undercut and cracks. The weld defects that are considered in this dissertation typically range between 2 and 5 mm in height and up to 200 mm in length [1.2-4]. Next to the occurrence of defects in (or adjacent to) the weld metal (WM), the welding process potentially involves other detrimental effects. First, the process might result in a misalignment (e) between the connected pipe sections. Second, the heat input going with the welding process potentially deteriorates the material properties of the base material (BM) adjacent to the weld metal. This zone is referred to as the heat affected zone (HAZ). The above is schematically shown in Figure 1.1.

In order to reveal the presence of defects, a 100% weld inspection is required for pipelines installed in built-up areas [1.5]. Non-destructive inspection is performed by means of ultrasonic and/or radiographic techniques. These techniques provide insight in the defect length (and height). Based on these dimensions, a defect assessment procedure can be performed. In other words, an evaluation about whether or not the encountered defects are tolerable.

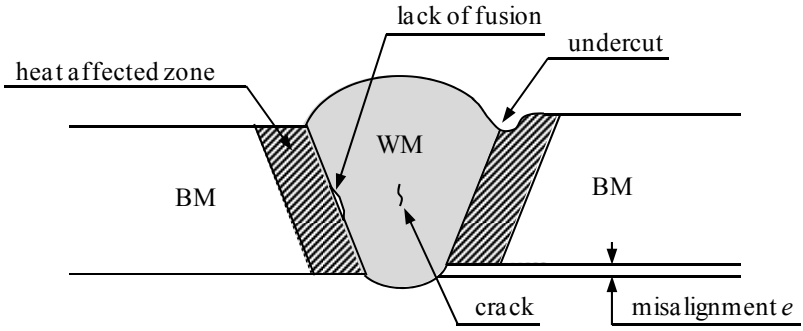

Figure 1.1. Schematic representation of different types of weld defects

1.1.2. Defect assessment

In general, defect assessment procedures comprise multiple levels of complexity, where a higher complexity results in higher defect acceptance. A first assessment level is typically based on a screening of defect dimensions against workmanship criteria. Such criteria require limited input parameters (e.g. only defect type and length $2c$) and, for individual defects, tend to allow defects no longer than 50 mm [1.6-8]. The defect height (a) is in this case of minor importance; sizing of the height is not required. Although this method takes advantage of its simplicity, it potentially leads to overly conservative assessments. As the cost of a weld repair can be estimated as high as ten times the cost of a normal weld [1.9], it becomes clear that pipeline constructors aim at minimizing repair welding, of course without sacrificing safety. Accordingly, a higher level approach consisting of an engineering critical

assessment (ECA) is often advised. This assessment method aims at allowing larger defects, based on more detailed material characterization and taking into account the exact pipe and defect dimensions and loading conditions. Within an ECA, detailed defect sizing is required. Next to the defect length, the defect height becomes a primary variable. Consequently, this approach implies extra costs, originating from e.g. the material testing and non-destructive evaluation. It is believed that this cost can be compensated for by the lower weld repair rate if larger defects become acceptable [1.10].

1.1.3. Stress & strain based design approach

When assessing the severity of weld defects, the loading condition to which the pipeline is subjected during construction and operation is of major importance. Traditionally, a stress based approach has been considered for onshore applications, where the service stress originates from the internal pressure (p). In this case, the hoop stress (σ_{hoop}) is limited to the design stress (σ_{design}), which typically represents a certain percentage of the material's specified minimum yield strength (e.g. 72% or 80% [1.11]). This hoop stress is calculated as follows:

$$\sigma_{hoop} = p\frac{D-2t}{2t} \approx p\frac{D}{2t} \tag{1.1}$$

In the above equation, D represents the pipe diameter and t the wall thickness of the pipe. The nominator can be simplified as illustrated, since large diameter pipelines with a relatively high D/t-ratio are of primary concern.

Stress based pipeline design codes provide limited guidance on the design and assessment of pipelines that may experience high local strains in service. However, as fossil fuel reserves diminish, gas and oil are more and more extracted from new fields that are typically located in harsh environments (e.g. arctic regions, areas prone to landslides [1.12-14]). These environments impose extra challenges; the pipelines might become subjected to large (plastic) deformations in service [1.15]. Although both tensile and compressive deformations should be considered, this dissertation solely focuses on the tensile deformations. Considering a traditional, stress based design approach, undesirable effects are controlled through a safety margin with respect to the characteristic strength of the material, resulting in a design stress σ_{design}. The characteristic strength (σ_{max}) is usually taken as the stress at 0.5% strain ($R_{t;0.5}$). Therefore the strain corresponding to the service load is reduced below the elastic limit (i.e. smaller than 0.5% - Figure 1.2.a) [1.16]. As a result, a substantially different defect assessment approach is required, a so-called strain based design.

Within a strain based design framework, the maximum allowed service load is expressed in terms of tensile strain (ε_{max}) instead of tensile stress (i.e. σ_{max}). Accordingly, applying a safety margin leads to a design strain, ε_{design}, that can exceed the elastic limit (Figure 1.2.b).

When assessing the criticality of defects, surface breaking defects are generally assumed (Figure 1.3). For that reason, in case of embedded defects, their height is converted to an equivalent surface breaking defect height. It is thereby assumed that buried defects are less severe compared to their surface breaking equivalent [1.17-

19]. Although, a recent publication by Østby et al. [1.20] put questions to the validity of the stress based conversion formulae within a strain-based context. Nevertheless, in the remainder of this dissertation solely surface breaking defects are considered.

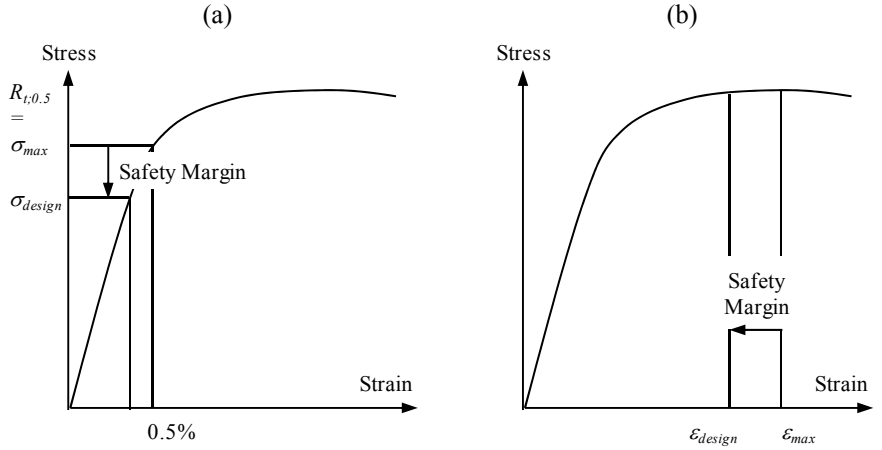

Figure 1.2. Schematic representation of stress based (a) and strain based design (b).

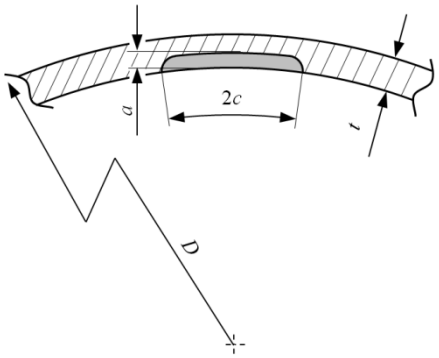

Figure 1.3. Schematic representation of surface breaking defect with depth *a* and arc length 2*c* for a pipe with diameter *D* and wall thickness *t*.

1.2 Strain based ECA methods

Nowadays, several strain based defect assessment procedures for pipeline girth welds are available. These can roughly be divided in three categories:

- tangency approach
- failure assessment diagram
- empirical equations

Regardless the approach, these methods aim to evaluate the criticality of a defect given a minimum required tensile strain capacity. Within the framework of this dissertation, preference will be given to the inverse question: how to accurately determine the tensile strain capacity of a girth welded specimen with a given initial crack size. Thereby, uncertainties going with the sizing of weld defects are omitted. This is related to the research area of those specialized in non-destructive inspection techniques.

1.2.1. Tangency approach

Within the tangency approach, two potential failure modes are considered:

- unstable ductile crack extension, and
- plastic collapse.

The latter represents a condition where failure is not governed by crack growth but by necking of the material. This failure case results in a maximum in the applied force versus remote strain[1] diagram. Consequently, the tensile strain capacity is defined as the strain corresponding to the maximum force.

When evaluating failure due to unstable ductile crack extension, the load transferred to the crack (or crack driving force) is to be characterized. This is done by either the *J*-integral or the Crack Tip Opening Displacement (CTOD) [1.21]. Shih has shown that both parameters are linearly related to each other [1.22]. Unless specifically stated, the CTOD is defined by the 90° intercept method (δ_{90}) in this dissertation [1.23] (Figure 1.4).

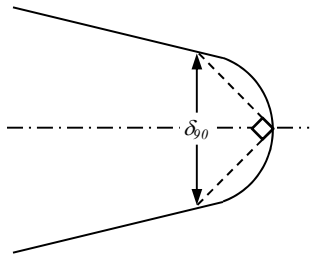

Figure 1.4. Definition of CTOD based on 90° intercept method

Considering the CTOD, it is possible to relate this parameter to:

- the amount of ductile crack extension; the material's tearing resistance (δ_{mat})
- the magnitude of the remotely applied strain; the applied crack driving force (δ_{CDF})

When combining both characteristics, the amount of stable crack extension can be predicted for a given remote strain. Eventually, this leads to the determination of the so-called tensile strain capacity (ε_{max}), which has to fulfill the following requirements:

[1] remote strain (ε_{remote}) is defined as the strain measured in a zone remote from the cracked ligament that, under tensile loading, deforms uniformly.

$$\delta_{CDF} = \delta_{mat} \tag{1.2}$$

$$\frac{\partial \delta_{CDF}}{\partial a} = \frac{\partial \delta_{mat}}{\partial a} \tag{1.3}$$

This procedure is graphically illustrated in Figure 1.5. The red curve represents the material's tearing resistance for an initial crack depth a_0, whereas the black (dotted) lines indicate the crack driving force at varying remote strain levels. The intersections between the tearing resistance curve and the crack driving force curves indicate the amount of stable ductile crack extension (Δa) at given remote strain levels. For a remote strain level $\varepsilon_{remote} = \varepsilon_{max}$ the conditions in Eq. (1.2) and (1.3) are fulfilled. For a strain level exceeding ε_{max}, stable tearing is no longer achievable. Therefore, the predicted tensile strain capacity equals ε_{max}.

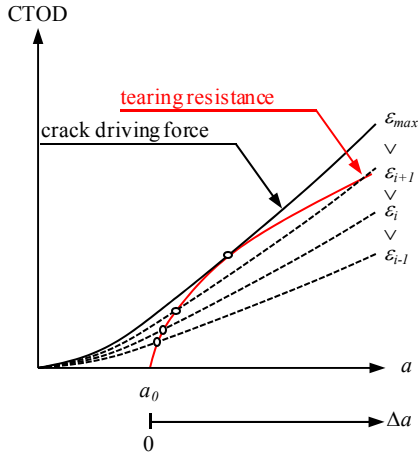

Figure 1.5. Schematic illustration of tangency method

Based on a comparison with numerical simulations including crack growth using a damage mechanics criterion (i.e. the Gurson-Tvergaard-Needleman damage model [1.24]) Østby et al. [1.25] concluded that the tangency approach is conservative.

This approach forms the baseline for the strain based defect assessment procedures proposed by:

- Exxon Mobil [1.26, 27],
- Center for Reliable Energy Systems – British Petroleum (CRES-BP) [1.28-30],
- SINTEF [1.31], and
- standard DNV-OS-F101 (as an extended option in case the FAD approach appears inadequate) [1.32].

The accuracy of such approach depends on two aspects. First, the accuracy of determining the crack driving force curves, which is strongly related to the considered assessment level within the above assessment procedures. The lower assessment levels require only limited input data and material characterization (in some cases only tensile strength). As a result, multiple – worst case – assumptions

are made (e.g. regarding the weld misalignment) for the evaluation of the crack driving force. In contrast, the higher assessment levels are typically based on detailed finite element simulations of cracked geometries with steady, non-growing cracks. As such, the evaluation of the crack driving force accounts for the full details regarding the stress-strain properties of the different materials as well as the exact geometrical properties and loading conditions. Second, the accuracy of the tangency method depends on an accurate determination of the material's tearing resistance. In contrast to the characterization of the tensile strain properties, which can be performed in accordance to standards [1.33], no standard procedures are available for the evaluation of the tearing resistance. This first requires the selection of an appropriate (small scale) test specimen that yields representative, limitedly conservative estimates of the tearing resistance. Second, suitable, well validated test methods should be established to measure both the ductile crack extension and crack driving force (CTOD).

Instead of considering the material's tearing resistance, alternatively a single critical value of the CTOD representing crack initiation can be considered. In this case, ductile crack extension is not accounted for; failure is predicted when the crack driving force exceeds this initiation toughness. This involves a (conservative) simplification of the abovementioned tangency approach, as the remote strain level will not yet have reached its maximum at ductile crack initiation. This method forms the baseline for the Annex C of the standard CSA Z662 [1.6].

1.2.2. Failure assessment diagram

Within the failure assessment diagram (FAD) approach, two failure modes are considered:

- fracture, and
- collapse.

Remark that, in contrast to section 1.2.1, fracture is explicitly considered. This widens the area of applicability to brittle materials. Solely considering unstable ductile crack extension restricts the analysis to ductile materials for the tangency approach. These two failure modes are reflected by the two axes of the failure diagram, the vertical one (K_r) represents the susceptibility to fracture whereas the horizontal one (L_r) represents the collapse limit state (Figure 1.6).

For the assessment of defects under strain based conditions, a traditional stress based FAD or a strain based FAD are used. The stress based FAD provides the basis of the Norwegian offshore standard DNV-OS-F101 [1.32, 34]. Although application in the plastic regime is claimed, this approach is essentially stress based with allowable stress levels beyond yielding as it goes back to the BS 7910-2005 Level 3B tearing assessment [1.35]. This implies that the material's specific stress-strain curve is required to convert the applied strains into stresses. Amongst others, the ductile tearing resistance is also considered as input for this defect assessment procedure [1.34].

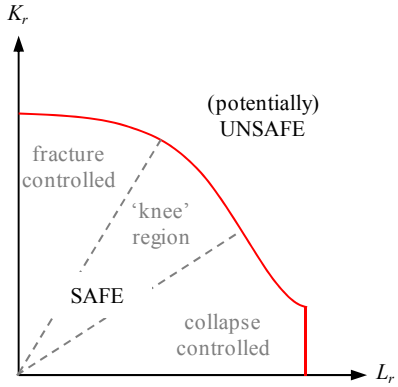

Figure 1.6. Schematic illustration of FAD approach

In the strain based FAD (SB-FAD) proposed by P.J. Budden [1.36], the proximity to collapse is expressed in terms of strain rather than stress. This also requires knowledge of the exact stress-strain properties. The applied strain is limited to the strain corresponding to the material's flow strength[2], which clearly adds conservativeness [1.36, 37]. This strain based FAD provides three assessment levels. At the highest assessment level, finite element simulations can be considered for the evaluation of the crack driving force [1.38]. This allows the incorporation of e.g. mismatch effects. Conversely, internal pressure effects cannot be considered. Furthermore, this approach is known to yield inaccurate, often unconservative, estimates for deep defects and materials materials with a high *Y/T*-ratio [1.37, 39]. Nevertheless, this approach is intended to be standardized in the 2013 revision of R6 [1.38, 40].

1.2.3. Empirical equations

The previously described approaches rely on a sound theoretical basis, rooted in the elastic-plastic fracture mechanics theory. Alternatively, relying on an extensive database of experimental data might also allow predicting the tensile strain capacity. At Ghent University, a vast amount of data is available originating from curved wide plate (CWP) testing (see Chapter 2). A simple analytical equation has been proposed to evaluate the tensile strain capacity [1.41].

$$\varepsilon_{\max} = \left(\frac{Y/T_{BM}+1}{1-Y/T_{BM}}\right)\left(\frac{0.5-C_{mm}\,uEL\,MM_{FS}}{C_d}\right)\left(\frac{2ca}{Wt}\right)+C_{mm}\,uEL\,MM_{FS} \qquad (1.4)$$

[2] The flow strength (σ_{FS}) is defined as the average of the material's yield and tensile strength

With:

Y/T_{BM}	yield-to-tensile strength ratio of the base metal
C_{mm}	correction factor for weld strength mismatch variability
C_d	correction factor for decreasing influence of mismatch with increasing crack size
uEL	uniform elongation of the base metal
MM_{FS}	flow strength mismatch (see section 1.3)

Application of this equation requires only limited input data and material characterization (it is important to stress that also a minimum level of toughness should be demonstrated) and therefore allows for a hands on evaluation of the maximum defect size, given a certain required strain capacity (or vice versa).

It should however be noted that the application area is strictly limited, based on the limitations put on the test conditions (e.g. steel grade, pipe diameter). In addition, the use of CWP test results omits the potential influence of the internal pressure present in a pipeline and the associated biaxial loading conditions. Without going into detail, internal pressure has the potential to strongly reduce the tensile strain capacity. It might therefore be questioned if the CWP test still yields relevant estimates of the tensile strain capacity of pressurized pipes or if a conversion factor is needed? The most recent version of the UGent procedure by Denys et al. [1.41] announces the use of such conversion factor. This factor is subject of the current research project.

1.3 Key factors in assessment procedures

When it comes to evaluating the tensile strain capacity, the influence of several parameters is reported in literature. Without aiming to be complete, this paragraph provides an overview of such parameters included in different standards and procedures. In addition, some parameters are listed whose influence is described in literature but not (yet) considered in the mentioned standards and procedures.

Regarding the material properties, the weld metal strength mismatch is included in all but one of the studied defect assessment procedures. This mismatch expresses the difference between the strength properties of the pipe and weld metal. It should however be noted that different definitions apply, depending on the considered stress level. The different definitions are listed in Table 1.1. In the remainder of this dissertation, the focus is on the flow strength mismatch definition, whereby a material's flow strength is defined as the average of its yield and tensile strengths. This definition was selected since it has shown an excellent (linear) relation with the tensile strain capacity [1.42].

Table 1.1. Mismatch definitions

reference stress		definition	Eq.
yield strength	σ_0	$MM_{YS} = \frac{\sigma_{0;WM} - \sigma_{0;BM}}{\sigma_{0;BM}}$	(1.5)
flow strength	σ_{FS}	$MM_{FS} = \frac{\sigma_{FS;WM} - \sigma_{FS;BM}}{\sigma_{FS;BM}}$	(1.6)
tensile strength	σ_{TS}	$MM_{TS} = \frac{\sigma_{TS;WM} - \sigma_{TS;BM}}{\sigma_{TS;BM}}$	(1.7)

The effect of internal pressure on the tensile strain capacity is accounted for by most defect assessment procedures[3]. This parameter is known to have a potential detrimental effect on the tensile strain capacity, though an exact quantification remains crucial for the defect assessment. To that extent, two procedures provide explicit guidance on this quantification. First, the ExxonMobil procedure assumes that the tensile strain capacity of pipes is reduced by a factor of 1.85 when applying internal pressure [1.26]. Fairchild et al. thereby explicitly state that this correction factor does not aim at being conservative. It should rather be interpreted as an average reduction. To the authors' opinion, such approach is acceptable as the overall conservativeness of the assessment procedure is sufficiently high; there is no need to add additional safety factors. A second relationship is found in the CRES-BP procedure. A dependency on the relative crack depth (a/t) is introduced to conservatively predict the tensile strain capacity of unpressurized pipes ($\varepsilon_{max;up}$) from the pressurized pipes' tensile strain capacity ($\varepsilon_{max;pp}$). This results in the following expression:

$$\frac{\varepsilon_{\max;up}}{\varepsilon_{\max;pp}} = 2.25 - 2\frac{a}{t} \tag{1.8}$$

Such quantification remains unknown for the empirical equation based on curved wide plate test data. It is therefore suggested to establish a so-called pressure correction function, which allows estimating the tensile strain capacity of a pressurized pipe based on curved wide plate test data.

[3] It should be noted at this point that most pressure correction factors have only recently been included in the assessment procedures. These factors were not yet considered / publically available at the start of this PhD project.

	Description		Tensile strain capacity decreases if…	Defect assessment procedures: Exxon Mobil	CRES-BP	CSA Z662 Annex C	SINTEF	DNV OS-F101	SB-FAD	UGent	References
Geometry	Defect depth	a	$a\uparrow$	●	●	●	●	●	●	●	[1.43, 44]
	Defect length	$2c$	$2c\uparrow$	●	●	●	●	●	●	●	[1.43, 44]
	Pipe wall thickness	t	$t\downarrow$	●	●	●	●	●	●	●	[1.43, 44]
	Pipe wall thickness variation			○	○			●	○		
	Diameter	D		○	○		●	●	●		[1.43]
	Misalignment	e	$e\uparrow$	◑	●		●	●	○		[1.45, 46]
	Weld geometry			○	●			●	○		[1.47, 48]
	Defect location (surface breaking or embedded / WMC or HAZ / ...)			○	○	●[3]		○[4]	○		[1.18, 20, 49]
Load	Internal pressure	p	pressure is applied	●	●		●	○		●	[1.43, 48, 50, 51]
	Welding residual stresses							●	◑		[1.52]

	Description		Tensile strain capacity decreases if…	Defect assessment procedures: Exxon Mobil	CRES-BP	CSA Z662 Annex C	SINTEF	DNV OS-F101	SB-FAD	UGent	References
Material properties	Uniform elongation BM	uEL_{BM}	uEL_{BM} ↓	◑	●			●	●	●	[1.53]
	Yield-to-tensile strength ratio BM	Y/T_{BM}		○	●	●	●	●	●	●	[1.43, 48, 54]
	Weld metal strength mismatch	MM	MM ↓	●	●		●	○	○	●	[1.42, 55-57]
	HAZ softening		softening ↑	○[1]	○[2]			○	○		[1.58, 59]
	Tearing resistance		toughness ↓	◑	◑		●	●			[1.60-62]
	Initiation toughness				◑	●					
	Charpy impact toughness				◑					●	[1.63]
	Heterogeneity		heterogeneity ↑					●		●	[1.61, 62, 64, 65]
	Anisotropy										[1.46, 66-68]
	Strain aging										[1.54, 69]

Legend:

- ● Required input parameter
- ◑ Optional input parameter
- ○ Optional input parameter requiring FEA calculations

Footnote:

[1]For API-5L X80 material, a softening of 10% is by default assumed for the more basic assessment levels.

[2]Except for the FEA assessment level, a 10% softening is assumed by default

[3]Distinction is to be made between surface breaking and embedded defects

[4]It is assumed that surface breaking defects are the most critical ones

1.4 Summary and conclusions

In this chapter a review of nowadays girth weld defect assessment procedures has been presented. More specifically, the procedures that are relevant for strain based design applications, in which pipelines are potentially subjected to large (plastic) deformations. These procedures are divided in three groups. A first group makes use of the tangency approach, which allows conservatively estimating the tensile strain capacity based on the material's tearing resistance and the crack driving force curves. The latter are determined from analytical equations prescribed in the respective procedures, though might also be obtained from finite element simulations to reduce the potential conservatism. A second approach is based on the failure assessment diagram. From a theoretical perspective, this approach is equivalent to the tangency approach [1.70]. Preference will however be given to the tangency method as it allows to clearly distinguish fracture related failure from plastic collapse. For the third defect assessment approach, an empiric equation of tensile strain capacity as function of geometrical and material properties was derived as a lower bound to experimental data obtained from curved wide plate testing. This approach does however not account for the influence of internal pressure.

These literature observations revealed the following relevant research topics regarding the evaluation of the tensile strain capacity:

- selection of suitable small scale test specimen and establishing a procedure for the evaluation of the tearing resistance, and
- quantification of the influence of internal pressure to relate the tensile strain capacity of pressurized pipes to CWP specimens.

These research topics serve as the baseline for this dissertation. In the next chapter, a more elaborate discussion is presented based on these issues, eventually resulting in an overview of this dissertation.

1.5 Bibliography

[1.1] Viswanathan, V., Gandy, D., and Findlan, S., 2003, "Power Industry Experiences Surge in Welding Research", Welding Journal, pp. 40-43.

[1.2] Andrews, R. M., and Morgan, L. L., 2004, "Integration of Automated Ultrasonic Testing and Engineering Critical Assessment for Pipeline Girth Weld Defect Acceptance", Pipeline Technology Conference, Ostend, Belgium, pp. 655-668.

[1.3] Bouma, T., and Denys, R. M., 2004, "Automated Ultrasonic Inspection of High-Performance Pipelines: Bridging the Gap between Science and Practice", Pipeline Technology Conference, Ostend, Belgium, pp. 643-654.

[1.4] Moles, M., 2009, "Accurate Pipeline Defect Sizing Using DSP", Pipeline Technology Conference, Ostend, Belgium, pp. 669-682.

[1.5] European Committee for Standardization, 2010, EN 12732: Gas Supply Systems. Welding Steel Pipework. Functional Requirements.

[1.6] Canadian Standards Association, 2011, Z662 - 11: Oil and Gas Pipeline Systems.

[1.7] 2010, API 1104: Welding of Pipelines and Related Facilities.

[1.8] Knauf, G., and Hopkins, P., 1996, "The EPRG Guidelines on the Assessment of Defects in Transmission Pipeline Girth Welds", 3R International, 35, pp. 620-624.

[1.9] Ahmed, H., Abbas, M. I., and Shahen, M. A. K., 2013, "Girth Weld Fitness after Multiple SMAW Repairs", Pipeline and Gas Journal, 240, pp. 1-4.

[1.10] Lee, K. Y., 2008, "Reducing Pipeline Construction Costs with Girth Weld ECA", Pipeline and Gas Journal, 235, pp. 16-17.

[1.11] McLamb, M., Hopkins, P., Marley, M., and Nessim, M., 2002, "A Justification for Designing and Operating Pipelines up to Stresses of 80% Smys", International Pipeline Conference, Calgary, Alberta, Canada, paper n° IPC02-27007.

[1.12] DNV, Major New Oil Discovery in the Barents Sea, via: www.dnv.com accessed on: 02-02-2012.

[1.13] Lillig, D. B., 2008, "The First (2007) ISOPE Strain Based Design Symposium - a Review", International Offshore and Polar Engineering Conference, Vancouver, Canada, pp. 1-12.

[1.14] Lillig, D. B., Newbury, B. D., and Altstadt, S. A., 2009, "The Second (2008) ISOPE Strain Based Design Symposium - a Review", International Offshore and Polar Engineering Conference, Osaka, Japan, pp. 1-10.

[1.15] Arslan, H., Hamilton, J., Lele, S., Minnaar, K., Albrecht, B., Cook, M. F., and Wong, P., 2010, "Strain Demand Estimation for Pipelines in Challenging Arctic and Seismically Active Regions", International Pipeline Conference, Calgary, Alberta, Canada, paper n° IPC2010-31505.

[1.16] Vitali, L., Torselletti, E., Marchesani, F., and Bruschi, R., 1996, "Use (and Abuse) of Strain Based Criteria in Offshore Pipeline Technology", Advances in Subsea Pipeline Engineering and Technology, Aberdeen, UK, paper n° ASPECT-96-135.

[1.17] Wang, Y. Y., Liu, M., Horsley, D., and Zhou, J., 2006, "A Quantitative Approach to Tensile Strain Capacity of Pipelines", International Pipeline Conference, Calgary, Alberta, Canada, paper n° IPC2006-10474.

[1.18] Wang, Y. Y., Cheng, W., and Horsley, D., 2004, "Tensile Strain Limits of Buried Defects in Pipeline Girth Welds", International Pipeline Conference, Calgary, Alberta, Canada, paper n° IPC04-0524.

[1.19] Olso, E., Berg, E., Holthe, K., Nyhus, B., Skallerud, B., Thaulow, C., and Ostby, E., 2008, "Effect of Embedded Defects in Pipelines Subjected to Plastic Strains During Operation", International Offshore and Polar Engineering Conference, Vancouver, Canada, pp. 143-148.

[1.20] Ostby, E., Nyhus, B., and Thaulow, C., 2011, "Small-Scale Testing of the Effect of Embedded Defect Position in the Thickness Direction of an X65 UOE Pipe", International Offshore and Polar Engineering Conference, Maui - USA, pp. 593-599.

[1.21] Anderson, T. L., 1995, "Fracture Mechanics: Fundamentals and Applications", CRC press, Texas.

[1.22] Shih, C. F., 1981, "Relationships between the J-Integral and the Crack Opening Displacement for Stationary and Extending Cracks", Journal of Mechanics and Physics of Solids, 29, pp. 305-326.

[1.23] Rice, J. R., 1968, "A Path Independent Integral and the Approximate Analysis of Strain Concentration by Notches and Cracks", Journal of Applied Mechanics, 35, pp. 379-386.

[1.24] Gurson, 1977, "Continuum Theory of Ductile Rupture by Nucleation and Growth: Part I - Yield Criteria and Flow Rules for Porous Ductile Media", Journal of Engineering Materials and Technology, 99, pp. 2-15.

[1.25] Ostby, E., Thaulow, C., and Nyhus, B., 2007, "A New Approach to Ductile Tearing Assessment of Pipelines under Large-Scale Yielding", International Journal of Pressure Vessels and Piping, 84, pp. 337-348.

[1.26] Fairchild, D. P., Kibey, S., Tang, H., Krishnan, V. R., Macia, M. L., Cheng, W., and Wang, X., 2012, "Continued Advancements Regarding Capacity Prediction of Strain-Based Pipelines", International Pipeline Conference, Calgary, Alberta, Canada, paper n° IPC2012-90471.

[1.27] Fairchild, D. P., Macia, M. L., Kibey, S., Wang, X., Krishnan, V. R., Bardi, F., Tang, H., and Cheng, W., 2011, "A Multi-Tiered Procedure for Engineering Critical Assessment of Strain-Based Pipelines", International Offshore and Polar Engineering Conference, Maui, HI, United States, pp. 698-705.

[1.28] Wang, Y. Y., Liu, M., Zhang, F., Horsley, D., and Nanney, S., 2012, "Multi-Tier Tensile Strain Models for Strain-Based Design - Part 1: Fundamental Basis", International Pipeline Conference, Calgary, Alberta, Canada, paper n° IPC2012-90690.

[1.29] Liu, M., Wang, Y. Y., Song, Y., Horsley, D., and Nanney, S., 2012, "Multi-Tier Tensile Strain Models for Strain-Based Design - Part 2: Development and Formulation of Tensile Strain Capacity Models", International Pipeline Conference, Calgary, Alberta, Canada, paper n° IPC2012-90659.

[1.30] Liu, M., Wang, Y. Y., Horsley, D., and Nanney, S., 2012, "Multi-Tier Tensile Strain Models for Strain-Based Design - Part 3: Model Evaluation Agains Experimental Data", International Pipeline Conference, Calgary, Alberta, Canada, paper n° IPC2012-90660.

[1.31] Ostby, E., 2005, "Fracture Control - Offshore Pipelines: New Strain-Based Fracture Mechanics Equations Including the Effectsof Biaxial Loading, Mismatch and Misalignment", International Conference on Ocean, Offshore and Arctic Engineering, Halkidiki, Greece, paper n° OMAE2005-67518.

[1.32] Det Norske Veritas, 2012, OS-F101: Submarine Pipeline Systems.

[1.33] 2011, E8/E8m: Standard Test Methods for Tension Testing of Metallic Materials.

[1.34] Det Norske Veritas, 2006, RP-F108: Fracture Control for Pipeline Installation Methods Introducing Cyclic Plastic Strain.

[1.35] 2005, BS 7910: Guide to Methods for Assessing the Acceptability of Flaws in Metallic Structures.

[1.36] Budden, P. J., 2006, "Failure Assessment Diagram Methods for Strain-Based Design", Engineering Fracture Mechanics, 73, pp. 537-552.

[1.37] Budden, P. J., and Ainsworth, R. A., 2012, "The Shape of a Strain-Based Failure Assessment Diagram", International Journal of Pressure Vessels and Piping, 89, pp. 59-66.

[1.38] Horn, A., Trull, M., and Hertelé, S., 2013, "Failure Prediction of Curved Wide Plates Using the Strain-Based Failure Assessment Diagram with Correction for Constraint and Notch Radius", Pressure Vessels and Piping Conference, Paris, France, paper n° PVP2013-97562.

[1.39] Budden, P. J., and Smith, M. C., 2009, "Numerical Validation of a Strain-Based Failure Assessment Diagram Approach to Fracture", Pressure Vessels and Piping Conference, Prague, Czech Republic, paper n° PVP2009-77377.

[1.40] 2012, R6 - Assessment of the Integrity of Structures Containing Defects.

[1.41] Denys, R., Hertelé, S., Verstraete, M., and De Waele, W., 2011, "Strain Capacity Prediction for Strain-Based Pipeline Designs", International Workshop on Welding of High Strength Pipeline Steels, Araxá, Brazil, pp. 1-13.

[1.42] Hertelé, S., De Waele, W., Denys, R., Verstraete, M., and Horn, A., 2012, "Weld Strength Mismatch in Strain Based Flaw Assessment: Which Definition to Use?", Pressure Vessels and Piping Conference, Toronto, Canada, paper n° PVP2012-78306.

[1.43] Jayadevan, K. R., Ostby, E., and Thaulow, C., 2004, "Fracture Response of Pipelines Subjected to Large Plastic Deformation under Tension", International Journal of Pressure Vessels and Piping, 81, pp. 771-783.

[1.44] Ostby, E., Jayadevan, K. R., and Thaulow, C., 2005, "Fracture Response of Pipelines Subjected to Large Plastic Deformation under Bending", International Journal of Pressure Vessels and Piping, 82, pp. 201-215.

[1.45] Kibey, S. A., Minnaar, K., Issa, J. A., and Gioielli, P. C., 2008, "Effect of Misalignment on the Tensile Strain Capacity of Welded Pipelines", International Offshore and Polar Engineering Conference, Vancouver, Canada, pp. 90-95.

[1.46] Wang, Y.-Y., and Liu, M., 2007, "The Role of Anisotropy, Toughness Transferability and Weld Misalignment in the Strain Based Design of Pipelines", International Offshore and Polar Engineering Conference, pp. 3164-3171.

[1.47] Denys, R., Hertelé, S., and Verstraete, M., 2010, "Strain Capacity of Weak and Strong Girth Welds in Axially Loaded Pipelines", International Pipeline Technology Conference, Beijing, China, pp. 116-124.

[1.48] Gordon, J. R., Zettlemoyer, N., and Mohr, W. C., 2007, "Crack Driving Force in Pipelines Subjected to Large Strain and Biaxial Stress Conditions", International Offshore and Polar Engineering Conference, Lisbon, Portugal, pp. 3129-3140.

[1.49] Duan, D.-M., Wang, Y.-Y., Chen, Y., and Zhou, J., 2008, "Modeling and CMOD Mapping of Surface Cracked Wide Plates", International Pipeline Conference, Calgary, Canada, paper n° IPC2008-64425.

[1.50] Ostby, E., and Hellesvik, A. O., 2007, "Fracture Control - Offshore Pipeline JIP: Results from Large Scale Testing on the Effect of Biaxial Loading on Strain Capacity of Pipes with Defects", International Offshore and Polar Engineering Conference, Lisbon, Portugal, pp. 3231-3237.

[1.51] Ostby, E., and Hellesvik, A. O., 2008, "Large-Scale Experimental Investigation of the Effect of Biaxial Loading on the Deformation Capacity of Pipes with Defects", International Journal of Pressure Vessels and Piping, 85, pp. 814-824.

[1.52] Ainsworth, R. A., Budden, P. J., Oh, C. Y., and Kim, Y.-J., 2013, "The Treatment of Secondary Strains within a Strain-Based Failure Assessment Diagram", International Journal of Pressure Vessels and Piping, 104, pp. 14-20.

[1.53] Hertelé, S., De Waele, W., Denys, R., and Verstraete, M., 2011, "Sensitivity of Plastic Response of Defective Pipeline Girth Welds to the Stress-Strain Behavior of Base and Weld Metal", International Conference on Ocean, Offshore and Arctic Engineering, Rotterdam, The Netherlands, paper n° OMAE2011-49239.

[1.54] Wang, Y. Y., Liu, M., Gianetto, J. A., and Tyson, W. R., 2010, "Considerations of Linepipe and Girth Weld Tensile Properties for Strain-Based Design of Pipelines", International Pipeline Conference, Calgary, Alberta, Canada, paper n° IPC2010-31376.

[1.55] Kan, W. C., Weir, M., Zhang, M. M., Lillig, D. B., Barbas, S. T., Macia, M. L., and Biery, N. E., 2008, "Strain Based Pipelines: Design Consideration Overview", International Offshore and Polar Engineering Conference, Vancouver, Canada, pp. 174-181.

[1.56] Denys, R. M., 2008, "Weld Metal Strength Mismatch: Past, Present and Future", International Symposium to Celebrate Prof. Masao Toyoda's Retirement from Osaka University, pp. 115-148.

[1.57] Motohashi, H., and Hagiwara, N., 2007, "Analytical Study of Effects of Strength Matching on Strain Capacity", International Offshore and Polar Engineering Conference, Lisbon, Portugal, pp. 3101-3106.

[1.58] Wang, Y.-Y., Stephens, M., and Horsley, D., 2008, "Preliminary Analysis of Tensile Strain Capacity of Full Scale Pipe Tests with Internal Pressure", International Offshore and Polar Engineering Conference, Vancouver, Canada, pp. 40-47.

[1.59] Wilkowski, G., Rudland, D., Shim, D. J., Brust, F. W., and Babu, S., 2008, "Advanced Integration of Multi-Scale Mechanics and Welding Process Simulation in Weld Integrity Assessment", Engineering Mechanics Corporation of Columbus (Emc²), Columbus.

[1.60] Wang, Y. Y., Liu, M., and Horsley, D., 2007, "Apparent Toughness from Constraint Considerations and Direct Testing", International Offshore and Polar Engineering Conference, Lisbon, Portugal, pp. 3179-3185.

[1.61] Ostby, E., Hauge, M., Levold, E., Sandvik, A., Nyhus, B., and Thaulow, C., 2008, "Strain Capacity of SENT Specimens - Influence of Weld Metal Mismatch and Ductile Tearing Resistance", International Offshore and Polar Engineering Conference, Vancouver, Canada, pp. 64-71.

[1.62] Quintana, M. A., Babu, S., Major, J., Dallam, C., and James, M., 2010, "Weld Metal Toughness - Sources of Variation", International Pipeline Conference, Calgary, Alberta, Canada, paper n° IPC2010-31402.

[1.63] Denys, R., Andrews, R., Zarea, M., and Knauf, G., 2010, "EPRG Tier 2 Guidelines for the Assessment of Defects in Transmission Pipeline Girth Welds", International Pipeline Conference, Calgary, Alberta, Canada, paper n° IPC2010-31640.

[1.64] Hertelé, S., Verstraete, M., Van Minnebruggen, K., Denys, R., and De Waele, W., 2012, "Curved Wide Plate Testing with Advanced Instrumentation and Interpretation", International Pipeline Conference, Calgary, Alberta, Canada, paper n° IPC2012-90591.

[1.65] Wang, Y. Y., Liu, M., Weeks, T., Richards, M., and McColskey, D., 2010, "Broad Perspectives of Girth Weld Tensile Strain Response", International Pipeline Conference, Calgary, Alberta, Canada, paper n° IPC2010-31369.

[1.66] Hilgert, O., Zimmerman, S., and Kalwa, C., 2013, "Anisotropy - Benefits of UOE Line Pipe", International Pipeline Conference, Calgary, Alberta, Canada, paper n° IPC2012-90063.

[1.67] Liu, M., and Wang, Y. Y., 2007, "Modeling of Anisotropy of Tmcp and UOE Linepipes", International Offshore and Polar Engineering Conference, pp. 288-293.

[1.68] Mirone, G., and Corallo, D., 2013, "Stress-Strain and Ductile Fracture Characterization of an X100 Anisotropic Steel: Experiments and Modelling", Engineering Fracture Mechanics, 102, pp. 118-145.

[1.69] Klein, R., Collins, L., Hamad, F., Chen, X., and Bai, D., 2008, "Determination of Mechanical Properties of High Strength Linepipe", International Pipeline Conference, Calgary, Alberta, Canada, paper n° IPC2008-64101.

[1.70] European Fitnet for Service Network, 2006, FITNET FFS MK7 - Fracture Module.

Chapter 2

–

Research Approach from Full- to Sub-Scale

2.1. Introduction

In Chapter 1, the research context has been described and two research questions have been identified. On the one hand, the accurate evaluation of a metal's tearing resistance using laboratory scale specimens needs to be addressed. On the other hand, the quantification of the relationship between the tensile strain capacity in pressurized pipes and CWP specimens deserves attention. Both require an improved understanding of the relationship between full and sub-scale mechanical behaviour of welded structures subjected to tensile load. Referring to the tangency approach (section 1.2.1 in Chapter 1), this relationship comprises both the materials' tearing resistance and the crack driving force:

- *tearing resistance*: the tearing resistance is not only a material property, but also depends on the loading mode and test specimen geometry [2.1]. This dependency is also referred to as the crack tip constraint, which is discussed in full detail in section 2.2.
- *crack driving force*: in the framework of this dissertation, the crack driving force expresses the crack tip opening displacement (CTOD) as function of the remote strain (ε_{remote}). Ideally, this relation is identical for the sub- and full-scale specimen, as discussed in section 2.3.

Following the description of these theoretical concepts, based on a literature review, the research approach is presented in section 2.4. A clear distinction is made between the experimental and numerical (finite element) work. This section concludes with an outline of the work presented in the remainder of this dissertation.

2.2. Constraint

To assess the difference between the resistance curves obtained by means of full- and sub-scale testing, the constraint ahead of the crack tip is quantified based on an analysis of the crack tip stress fields. A number of analysis approaches are discussed below in section 2.2.1, introducing so-called constraint parameters. Experimental studies revealed that, using these parameters, the tearing resistance curves can be scaled to account for constraint effects [2.2-4]. Therefore, a comparison of these parameters derived at different testing scales allows the identification of a suitable test specimen. This is discussed in section 2.2.2 for pressurized pipes.

2.2.1. Constraint parameters

To characterize the crack tip stress fields, fracture mechanics theories traditionally relied on a single parameter (e.g. K_I[1] or J-integral). However, these theoretical frameworks are only valid under high constraint conditions. The actual crack tip stress fields might differ largely from the ones described by the single parameter theories. Consequently, effort has been spent to describe the crack tip stress fields more accurately by introducing a second parameter, for example the T-stress, the Q-parameter or the A_2-parameter [2.5-12]. Within this dissertation the T-stress is not considered, since the theoretical basis breaks down under elastic-plastic conditions [2.13, 14]. As a result, the relevance of this parameter can be questioned when plasticity effects are present [2.15]. The parameters Q and A_2 appear equivalent when considering the in-plane constraint. In contrast, the out-of-plane constraint is captured more accurately using the Q-parameter [2.15]. In addition, the calculation of the Q-parameter is more straight-forward. Therefore, the Q-parameter is selected for the current constraint analysis. Remark that this approach corresponds to other research institutes (e.g. University of Sao Paulo [2.16, 17], SINTEF [2.18, 19]).

The calculation of the Q-parameter is linked to the description of the crack tip stress fields using a single parameter. For an elastic-plastic homogeneous material, the crack tip stress fields (σ_{ij}) are described by the Hutchinson, Rice and Rosengren (HRR) equation [2.20, 21]. This equation considers only the first order term of the crack tip stress fields. Under low constraint conditions however, the higher order terms should also be taken into account. Based on an extensive set of finite element simulations, O'Dowd and Shih have found that these higher order terms represent a spatially uniform hydrostatic shift of the crack tip stress field [2.8, 9]. This hydrostatic shift can hence be characterized by a single parameter, Q.

$$\sigma_{ij} = (\sigma_{ij})_{\mathrm{HRR}} + \text{higher order terms} \tag{2.1}$$

$$\sigma_{ij} = (\sigma_{ij})_{\mathrm{HRR}} + Q\ \sigma_0\ \delta_{ij} \tag{2.2}$$

O'Dowd and Shih point out that this uniform shift is valid for radial distances (r, Figure 2.1) ahead of the crack tip between $J / \sigma_0 < r < 5\ J / \sigma_0$. Consequently, the Q-parameter is most commonly evaluated at a distance $r = 2\ J / \sigma_0$. In addition, this location is believed to be representative both for ductile and cleavage fracture [2.14, 22]. Remark furthermore that the distances are expressed as a function of the factor

[1] Mode I stress intensity factor, commonly used in linear elastic fracture mechanics.

J / σ_0. Therefore, the J-integral is seen as a measure for the size of the plastic zone, whereas the Q-parameter determines the magnitude of the crack tip stress field.

Although the original work of O'Dowd and Shih prescribes the use of the HRR solution as a reference field, this reference field can also be obtained from a plane strain Modified Boundary Layer (MBL) analysis (see also Appendix D). Considering the crack tip opening stress in the forward region ($\theta = 90°$, Figure 2.1), the Q-parameter is defined as:

$$Q = \frac{\sigma_{\theta\theta} - \sigma_{\theta\theta;MBL}}{\sigma_0} \qquad \bar{r} = r/\left(J/\sigma_0\right) = 2 \qquad \theta = 90° \tag{2.3}$$

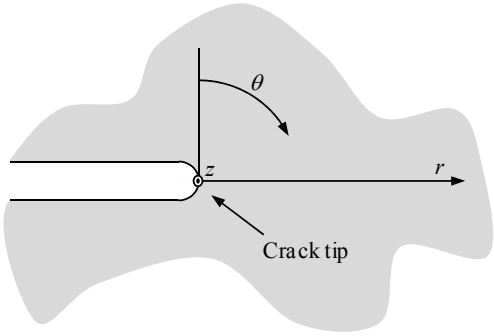

Figure 2.1. Definition of location relative to crack tip

In addition to the Q-parameter, the Q_m-parameter can be evaluated. This parameter is based on the hydrostatic stress ahead of the crack tip and is therefore more consistent with the interpretation as a triaxiality parameter [2.23]. The parameter Q_m is evaluated at the same location as the Q-parameter.

$$Q_m = \frac{\sigma_m - \sigma_{m;MBL}}{\sigma_0} \qquad \bar{r} = r/\left(J/\sigma_0\right) = 2 \qquad \theta = 90° \tag{2.4}$$

The hydrostatic stress (σ_m) is defined as:

$$\sigma_m = \frac{\sigma_{ii}}{3} \tag{2.5}$$

In general, both Q and Q_m yield similar values [2.23, 24], although Q_m is known to capture out-of-plane constraint effects more sensitively. This out-of-plane constraint is believed to be of importance for ductile failure, in contrast to cleavage where the in-plane constraint is of major importance [2.25]. As a result, both the Q and Q_m parameter have been studied in the remainder of this dissertation. However, only Q-values will be reported unless significant differences between Q and Q_m have been observed.

As the definition of the Q-parameter only takes into account the crack tip stresses at one selected location, the self-similarity between the actual and reference crack tip stress fields needs to be evaluated. The parallelism between both crack tip stress fields is evaluated by comparing the Q-parameters evaluated at a normalized distance ahead of the crack tip $r = J / \sigma_0$ and at $r = 5\, J / \sigma_0$ [2.26, 27].

$$\Delta Q = \frac{\left| Q_{\bar{r}=1} - Q_{\bar{r}=5} \right|}{4} \tag{2.6}$$

Based on results published in literature, this difference should be smaller than 0.1 to obtain a description of the crack tip stress fields that is independent of the radial distance from the crack tip [2.14, 28]. High ΔQ values originate for instance from bending stresses.

Whereas the *J-Q* and *J-Q*$_m$ frameworks aim at accurately describing the crack tip stress fields, other parameters could as well be introduced to quantify the crack tip constraint. One such parameter is the stress triaxiality, *h*, defined as the ratio of the hydrostatic stress (σ_m) to the Von Mises equivalent stress (σ_e) [2.29, 30]. This parameter is calculated at the same radial position with respect to the crack tip.

$$h = \frac{\sigma_m}{\sigma_e} \qquad \bar{r} = r/\left(J/\sigma_0\right) = 2 \qquad \theta = 90° \tag{2.7}$$

As the primary aim in this dissertation is to quantify the constraint, rather than to describe the stress fields, the stress triaxiality parameter gains interest. Remark that an excellent correlation between this parameter *h* and the *Q*-parameter has been reported in literature. This correlation depends on the material properties though appears independent of the specimen geometry, deformation level and crack dimensions [2.15, 29-31].

2.2.2.Selection of test specimen configuration

This section aims to identify a suitable laboratory scale specimen for the evaluation of the tearing resistance that is representative for the structural behaviour. Bearing in mind the link between the tearing resistance and the constraint parameters, this identification process is based on a comparison of the constraint conditions of laboratory scale test specimens and a pressurized pipe.

Different fracture mechanics test specimens are available. The most frequently reported types are listed below and schematically represented in Figure 2.2.

- *Single edge notch bending (SENB)*: the evaluation of the tearing resistance using this specimen is standardized [2.32, 33]. It is traditionally used in pipeline defect assessment and prescribed by international standards.
- *Compact tension (CT)*: test procedures for this specimen are also standardized [2.32, 33].
- *Single edge notch tension (SENT)*: several configurations of the SENT specimen are reported. One important difference relates to the boundary conditions. Rotation in the end grips might be restricted (i.e. clamped conditions; SENT$_c$) or free (i.e. pinned conditions; SENT$_p$).
- *Double edge notch tension (DENT)*
- *Centre cracked tension (CCT)*

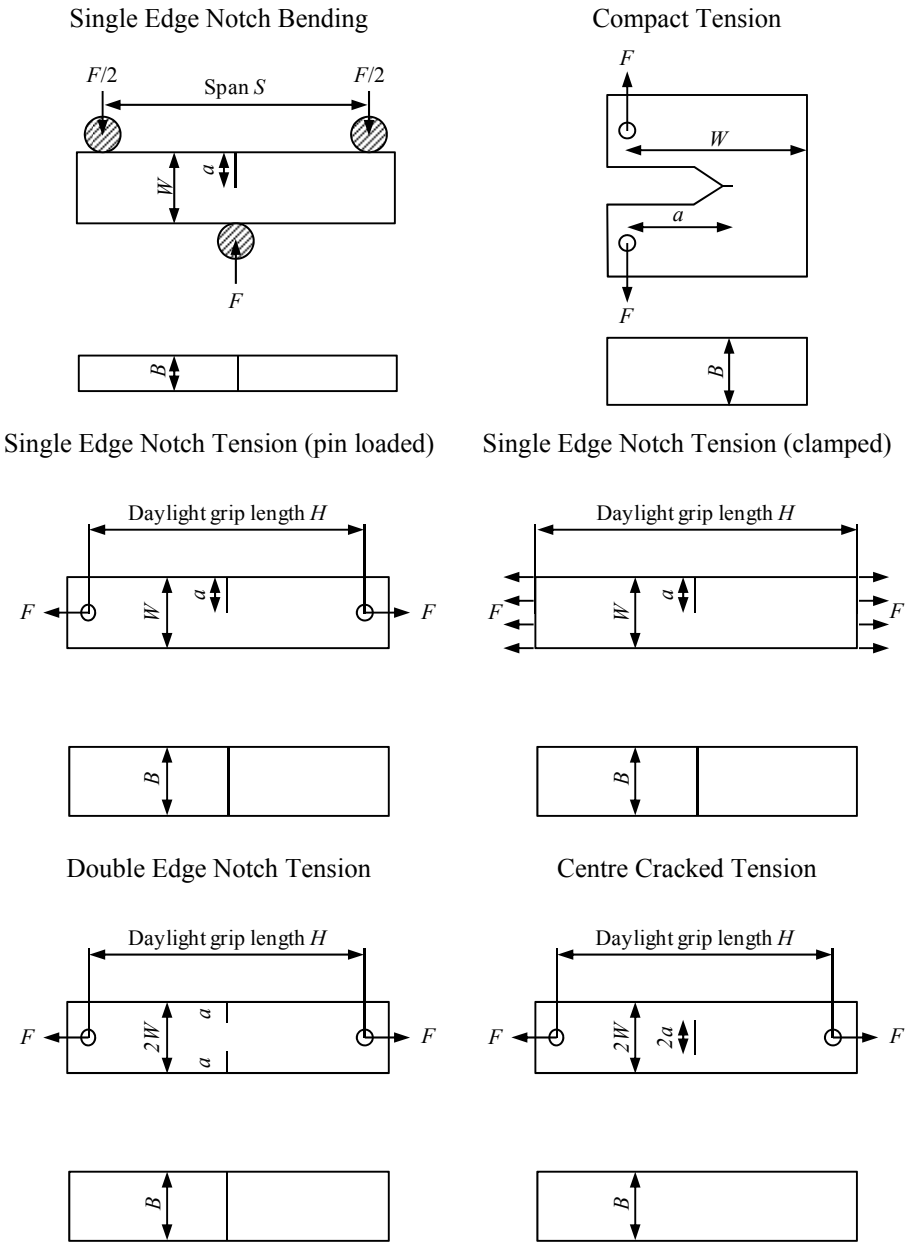

Figure 2.2. Schematic representation of laboratory scale fracture mechanics test specimens

For all specimens, the thickness is most commonly taken equal to or as close as possible to the wall thickness. This is of particular interest for materials with pronounced heterogeneity in the through thickness direction. This heterogeneity can be observed for both base and weld metals [2.34-36].

Besides these specimen types, the CWP test is widely accepted for pipeline girth weld testing [2.37, 38]. These CWP specimens contain a surface breaking notch, typically located at the weld metal center (WMC) line or heat affected zone (defect depth = a, defect length = $2c$). As the CWP specimens are extracted from a pipe, their curvature is defined by the pipe's diameter (Figure 2.3). In addition, the wall thickness and weld geometry are conserved, i.e. the weld cap reinforcement is not removed. The geometrical properties adopted in this thesis correspond to the UGent guidelines for CWP testing [2.39], which prescribe specimens with an arc length $2W$ of 300 mm and a 900 mm long prismatic section ($2L$).

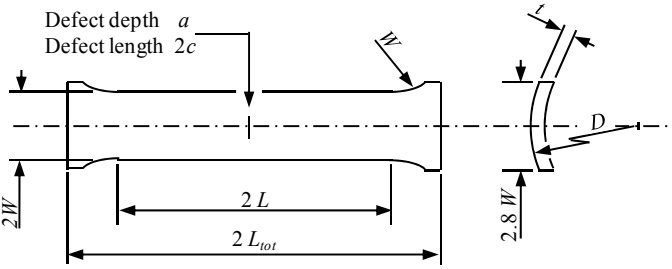

Figure 2.3. Schematic representation of CWP specimen [2.39].

Before studying the constraint in these laboratory scale specimens, the evolution of the constraint parameters for full-scale pipes is studied as a function of the load applied to the crack. The latter is expressed by the J-integral. A non-linear constraint evolution is observed (Figure 2.4). With increasing load levels (increasing J-integral), the constraint decreases [2.13, 16, 40]. This is referred to as loss of constraint. This loss of constraint appears only limitedly dependent on the material strain hardening properties [2.27] and curvature (D/t-ratio) [2.41], though depends on the relative crack depth (a/t). The constraint increases with increasing initial crack depths, as is as well observed from simulated tearing resistance curves.

Regarding the loading mode, no differences in constraint are reported in literature between tension and bending loading [2.40-42]. This is related to the fact that pipes with a high D/t-ratio are primarily concerned. Hence, defects located in the zone subjected to tension are subjected to the maximum crack driving force. For these defects, a global bending loading results in an approximately uniform tensile stress across the wall thickness of the pipe. As a result, the stress distribution does not differ significantly between specimens loaded in tension or bending.

Another loading parameter that potentially affects the level of constraint is the internal pressure. In literature, the influence of this internal pressure is not uniquely described. A minor shift of the constraint is predicted based on J-Q calculations in [2.30, 43, 44] (Figure 2.5). On the other hand, no significant influence of the internal pressure on the tearing resistance has been reported, both from a numerical and an experimental point of view, in [2.40, 45-49]. Consequently, further research seems required.

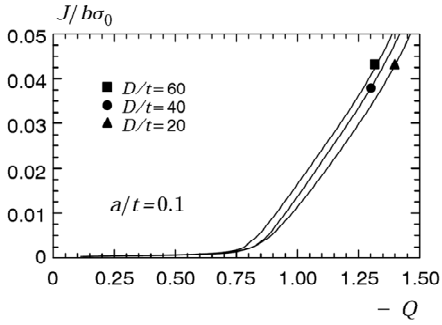

Figure 2.4. Constraint evolution in pipe specimens subjected to tension loading[2] [2.41].

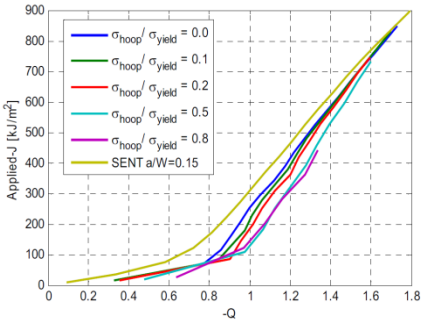

Figure 2.5. Influence of internal pressure on constraint evolution of pressurized pipe specimen with relative crack depth $a/t = 0.15$, relative to constraint evolution of SENT specimen with identical relative crack depth[3] [2.30].

After reviewing the constraint evolution for pipe specimens, the focus is again on the selection of a suitable laboratory scale test specimen. From the specimens introduced above, the CT specimen shows no loss of constraint upon loading [2.50]. The same applies for standard, deeply notched ($a/W = 0.5$) SENB specimens [2.18, 50]. As a result, both specimens are commonly referred to as high constraint specimens. Their crack tip stress fields can be described by the HRR-field without additional parameters [2.18, 51]. This contrasts to the constraint evolution for pipe specimens, which showed a pronounced loss of constraint (crack tip stress fields clearly below HRR-field). Consequently, SENB and CT specimens should not be used for the characterization of the tearing resistance for the strain based assessment of pipeline girth weld defects [2.40, 42, 52].

In contrast, SENB specimens with a shallow notch ($a/W << 0.5$, e.g. 0.2) show a clear loss of constraint upon loading, which however remains limited compared to SENT specimens with the same initial relative crack depth [2.18]. This relative crack depth also shows a pronounced influence on the constraint evolution in SENT specimens. In addition, relative to the SENB specimens, the constraint evolution for the SENT specimens indicates a more limited conservatism with respect to pipe

[2]The parameter b represents the remaining ligament thickness ($b = t - a_0$)

[3] $\sigma_{yield} = \sigma_0$ = yield strength

specimens (Figure 2.5) [2.30, 40, 41]. This explains the recent interest in SENT testing for the characterization of tearing resistance. In general, preference is given to the clamped SENT specimen [2.53, 54]. Provided the daylight grip length is large enough (e.g. $H = 10\ W$), the boundary conditions are more uniquely defined compared to pinned specimens and the constraint is not subjected to small variations of the pin position [2.41].

The CCT panel potentially shows a lower constraint than the pipe specimen and should therefore not be considered. The DENT specimen, however, also approximates the constraint in a pipe specimen [2.55].

Finally, comparing the CWP test and the pipe specimen, no unique correlation is found in literature. Some results indicate that the tearing resistance in CWP specimens is higher, whilst others show a constraint match between both specimen types [2.56-59]. Further research is required with respect to this point.

2.2.3.Summary

The difference between the tearing resistance curves for full- and sub-scale specimens relates to the constraint ahead of the crack tip. Both the Q- and h-parameter are believed to allow for an accurate evaluation of this constraint under elastic-plastic conditions. The J-Q theory additionally allows quantifying the crack tip stress fields, whilst the triaxiality parameter h only allows quantifying the constraint.

These parameters have already been extensively used for constraint studies. A literature review revealed a pronounced loss of constraint upon the development of plasticity for pipe specimens. The dependency of this constraint evolution on the biaxial loading (due to internal pressure) however requires further investigation. Regarding the selection of a suitable sub-scale specimen, the SENB and CT specimens do not show a loss of constraint upon loading. Consequently, these should not be considered for the strain based assessment of pipeline girth weld defects.

The constraint in SENT and DENT specimens most closely approximates the pipe specimens (in a conservative way, i.e. slightly higher constraint). From a practical point of view, the SENT specimen is preferred in this dissertation. First, the required test capacity for SENT testing is only about half of the required capacity for DENT testing. Analogous, the amount of test material required per test is higher for DENT testing. This also implies a more pronounced thickness reduction for DENT testing, since the final specimens need a rectangular cross section fitting the originally curved pipe [2.60, 61]. At last, it is noted that the preparation and analysis of DENT specimens is more challenging, as two different cracks need to be monitored.

The constraint in CWP specimens is believed to be representative for pipe specimens. However, a clear description of the constraint evolution in CWP specimens is currently lacking in literature. Given the historical interest in CWP testing, a more dedicated analysis is desired.

2.3. Crack driving force

Numerous parameters impact the crack driving force curve. These can be divided in three groups:

- geometrical parameters (relative defect size, misalignment, …),
- material parameters (strain hardening capacity, mismatch, …), and
- loading conditions (axial tension, internal pressure, …).

For a qualitative description of these parameters' effect on the crack driving force curves, the reader is referred to section 1.3 of Chapter 1. Note that this section describes the influence of several parameters on the tensile strain capacity. Constraint effects are however restricted to the tearing resistance. Hence, bearing in mind the tangency approach, the effect of the listed parameters on the crack driving force in pipe specimens is directly related to the results presented in this overview.

A detailed comparison of the crack driving force in SENT and pipe specimens is not presented, as the primary aim for SENT testing is not to obtain the tensile strain capacity. Contrary, CWP specimens have since long been used for the evaluation of the tensile strain capacity [2.62, 63]. The relation between the crack driving force in tensile loaded CWP and pipe specimens (without internal pressure) is not reported in literature. Though, it is generally believed that CWP testing yields a conservative estimate, given the limited width of the plate sections relative to the full pipe geometry and the similarity in the loading conditions. However, the biaxial loading, resulting from the internal pressure, has shown to drastically increase the crack driving force and hence reduce the tensile strain capacity [2.45, 64-66].

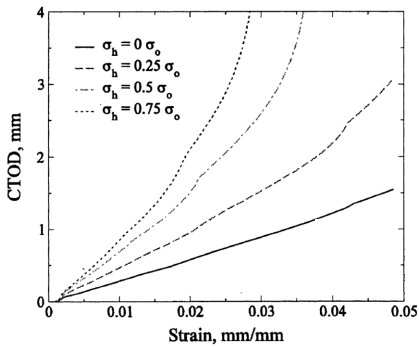

Figure 2.6. Influence of internal pressure (expressed in terms of $\sigma_h = \sigma_{hoop}$) on crack driving force as function of the remote strain for pipe specimens [2.65]

As a result, the crack driving force is unlikely to match between pressurized pipes and CWP specimens. Therefore, the curved wide plate test method might be modified to increase the crack driving force, e.g. by incorporating an out-of-plane loading component. However, the impact on the crack tip constraint should in that case be considered as well. Alternatively, a correction function can be developed relating the crack driving force for both test specimens. More generally, such correction function could also be developed with respect to the tensile strain capacity. Such approach, in particular when focusing on the tensile strain capacity, has the advantage that it can be applied to historical data. As a result, it can easily be included in the empirical defect assessment procedure that is based on curved wide plate test results (Chapter 1, section 1.2.3). Therefore, in this dissertation preference will be given to the development of a suitable correction function.

2.4. Research approach

Based on the results presented in section 2.2 and 2.3, the following is concluded:

- A large number of parameters have an influence on the constraint and the crack driving force.
- The constraint in SENT specimens approximates the constraint in pipe specimens, with a limited degree of conservatism.
- The crack driving force curves of pressurized pipes and CWP specimens tend to differ due to the presence of internal pressure.

The latter supports the need for a correction function that quantitatively describes the difference in tensile strain capacity between pressurized pipes and CWP specimens. Establishing such correction function could be based on a fully experimental approach. More specifically, by means of testing a series of flawed CWP specimens and pressurized pipe sections (limited in length, e.g. four times the diameter [2.65, 67]) up to failure. Such approach clearly benefits from the absence of scaling effects. However, full scale testing involves some disadvantages:

- Full scale testing requires extremely high loading capacities (tensile force typically in the range of 10 MN). In combination with the internal pressure, this implies that serious safety precautions have to be foreseen.
- The test results are often difficult to interpret due to a lack of knowledge regarding the actual material properties of the tested section. The exact weld metal properties cannot be determined. Although a dummy weldment might be considered, the inherent weld to weld variability will unmistakably complicate the interpretation [2.68].

The latter additionally complicates a comparison between the tensile strain capacities of pipe and CWP specimens. Hence, a fully experimental approach for the quantification of the relative strain capacity is discouraged. Similarly, the large number of parameters as well as the potential scatter of the material properties, point out the limitations of a fully experimental approach towards the evaluation of the ductile tearing resistance. In line with the trend towards numerical analysis (e.g. finite element simulations), a mixed numerical-experimental approach is therefore adopted in this dissertation. Both the numerical and experimental part is further elaborated on in the following sections.

2.4.1.Experimental

Experiments are vital to assess the actual behaviour of structures, given for instance the variability of material properties. A well performed and interpreted experiment is crucial for a correct defect assessment. Although this might seem trivial to insiders, a successful interpretation of the test results necessitates the use of well defined procedures. This is because the success largely depends on:

- *the generic character of the test results*: the lab where a girth weld defect is assessed should not have an influence on the outcome of the test. This requires well documented test procedures, eliminating/minimizing the possibility of misleading interpretations.
- *the need for high-end tools*: a correct interpretation of the test results should not be privileged to those having access to extensive budgets and/or skills (e.g. finite element tools). On the contrary, the use of common test facilities and analytical procedures is advised, preferably including equivalent alternatives. These high-end tools should however be allowed for, e.g. by incorporating different testing levels.
- *compatibility*: the test results should be compatible with the analytical formulae presented in the assessment procedures. As a result, the assumptions made in the assessment procedure should also be accounted for in the testing procedures (and vice versa).

To this extent, this work aims not only to present test results but also to present well supported test methods that can be used in combination with the previously presented defect assessment procedures. The availability of these test methods should accommodate experimental parametric studies, e.g. evaluation of welding conditions.

Next to the question "*how to test?*", the question "*what type of test?*" is crucial. In other words, what do we want to measure? With respect to pipeline girth weld defect assessment, distinction is to be made between tests aiming at:

- generating input data for defect assessment procedures and,
- a direct experimental evaluation of the tensile strain capacity.

Related to the first aim, distinction is to be made between tests evaluating the tensile stress-strain properties and tests evaluating the tearing resistance. The first are well standardized, in contrast to the latter. Therefore, this dissertation will focus on SENT testing, given the stated constraint match with full scale testing (section 2.2).

Related to the second aim, both full scale testing and CWP testing can be considered. Despite neglecting the internal pressure effect, the latter is selected in this dissertation as CWP testing clearly shows the following advantages:

- *cost per test*: performing a CWP test is cheaper than performing a full scale test.
- *capacity*: regardless the pipe diameter, the required test capacity remains relatively limited, since specimens with a fixed width are considered.
- *historical data*: the availability of historical data allows to put nowadays test results in a historical perspective and to set up guidelines for defect assessment based on these results.
- *material characterization*: as the CWP sample only considers part of the pipe's circumference, it remains possible to characterize the selected weld by e.g. all weld metal or SENT testing adjacent to the CWP specimen. Given the potential variability in actual weld properties, both with respect to the circumferential position as with respect to the weld-to-weld variability, this is no evidence in case of full scale testing.

In conclusion, this disserations aims at developing robust, well validated testing procedures for both SENT and CWP specimens.

2.4.1.1. SENT testing

A variety of specimen geometries are reported in literature [2.17, 53, 54]. The SENT specimens considered in this work have a square cross section (i.e. thickness (B) over width (W) ratio equals unity, $B / W = 1$) and a daylight grip length (H) equal to $10W$ (Figure 2.7). This configuration was chosen in preference to the over-square specimens ($B / W = 2$) because of the following:

- *test capacity*: the test capacity required for testing over-square specimens is approximately double as compared to the square specimens.
- *resistance curve*: a comparative study indicated no significant difference between the square and over-square specimens [2.69].

After extracting the specimens, a notch is introduced through saw-cutting. The cutting blade used for the final pass is extremely sharp and thin resulting in an initial notch root radius of 0.075 mm. Fatigue pre-cracking is not applied. This would complicate the control of the initial crack depth and is not required for sufficiently ductile materials (e.g. ExxonMobil test procedure for SENT testing [2.70] and Akourri et al. for SENB specimens [2.71]).

Due to the difference in constraint between the (plane strain) mid-thickness and the (plane stress) side of the specimen, crack tunneling is expected [2.72]. Some researchers have reported that this tunneling results in a deteriorated accuracy for the crack growth measurements [2.73]. V-shaped side grooves are machined at both sides of the test specimen to promote uniform crack extension; achieving a total thickness reduction of 15% (B_N = net thickness = $0.85W$) as advised by Shen et al. [2.74]. These side grooves conform the ASTM E1820 requirements, i.e. opening angle less than 90° and a root radius of 0.5 ± 0.2 mm [2.32].

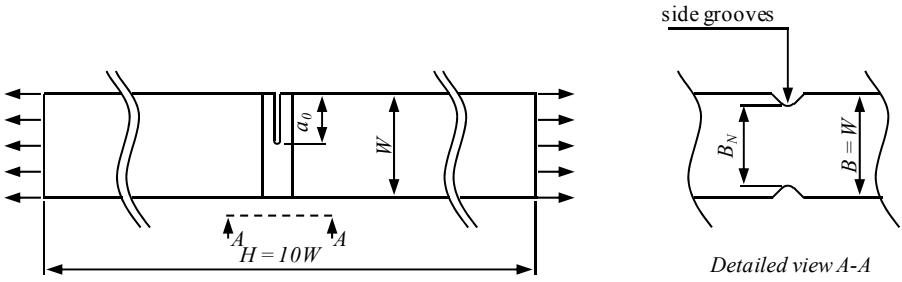

Figure 2.7. Schematic representation of SENT specimen considered in this dissertation

The specimens are clamped using hydraulic grips mounted in a 150 kN tensile test rig and loaded in constant displacement rate mode (0.01 mm/sec). The specimens are loaded beyond maximum force in the load-displacement curve. To obtain a sufficient amount of ductile crack extension, the tests are continued until the force drops back to 80% of the maximum recorded value.

2.4.1.2. Medium wide plate testing

As is the case for SENT testing, a variety of specimen dimensions are reported in literature for curved wide plate specimens [2.75-78]. The UGent guidelines prescribe the use of a 300 mm wide (2 W) section with a prismatic length (2 L) of 900 mm (Figure 2.3) [2.39]. The corresponding length-to-width ratio ($L/W = 3$) appeared sufficient to obtain accurate remote strain measurements [2.37, 79].

Nevertheless, in the experimental framework of this dissertation preference is given to a so-called medium wide plate (MWP) specimen. In a previous PhD project [2.80], this test specimen was introduced and the test procedure was optimized for research purposes, e.g. including full instrumentation. These MWP tests are carried out using Laboratory Soete's 2500 kN tensile test rig (Figure 2.9). This test rig benefits from a large visibility of the test specimen, which is of primary importance for the application of the digital image correlation technique, as discussed in Chapter 6.

The geometrical dimensions of the MWP specimen are presented in Figure 2.8. Note that the thickness (t) and curvature (D) of the specimen remain undefined as these parameters depend on the geometry of the parent pipe. The notch at the specimen's central section is, in accordance to the SENT procedure, applied through saw-cutting with a similar, ultimately fine cutting blade.

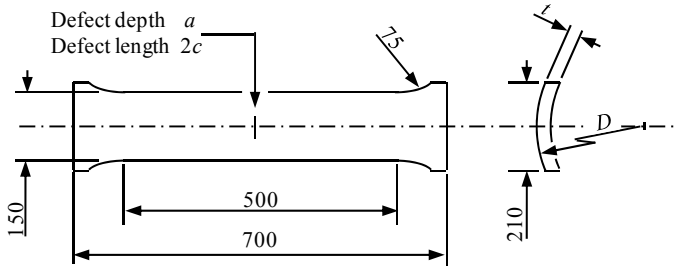

Figure 2.8. Geometry of MWP test specimen

To enable mounting of the specimen in the test rig, it is welded to end blocks. To lower the stress in the connecting weld, the specimen gradually widens at the end. This is referred to as the specimen's shoulders. The specimen is loaded in tension with a constant displacement rate of 0.01 mm/sec.

Figure 2.9. MWP specimen mounted in Laboratory Soete's 2500 kN tensile test rig

2.4.1.3. Specimen sampling

The majority of the test specimens discussed in this dissertation are extracted from girth welded pipe sections. Figure 2.10 shows a roll-out of a pipe section containing a girth weld, indicating the relative position and types of the extracted specimens. Taking into account the heterogeneous nature of weldments, the SENT specimens are extracted adjacent to the MWP specimen. For each MWP test, a total of three to six SENT test specimens are extracted. This is because the SENT specimen samples a smaller amount of material. Hence, the results might be more susceptible to natural variations of the material properties. In addition, tensile test specimens are extracted from the same pipe section. The axial properties of the base metal of both pipe pups (referred to as "pipe A" and "pipe B" in Figure 2.10) are characterized by means of full thickness flat strip tensile test specimens. The weld metal is characterized using all weld metal round bar specimens extracted in the pipe's circumferential direction. Both types of tensile test specimens are in accordance to the standard EN 10002 [2.81]. In addition, a small piece of weld metal is taken out for a weld macrograph and hardness measurements.

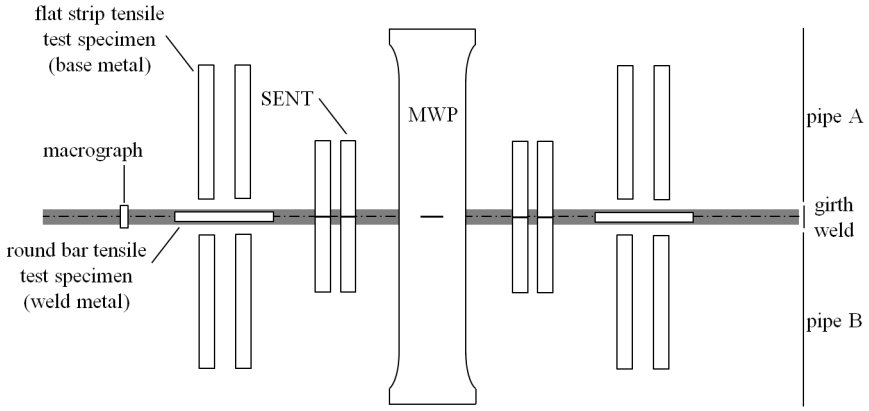

Figure 2.10. Sampling position of MWP, SENT and tensile specimens

2.4.2. Numerical - finite element analysis

The continuously increasing number of research papers based on finite element simulations is not surprising as these have some clear advantages over experiments:

- *Price:* performing experiments involves a high material cost. In addition, the test preparation and analysis is often time consuming. Therefore, simulations are typically considered for evaluating the influence of a broad range / large number of parameters.
- *Controllability:* it is possible to simulate the influence of one single parameter while keeping others fixed. In an experimental setup such conditions can hardly be obtained. Simulations are therefore helpful to gain insight in the underlying phenomena.
- *Scale & capacity:* testing of large complex systems often requires large test capacities. In contrast, for simulations, the calculation effort remains relatively limited.

Although simulations might seem an attractive alternative at this point, conclusions drawn solely from simulations should not be generally accepted. One should take into account the assumptions made in the model. Based on these assumptions one tries to represent the actual nature of a given problem. Focusing on the assessment of girth weld defects, the influence of anisotropic material behaviour, material heterogeneity and weld residual stresses are often overlooked. It remains therefore vital to have a sound validation of the finite element model, where the results predicted by the numerical models are compared to actual test results or results available in literature.

Within this dissertation, an extensive set of finite element models is used:

- *(Un)pressurized pipes (up/pp)*: this full scale specimen is taken as a general reference throughout this work as it is believed to closely represent the actual conditions in the field. Hence, this specimen has been considered for the evaluation of constraint and tensile strain capacity.
- *Curved Wide Plate (CWP) and Medium Wide Plate (MWP)*: the CWP specimen is commonly used to evaluate the tensile strain capacity of pipes with girth weld defects. Since there exists a clear need to compare the so-obtained tensile strain capacity to the one from the pipe specimens, this model is given special attention. To that extent, the constraint in the CWP specimen has also been evaluated. In addition, this model was also considered to enhance the interpretation of MWP test results.
- *Single Edge Notch Tensile (SENT)*: the tearing resistance is an important input factor for most defect assessment procedures. In an attempt to further improve the understanding of the experimental test results, a finite element model of this specimen has been developed.

It should be noted at this point that the tangency approach (Chapter 1) is adopted to simulate ductile tearing and estimate the tensile strain capacity. Hence, ductile crack extension by means of a damage mechanics approach is incorporated in none of the above finite element models.

To accommodate parametric studies, a large number of simulations are required. A parametric programming approach was considered, following the framework

presented in the PhD by Stijn Hertelé [2.80]. Accordingly, the pre- and post-processing is controlled by Python scripts, allowing for a well structured analysis and evaluation of the requested properties (Figure 2.11). In addition, such approach allows interconnecting different models and guarantees a similar, structured mesh design, e.g. the exact same mesh design is used for CWP specimens and (pressurized) pipes.

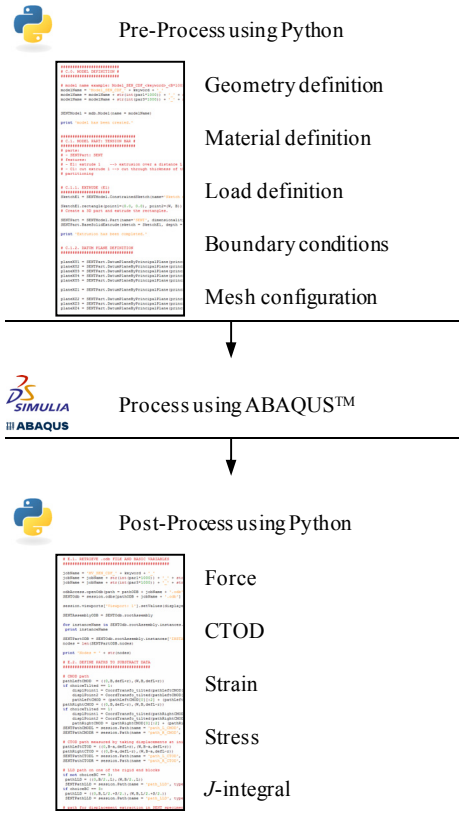

Figure 2.11. Schematic overview of ABAQUS™ scripting approach

2.4.3.Outline of this work

As regards the conclusions of the first chapter, this dissertation is divided in two parts. A first part aims at evaluating and interpreting test results, merely focusing on the tearing resistance. A second part focuses on the comparison between curved wide plate and full scale tests. Throughout the entire dissertation, a mixed numerical-experimental approach is followed.

The evaluation of tearing resistance is divided in three parts. In **chapter 3**, the focus is on ductile crack extension. This represents the horizontal axis of the resistance curve. Two methods are presented and thoroughly validated based on both SENT and MWP tests. In **chapter 4** the focus is on the vertical axis of the resistance curve, the crack driving force. Again, several methods are presented and compared for both SENT and MWP tests. The resulting resistance curves are finally discussed in **chapter 5**.

In addition to ductile tearing, the deformation field around a crack has also been studied as it is believed to relate to the structural response and failure mode. These deformation fields have been determined using a full field deformation imaging technique [2.82]. In **chapter 6** characteristic patterns and test observations are discussed.

The comparison between CWP and full scale tests is divided in two chapters. In **chapter 7** a numerical comparison is made between the constraint in curved wide plate and (pressurized) pipe specimens. This supports the use of the tangency approach using the same resistance curve for both CWP and (pressurized) pipe specimens. Consequently, the tensile strain capacity can be compared for both specimen types. A suitable correction function to convert the tensile strain capacity between CWP and (pressurized) pipe specimens is presented in **chapter 8**.

Final conclusions and recommendations for future research are formulated in the final **chapter 9**. The above is schematically represented in Figure 2.12.

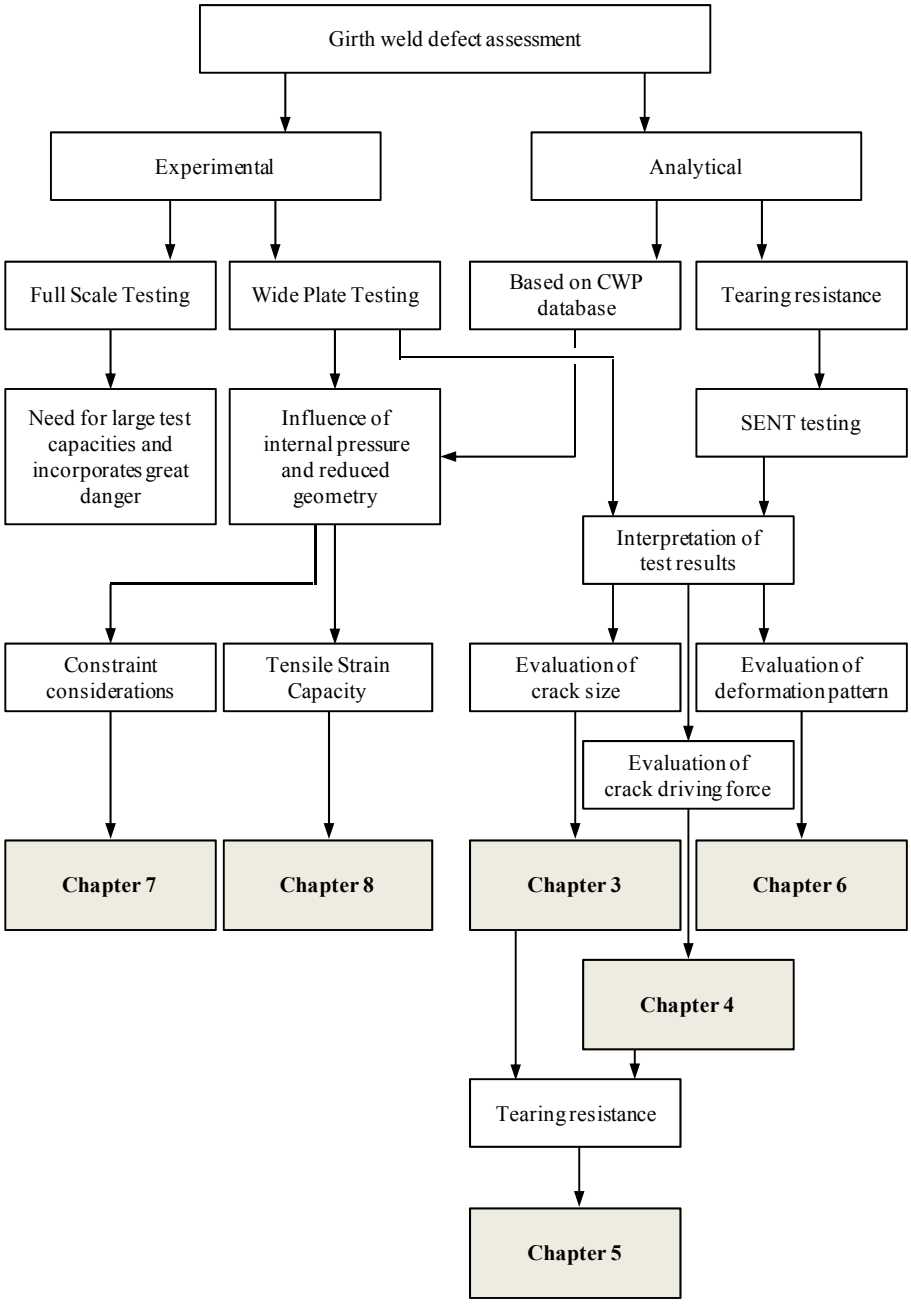

Figure 2.12. Outline of this dissertation

2.5. Bibliography

[2.1] Anderson, T. L., 1995, "Fracture Mechanics: Fundamentals and Applications", CRC press, Texas.

[2.2] Chao, Y. J., and Zhu, X. K., 2000, "Constraint-Modified J-R Curves and Its Application to Ductile Crack Growth", International Journal of Fracture, 106, pp. 135-160.

[2.3] Zhu, X. K., and Jang, S. K., 2000, "J-R Curves Corrected by Load-Independent Constraint Parameter in Ductile Crack Growth", Engineering Fracture Mechanics, 68, pp. 285-301.

[2.4] Zhu, X. K., and Leis, B. N., 2006, "Application of Constraint Corrected J-R Curves to Fracture Analysis of Pipelines", Journal of Pressure Vessel Technology, 128, pp. 581-589.

[2.5] Al-Ani, A. M., and Hancock, J. W., 1991, "J-Dominance of Short Cracks in Tension and Bending", Journal of Mechanics and Physics of Solids, 39, pp. 23-43.

[2.6] Betegon, C., and Hancock, J. W., 1991, "Two-Parameter Characterization of Elastic-Plastic Crack Tip Fields", ASME journal of applied mechanics, 58, pp. 104-113.

[2.7] Du, Z. Z., and Hancock, J. W., 1991, "The Effect of Non-Singular Stresses on Crackt-Tip Constraint", Journal of Mechanics and Physics of Solids, 39, pp. 555-567.

[2.8] O'Dowd, N. P., and Shih, C. F., 1991, "Family of Crack-Tip Fields Characterized by Triaxiality Parameter: Part I - Structure of Fields", Journal of Mechanics and Physics of Solids, 39, pp. 989-1015.

[2.9] O'Dowd, N. P., and Shih, C. F., 1992, "Family of Crack-Tip Fields Characterized by Triaxiality Parameter: Part II - Application", Journal of Mechanics and Physics of Solids, 40, pp. 939-963.

[2.10] Chao, Y. J., Yang, S., and Sutton, M. A., 1994, "On the Fracture of Solids Characterizd by One or Two Parameters: Theory and Practice", Journal of Mechanics and Physics of Solids, 42, pp. 629-647.

[2.11] Nikishkov, G. P., 1995, "An Algorithm and a Computer Program for the Three-Term Asymptotic Expansion of Elastic-Plastic Crack Tip Stress and Displacement Fields", Engineering Fracture Mechanics, 50, pp. 65-83.

[2.12] Yang, S., Chao, Y. J., and Sutton, M. A., 1993, "Higher Order Asymptotic Fields in a Power-Law Hardening Material", Engineering Fracture Mechanics, 45, pp. 1-20.

[2.13] Cravero, S., and Ruggieri, C., 2003, "A Two-Parameter Framework to Describe Effect of Constraint Loss on Cleavage Fracture and Implications for Failure Assessments of Cracked Components", Journal of Brazilian Society of Mechanical Sciences and Engineering, 15, pp. 403-412.

[2.14] Dodds, R. H., Shih, C. F., and Anderson, T. L., 1993, "Continuum and Micromechanics Treatment of Constraint in Fracture", Office of Nuclear Regulatory Research, Washington D.C.

[2.15] Hebel, J., Hohe, J., Friedmann, V., and Siegele, D., 2007, "Experimental and Numerical Analysis of in-Plane and out-of-Plane Crack Tip Constraint Characterization by Secondary Fracture Parameters", International Journal of Fracture, 146, pp. 173-188.

[2.16] Cravero, S., and Ruggieri, C., 2005, "Correlation of Fracture Behavior in High Pressure Pipelines with Axial Flaws Using Constraint Designed Test Specimens - Part I: Plane Strain Analysis", Engineering Fracture Mechanics, 72, pp. 1344-1360.

[2.17] Silva, L. A. L., Cravero, S., and Ruggieri, C., 2006, "Correlation of Fracture Behavior in High Pressure Pipelines with Axial Flaws Using Constraint Designed Test Specimens - Part II: 3d Effects on Constraint", Engineering Fracture Mechanics, 73, pp. 2123-2138.

[2.18] Thaulow, C., Ostby, E., Nyhus, B., Zhang, Z. L., and Skallerud, B., 2004, "Constraint Correction of High Strength Steel - Selection of Test Specimens and Application of Direct Calculations", Engineering Fracture Mechanics, 71, pp. 2417-2433.

[2.19] Thaulow, C., Ostby, E., Nyhus, B., Olden, V., and Zhang, Z. L., 2002, "The Philosophy of Constraint Correction", International Symposium on High Strength Steel, Stiklestad, Norway, pp. 1-19.

[2.20] Hutchinson, J. W., 1968, "Singular Behaviour at End of a Tensile Crack in a Hardening Material", Journal of Mechanics and Physics of Solids, 16, pp. 13-31.

[2.21] Rice, J. R., and Rosengren, G. F., 1968, "Plane Strain Deformation near a Crack Tip in a Power-Law Hardening Material", Journal of Mechanics and Physics of Solids, 16, pp. 1-12.

[2.22] Ritchie, R. O., and Thompson, A. W., 1985, "On Macroscopic and Microscopic Analyses for Crack Initiation and Crack Growth Toughness in Ductile Alloys", Metallurgical Transactions A, 16, pp. 233-248.

[2.23] O'Dowd, N. P., and Shih, C. F., 1992, "Two-Parameter Fracture Mechanics Theory and Applications", United States Naval Surface Warfare Center - Carderock Division, London.

[2.24] Ainsworth, R. A., Sattari-Far, I., Sherry, A. H., Hooton, D. G., and Hadley, I., 2000, "Methods for Including Constraint Effects within the Sintap Procedures", Engineering Fracture Mechanics, 67, pp. 563-571.

[2.25] Neimitz, A., and Galkiewicz, J., 2006, "Fracture Toughness of Structural Components: Influence of Constraint", International Journal of Pressure Vessels and Piping, 83, pp. 42-54.

[2.26] Ranestad, O., Zhang, Z. L., and Thaulow, C., 1999, "Quantification of Geometry and Material Mismatch Constraint in Steel Weldments with Fusion Line Cracks", International Journal of Fracture, 99, pp. 211-237.

[2.27] Pavankumar, T. V., Chattopadhyay, J., Dutta, B. K., and Kushwaha, H. S., 2000, "Numerical Investigations of Crack-Tip Constraint Parameters in Two-Dimensional Geometries", Pressure Vessels and Piping, 77, pp. 345-355.

[2.28] O'Dowd, N. P., and Shih, C. F., 1995, "Two-Parameter Fracture Mechanics: Theory and Applications", ASTM, Standard Technical Publication 1207.

[2.29] Henry, B. S., and Luxmoore, A. R., 1997, "The Stress Triaxiality Constraint and the Q-Value as a Ductile Fracture Parameter", Engineering Fracture Mechanics, 57, pp. 375-390.

[2.30] Cravero, S., Bravo, R. E., and Ernst, H. A., 2008, "Constraint Evaluation and Effects on J-R Resistancecurves for Pipes under Combined Load Conditions", International Offshore and Polar Engineering Conference, Vancouver, British Columbia, Canada, pp. 149-156.

[2.31] Yuan, H., and Brocks, W., 1998, "Quantification of Constraint Effects in Elastic-Plastic Crack Front Fields", Journal of Mechanics and Physics of Solids, 46, pp. 219-241.

[2.32] American Society of Testing and Materials, 2011, E1820 - Standard Test Method for Measurement of Fracture Toughness.

[2.33] British Standards Institution, 1991, BS 7448-1: Fracture Mechanics Toughness Tests. Method for Determination of Kic, Critical CTOD and Critical J Values of Metallic Materials.

[2.34] Wang, Y.-Y., and Liu, M., 2007, "The Role of Anisotropy, Toughness Transferability and Weld Misalignment in the Strain Based Design of Pipelines", International Offshore and Polar Engineering Conference, pp. 3164-3171.

[2.35] Klein, R., Collins, L., Hamad, F., Chen, X., and Bai, D., 2008, "Determination of Mechanical Properties of High Strength Linepipe", International Pipeline Conference, Calgary, Alberta, Canada, paper n° IPC2008-64101.

[2.36] Ostby, E., Sandvik, A., Levold, E., Nyhus, B., and Thaulow, C., 2009, "The Effects of Weld Metal Mismatch and Crack Position on the Strain Capacity in SENT Specimens in an X65 Material", International Offshore and Polar Engineering Conference, Osaka, Japan, pp. 162-168.

[2.37] Hertelé, S., De Waele, W., Denys, R., and Verstraete, M., 2012, "Investigation of Strain Measurements in (Curved) Wide Plate Specimens Using Digital Image Correlation and Finite Element Analysis", Journal of Strain Analysis for Engineering Design, 47, pp. 276-288.

[2.38] Stephens, M., Petersen, R., Wang, Y. Y., Gordon, J. R., and Horsley, D., 2010, "Large Scale Experimental Data for Improved Strain-Based Design Models", International Pipeline Conference, Calgary, Alberta, Canada, paper n° IPC2010-31396.

[2.39] Denys, R., and Lefevre, A. A., 2009, "UGent Guidelines for Curved Wide Plate Testing", Pipeline Technology Conference, Ostend, Belgium, paper n° Ostend2009-110.

[2.40] Xu, J., Zhang, Z. L., Ostby, E., Nyhus, B., and Sun, D. B., 2010, "Constraint Effect on the Ductile Crack Growth Resistance of Circumferentially Cracked Pipes", Engineering Fracture Mechanics, 77, pp. 671-684.

[2.41] Cravero, S., and Ruggieri, C., 2004, "Integrity Assessment of Pipelines Using SE(T) Specimens", International Pipeline Conference, Calgary, Alberta, Canada, paper n° IPC04-0033.

[2.42] Pisarski, H. G., and Wignall, C. M., 2002, "Fracture Toughness Estimation for Pipeline Girth Welds", International Pipeline Conference, Calgary, Alberta, Canada, paper n° IPC2002-27094.

[2.43] Kim, Y.-J., Chung, K.-H., Kim, J.-S., and Kim, Y.-J., 2004, "Effect of Biaxial Loads on Elastic-Plastic J and Crack Tip Constraint for Cracked Plates: Finite Element Study", International Journal of Fracture, 130, pp. 803-825.

[2.44] Burdekin, F. M., and Xu, W. G., 2003, "Effects of Biaxial Loading and Residual Stresses on Constraint", International Journal of Pressure Vessels and Piping, 80, pp. 755-773.

[2.45] Ostby, E., and Hellesvik, A. O., 2007, "Fracture Control - Offshore Pipeline JIP: Results from Large Scale Testing on the Effect of Biaxial Loading on Strain Capacity of Pipes with Defects", International Offshore and Polar Engineering Conference, Lisbon, Portugal, pp. 3231-3237.

[2.46] Ostby, E., and Hellesvik, A. O., 2008, "Large-Scale Experimental Investigation of the Effect of Biaxial Loading on the Deformation Capacity of Pipes with Defects", International Journal of Pressure Vessels and Piping, 85, pp. 814-824.

[2.47] Gioielli, P. C., Minnaar, K., Macia, M. L., and Kan, W. C., 2007, "Large-Scale Testing Methodology to Measure the Influence of Pressure on Tensile Strain Capacity of a Pipeline", International Offshore and Polar Engineering Conference, Lisbon, Portugal, pp. 3023-3027.

[2.48] Tyson, W. R., Shen, G., and Roy, G., 2007, "Effect of Biaxial Stress on ECA of Pipelines under Strain-Based Design", International Offshore and Polar Engineering Conference, Lisbon, Portugal, pp. 3107-3113.

[2.49] Sakimoto, T., Igi, S., and Kubo, T., 2009, "The Influence of Internal Pressure on Ductile Fracture Behavior from a Surface Defect on a Pipe", International Offshore and Polar Engineering Conference, Osaka, Japan, pp. 125-131.

[2.50] Nevalainen, M., and Dodds, R. H., 1996, "Numerical Investigation of 3-D Constraint Effects on Brittle Fracture in SE(B) and C(T) Specimens", International Journal of Fracture, 74, pp. 131-161.

[2.51] Xu, J., Zhang, Z. L., Ostby, E., Nyhus, B., and Sun, D. B., 2009, "Effects of Crack Depth and Specimen Size on Ductile Crack Growth of SENT and Senb Specimens for Fracture Mechanics Evaluation of Pipeline Steels", International Journal of Pressure Vessels and Piping, 86, pp. 787-797.

[2.52] Minnaar, K., Gioielli, P. C., Macia, M. L., Bardi, F., and Biery, N. E., 2007, "Predictive Fea Modeling of Pressurized Full-Scale Tests", International Offshore and Polar Engineering Conference, Lisbon, pp. 3114-3120.

[2.53] Shen, G., Gianetto, J. A., and Tyson, W. R., 2009, "Measurement of J-R Curves Using Single Specimen Technique on Clamped SE(T) Specimens", International Offshore and Polar Engineering Conference, Osaka, Japan, pp. 92-99.

[2.54] Det Norske Veritas, 2006, RP-F108: Fracture Control for Pipeline Installation Methods Introducing Cyclic Plastic Strain.

[2.55] Verstraete, M., Hertelé, S., Van Minnebruggen, K., Denys, R., and De Waele, W., 2013, "Considerations in Selecting Laboratory Scle Test Specimens for Evaluation of Fracture Toughness", Sustainable Construction and Design, 4, pp. 1-9.

[2.56] Cheng, W., Tang, H., Gioielli, P. C., Minnaar, K., and Macia, M. L., 2009, "Test Methods for Characterization of Strain Capacity: Comparison of R-Curves from SENT/CWP/FS Tests", Pipeline Technology Conference, Ostend, Belgium, paper n° Ostend2009-040.

[2.57] Wang, Y. Y., Liu, M., Song, Y., Petersen, R., Stephens, M., and Gordon, R., 2011, "Second Generation Models for Strain-Based Design", Pipeline Research Council International, Houston, Texas, United States.

[2.58] Wang, Y. Y., Liu, M., Zhang, F., Horsley, D., and Nanney, S., 2012, "Multi-Tier Tensile Strain Models for Strain-Based Design - Part 1: Fundamental Basis", International Pipeline Conference, Calgary, Alberta, Canada, paper n° IPC2012-90690.

[2.59] Huh, N.-S., Kim, Y.-J., Choi, J.-B., Kim, Y.-J., and Pyo, C.-R., 2004, "Prediction of Failure Behavior for Nuclear Piping Using Curved Wide-Plate Test", Journal of Pressure Vessel Technology, 126, pp. 419-425.

[2.60] Zhang, J. X., and Shi, Y. W., 1997, "The Effect of Welding Mechanical Heterogeneity on Fracture Toughness Feature of Base Metal", International Journal of Pressure Vessels and Piping, 72, pp. 199-202.

[2.61] Marie, S., Gilles, P., and Ould, P., 2009, "Determination of Ductile Tearing Resistance in Weld Joints", Pressure Vessels and Piping Conference, Prague, Czech Republic, paper n° PVP2009-77297.

[2.62] Knauf, G., and Hopkins, P., 1996, "The EPRG Guidelines on the Assessment of Defects in Transmission Pipeline Girth Welds", 3R International, 35, pp. 620-624.

[2.63] Denys, R. M., and De Waele, W., 2009, "Comparison of API 1104 - Appendix a Option 1 and EPRG-Tier 2 Defect Acceptance Limits", Pipeline Technology Conference, Ostend, Belgium, paper n° Ostend2009-113.

[2.64] Gordon, J. R., Zettlemoyer, N., and Mohr, W. C., 2007, "Crack Driving Force in Pipelines Subjected to Large Strain and Biaxial Stress Conditions", International Offshore and Polar Engineering Conference, Lisbon, Portugal, pp. 3129-3140.

[2.65] Jayadevan, K. R., Ostby, E., and Thaulow, C., 2004, "Fracture Response of Pipelines Subjected to Large Plastic Deformation under Tension", International Journal of Pressure Vessels and Piping, 81, pp. 771-783.

[2.66] Wang, Y.-Y., Stephens, M., and Horsley, D., 2008, "Preliminary Analysis of Tensile Strain Capacity of Full Scale Pipe Tests with Internal Pressure", International Offshore and Polar Engineering Conference, Vancouver, Canada, pp. 40-47.

[2.67] Kibey, S. A., Lele, S. P., Tang, H., Macia, M. L., Fairchild, D. P., Cheng, W., Noecker, R., Wajutelewicz, P. J., Newbury, B., Kan, W. C., and Cook, M. F., 2011, "Full-Scale Test Observations for Measurement of Tensile Strain Capacity of Welded Pipelines", International Offshore and Polar Engineering Conference, Maui, Hawaii, USA, pp. 660-667.

[2.68] Denys, R., Hertelé, S., Verstraete, M., and De Waele, W., 2011, "Strain Capacity Prediction for Strain-Based Pipeline Designs", International Workshop on Welding of High Strength Pipeline Steels, Araxá, Brazil, pp. 1-13.

[2.69] Wang, S., Kibey, S., Minnaar, K., Macia, M., Fairchild, D. P., Kan, W. C., Ford, S. J., and Newburry, B., 2011, "Strain-Based Design - Advances in Prediction Methods of Tensile Strain Capacity", International Journal of Offshore and Polar Engineering, 21, pp. 1-7.

[2.70] ExxonMobil, 2010, "Measurement of Crack Tip Opening Displacement (CTOD) - Fracture Resistance Curves Using Single-Edge Notched Tension (SENT) Specimens", ExxonMobil Upstream Research Company, Houston.

[2.71] Akourri, O., Louah, M., Kifani, A., Gilgert, G., and Pluvinage, G., 2000, "The Effect of Notch Radius on Fracture Toughness J(Ic)", Engineering Fracture Mechanics, 65, pp. 491-505.

[2.72] Lan, W., Deng, X., and Sutton, M. A., 2010, "Investigation of Crack Tunneling in Ductile Materials", Engineering Fracture Mechanics, 77, pp. 2800-2812.

[2.73] Riemelmoser, F. O., Pippan, R., Weinhandl, H., and Kolednik, O., 1999, "The Influence of Irregularities in the Crack Shape on the Crack Extension Measurement by Means of the Direct-Current-Potential-Drop Method", Journal of Testing and Evaluation, 27, pp. 42-46.

[2.74] Shen, G., Tyson, W. R., Gianetto, J. A., and Park, D.-Y., 2010, "Effect of Side Grooves on Compliance, J-Integral and Constraint of Clamped SE(T) Specimen", Pressure Vessels and Piping Conference, Bellevue, Washington, USA, paper n° PVP2010-25164.

[2.75] Minami, F., Takashima, Y., and Ohata, M., 2011, "Constraint-Based Assessment of CTOD Toughness Requirement for High-Strain Line Pipe", International Journal of Offshore and Polar Engineering, 21, pp. 129-140.

[2.76] Igi, S., and Suzuki, N., 2007, "Tensile Strain Limits of X80 High-Strain Pipelines", International Offshore and Polar Engineering Conference, Lisbon, Portugal, pp. 3081-3087.

[2.77] Stephens, M., Randy, T., Petersen, R., Wang, Y. Y., and Horsley, D., 2009, "An Experimental Basis for Improved Strain-Based Design Models", International Offshore and Polar Engineering Conference, Osaka, Japan, pp. 29-35.

[2.78] Richards, M., Weeks, T., McColskey, D., Wang, B., and Wang, Y. Y., 2010, "Fatigue Pre-Cracking Curved Wide Plates in Bending", International Pipeline Conference, Calgary, Alberta, Canada, paper n° IPC2010-21468.

[2.79] Fairchild, D. P., Cheng, W., Ford, S. J., Minnaar, K., Biery, N. E., Kumar, A., and Nissley, N. E., 2007, "Recent Advances in Curved Wide Plate Testing and Implications for Strain-Based Design", International Offshore and Polar Engineering Conference, Lisbon, pp. 3013-3022.

[2.80] Hertelé, S., 2012, "Coupled Experimental-Numerical Framework for the Assessment of Strain Capacity of Flawed Girth Welds in Pipelines", Ph.D. thesis, Ghent University, Ghent, Belgium.

[2.81] Deutsches Institut für Normung, 2009, DIN EN 10002: Testing of Metallic Materials - Tensile Test Pieces.

[2.82] Sutton, M. A., Orteu, J.-J., and Schreier, H. W., 2009, "Image Correlation for Shape, Motion and Deformation Measurements", Springer, New York.

Chapter 3

–

Evaluation of Ductile Crack Extension

3.1. Introduction

The aim of this chapter is to develop sound and robust methods for the experimental evaluation of ductile crack extension, Δa. In essence, two techniques are available to determine the crack extension, namely the multiple specimen technique and the single specimen technique. For SENT testing, the multiple specimen technique is prescribed by the DNV recommended practice DNV-RP-F108 [3.1]. A set of specimens, at least six, is loaded to different load levels. Subsequently, these specimens are broken up in a brittle way and the amount of ductile crack extension is measured. Although successful applications are described in literature [3.2, 3], such technique involves high labor and material costs. On the other hand, the single specimen technique aims to monitor the ductile crack extension during the test. The predicted ductile crack extension can then, by means of validation, be compared to the one measured post-mortem. This last operation can be done following the ASTM E1820 nine points average method [3.4].

In the remainder of this chapter, the main focus is on the following two experimental methods to measure the ductile crack extension using the single specimen technique:

- Unloading Compliance (UC) method
- Direct Current Potential Drop (DCPD) method

Both methods are allowed for the evaluation of the tearing resistance using SENB and CT specimens in the ASTM E1820 standard [3.4], though a thorough validation for SENT and CWP/MWP specimens is currently missing.

3.2. Materials and specimens

In order to thoroughly validate the presented methods, a variety of SENT specimen configurations are tested. An overview of the tested specimens is provided in Appendix A. These specimens cover a wide range of:

- *pipe grades*: grades API-5L X65 to API-5L X80
- *relative crack depths*: $0.2 \leq a_0/W \leq 0.6$
- *mismatch levels*: $0\ \% \leq MM_{FS} \leq 33\ \%$
- *welding processes*: SMAW and GMAW
- *Y/T-ratios of the base metal*: $0.82 \leq Y/T_{BM} \leq 0.92$

Additionally, the measurement of ductile crack extension is applied to five MWP tests. Details of these MWP tests are also listed in Appendix A. The initial crack depths reflect those commonly considered in CWP testing [3.5]. In contrast, the lengths are deliberately chosen relatively large to assure failure by means of unstable ductile crack extension rather than by plastic collapse.

It is finally noted that all welded specimens have a notch at the WMC line; no HAZ defects are examined.

3.3. Measurement methods

3.3.1. Unloading Compliance

The compliance C, expressed in mm / kN, is the inverse of a specimen's stiffness. A direct relation is assumed between this compliance and the crack dimensions. An increase of the compliance signals crack extension. To evaluate a SENT specimen's compliance during the test, it is partially unloaded and reloaded at predefined intervals of CMOD, as proposed by Shen et al. [3.6, 7]. The slope of a linear regression line through the unloading data is then defined as the compliance (Figure 3.1).

$$C = \frac{\Delta CMOD}{\Delta F} \tag{3.1}$$

For the tests described in this thesis, the force is obtained from the load cell of the tensile test rig. The CMOD is obtained from double clip gauge readings, as discussed in Chapter 4. For the SENT tests, the unloading and reloading cycles are adopted from the recommended practice provided by CANMET MTL in the framework of a round robin test program [3.8].

- Six unloading cycles are performed in the elastic regime when the applied force equals P_m.

  $$P_m = \frac{1}{2}\frac{\sigma_0 + \sigma_{TS}}{2}(W - a_0)B_e \tag{3.2}$$

  Where the effective width (B_e) is determined from the following equation:

  $$B_e = B - \frac{(B - B_N)^2}{B} \tag{3.3}$$

  The amount of unloading is force controlled and equals $P_m/2$.

- Following these elastic unloading cycles, subsequent unloading cycles are performed at fixed CMOD intervals. In all cycles the amount of unloading is force controlled and also equals $P_m/2$. For the first five plastic unloading cycles these CMOD intervals equal 0.02 mm, subsequently intervals of 0.04 mm are used. The test is stopped when the applied tensile force no longer exceeds 80% of its maximum (F_{max}).

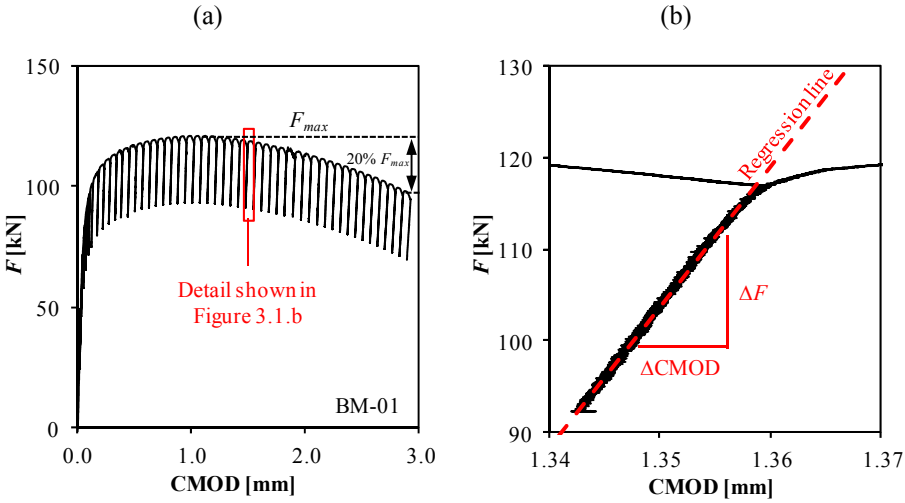

Figure 3.1. Example load versus CMOD diagram for specimen BM-01 (a) with detail of unloading cycle and linear fit determining the compliance (b)

Past experience has shown that the evaluation of compliance is not straightforward for MWP testing [3.9] and is therefore not considered for the evaluation of the ductile crack extension in MWP testing in this dissertation.

To calculate the crack size from the experimentally determined compliances, a transfer function is required. This transfer function can be determined from either finite element simulations or analytical expressions. In section 3.3.1.1, attention is given to the development and validation of a 3D finite element model for the evaluation of compliances. The use of analytical expressions is discussed in section 3.3.1.2.

3.3.1.1 Numerical evaluation of compliances

A 3D finite element model of an edge notched specimen with a steady (non-growing) crack is developed for ABAQUS™ version 6.11. This model is generated using a parametric Python script, allowing systematically generating, meshing and analyzing multiple models with different geometrical and/or material properties (section 2.4.2 of Chapter 2).

Geometrically, the model is defined by its length (H), width (B), thickness (W) and relative crack depth (a/W-ratio). The crack is modeled as initially blunted; a comparative study indicated that a root radius of 0.075 mm (similar to the experiments) also represents the compliance response of an infinitely sharp cracked specimen. Due to the transversal symmetry, only one half of a SENT specimen is modeled, symmetry boundary conditions being applied on one side surface. In order to match the clamped boundary conditions in the test rig, all displacements are defined on the free ends of the specimen, the rotations being restricted.

The specimen is meshed using linear brick elements with reduced integration scheme (ABAQUS^{TM} type C3D8R). A refined, spider-web mesh is applied in the vicinity of the crack tip (Figure 3.2.a). A mesh convergence study assured mesh independent compliance calculations. According to this study, an appropriate mesh consists of approximately 12500 nodes.

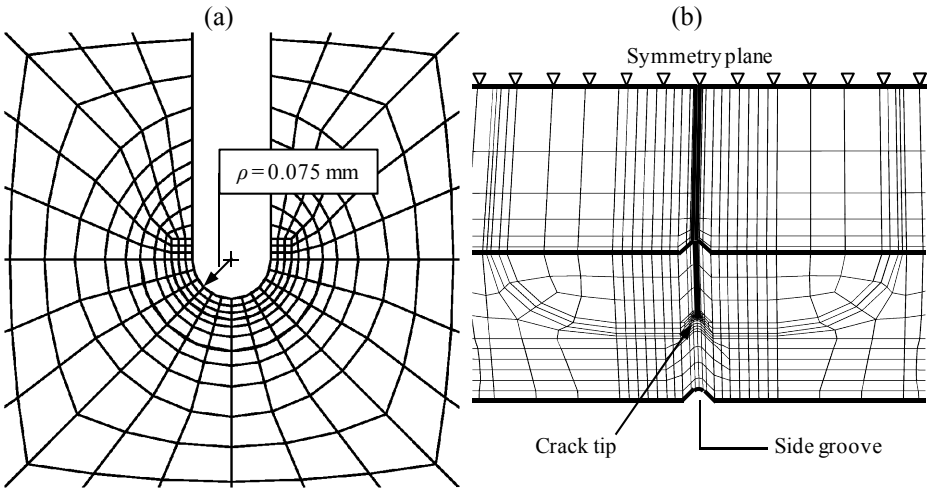

Figure 3.2. Spider-web mesh in the vicinity of the crack tip (a) and mesh of the specimen after application of coordinate transformation creating side grooves (b)

To allow the analysis of side grooved specimens, a coordinate transformation is applied to part of the nodes. Such technique has already been successfully applied to model side grooves in SENB and CT specimens [3.10]. This transformation allows for a flexible groove design without significant mesh distortion, as shown in Figure 3.2.b. In accordance with the experimental test specimens, a total thickness reduction of 15% is modeled using side grooves with an opening angle of 90° and a root radius of 0.4 mm.

Material-wise, two definitions are used. First, a purely linear elastic material is investigated, defined by its Young's modulus (E = 206980 MPa) and Poisson coefficient (ν = 0.3). Secondly, an elastic-plastic stress-strain response is implemented via a point-wise material definition and assuming incremental plasticity, allowing for an elastic-plastic analysis with finite strain assumptions.

Depending on the assigned material properties, the compliances are evaluated in a different way. First, when assigning linear elastic material properties, the displacement of the specimen's ends is monotonically applied. A linear relationship between the applied force and the CMOD is obtained. Hence, the compliance is straightforwardly calculated from the slope of this linear relationship. This compliance is constant for all loading levels. When plotting the compliance against the relative crack depth (Figure 3.3.a), a monotonically increasing trend is observed for increasing crack sizes. In the remainder of this work, this compliance is referred to as the elastic compliance.

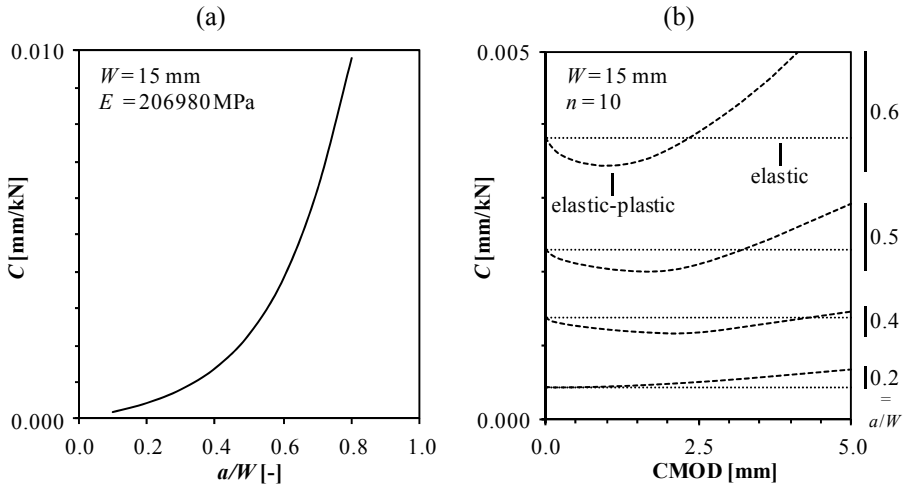

Figure 3.3. Evolution of elastic compliances as function of crack depth (a) and evolution of elastic-plastic (dashed lines) and elastic (dotted lines) compliances upon loading of the specimen for Ramberg-Osgood type of material with strain hardening exponent n = 10 (b)

Second, when assigning elastic-plastic material properties, the displacement is no longer monotonically applied in the FE model. Instead, unloading/reloading cycles are simulated at pre-defined load line displacement levels (every 0.1 mm). During these unloading cycles the compliances are evaluated, similar to the experimental practice. Such simulation approach has already shown effectiveness in predicting ductile crack extension for curved wide plate and full scale pipe tests [3.11-14]. When comparing the elastic compliances to these elastic-plastic compliances, it is observed that they initially coincide (Figure 3.3.b). However, upon loading the elastic-plastic compliances show a non-constant evolution. For deeply notched specimens (e.g. a/W = 0.6), a decrease of the compliances is first observed, followed by an increase at higher CMOD levels. In contrast, for shallow notched specimens (e.g. a/W = 0.2), the compliance increases almost linearly with CMOD.

In general, the same trend is observed for the experimentally obtained compliances, though slight differences are observed e.g. depending on the strain hardening properties of the material. By means of example, the compliance evolution is presented for tests on specimens with initial crack depth a_0 / W = 0.5 (Figure 3.4.a) and a_0 / W = 0.2 (Figure 3.4.b). It is clear that relying on the elastic compliances to evaluate the ductile crack extension, would result in an apparent negative crack extension for the deeply notched specimens, a commonly reported problem in SENT testing [3.15, 16]. This unrealistic observation originates from a decrease in the compliance at the early loading stage. A comparable phenomenon has also been observed for SENB and CT specimens [3.17, 18].

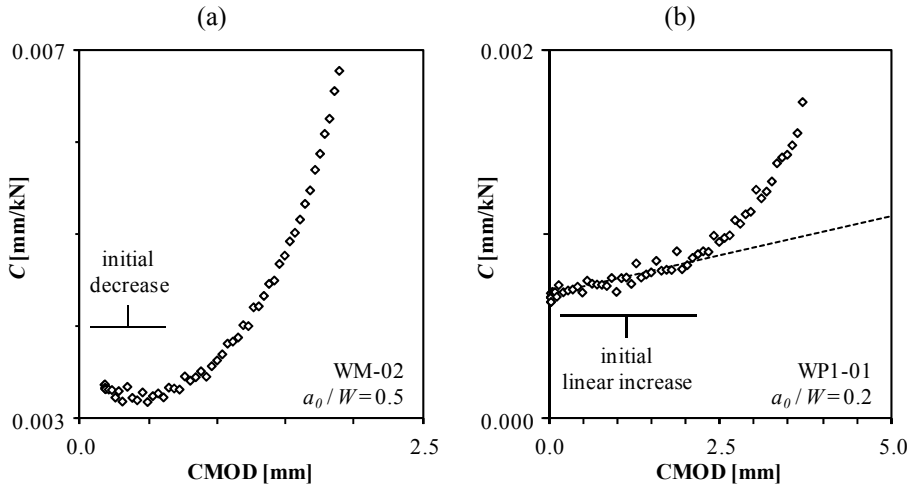

Figure 3.4. Evolution of experimentally obtained compliances for a deeply (a) and a shallow (a) notched specimen

The reason behind these non-constant compliances for specimens with steady (non-growing) cracks under elastic-plastic conditions is twofold. The compliance evolution is controlled by a rotation and a necking effect. First, the focus is on the rotation effect. This effect is present from the early loading stages onwards and is related to the offset (d_F) between the centroid of force in the cracked ligament (F_{res} in Figure 3.5.a) and the centre of the remotely applied load (F). This offset causes a bending moment (M_{res}) in the cracked section and hence results in a rotation. This rotation leads to a decrease in compliance, previously referred to as apparent negative crack extension. To evaluate this assumption, the numerically obtained compliance evolution in SENT and DENT specimens is compared. In a DENT specimen, no offset between both forces (F_{res} and F) is expected given the symmetry in the specimen geometry. Figure 3.5.b illustrates the absence of any compliance decrease in the DENT specimen. This contrasts the deeply notched SENT specimen, which shows a pronounced decrease of the compliance during the early loading stage. The offset between F and F_{res} also explains the experimental observations in Figure 3.4, where the decrease in compliance is observed for specimens with deep cracks and absent for shallow notched specimens ($a_0/W = 0.2$). In case of shallow notched specimens the misalignment is close to zero given the non-uniform distribution of the longitudinal stress fields in the through-thickness direction (σ_{xx} as function of r in Figure 3.5.a).

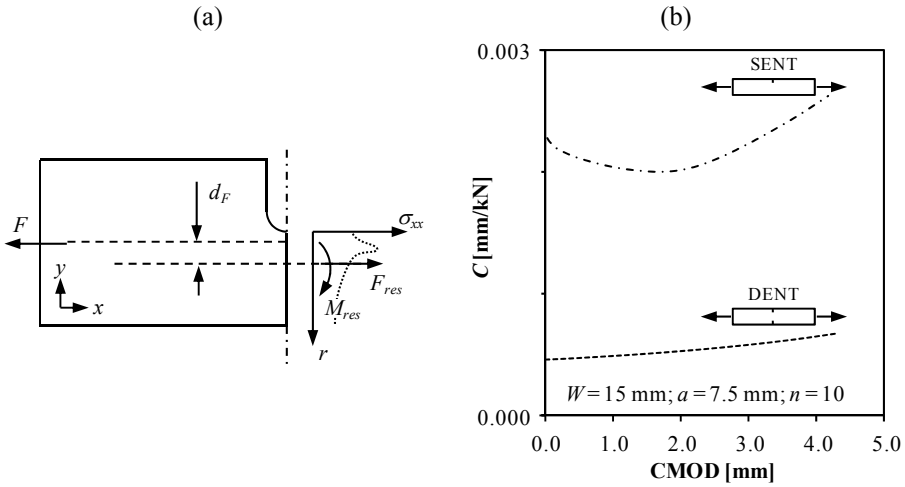

Figure 3.5. Schematic illustration of misalignment between applied force and resulting force in cracked ligament (a) and influence of rotation effect on compliance evolution by comparison between SENT and DENT specimen in the absence of ductile tearing (b)

The second mechanism causing a non-constant compliance is necking. Necking causes a compliance increase due to the reduction of the remaining ligament area. This has an effect on the compliance similar to crack extension and might therefore result in an overestimation of the ductile crack extension. To verify the influence of necking on the compliance evolution, simulations of SENT specimens with identical initial crack depths but varying post-necking characteristics are performed. Two different types of materials are analyzed. Their strain hardening behaviour prior to necking is taken identical to the material used for the validation tests discussed later on in this section. The post-necking characteristics, in contrast, are varied between a linear and a power-law extrapolation, as described by Ling et al. [3.19] (Figure 3.6.a). Figure 3.6.b indicates that an increase of the post-necking strain hardening causes a reasonable deflection of the compliance evolution. This supports the assumption that the increase in the compliance curve, in absence of ductile tearing, is indeed necking dominated.

In general, this necking dominated zone is mostly present beyond maximum force. Although, in the absence of the rotation effect – for shallow notched specimens – the necking already influences the compliance evolution from the early loading stages onwards. This is attributed to the blunting of the crack, where excessive plastic deformation and thus necking takes place in the vicinity of the crack tip. This also results in a reduction of the remaining ligament area. In this case, the compliance evolution of the SENT specimens is comparable to the compliance evolution of the DENT specimens. A similar linear increase of the compliance as function of the CMOD is observed from the beginning of the test onwards (see Figure 3.5.b).

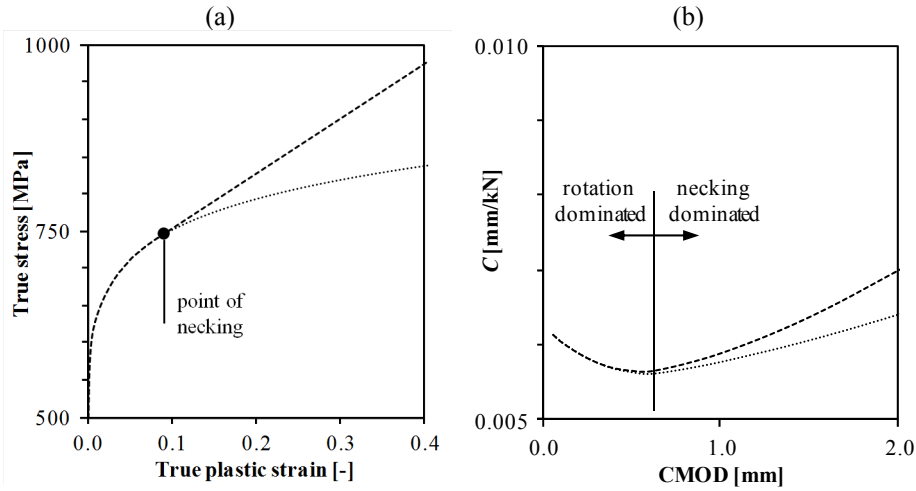

Figure 3.6. Influence of post-necking characteristics (a) on compliance evolution for SENT specimens with $a_0/W = 0.5$ in absence of ductile tearing (b)

It is concluded that the non-constant compliance of SENT specimens without ductile crack extension is dominated by a rotation and a necking effect. The first is most pronounced for deeply notched specimens and causes a compliance decrease. The latter takes over around maximum force and results in a compliance increase. However, the shallower the initial notch, the less pronounced the rotation effect. Eventually, no influence of the specimen's rotation is observed and the compliance linearly increases as function of the CMOD for shallow notch depths (e.g. $a_0/W = 0.2$).

As a result, the moment of crack initiation can be identified based on either of the following observations:

- In case the rotation effect dominates the initial compliances, initiation is most likely to take place during the initial decreasing phase and not during the necking dominated phase [3.7]. This is understood as plastic collapse is an unlikely failure mode for SENT specimens. This is supported by the experimental result presented in Figure 3.8.a, where an increase of the compliance takes place prior to entering the necking dominated zone. In view of this observation, crack initiation is supposed to take place when the experimentally obtained compliance deviates from the decreasing trend.
- In absence of the rotation effect, the initial compliances increase linearly as function of the CMOD. It is therefore supposed that any deviation from this linear trend indicates the occurrence of crack initiation.

Basically, this approach is comparable to the offset method, in which the compliances are considered from the minimum onwards. This method is used for the compliance evaluation in SENB and CT testing [3.18, 20, 21]. As a result, only the compliances beyond crack initiation are considered. This method will be discussed in further detail in section 3.3.1.2.

To verify the simulation results discussed above, the finite element model is first validated by evaluating the simulated compliances obtained from linear elastic simulations. These compliances are used as input for the analytical formulae from Shen et al. [3.6], summarized in section 3.3.1.2. As such, the calculated relative crack size can be compared to the relative crack size in the FE model. The linear elastic compliance simulations are performed for 3D side grooved specimens, with relative crack depths ranging between 0.10 and 0.80 in steps of 0.10. Figure 3.7 compares the relative crack depths calculated from the obtained compliances with the relative crack depths of the FE models. Only a minor deviation is observed, which is attributed to the difference between the 2D plane strain modeling approach considered for the analytical equations from Shen et al. and the 3D simulations including side grooves considered in this thesis.

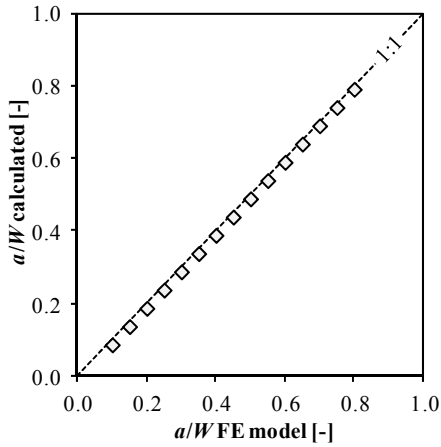

Figure 3.7. Evaluation of a/W obtained from linear elastic FE analysis by means of analytical framework presented in section 2.3

A second validation is performed considering elastic-plastic material properties. For this validation, a set of experimental SENT tests with homogeneous base metal properties and varying relative initial crack depths is selected, namely tests BM-01 till BM-06 (Appendix A). The simulated SENT specimens have identical dimensions and material properties as the experimental ones. The simulated crack depths vary between 1.5 mm and 12.0 mm in steps of 0.5 mm. Figure 3.8.a shows the obtained compliance curves for crack depths from 8.5 mm to 10.5 mm. Also plotted are the experimental data for test BM-06. The initial compliance decrease observed in the experimental data closely matches the evolution of the simulated compliance curves with a constant crack depth. Moreover, the magnitude of this decrease is well captured by the simulations as both curves initially coincide. For higher CMOD levels the simulated compliance curves increase. However, the experimental data show a more drastic increase. This suggests the occurrence of ductile crack extension, which is not incorporated in the FE models. To quantify the amount of ductile crack extension, the experimental compliances are converted to the corresponding crack lengths by means of linear interpolation between the simulated compliance curves. Figure 3.8.b presents a comparison between the post-mortem measured crack extension using the nine points average method (Δa_{9p}) and the simulated crack extensions (Δa_{sim}) for tests BM-01 to BM-06. An excellent correspondence is observed. All but one predicted crack extensions are within 5% of

the measured crack extensions. This validation adds further believe to the accuracy of the presented model in describing the phenomena taking place during experimental SENT testing.

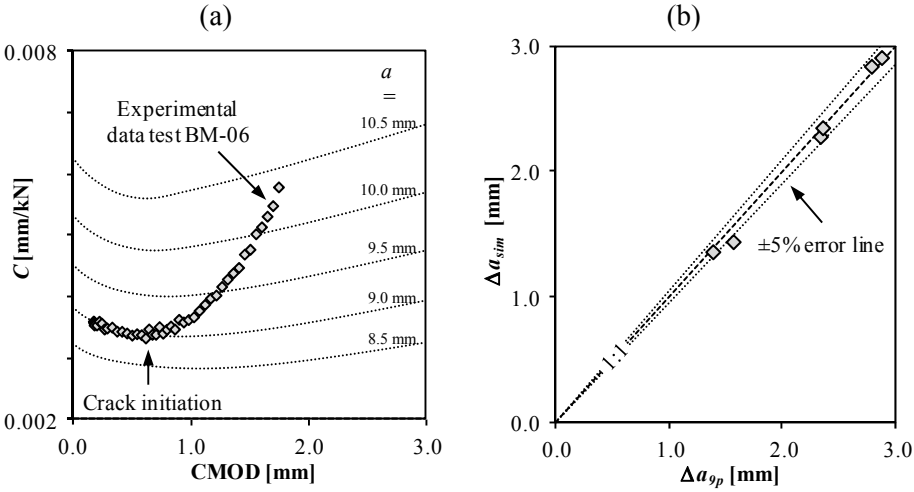

Figure 3.8. Compliance evolution obtained from elastic-plastic simulations with experimental compliances obtained from test BM-06 (a) and evaluation of predicted ductile crack extension (Δa_{sim}) based on mapping of experimental compliances on simulated compliance curves (b)

3.3.1.2 Analytical evaluation of compliances

Given the complexity of the elastic-plastic finite element simulations required to correctly interpret the compliances, a clear need exists for a more hands on, analytical approach. Traditionally, such analytical approach is based on linear elastic compliance equations (e.g. ASTM E1820 for SENB testing [3.4]). For SENT testing, several equations are reported in literature that link the compliance to the crack size (typically crack depth) based on elastic 2D finite element simulations [3.6, 22-24]. A comparative study indicated only minor differences between these equations. The formulation proposed by Shen et al. is considered in the remainder of this work [3.6]. Remark that this equation already indicated a good correspondence to the compliances obtained from 3D simulations, despite it has been derived from a 2D plane strain model (section 3.3.1.1). This approach starts from a generalized *m*-th degree relation between the compliance and the relative crack depth (a/W).

$$\frac{a}{W} = \sum_{i=0}^{m} r_i U^i \tag{3.4}$$

In the above equation, U is calculated from the specimen's effective thickness (B_e), compliance (C) and Young's modulus (E).

$$U = \frac{1}{1+\sqrt{B_e C E}} \tag{3.5}$$

Shen et al. [19] determined the coefficients r_i from 2D plane strain finite element simulations of SENT specimens with a relative crack depth ranging between 0.05 and 0.95. These curve fitting parameters are listed in Table 3.1 (m = 8).

Table 3.1. Curve fitting constants for parameters in Eq. (3.5)

r_0	r_1	r_2	r_3	r_4	r_5	r_6	r_7	r_8
2.072	-16.411	79.600	-211.670	236.857	27.371	-179.740	-86.280	171.764

Equation 3.4 benefits from its simplicity. Although, it should be remarked that analogous to the relationship displayed in Figure 3.3.a, a monotonically increasing relationship is assumed between compliance and crack size. Consequently, the initial decrease of the compliance function that might be observed in experimental testing is not captured. This would result in a prediction of crack closure, which does not have any physical relevance. Therefore the following evaluation method is proposed, based on the finite element results and experimental observations:

- If the compliance curve shows a minimum, discard all compliance data prior to this minimum in the experimentally measured compliance curve.
- If the compliance curve does not show a minimum, it shows a linear increase of the compliances in the early stage of the test. In this case, discard all compliance data prior to the deviation from this linear trend.
- Transfer the remaining compliances to crack lengths using the linear elastic relationship in Eq. (3.4) & (3.5).

To evaluate this method, the moment of crack initiation is studied for deeply notched specimens. To that extent, six specimens with identical initial dimensions taken from the same pipe are tested to varying load levels. Following the testing, the specimens are broken up after cooling to -195 °C in liquid air (cfr. number 1 in Figure 3.9.a) and the fracture surface (of part xx-r) is evaluated using scanning electron microscopy (SEM – Figure 3.9.b). Finally, the remainder half of the specimens is cut longitudinally (cfr. number 2 in Figure 3.9.a). These cross sections (xx-l1 and xx-l2) are evaluated using optical microscopy after etching with a 2% Nital solution (Figure 3.9.c).

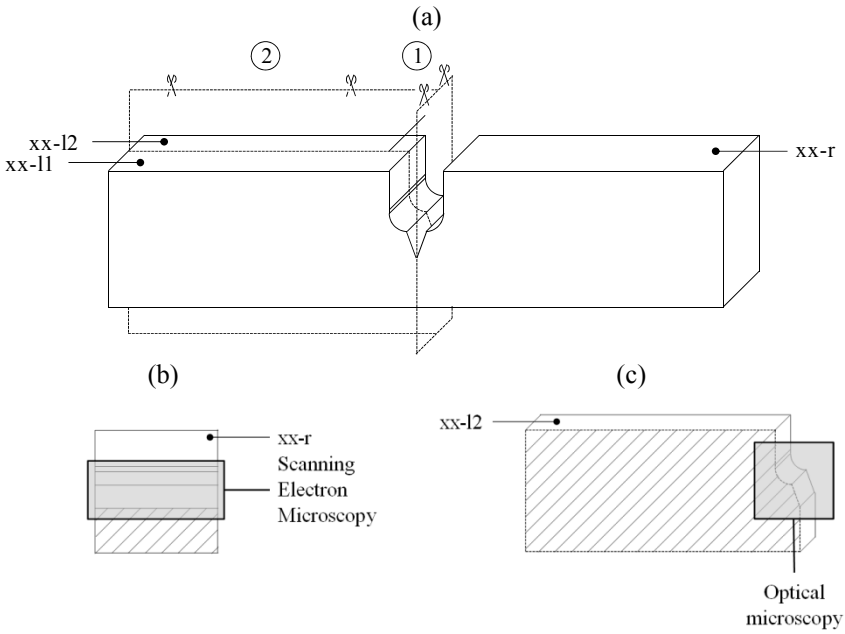

Figure 3.9. Overview of sectioning specimens for evaluation of crack initiation

As the initial decrease of the compliance is more pronounced for deeper cracks, six specimens with an initial relative crack depth a_0/W of 0.5 are tested. The specimens are taken from a non-welded grade API-5L X80 material exhibiting round-house yielding behaviour (details listed in Table 3.2). The end of each test is schematically indicated in Figure 3.10 by means of the vertical red dashed lines (see also Table 3.3). From the indicated end levels, and based on the hypothesis outlined above, crack initiation is expected to take place somewhere between tests Ini-2 and Ini-4, around the minimum of the compliance curve. The exact localization of the minimum is somewhat complex due to the observed scatter in the compliance measurements. Notwithstanding the scatter, no extension is expected for test Ini-1. In contrast, significant crack extension is expected for tests Ini-5 and Ini-6.

Table 3.2. Material properties for tests “Ini-x” obtained from tensile testing of a full thickness strip

σ_0	σ_{TS}	uEL
[MPa]	[MPa]	[%]
583	678	9.28

Table 3.3. Overview of tests performed for the evaluation of crack initiation

Test n°	$CMOD_{max}$ [mm]	C_{final} [10^{-3} mm/kN]
Ini-1	0.62	2.37
Ini-2	0.73	2.36
Ini-3	0.84	2.39
Ini-4	0.96	2.47
Ini-5	1.21	2.54
Ini-6	2.00	3.94

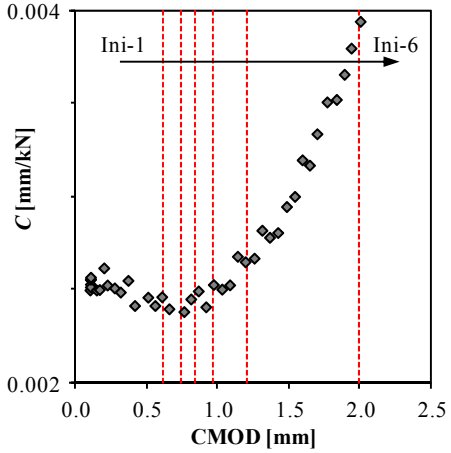

Figure 3.10. Compliances obtained for test Ini-6 and schematic representation of end-levels for tests Ini-1 to Ini-6

The cross sections obtained through optical microscopy (as described in Figure 3.9) indicate a clear transition from a blunted crack tip towards a significant amount of crack extension as the final CMOD level increases (Figure 3.11). Figure 3.11.a, representing test Ini-1, confirms that no crack initiation has taken place, which is expected as the compliance has not yet reached its minimum (Figure 3.10). At this level, the applied load only caused crack tip blunting. For increasing load levels, at least some local crack initiation is observed. However, only from specimen Ini-4 onwards the forced brittle fracture took place along the path of the ductile crack extension. For specimens Ini-2 and Ini-3 the initiated crack has not extended in such way that it controls the forced brittle fracture. It is therefore assumed that the observed crack initiation at these levels is a localized phenomenon not yet extending along the entire crack front.

Looking at the SEM images of the final fracture surfaces (Figure 3.12), the above observations can be understood. Indicated in these SEM images are the final saw cut (dotted line), the transition between the crack blunting/extension and the forced brittle fracture (solid line) and the approximate location of the macrograph discussed previously (vertical solid line). For specimen Ini-2 the transition between the forced brittle fracture and deformation obtained during the initial loading shows an irregular, non-planar crack path. Ductile crack extension is observed along the left part of Figure 3.12.a, which is however not the case along the entire crack front. Consequently, it is concluded that crack extension has not taken place at the level corresponding to specimen Ini-2. This observation is in agreement with the observations from the optical microscopy; crack extension is observed although it comprises a local observation.

Focusing on the fracture surface of specimen Ini-3 (Figure 3.12.b), a certain amount of crack extension is clearly visible at both sides of the specimen, where the presence of side grooves locally increases the constraint and therefore enhances ductile crack extension. In addition, some crack extension is observed in the right half of the specimen. It is concluded for this specimen that crack extension has taken place more or less along the entire crack front. This supports the hypothesis of section 3.3, as the final compliance for this test closely matches the lowest level reached throughout the test, considering the experimental scatter in the compliance data.

Finally, for specimen Ini-4 the crack has clearly extended along the entire width of the initial crack. This crack extension is also clearly observed from the optical microscopy where the plane of final brittle fracture coincides with the plane of crack extension, indeed suggesting that crack extension might have taken place along (close to) the entire crack front.

This study indicates that crack extension is expected close to the location of minimum compliance. For load levels prior to the minimum of the compliance curve, no crack extension is observed along the entire crack front. Once the compliance has passed through a minimum, crack extension was expected and is indeed observed along the entire crack front.

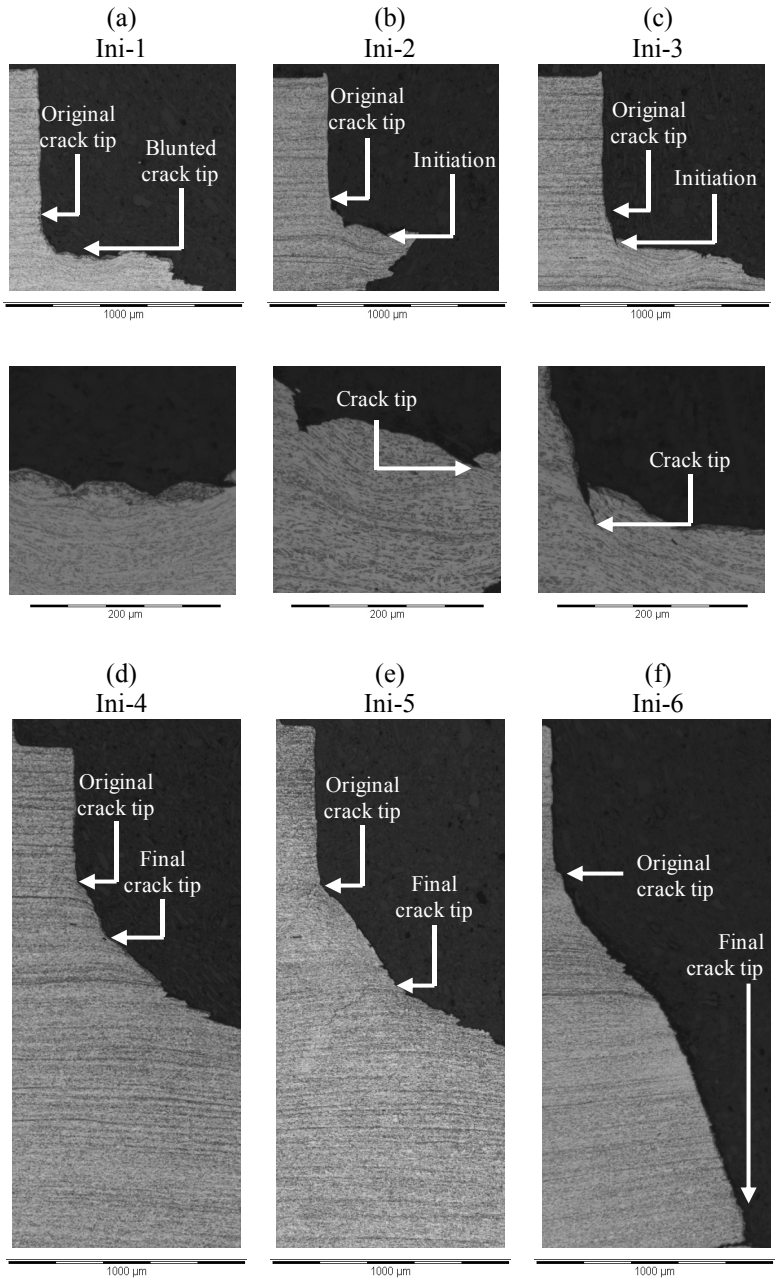

Figure 3.11. Macrographic cross sectional view of crack tip region

(a)
Ini-2

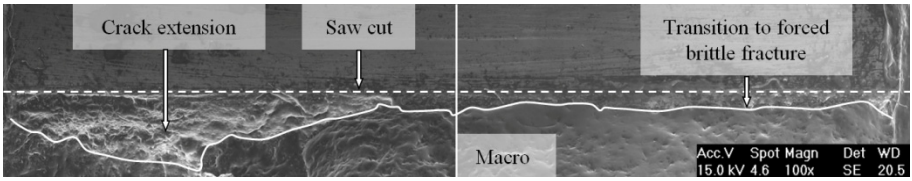

(b)
Ini-3

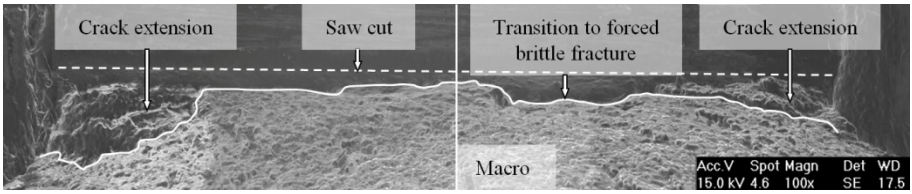

(c)
Ini-4

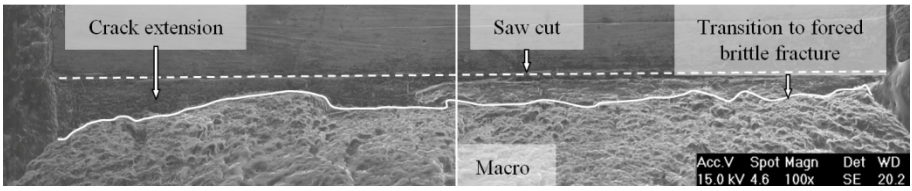

Figure 3.12. Cross-sectional overview of fracture surfaces obtained from SEM analyses

The proposed evaluation method is essentially based on the use of elastic compliances. However, the simulations in section 3.3.1.1 indicate that the actual (elastic-plastic) compliances are not constant. When the evolution of the elastic-plastic compliances is compared to the elastic ones, an excellent correspondence is observed in the initial phase (CMOD near zero, Figure 3.3.b). However, as the applied load in terms of CMOD increases, the elastic-plastic compliance diverges from the elastic compliance. This effect is more pronounced for deeper cracks.

When the ductile crack extension is determined, not only the absolute values of the compliances are of interest. Of bigger importance are the compliance changes, since these changes are eventually related to the crack extension. In view of this, the compliance changes with crack size ($\partial C / \partial a$) for fixed CMOD levels are determined (Figure 3.13). This change depends on the applied CMOD level for elastic-plastic materials and hence differs from a purely elastic approach. At high CMOD levels (e.g. CMOD = 2.0 mm), this results in an overestimation of the ductile crack extension for deep cracks ($a_0/W = 0.6$); the assumed compliance change per unit crack extension is smaller than the actual. Accordingly, the predicted crack extension given a fixed amount of compliance change is higher when the elastic compliances are considered. In contrast, an underestimation of the crack extension might occur for shallow notched specimens ($a_0/W = 0.2$).

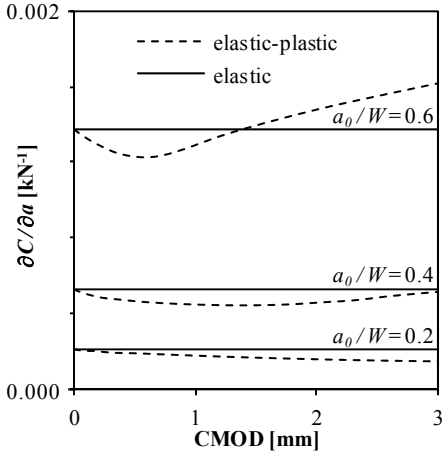

Figure 3.13. Influence of considering elastic material behaviour versus elastic-plastic material behaviour on compliance evolution

3.3.1.3 Crack initiation and blunting

The proposed method only considers the compliance data from crack initiation onwards. Consequently, the crack extension through crack tip blunting (Δa_b) is not accounted for. This blunting is added after completion of the test and can be estimated from the CTOD at initiation ($CTOD_{ini}$) [3.25]. The predicted total crack extension ($\Delta a_{t,uc}$) therefore equals the sum of the crack extension predicted by the UC method (Δa_{uc}) and the crack extension attributed to crack tip blunting.

$$\begin{aligned} \Delta a_b &= CTOD/2 && CTOD \le CTOD_{ini}/2 \\ \Delta a_b &= CTOD_{ini}/2 && CTOD \ge CTOD_{ini}/2 \end{aligned} \tag{3.6}$$

$$\Delta a_{t,uc} = \Delta a_{b,uc} + \Delta a_{uc} \tag{3.7}$$

3.3.1.4 Precision

The precision[1] of the proposed method, in terms of crack extension, depends on the noise of the determined compliances. This noise is evaluated from the compliances measured during the six unloading and reloading cycles in the elastic regime. The used clip gauges have an accuracy of ±1 µm, on average resulting in an experimentally measured standard deviation for these six compliances equal to 27.74 10^{-6} mm / kN. Assuming a normal distribution for these compliances, a 95% confidence interval is determined by multiplying this standard deviation by a factor 1.96. As a result, the precision of the compliance measurements equals 53.78 10^{-6} mm / kN.

To evaluate the influence of this compliance precision on the crack extension, a calibration curve needs to be constructed. By means of example, the curve shown in Figure 3.14.a is considered. The observed precision in terms of crack extension strongly depends on the relative crack depth (Figure 3.14.b), which is expected from the calibration curve. The precision varies between ± 0.02 W for shallow cracks and ± 0.002 W for deeply notched specimens. For a 15 mm wide specimen, this results in a precision of ± 0.3 mm and ± 0.03 mm for a shallow and deep notch respectively. The average crack extension for all tests in this dissertation equals 2.52 mm. For shallow notched specimens, the precision represents approximately 10% of the crack extension. This observation stresses the need for clip gauges with a high accuracy, since errors exceeding this level are preferably avoided.

[1] As defined in Appendix C

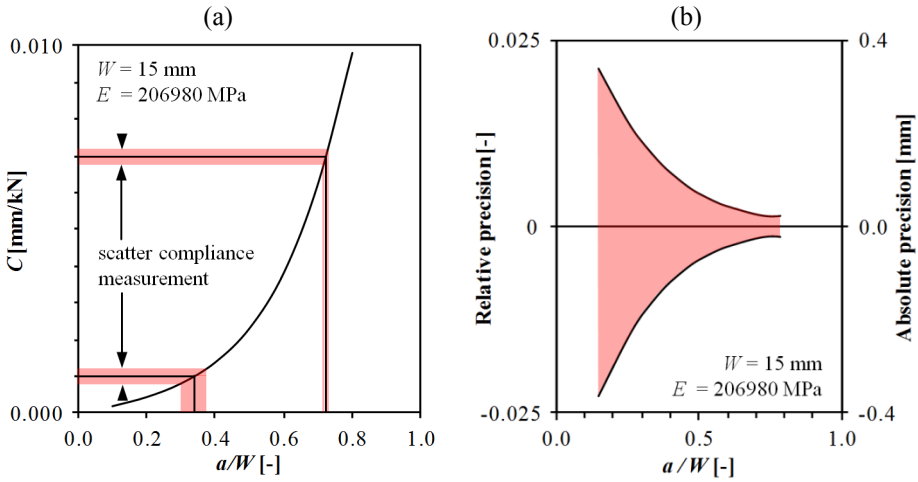

Figure 3.14. Example calibration curve (a) and resulting precision (relative to specimen width) of compliance method as function of relative crack depth (b)

3.3.2. Direct Current Potential Drop method

Considering the potential drop method to measure ductile crack extension, two variants are commonly reported in literature. The first makes use of direct current, the second of alternating current. Hence, the methods are referred to as the direct current potential drop (DCPD) method and the alternating current potential drop (ACPD) method respectively. Both rely on the same basic principle; when applying a current through the specimen the potential drop across a defect is monitored and linked with the resistance created by the (growing) defect.

First, the focus is on the direct current potential drop method. The main advantage over the ACPD method, is the relative simplicity of the involved components. This method only requires a constant current source and a voltage measurement device [3.26]. The primary requirements for the current source are:

- *low ripple and noise* (typically below ± 0.01%): otherwise the measured voltage tends to be highly fluctuating, resulting in a worse precision.
- *high current output* (typically 0.1 A per mm² of the specimen's cross sectional area): this current source should be able to deliver a sufficiently high current, to obtain measurable potential drop values. Typically, the measured signal is in the mV-range.

The voltage measurement device should have a high precision (typically μV-range), to allow detecting small potential drop changes.

Second is the alternating current potential drop technique. Whereas direct current uniformly spreads through the specimen, this alternating current tends to concentrate around the surface of the test specimen (skin effect). Consequently, to obtain a detectable output voltage, a significantly smaller magnitude of the input current is required. On the other hand, the skin effect also implies that this method only allows detecting surface-breaking defects [3.27]. Furthermore, the measured signals as well as the input currents are more susceptible to the influences of surrounding electronic devices; these create secondary pick-up voltages and subsequently tend to increase the noise. This effect is particularly pronounced in areas where high power applications are present. To overcome this detrimental effect, the input current is typically in the kHz range. This allows using high pass or band width filters, as the pick-up signals are typically dominated by a 50Hz component from the net frequency. Unfortunately, this implies the need for a relatively complex measurement device. Another disadvantage of the ACPD technique is the capacitance effect, which induces a voltage change across the crack that depends on the distance between the crack faces. Therefore, relating the measured potential drop to the crack length is less straightforward. Taking into account these disadvantages, the DCPD method is selected over the ACPD method within this dissertation.

3.3.2.1 Principle

Using the DCPD method, the potential drop (V) measured between two points, located at a distance $2D_{meas;1}$ across the crack, is influenced by the conductance of the material (C_m) and, evidently, the current through the cracked ligament (I_a). This is clear from the following relationship (with a representing the crack depth):

$$V \propto \frac{I_a \cdot a}{C_m} \tag{3.8}$$

At first, it should be noted that the temperature during the test might not be constant (e.g. small variations of the ambient temperature). Consequently, as the conductance of metals tends to decrease as temperature increases, the measured potential drop might change [3.28]. To filter out this effect, a second specimen can be placed in series with the tested specimen; the same current flows through both specimens. This second specimen should be subjected to the same temperature variations. However, it is neither mechanically loaded nor contains a crack. Consequently, potential drop changes in this second specimen are solely attributed to temperature changes. Subsequently, the measured potential drop across the crack can be normalized by the potential drop measured in the second specimen to eliminate any temperature effect [3.29].

Second, the current flowing through the cracked ligament should be constant. Note first that the current delivered by the power source (I_s) is split in two parts. It partially flows through the cracked ligament (I_a) and partially leaks through the test rig (I_l).

$$I_s = I_a + I_l \tag{3.9}$$

As long as the leak current remains constant during the test and the power source delivers a constant current, the measured potential drop across the crack will be independent of the current. However, it is possible that - upon loading - the current leakage increases as the resistance at contact between the test specimen and the test rig decreases (e.g. due to an increase of the contact surface). To overcome this anomaly, the specimen should be isolated from the test rig, which is not straightforward.

To overcome both abovementioned issues, a so-called two probe measurement is considered [3.30-33]. Two reference probes are positioned at a distance $D_{meas;2}$ from the crack and a distance $D_{meas;3}$ relative to each other. The measured signal, V_{ref}, is susceptible to power source variations, conductance changes and current variations. As a result, the normalized potential drop becomes solely dependent on the crack size:

$$\frac{V}{V_{ref}} \propto a \tag{3.10}$$

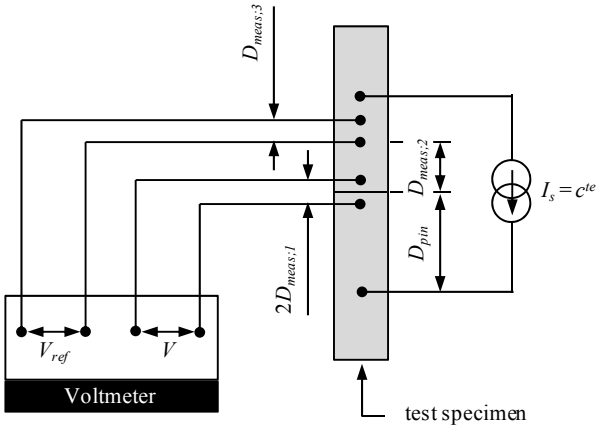

Figure 3.15. Two-probe DCPD technique

Fracture toughness testing often involves the formation of a plastic zone around the crack tip. This plastic zone is known to influence the potential drop across the crack [3.34, 35]. Illustrated in Figure 3.16. are the three phases commonly observed when plotting the potential drop against the CMOD [3.36-38]. At first, a sudden increase in the measured potential drop across the crack might be observed (Phase I). This increase is attributed to the elimination of a potentially reduced resistance due to local contact or the presence of electrically conductive debris in the crack after separation of the crack faces. Second, a linear blunting phase is observed (Phase II). During this phase, the increase of the potential drop originates from the development of a plastic zone around the crack tip. When the potential drop deviates from this linear trend (blunting line), crack initiation is assumed [3.36, 39]. This defines the transition from Phase II to Phase III. During this third phase, the ductile crack extension takes place. To correlate the measured potential drop to a physical crack extension, only the voltage difference between the actual measured signal and the linear blunting line should be considered. This correlation relies on a calibration curve, which can either be obtained from an analytical expression or from finite element simulations, as outlined in the following sections.

Remark that the blunting line in Figure 3.17 is extended beyond the moment of crack initiation. This suggests that the plastic deformation extends, even after crack initiation. This is confirmed by full field strain measurements, discussed in detail in Chapter 6.

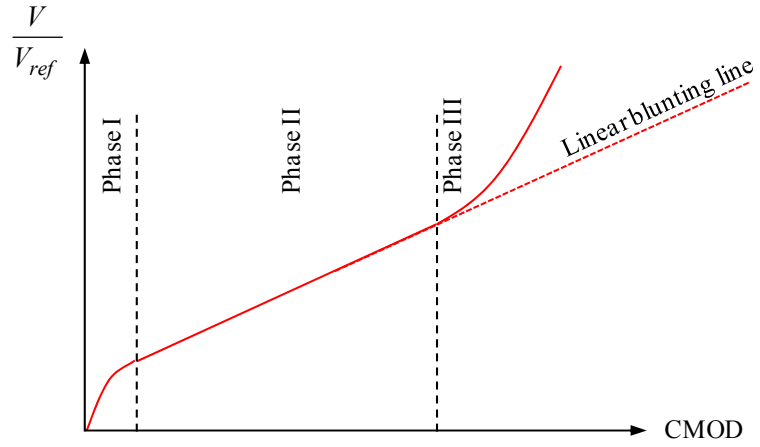

Figure 3.16. Three phases of relative potential drop signal typically observed during fracture toughness testing

3.3.2.2 Positioning of current and measurement pins

An important issue in the interpretation of the test results is the positioning of the current in- and output pins and the measurement pins. First, the position of the current pins is discussed. As indicated in Figure 3.17.a, the closer the input pins are located towards the crack, the higher the measured potential drop across the crack. This is in agreement with results published for CT specimens [3.40]. Although this potentially enhances the measurability of the potential drop, a dependency on the input pin position is also created. Therefore, the current in- and output pins are preferably placed remote from the crack in such way that a zone of uniform electrical potential is obtained between the current in- and output pin position and the crack.

For SENT specimens, a validated parametric finite element model (see §3.3.2.4) is used to determine a suitable pin location for a variety of material and geometrical properties (Table 3.4). First, the discontinuity around the current in- and output pins is studied. To this extent, the standard deviation of the potential field in a plane parallel to the crack is evaluated. Assuming that this standard deviation, normalized by the average value in that plane, should not exceed 1.0%, a stabilization distance, D_{stab}, can be determined (see also Figure 3.17.b and c). Second, the discontinuity around the crack is studied, which also spreads along the specimen's longitudinal direction. The distance over which this discontinuity is observed is affected by the crack size. Simulations indicated that it is a conservative estimation to take this distance equal to the stabilization distance. Hence, the minimum distance for the current pins, D_{pin}, is defined as twice the stabilization distance D_{stab}, to account for the discontinuity in the potential field originating around the crack. As a result, both effects do not mutually affect each other. This leads to the following expression for the pin distance:

$$D_{pin} \geq 18\left(\frac{IW^3}{C_m}\right)^{0.24} + 2 \tag{3.11}$$

This expression is evaluated for an input current of 25 A, which is applied for all SENT tests described in this thesis. As a typical conductance value for metals is between 2000 S/mm and 8000 S/mm, it is clear that considering a pin distance equal to four times the specimen's width satisfies the above concerns (Figure 3.17.d).

Table 3.4. Studied parameter values for selecting appropriate current pin positions in SENT specimens (all combinations studied)

Conductance C_m [S/mm]	Current I_s [A]	Width W [mm]
1000	10	10
2000	20	15
4000	30	20
8000	40	25
16000	50	30

For MWP specimens, a comparable study is performed, with the current input pins located in the specimen's shoulder. In all cases, a uniform potential field is obtained in the MWP's prismatic section.

Second, the position of the reference probes is studied. For these positions, the following should be accounted for:

- *crack growth*: the measurement of the reference potential drop should be independent of the crack size.
- *plasticity*: as indicated by the blunting line in Figure 3.16., the occurrence of plastic deformation in the region where the reference pins are located should be avoided, as it potentially increases the measured potential.

The influence of crack growth has been studied together with the influence of the current pin position, as discussed in the previous section. Hence, for SENT specimens, the reference probes should be located at a distance:

$$D_{meas;2} \geq D_{stab} \tag{3.12}$$

In practice, the distance $D_{meas;2}$ is chosen equal to twice the width, W, of the specimen. It is noted that the reference voltage, V_{ref}, might depend on the current pin position, which does however not affect the functionality of the reference measurement.

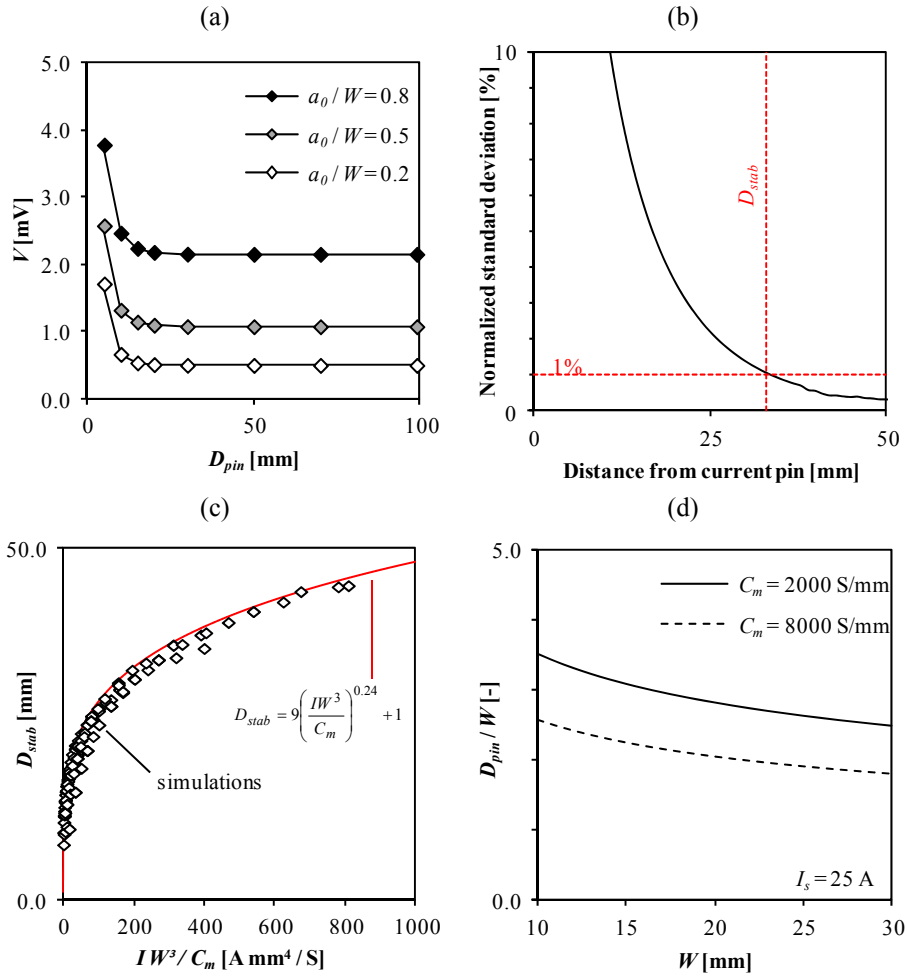

Figure 3.17. Influence of current input pin position on measured potential drop across the crack in SENT specimens (a), evaluation of variability of potential field (b) with concrete obtained stabilization distance (c) and required pin distance for SENT specimen with applied current of 25A (d)

To study the potential effect of plasticity on the reference potential measurement, the DIC technique has been used (section 6.3 in Chapter 6). Regarding the SENT specimens, a typical deformation pattern consists of two shear lines originating from the crack tip under a 45° angle. Accordingly, the plastically deforming zone will not extend beyond an axial length of $2W$, as required by the crack growth criterion (Eq.(3.12)). In addition, the drill holes used to attach the reference probes are unlikely to influence the deformation pattern around the crack tip.

Regarding the MWP specimens, the preferred position for the reference pins is in the specimen's shoulder. As such, the drill holes required for the attachment of the probes do not influence the deformation pattern in the prismatic section where the remote strain is measured. Furthermore, finite element simulations indicated that the reference probe measurements are independent of the crack size. However, plastic deformation might occur in this area. Figure 3.18. shows the residual plastic deformation after unloading of the specimen for test WP-5. The left shoulder dimensions are optimized for potential drop measurements, in contrast to the right one. Some residual plastic deformation is observed in the un-modified shoulder. For the optimized shoulder, plastic deformation is observed in a 45° area originating from the edges of the prismatic section. Accordingly, setting the length of the shoulder equal to $2W$ assures the presence of a plasticity-free zone to position the reference probes. As a result, the reference probes are close to the current input pins and the measured reference potential depends on the exact current pin position. However, this is not an issue as it does not alter the reference potential throughout the test.

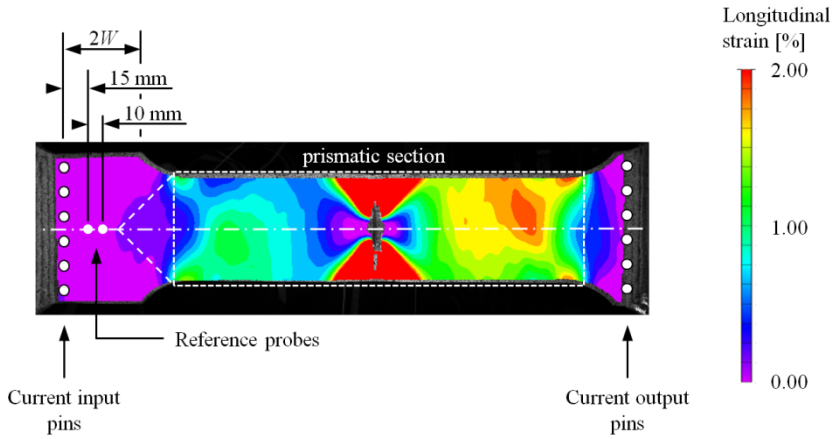

Figure 3.18. Position of reference probes and evaluation of strain pattern after complete unloading of the MWP specimen of test WP-5

Third, the position of the measurement probes located across the crack is evaluated. Both for the SENT and MWP specimens, placing the pins closer to the crack (decreasing $D_{meas;1}$) results in higher sensitivity to crack extension (Figure 3.19.a). However, the magnitude of the measured signal decreases (Figure 3.19.b).

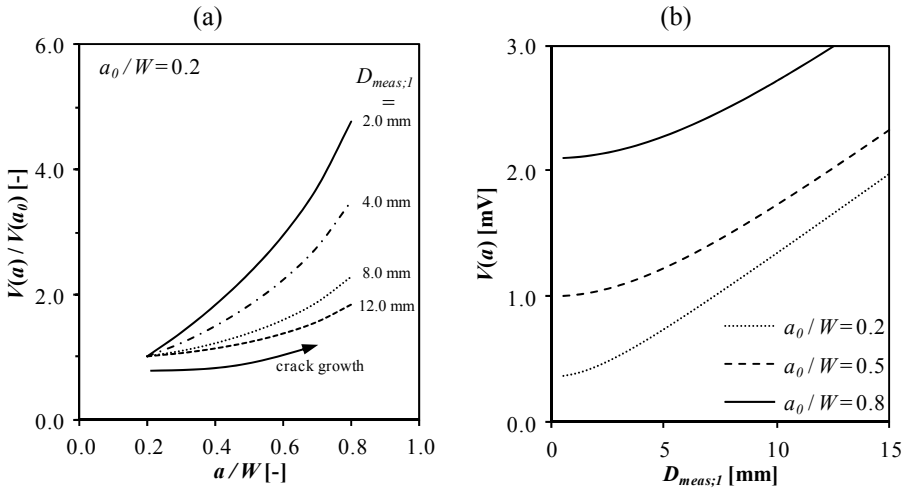

Figure 3.19. Influence of position of voltage measurement pins in relative (a) and absolute terms (b) for SENT specimens

Given the need for drill holes to attach the knives for the double clip gauge measurement, as outlined in Chapter 4, preference is given to this position for the measurement of the potential drop across the crack. This results in a distance $D_{meas;1}$ that theoretically equals 9.0 mm for the SENT and 5.0 mm for the MWP specimens.

3.3.2.3 Analytical evaluation of measured signals

Converting the measured potential drop to a crack length can be based on either analytical equations or finite element simulations. The use of an analytical equation is preferred, since it yields quicker results and requires fewer skills for a correct interpretation. However, analytical equations are only available for simple, standardized geometries, and not for MWP specimens with potentially complicated geometry (i.e. weld cap reinforcement, misalignment, …). Accordingly, the remainder of this section focuses on SENT specimens.

In 1965, Johnson et al. [3.41] published an analytical equation for the evaluation of crack sizes from direct current potential drop readings. This equation assumes a uniform current field remote from the cracked ligament, which has previously been discussed for the SENT specimens in this work (section 3.3.2.1). Notwithstanding being originally developed for CCT specimens, this equation can also be considered for SENT and SENB specimens. This results in Eq.(3.13), relating the potential drop for the actual crack depth ($V(a)$) to the potential drop for the initial crack depth ($V(a_0)$) [3.42].

$$\frac{V(a)}{V(a_0)} = \frac{\cosh^{-1}\left(\dfrac{\cosh\left(\pi D_{meas;1}/4W\right)}{\cos\left(\pi a/2W\right)}\right)}{\cosh^{-1}\left(\dfrac{\cosh\left(\pi D_{meas;1}/4W\right)}{\cos\left(\pi a_0/2W\right)}\right)} \tag{3.13}$$

Remark that evaluating the potential drop using the above equation does not require knowledge of the material's conductance, nor does it depend on the applied current. Solely the specimen's geometry and the position of the measurement probes influence the predicted crack extension.

3.3.2.4 Numerical evaluation of measured signals

Both for the SENT and MWP specimens, a 3D parametric coupled thermal-electric finite element model is developed for ABAQUS^{TM} version 6.11. The SENT model is used to validate the modeling technique, by comparing the results with the Johnson equation, and to determine the optimum location for the current and measurement pins (section 3.3.2.2). The MWP model is additionally used for the interpretation of the test results.

First, the SENT model is introduced. The geometry of this model is taken from the model outlined in section 3.3.1.1 for the evaluation of the compliances (i.e. half model with longitudinal symmetry and spider web mesh around initially blunted crack). The material properties are defined in terms of the material's conductance (C_m). Homogeneous material properties are assumed, regardless the presence of a weld. The model geometry is not deformed during loading but solely subject to a constant current, which is applied through two remotely positioned current pins (Figure 3.20.a). To determine the electric potential in each node, a reference potential is required. Accordingly, the center of the specimen, opposite to the crack mouth is grounded. This region is mainly selected to obtain electric potential fields that are symmetrical around the crack (Figure 3.20.b).

The validity of the FEA results is checked by evaluating the potential drop across the crack relative to the potential drop for an assumed initial crack with $a_0/W = 0.2$. This normalized potential drop is compared to the right hand side of the Johnson equation, Eq.(3.13). An excellent correspondence is observed, providing confidence in this method (Figure 3.21). Second, the observed correspondence suggests that 3D effects can be neglected, as the Johnson equation has originally been developed based on 2D assumptions.

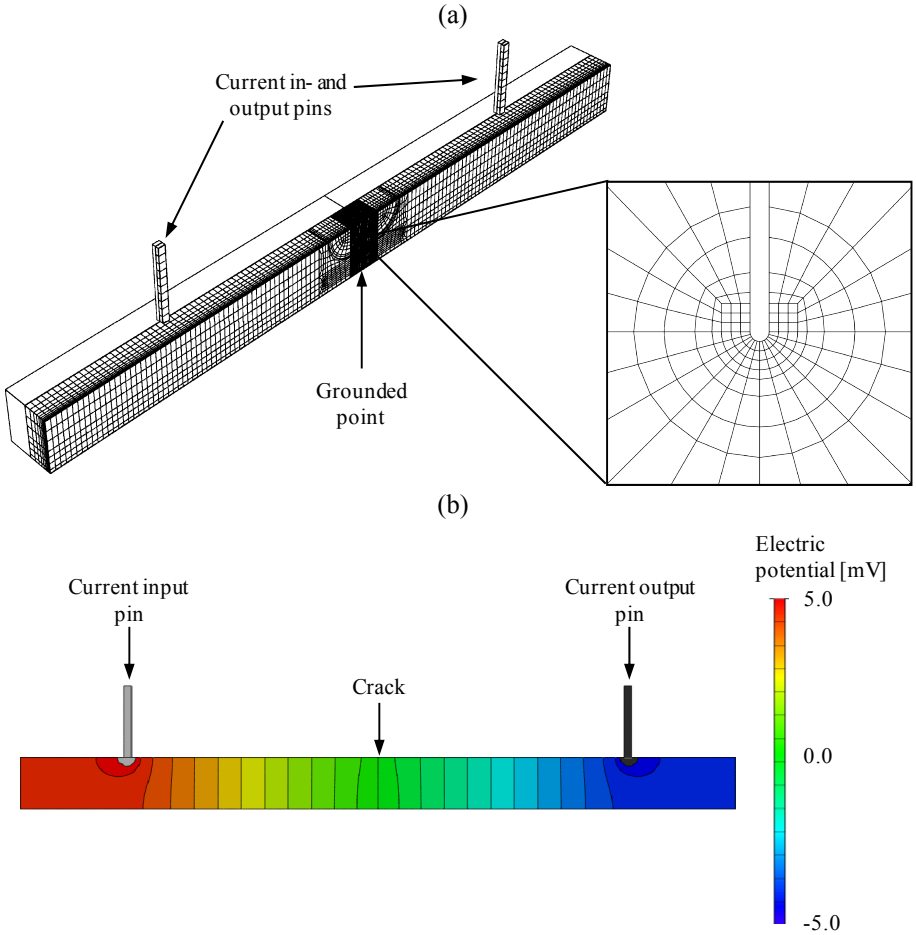

Figure 3.20. Overview of 3D SENT FE model for potential drop evaluation (a) and characteristic electric potential field in the symmetry plane indicating slight non-uniformity of the electric potential field near crack and current in- and output pins (b).

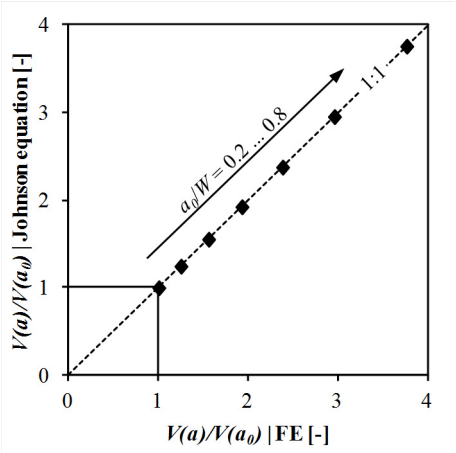

Figure 3.21. Comparison of analytically calculated and FEA simulated normalized potential drop in SENT specimens

The description of the MWP geometry is somewhat more complicated compared to the SENT specimen, as the model needs to account for plate curvature, weld cap reinforcement,… The model considered in this study is adopted from the parametric script developed by Hertelé et al. [3.43]. This model starts from a simplified geometry, which is modified by means of coordinate transformations. As a result, the weld cap reinforcement, misalignment, etcetera are adequately described by the model (Figure 3.22).

The defect size is controlled by two parameters, namely the defect depth, *a,* and the defect length, 2*c*. These two parameters uniquely define the semi-elliptical shape of the crack. For evaluating the amount of crack extension, it is assumed that the crack length remains constant. This is a fair approximation for MWP tests; crack extension in the pipe's circumferential direction is limited [3.44, 45].

Analogous to the SENT model, the material properties are defined by the conductance of the material. A uniform conductance is assigned to the model, regardless the presence of weld metal. The current input is modeled using a discrete number of input pins, located in the specimen's shoulder.

The specimen is meshed using linear brick elements with reduced integration scheme (ABAQUS^{TM} type DC3D8E). A mesh convergence study assured mesh independent electric potential calculations. According to this study, an appropriate mesh consists of approximately 20000 nodes.

(a)

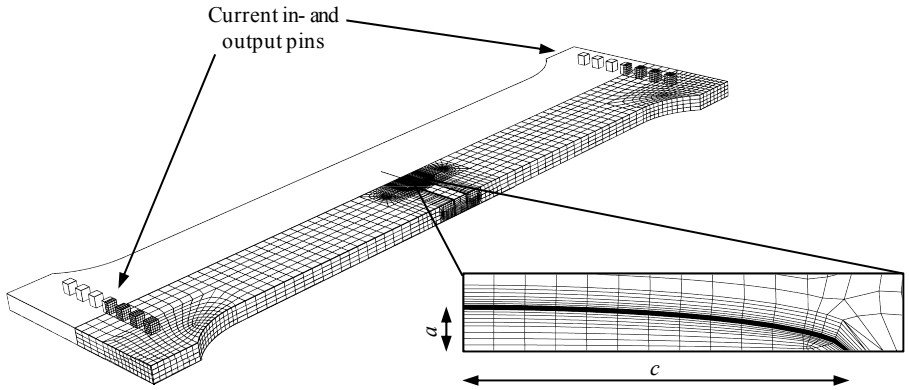

(b)

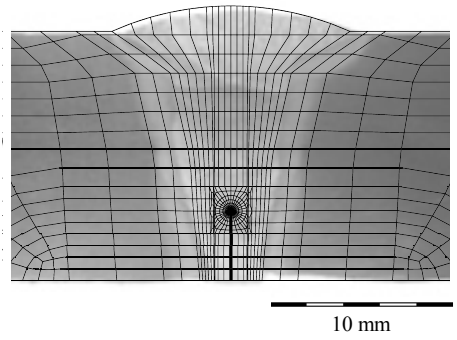

Figure 3.22. Overview of finite element mesh (consisting of approx. 20000 elements) in MWP specimen with detail of semi-elliptical crack dimensions (a) and overlay plot of mesh after coordinate transformations with etched macrograph for test WP-2

From the simulated electric potential field, the potential drop across the crack is calculated. By doing so for increasing crack depths (a), a transfer function is obtained to convert the measured potential drop to the corresponding crack depth. By means of example, a comparison is made between the transfer function for SENT and MWP specimens with identical conductance properties ($C_m = 2000$ S). In addition, the width of the SENT specimens equals the wall thickness for the MWP specimens ($W = t = 15$ mm). The applied current equals 25 A for the SENT specimen and 150 A for the MWP specimen. Both current magnitudes are well in accordance with the ones used during the experiments. On average the magnitude of the SENT potential signals is seven times higher than the MWP potential signals, notwithstanding the applied current is six times smaller for this SENT specimen (Figure 3.23.a). However, when considering the relative voltage change, the trend is comparable for both specimen types (Figure 3.23.b). The MWP specimen appears slightly less sensitive to crack extension, which is understood from the smaller relative change in net section with increasing crack size for this specimen.

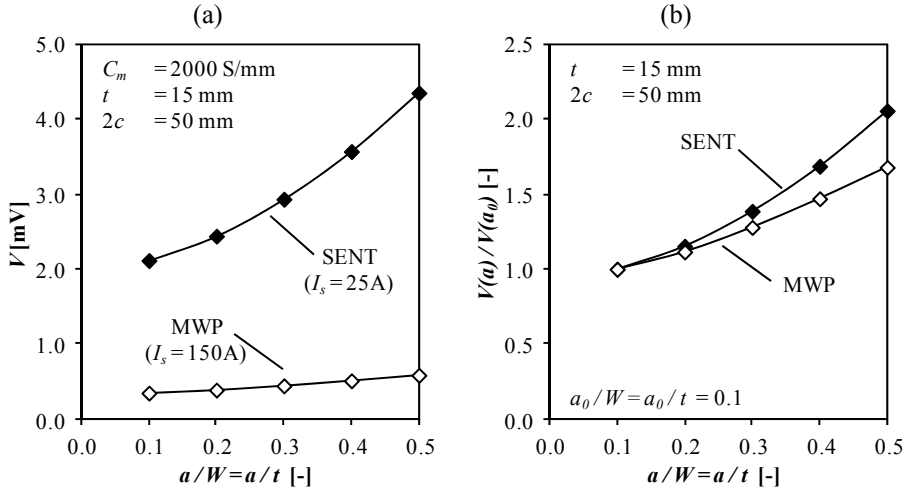

Figure 3.23. Evaluation of electric potential magnitude (a) and normalized trend (b) for SENT and MWP specimens with comparable material properties and defect sizes considering current magnitudes equal to the ones used in the experiments

3.3.2.5 Crack initiation and blunting

Analogous to the unloading compliance method, the potential drop method only considers the ductile crack extension after initiation. As a result, the predicted total amount of ductile crack extension (Δa_t) consists of both the crack extension predicted by the PD method (Δa_{pd}) and the crack extension attributed to crack tip blunting (Δa_b). The latter is calculated from the CTOD at initiation ($CTOD_{ini}$ – Eq.(3.6)) [3.25].

$$\Delta a_{t,pd} = \Delta a_{b,pd} + \Delta a_{pd} \tag{3.14}$$

3.3.2.6 Precision

The precision[2] of the potential drop method depends on a number of factors. First, the voltage measurement device is considered. Within the range selected for the fracture toughness tests described in this dissertation, a precision of 10 nV is obtained. Taking into account the magnitude of the measured signal (typically between 0.1 and 1.0 mV), this results at least in a precision of 0.1‰.

A second important factor is the location of the voltage measurement pins. It has been demonstrated previously (e.g. Figure 3.19) that the distance between the pins might strongly influence the electric potential reading. The distance between these pins is typically determined using a caliper, which has a precision of 0.01 mm, though the accuracy[2] is around 0.1 mm. In addition, the pin position is assumed symmetrical around the crack (e.g. Johnson equation - section 3.3.2.3), which is clearly not evident in practice. The impact of this lacking precision is evaluated by studying a representative SENT and MWP geometry. The following error function is defined to evaluate the impact of an erroneous positioning.

$$error = \frac{\Delta a_{actual} - \Delta a_{nom}}{\Delta a_{nom}} \times 100 \tag{3.15}$$

With:

Δa_{nom} predicted crack extension using the nominal value for $D_{meas;1}$

Δa_{actual} predicted crack extension using the worst case value for $D_{meas;1}$

This error is typically between ±1% for the SENT and ±2% for the MWP specimen. The difference between both is attributed to the different location of the measurement pins as it has previously been shown that the closer the measurement pins are located to the crack, the higher the sensitivity to the pin position. A pin distance, $D_{meas;1}$, of 9.0 mm is selected for the SENT specimen and 5.0 mm for the MWP specimen, representing the experimentally considered conditions.

Finally, the actual geometry also has its influence on the predicted crack extension. For SENT specimens, the specimen's thickness, W, can be determined with an accuracy of 0.01 mm using a caliper. This results in an error of approximately 0.01%, as defined by Eq.(3.15). For MWP specimens, a variety of other parameters has an influence, such as the wall thickness, weld cap reinforcement, weld misalignment, … Their influence is not studied in detail, though the influence is in general limited to 1%, as indicated in Figure 3.25. As the differences between the modeled and actual geometry are never as pronounced as the ones illustrated, it is assumed that the influence of these anomalies is mostly limited. It is therefore concluded that the precision is primarily controlled by the positioning of the measurement probes, which should be given utmost attention during preparation of the tests.

[2] For a definition of precision and accuracy, the reader is referred to Appendix C

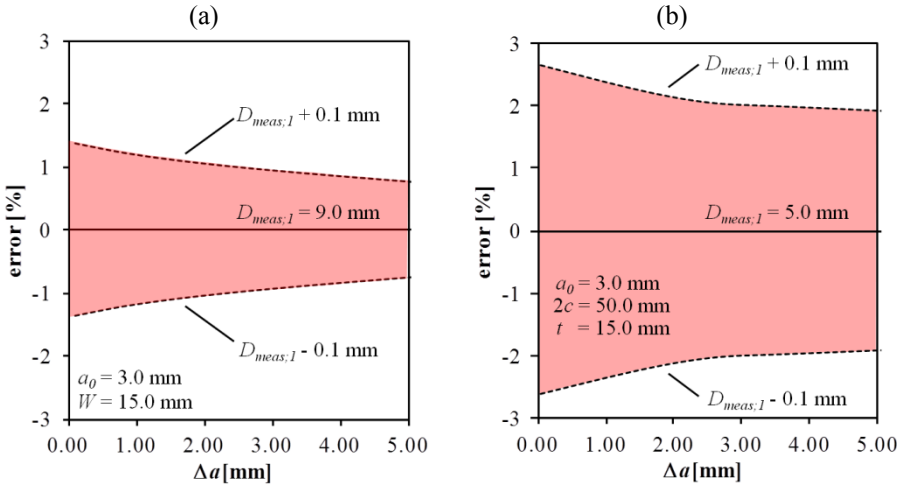

Figure 3.24. Evaluation of precision of measurement pin location on the predicted crack extension for SENT (a) and MWP (b) specimen

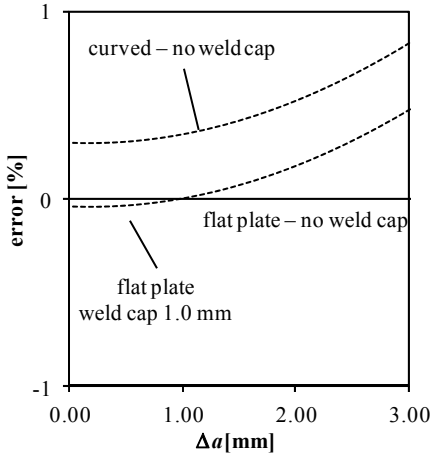

Figure 3.25. Influence of weld cap and plate curvature on predicted crack extension in MWP specimen

3.4. Results

The methods presented in section 3.3 are applied to all the tests described in section 3.2. This allows evaluating the accuracy of the different methods.

3.4.1. SENT testing

3.4.1.1 Evaluation method

To evaluate the accuracy of both the unloading compliance and the potential drop method, the calculated ductile crack extension is compared to the measured one. To that extent, after completion of the test, the specimens are first heat tinted at 200°C for 2 to 3 hours leading to oxidation of the fractured surface. Subsequently, the specimens are broken up in a brittle way after cooling the specimens in liquid air (Figure 3.26). The final crack extension is then determined using the nine points average method, as suggested by ASTM E1820 for SENB testing [14].

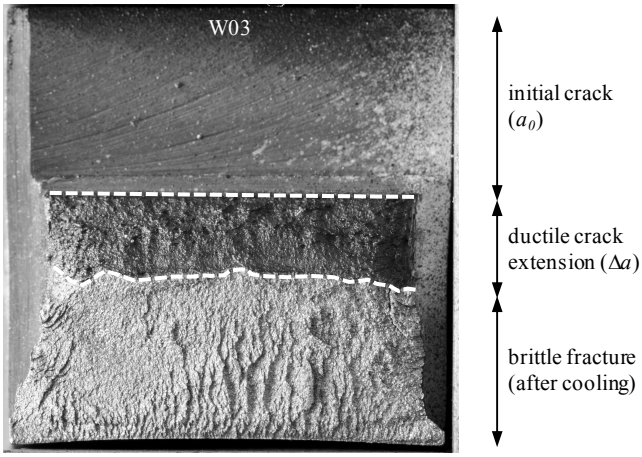

Figure 3.26. Example fracture surface after heat tinting

To analyze the accuracy, the standard deviation (*STD*) is calculated for the series of *N* tests considered, via the following formula:

$$STD = \sqrt{\frac{1}{N}\sum_{i=1}^{N}\left(\Delta a_{9p,i} - \Delta a_{t,uc/pd,i}\right)^2} \tag{3.16}$$

Based on this calculated standard deviation, and furthermore assuming a normal error distribution, a 95% confidence interval is determined. This allows evaluating the accuracy of the considered method as follows:

$$\Delta a_{t,uc/pd} = \Delta a_{9p} \pm 1.96\,STD \tag{3.17}$$

3.4.1.2 Accuracy

In general, Figure 3.27 indicates an excellent correspondence between the measured and calculated crack extension for both methods. This results in an overall accuracy of ± 0.34 mm (± 13%) and ± 0.31 mm (± 12%) for the unloading compliance and potential drop method respectively. This accuracy can be compared to the requirements in the ASTM E1820 standard for SENB testing [3.4]. It is stated that the difference should be limited to 15% of the average measured crack extension. It is concluded that this requirement is easily met with the current tests.

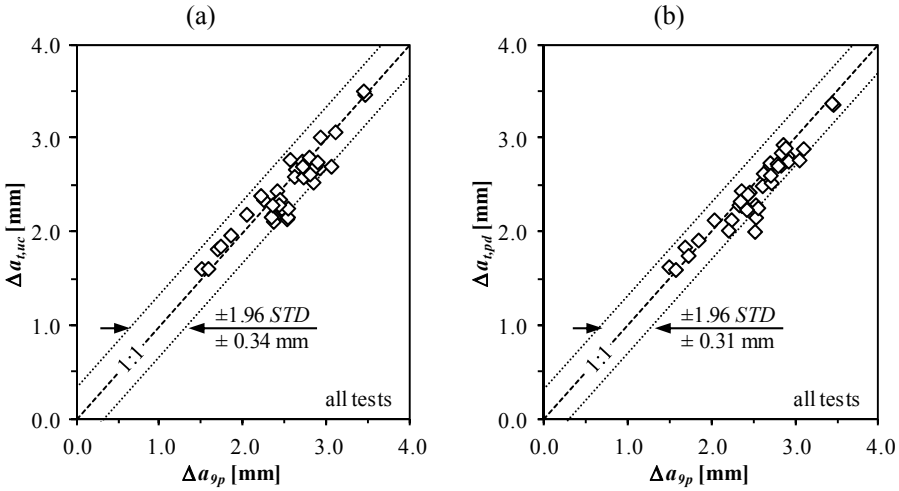

Figure 3.27. Evaluation of accuracy for unloading compliance (a) and direct current potential drop (b) method during SENT testing

3.4.1.3 Factors influencing accuracy

Several factors are expected to influence this accuracy. In the remainder of this section, the following factors are discussed:

- Presence of natural weld metal defects
- Initial crack size
- Crack front straightness

First, the focus is on the presence of natural weld metal defects. By means of example the measured and calculated ductile crack extension are compared for the welded SENT tests numbered WP2-xx and WP3-xx (Figure 3.28). These tests result in data points that are located close to or below the lower bound of the 95% confidence interval obtained using all test data (section 3.4.1.2 - indicated by the dotted lines in Figure 3.28). This observation is attributed to the presence of natural weld metal defects. In Figure 3.29, the fracture surface for specimen WP2-03 is shown. Multiple natural defects can easily be observed (white arrow signs). These natural defects contribute to the crack extension as measured by the nine points average method, though do not necessarily increase the potential drop across the crack during the test. Most likely, this potential drop was already present at the start of the test. The same applies for the unloading compliance method: the natural defects already decreased the initial compliance and are therefore not accounted for in the crack extension measurements during the test.

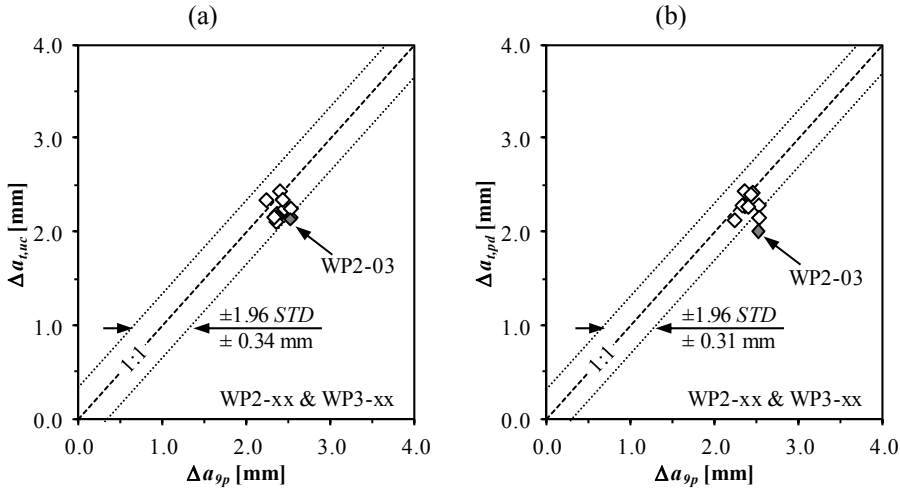

Figure 3.28. Comparison of overall accuracy and test data for SENT tests WP2-xx and WP3-xx for unloading compliance (a) and direct current potential drop (b) method

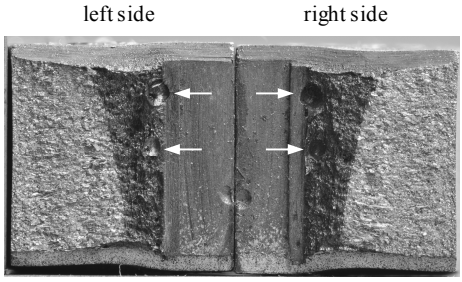

Figure 3.29. Fracture surface for specimen WP2-03 clearly showing the presence of natural weld defects in the zone of ductile crack extension (indicated by white arrow signs)

Given the absence of these natural defects in base metal tests, a better correspondence is expected between the measured and calculated crack extension. This particularly holds for the potential drop method, where the data points are clearly contained within the 95% confidence interval (Figure 3.30.b). For the unloading compliance method, the results are somewhat biased since these base metal specimens have a wide range of relative crack depths. It has previously been shown (§3.3.1.1) that for specimens with a high initial crack depth the crack extension tends to be overestimated. In contrast, an underestimation is expected for shallow cracks. This effect is indeed observed though the influence is clearly limited, indicating that the proposed method for the evaluation of the unloading compliance data performs satisfactorily.

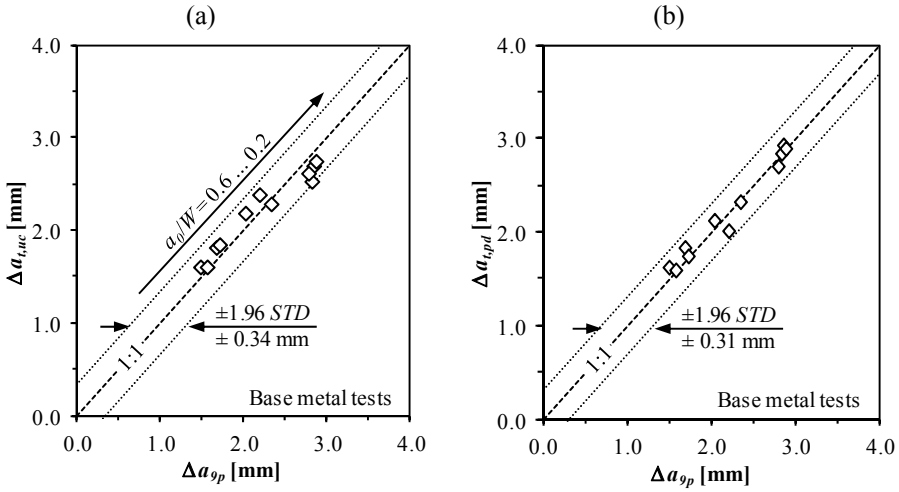

Figure 3.30. Evaluation of accuracy for unloading compliance (a) and direct current potential drop (b) method for homogeneous base metal SENT tests

A third factor that potentially influences the accuracy of the crack extension measurements, is the straightness of the crack front (e.g. tunneling) [3.46]. For the tests performed in the framework of this thesis, an inverse tunneling is often observed. This most likely indicates that the thickness reduction resulting from applying the side grooves is too high. To evaluate the influence of the crack front straightness, the parameter s_{cr} is introduced. This is calculated as the ratio of the standard deviation of the crack depths measured using the nine points average method (Δa_i) to the nine points averaged crack extension (Δa_{9p}).

$$s_{cr} = \sqrt{\frac{1}{9}\sum\left(\Delta a_i - \Delta a_{9p}\right)^2} \Big/ \Delta a_{9p} \tag{3.18}$$

In Figure 3.31.a these values are plotted against the relative error of the potential drop method for specimens WM-07 till WM-15. These specimens are selected since they are obtained from the same weld; though differ significantly in crack front straightness due to the different notching position (inner diameter vs. outer diameter vs. through thickness notch – see also Chapter 5). A minor dependency on the crack front straightness is observed, though in general the influence of the crack front straightness is limited. In particular when realizing the extreme non-uniformity of some specimens involved in this series, e.g. specimen WM-15 shown in Figure 3.31.b.

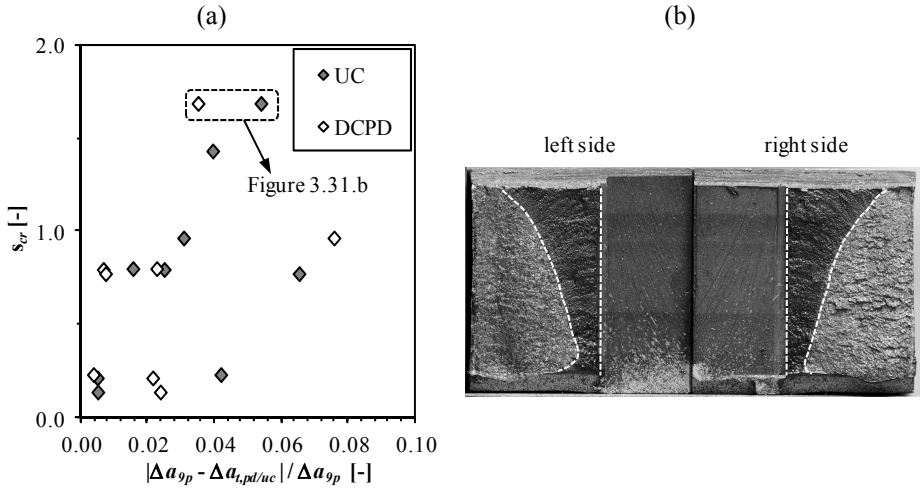

Figure 3.31. Influence of crack front straightness on accuracy of predicted crack extension for potential drop method for specimens WM-07 to WM-15 (a) and fracture surface showing highly non-uniform crack extension for specimen WM-15 (b)

3.4.1.4 Crack initiation

Apart from the final crack extension, the moment of crack initiation is also compared for both methods. An excellent correspondence is observed (Figure 3.32). This again supports the equivalence of both measurement methods. It also adds belief to the proposed methods, in particular for selecting the moment of crack initiation using the unloading compliance method.

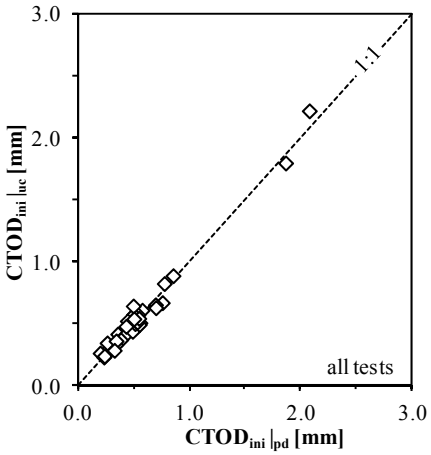

Figure 3.32. Predicted moment of crack initiation for unloading compliance method versus potential drop method for all SENT tests

3.4.2.MWP testing

In contrast to the SENT specimens, the MWP specimens are not broken up in a brittle way after completion of the test. As an alternative, a macrograph is made at the center of the crack (Figure 3.33). This allows evaluating both the crack growth at this deepest point and the final crack tip opening displacement, as discussed in Chapter 4.

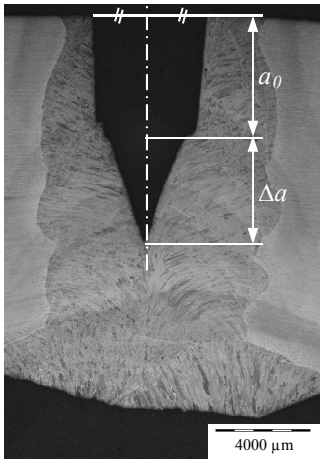

Figure 3.33. Example macrograph taken at the middle of the crack after completion of the test (WP-05)

By means of example, the potential drop measurements for specimen WP-01 are shown together with the force, strain and CMOD measurements (Figure 3.34). It is observed that the point of crack initiation, as predicted by the potential drop method (Figure 3.34.c), corresponds to the moment at which the CMOD increases more than linear with the remote strain (Figure 3.34.b). This is well before maximum force, as indicated in Figure 3.34.a. Figure 3.34.d shows the obtained resistance curve together with the measured final crack extension; a slight overestimation is observed.

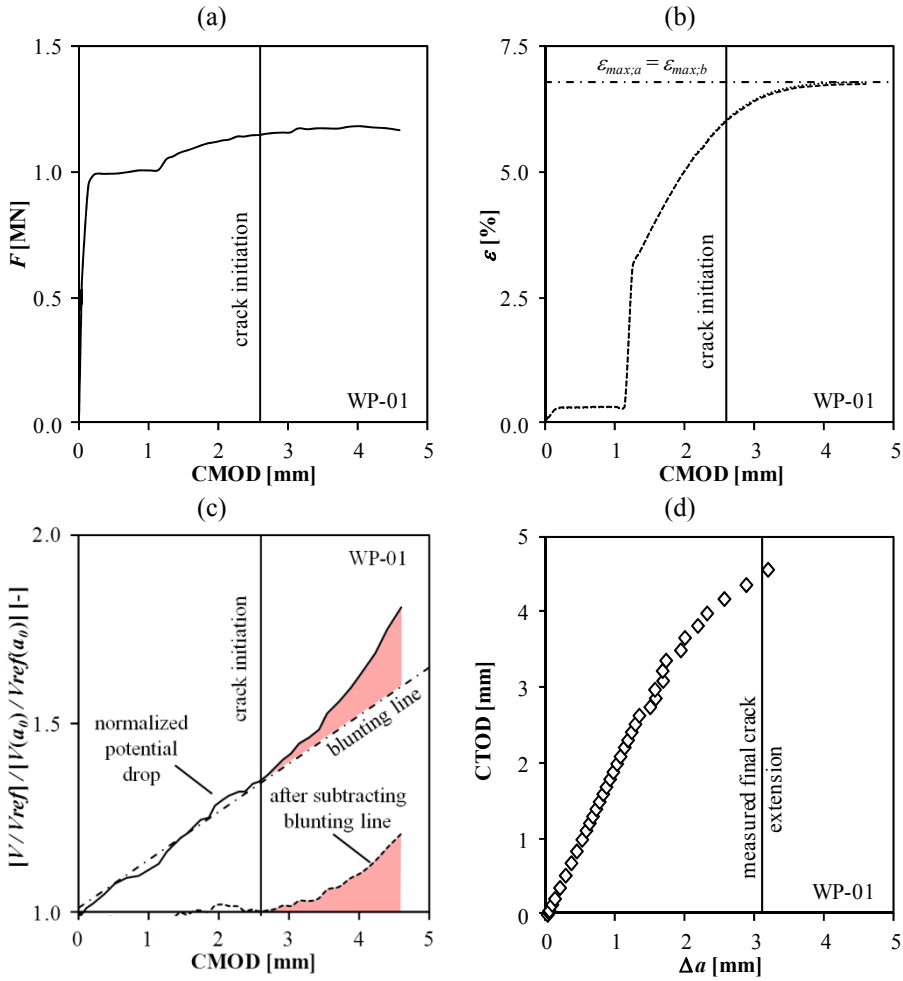

Figure 3.34. Evaluation of ductile crack extension in specimen WP-01: force – CMOD diagram (a), remote strain – CMOD diagram (b), potential drop – CMOD diagram (c) and tearing resistance (d)

Similar observations are made for the other specimens, though in general the amount of ductile crack extension is slightly underestimated (Figure 3.35). For one specimen, WP-03, the crack extension is even largely underestimated. This is understood from the macrograph (Figure 3.36), a clear deviation of the crack path is observed. This deviation is caused by the presence of a natural weld defect but might also be attributed to the weld strength overmatching. The strain concentrates in the lower strength base metal at the left side, which directs the crack path towards this lower strength material. During the sectioning process, preparing the macrograph, it appeared furthermore that the crack extension did not take place along the entire length of the crack. Consequently, the assumptions made in the finite element model are violated; the crack extension does not result in an elliptical crack front. It is clear that this test points out the limitations of the presented potential drop method.

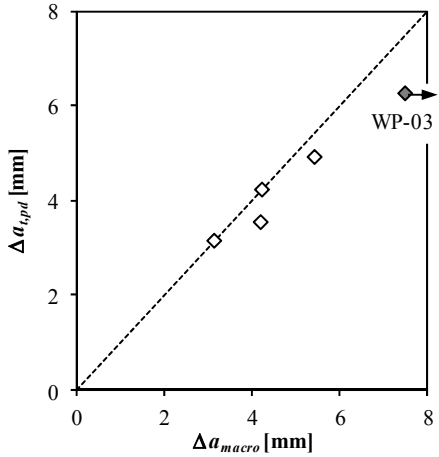

Figure 3.35. Comparison between measured and predicted ductile crack extension for MWP tests

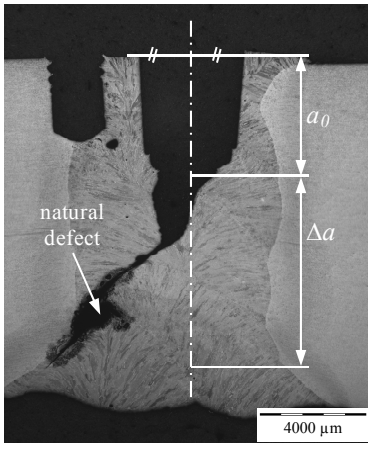

Figure 3.36. Macrograph taken after completion of the test (WP-03)

The observed underestimation is not well understood so far, though is most likely related to the excessive plastic deformation taking place around the crack. Amongst others, this results in a constant change of the measurement probes' location relative to the crack. More specifically, it might be assumed that this distance increases. A larger crack extension would be predicted when increasing this distance. Unfortunately, the current modeling approach does not allow the analysis of such highly deformed geometries. This might be an interesting topic for future research.

3.5. Conclusions

For the evaluation of a material's tearing resistance, an accurate sizing of the defects during testing is required. In this chapter, two methods have been studied, namely the unloading compliance and the direct current potential drop method. The latter has been used for both SENT and MWP testing, the first has solely been considered in SENT testing.

Focusing on the SENT testing, the presented methods are schematically summarized in Figure 3.37 and Figure 3.38 for the unloading compliance and potential drop methods respectively. For both methods the evaluation of the moment of crack initiation is most crucial, experience might be required in some cases. However, when comparing the moment of crack initiation, a nice correspondence between both methods is observed. In addition, the accuracy of both measurement methods is comparable, demonstrating that these methods are equivalent. It should however be noted that the following might affect the accuracy of the measurements:

- presence of defects
- relative initial crack size (unloading compliance only)

In contrast to the analytical solutions that are available in literature for the SENT specimens, detailed 3D finite element simulations are required for a correct interpretation of the potential drop measurements in MWP specimens. In all but one specimen, the presented potential drop method also allowed a correct evaluation of the final crack extension; only a minor underestimation is observed. Note however that the presented method appears solely applicable in case the crack extension can be approximated by a semi-elliptical crack front shape in the plane of the original crack.

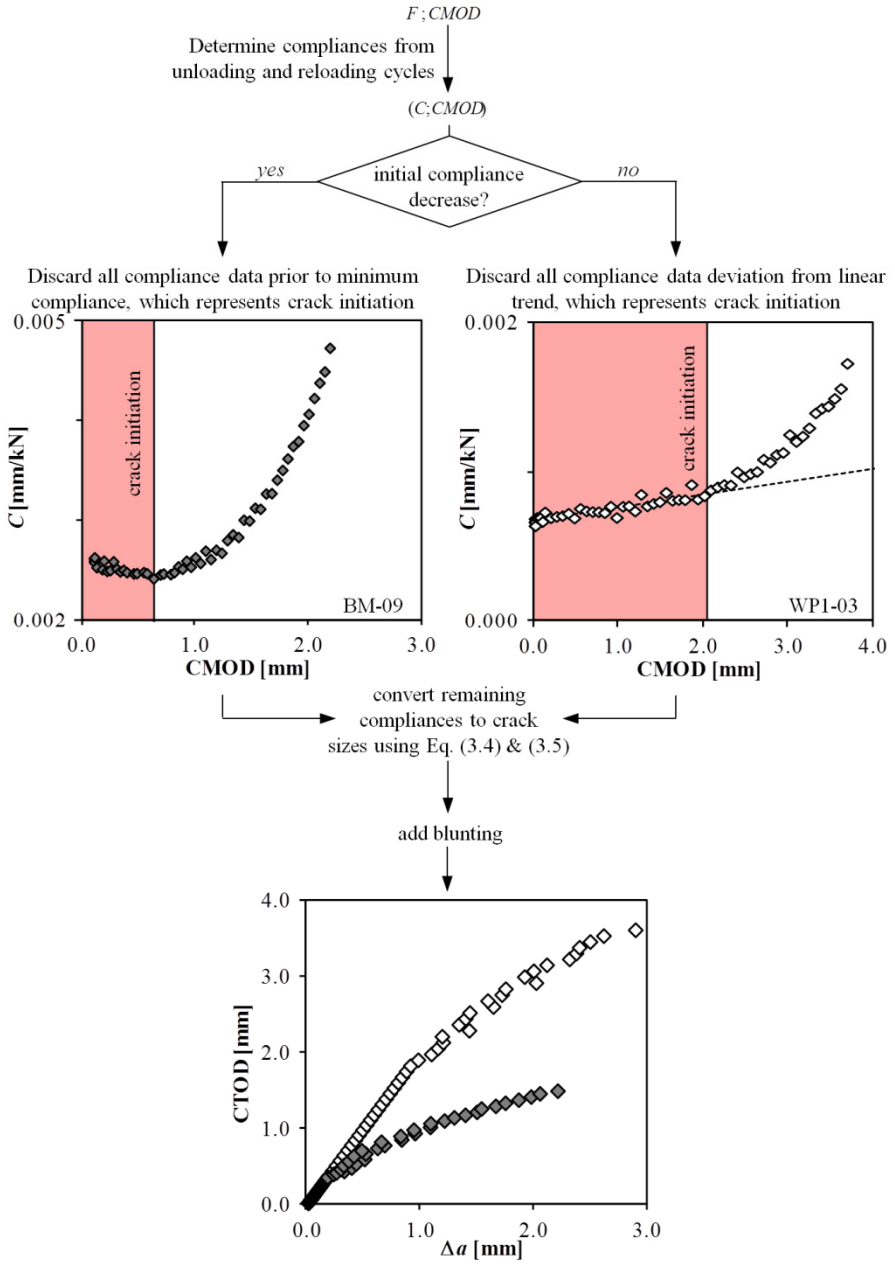

Figure 3.37. Overview of unloading compliance test procedure for SENT specimens

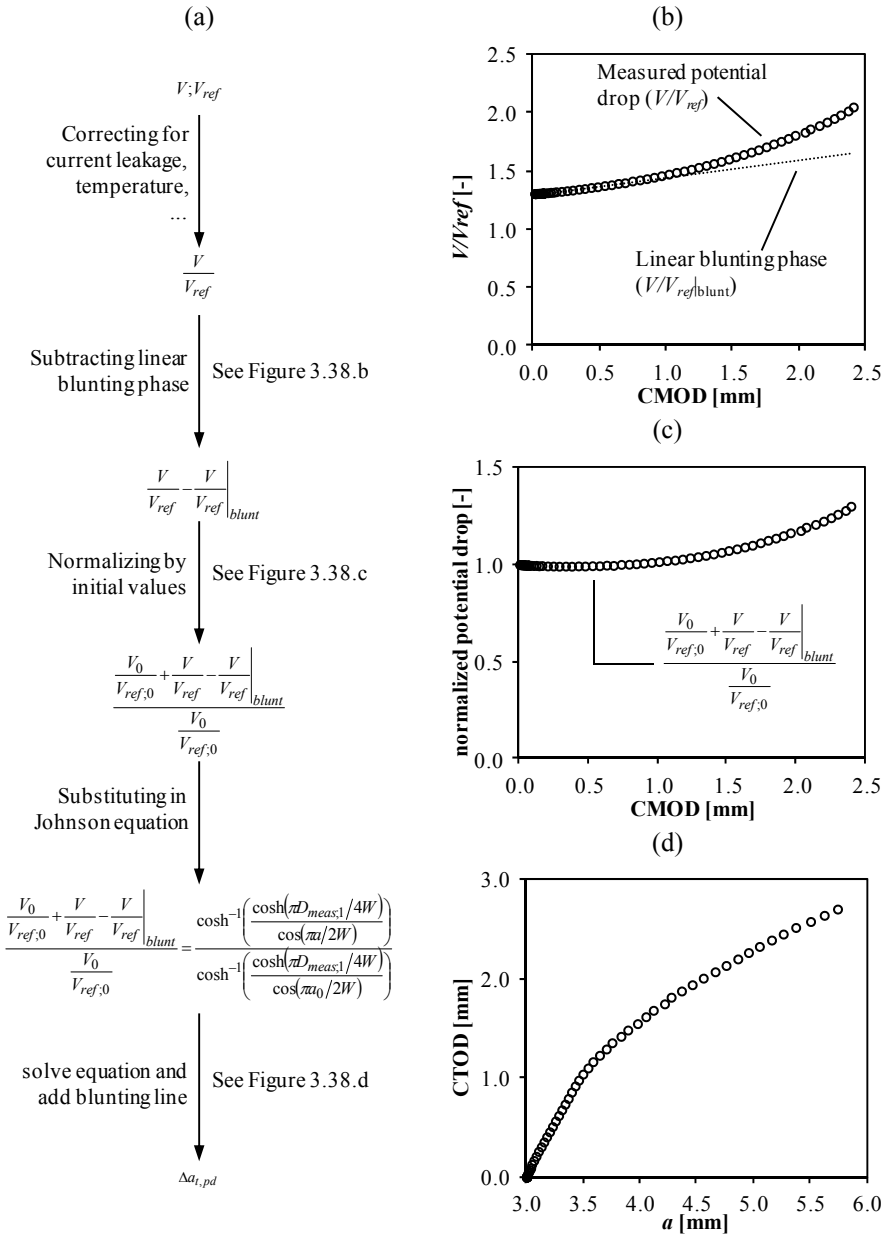

Figure 3.38. Processing of potential drop reading: mathematical overview (a) and detail of blunting line (b), normalized data after subtracting the blunting phase (c) and final predicted crack sizes (d)

3.6. Bibliography

[3.1] Det Norske Veritas, 2006, RP-F108: Fracture Control for Pipeline Installation Methods Introducing Cyclic Plastic Strain.

[3.2] Zhou, D. W., 2011, "Measurement and Modelling of R-Curves for Low-Constraint Specimens", Engineering Fracture Mechanics, 78, pp. 605-622.

[3.3] Pussegoda, L. N., Tiku, S., Park, D.-Y., Tyson, W. R., and Gianetto, J. A., 2012, "J-Resistance Results from Multi-Specimen and Single-Specimen Surface Notched SEN(T) Geometry", International Pipeline Conference, Calgary, Alberta, Canada, paper n° IPC2012-90565.

[3.4] American Society of Testing and Materials, 2011, E1820 - Standard Test Method for Measurement of Fracture Toughness.

[3.5] Denys, R., Andrews, R., Zarea, M., and Knauf, G., 2010, "EPRG Tier 2 Guidelines for the Assessment of Defects in Transmission Pipeline Girth Welds", International Pipeline Conference, Calgary, Alberta, Canada, paper n° IPC2010-31640.

[3.6] Shen, G., Gianetto, J. A., and Tyson, W. R., 2009, "Measurement of J-R Curves Using Single Specimen Technique on Clamped SE(T) Specimens", International Offshore and Polar Engineering Conference, Osaka, Japan, pp. 92-99.

[3.7] Shen, G., and Tyson, W. R., 2009, "Crack Size Evaluation Using Unloading Compliance in Single-Specimen Single-Edge-Notched Tension Fracture Toughness Testing", Journal of Testing and Evaluation, 37, pp. 347-357.

[3.8] CANMET, 2010, "Recommended Practice: Fracture Toughness Testing Using SE(T) Samples with Fixed-Grip Loading", CANMET Materials Technology Laboratory, Ottawa.

[3.9] Hertelé, S., 2012, "Coupled Experimental-Numerical Framework for the Assessment of Strain Capacity of Flawed Girth Welds in Pipelines", Ph.D. thesis, Ghent University, Ghent, Belgium.

[3.10] Nevalainen, M., and Dodds, R. H., 1996, "Numerical Investigation of 3-D Constraint Effects on Brittle Fracture in SE(B) and C(T) Specimens", International Journal of Fracture, 74, pp. 131-161.

[3.11] Duan, D.-M., Wang, Y.-Y., Chen, Y., and Zhou, J., 2008, "Modeling and CMOD Mapping of Surface Cracked Wide Plates", International Pipeline Conference, Calgary, Canada, paper n° IPC2008-64425.

[3.12] Yoosef-Ghodsi, N., Duan, D.-M., Chen, Q., Petersen, R., and Fan, C., 2010, "Finite Element Analysis of Flaw Growth History", International Pipeline Conference, Calgary, Canada, paper n° IPC2010-31418.

[3.13] Gioielli, P., Cheng, W., Minnaar, K., and Fairchild, D. P., 2008, "Characterization of the Stable Tearing During Pipeline Strain Capacity Tests", International Offshore and Polar Engineering Conference, Vancouver, Canada, pp. 86-89.

[3.14] Hertelé, S., Verstraete, M., Van Minnebruggen, K., Denys, R., and De Waele, W., 2012, "Curved Wide Plate Testing with Advanced Instrumentation and

Interpretation", International Pipeline Conference, Calgary, Alberta, Canada, paper n° IPC2012-90591.

[3.15] Park, D.-Y., Tyson, W. R., Gianetto, J. A., Shen, G., and Eagleson, R. S., 2010, "Evaluation of Fracture Toughness of X100 Pipe Steel Using SE(B) and Clamped SE(T) Single Specimens", International Pipeline Conference, Calgary, Canada, paper n° IPC2010-31282.

[3.16] Drexler, E., Wang, Y.-Y., Sowards, J. W., and Dvorak, M. D., 2010, "SE(T) Testing of Pipeline Welds", International Pipeline Conference, Calgary, Canada, paper n° IPC2010-31325.

[3.17] Bertolino, G., Meyer, G., and Perez Ipiña, J., 2002, "Mechanical Properties Degradation at Room Temperature in Zry-4 by Hydrogen Brittleness", Materials Research, 5, pp. 125-129.

[3.18] Rosenthal, Y. A., Tobler, R. L., and Purtscher, P. T., 1990, "Jic Data Analysis Methods with A "Negative Crack Growth" Correction Procedure", Journal of Testing and Evaluation, pp. 301-304.

[3.19] Ling, Y., 1996, "Uniaxial True Stress-Strain after Necking", AMP Journal of Technology, 5, pp. 37-48.

[3.20] Seok, C.-S., 2000, "Correction Methods of an Apparent Negative Crack Growth Phenomenon", International Journal of Fracture, 102, pp. 259-269.

[3.21] Weiss, K., and Nyilas, A., 2006, "Specific Aspects on Crack Advance During J-Test Method for Structural Materials at Cryogenic Temperatures", Fatigue and Fracture of Engineering Materials and Structures, 29, pp. 83-92.

[3.22] Cravero, S., and Ruggieri, C., 2007, "Estimation Procedure of J-Resistance Curves for SE(T) Fracture Specimens Using Unloading Compliance", Engineering Fracture Mechanics, 74, pp. 2735-2757.

[3.23] Fonzo, A., Melis, G., Di Vito, G., Mannucci, G., Darcis, P., Richard, G., Quintanilla, H., and Armengol, M., 2009, "Measurement of Fracture Resistance of Pipelines for Strain Based Design", 17th Biennial Joint Technical Meeting on Pipeline Research, Milan, Italy, paper n° 8.

[3.24] ExxonMobil, 2010, "Measurement of Crack Tip Opening Displacement (CTOD) - Fracture Resistance Curves Using Single-Edge Notched Tension (SENT) Specimens", ExxonMobil Upstream Research Company, Houston.

[3.25] Landes, J. D., 1995, "The Blunting Line in Elastic-Plastic Fracture", Fatigue and Fracture Of Engineering Materials and Structures, 18, pp. 1289-1297.

[3.26] Wilkowski, G., Shim, D. J., Kalyanam, S., Wall, G., Mincer, P., Rider, D., Brust, F. W., and Rudland, D. L., 2009, "Using D-C Electric Potential for Crack Initiation/Growth Monitoring During Testing of Weld Metal Fracture Specimens", Pipeline Technology Conference, Ostend, Belgium, paper n° Ostend2009-018.

[3.27] Sposito, G., 2009, "Advances in Potential Drop Techniques for Non-Destructive Testing", Ph.D. thesis, Imperial College, London.

[3.28] Serway, R. A., 1998, "Principles of Physics", Saunders College Publishing, London.

[3.29] Hartt, W. H., 1991, "A Multiple Specimen Test Technique to Determine Fatigue Crack Growth Rates for Conditions Relevant to Offshore Structures", Florida Atlantic University, Boston, MA, USA.

[3.30] Cerny, I., 2004, "The Use of Dcpd Method for the Measurement of Growth of Cracks in Large Components at Normal and Elevated Temperatures", Engineering Fracture Mechanics, 71, pp. 837-848.

[3.31] Yee, R., and Lambert, S. B., 1995, "A Reversing Direct Current Potential Drop System for Detecting and Sizing Fatigue Cracks Along Weld Toes", Journal of Testing and Evaluation, 23, pp. 254-260.

[3.32] Lloyd, W. R., Reuter, W. G., and Weinberg, D. M., 1999, Crack Growth Monitoring in Harsh Environments by Electrical Potential Measurements.

[3.33] Anctil, A., Kula, E. B., and Dicesare, E., 1963, "Electric-Potential Technique for Determining Slow Crack Growth", US Army Materials Research Agency, Virginia, USA.

[3.34] Merah, N., 2000, "DC Potential Drop Calibration in Creep-Fatigue Loading Conditions", Journal of Testing and Evaluation, 28, pp. 301-306.

[3.35] Doig, P., and Abbott, K. R., 1984, "Single Specimen Fracture Toughness Testing of Low Strength Steel Plate Using the Direct Current Electrical Potential Method", Journal of Testing and Evaluation, 12, pp. 297-304.

[3.36] Chipperfield, C. G., 1976, "Detection and Toughness Characterisation of Ductile Crack Initiation in 316 Stainless Steel", International Journal of Fracture, 12, pp. 873-886.

[3.37] Srawley, J. E., and Brown, W. F. J., 1965, "Fracture Toughness Testing", National Aeronautics and Space Administration, NASA, Cleveland, Ohio, USA.

[3.38] Wilkowski, G., Wambaugh, J. O., and Prabhat, K., 1982, Single Specimen J-Resistance Curve Evaluations Using the DC Electric Potential Method and a Computerized Data Acquisition System.

[3.39] Wilkowski, G. M., and Maxey, W. A., 1984, STP 791, American Society for Testing and Materials, Review and Applications of the Electric Potential Method for Measuring Crack Growth in Specimens, Flawed Pipes and Pressure Vessels.

[3.40] Aronson, G. H., and Ritchie, R. O., 1979, "Optimization of the Electrical Potential Technique for Crack Growth Monitoring in Compact Test Pieces Using Finite Element Analysis", Journal of Testing and Evaluation, 7, pp. 208-215.

[3.41] Johnson, H. H., 1965, "Calibrating the Electric Potential Method for Studying Slow Crack Growth", Materials Research and Standards, pp. 442-445.

[3.42] Cadario, A., and Alfredsson, B., 2007, "Fatigue Growth of Short Cracks in Ti-17: Experiments and Simulations", Engineering Fracture Mechanics, 74, pp. 2293-2310.

[3.43] Hertelé, S., De Waele, W., Denys, R., Verstraete, M., and Van Wittenberghe, J., 2012, "Parametric Finite Element Model for Large Scale Tension Tests on Flawed Pipeline Girth Welds", Advances in Engineering Software, 47, pp. 24-34.

[3.44] Denys, R., and Lefevre, A. A., 2009, "Failure Characterization of a Girth Weld with Surface-Breaking Flaw under Tensile Load", Pipeline Technology Conference, Ostend, Belgium, paper n° Ostend2009-111.

[3.45] Ohata, M., Igi, S., Tamaguchi, R., Sakimoto, T., Kubo, T., and Minami, F., 2009, "Prediction of Tensile Strain Limit for Leak of High Pressure Pipe with Surface Crack", Pipeline Technology Conference, Ostend, Belgium, paper n° Ostend2009-0065.

[3.46] Riemelmoser, F. O., Pippan, R., Weinhandl, H., and Kolednik, O., 1999, "The Influence of Irregularities in the Crack Shape on the Crack Extension Measurement by Means of the Direct-Current-Potential-Drop Method", Journal of Testing and Evaluation, 27, pp. 42-46.

Chapter 4

–

Evaluation of Crack Driving Force

4.1. Introduction

The focus of this chapter is on the experimental quantification of the crack tip loading. The crack tip loading represents the vertical axis of a tearing resistance diagram and can be expressed in terms of *J*-integral or CTOD (section 4.2).

The main goal is an accurate evaluation of the crack tip loading in SENT specimens, since these are primarily considered for the evaluation of the tearing resistance. In addition, this chapter also presents a measurement method for CWP specimens. Although the objective of CWP testing is not to obtain the tearing resistance, knowledge of the crack tip loading has the potential to improve the understanding of the test result, e.g. failure mode or initiation toughness.

Therefore, this chapter aims at presenting a generally applicable method for the evaluation of the crack tip loading in both SENT and CWP specimens. By preference, the same method should be used for both specimens. This enhances the comparability of the test results and eliminates potential differences due to measurement errors related to the applied methods.

4.2. *J*-integral or CTOD

As stated in the introductory section, the crack tip loading can be evaluated by means of the *J*-integral or the CTOD, both yielding the same outcome from a theoretical perspective [4.1, 2].

4.2.1. *J*-integral

A first method to experimentally determine the *J*-integral is based on the plastic area under the load-displacement diagram [4.1]. This area can be related to the *J*-integral via dimensionless constants, the η_p-factors. For a variety of specimen geometries, these factors are listed in literature [4.3-5]. However, this method will not be adopted since no analytical formulae that account for weld metal strength mismatch effects are available for the evaluation of *J*-integral in CWP specimens.

A second method to evaluate the *J*-integral from experiments relies on the original definition by Rice, where *J* is calculated from a line integral along a random counter clockwise contour Γ surrounding the crack tip [4.6]:

$$J = \int_{\Gamma} \left(w dy - T_i \frac{\partial u_i}{\partial x} ds \right) \tag{4.1}$$

where T_i represents the traction vector and u_i the displacement vector. The strain energy density, *w*, is defined by:

$$w = \int_0^{\varepsilon_{ij}} \sigma_{ij} d\varepsilon_{ij} \tag{4.2}$$

Considering this definition, the *J*-integral can be determined from the deformation fields surrounding the crack tip region. To that extent, Frediani et al. [4.7] have evaluated the strains along the specimens' edges, which represent the contour Γ. As long as the deformations along these edges remain elastic, the stresses along these edges are subsequently calculated to obtain the strain density. At this point the application breaks down for the SENT specimens considered in this work, as gross plasticity takes place (see Chapter 6). For similar reasons, the work of Becker et al. [4.8], that is based on the analysis of a random contour using DIC measurements, appears insufficient. For MWP specimens, such method is impractical, since no strains can be visualized along a contour that surrounds the crack tip.

Since no method appears generally applicable for both SENT and CWP specimens, attention is directed towards the evaluation of the crack tip opening displacement.

4.2.2. CTOD

For standardized specimens, the CTOD is often determined using a single clip gauge located at the crack mouth [4.9]. This is an approximate method that estimates the location of the plastic hinge. For CWP testing, however, no guidance is given on such method. Therefore, this single clip gauge method is not considered in the remainder of this work.

A more promising method is the double clip gauge method, which recently gained increasing interest in SENT testing [4.10-13]. This method relies on the 90° intercept definition of CTOD starting from the original crack tip, whereby a_0 equals the depth of the original crack (Figure 4.1 - see also section 1.2.1 in Chapter 1). From the readings of two clip gauges mounted at different heights above the surface, the CTOD is calculated (for a more detailed description, see section 4.4.1). It is thereby assumed that the crack faces do not deform plastically, they behave as rigid arms rotating around a single point [4.14]. A major advantage of this method is the applicability to both SENT and MWP testing, which improves the comparability of the test results.

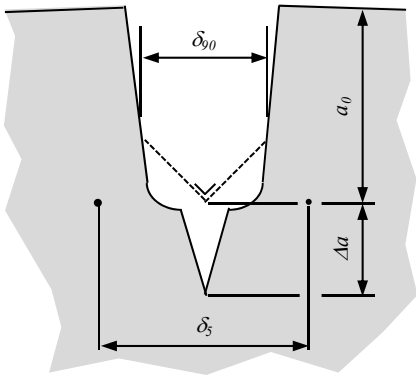

Figure 4.1. Illustration of CTOD definitions

Whereas the previous method relies on the 90° intercept method, the CTOD can also be defined as the displacement of two fixed points located at a fixed distance across the crack tip. Such definition is not expected to differ significantly from the previous

and was developed by the Helmholtz-Zentrum Geesthacht (formerly GKSS). They defined the CTOD as the displacement of two (virtual) points placed 5.0 mm apart, across the crack tip, hence the term δ_5 [4.15] (Figure 4.1). Full field deformation measurements can be considered for the evaluation of δ_5. However, application of this method is obviously restricted to situations where the crack tip region can be visually accessed. As a result, this method is solely considered for SENT specimens.

4.3. Materials and specimens

For the evaluation of the different CTOD measurement methods both SENT and MWP test results are considered. First, the SENT specimens can be divided in welded and non-welded specimens, numbered "BM-xx" and "WM-xx" respectively (listed in Appendix A). The non-welded specimens are machined from a grade API-5L X80 pipe and have varying relative initial crack depths ranging between $a_0/W = 0.2$ and $a_0/W = 0.6$. The welded specimens are taken from two grade API-5L X80 pipes. The weld metal strength properties of the first set of three specimens are closely matching the pipe metal properties ($MM_{FS} = +1.0\%$); for the second set these strongly overmatch the pipe strength properties ($MM_{FS} = +33\%$).

Second, a set of five MWP specimens is considered. One specimen is taken from a flat plate of homogeneous material. The others are taken from pipes with varying grades and weld strength mismatch levels (see Appendix A).

4.4. Measurement methods

4.4.1.Double clip gauge method

Two small mounting pieces are bolted onto the specimen's top surface, facilitating the attachment of the clip gauges on the knife ends (Figure 4.2). To that extent, two 3.0 mm deep holes with a diameter of 1.9 mm are drilled at each side of the crack. Generally, these holes are located 4.5 mm apart from the cracked ligament, resulting in an initial clip gauge opening of 3.0 mm. The heights for the attachment of the clip gauges, h_1 and h_2, equal 2.0 and 8.0 mm respectively.

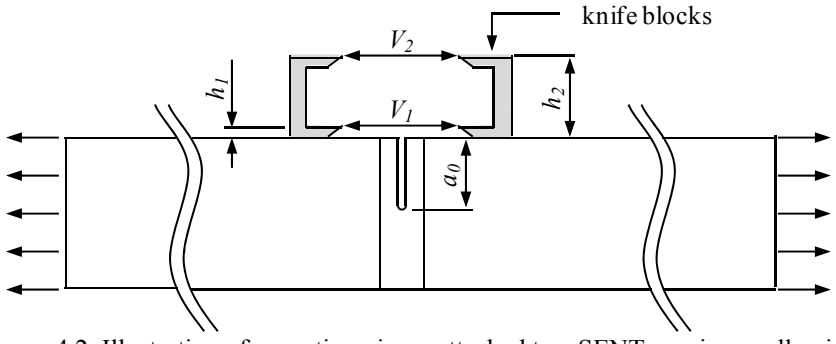

Figure 4.2. Illustration of mounting pieces attached to a SENT specimen, allowing to measure CTOD via double clip gauge method

From the change of both clip gauge readings, V_1 and V_2, the CTOD can subsequently be calculated:

$$\delta_{90} = 2\frac{V_2(a_0 + h_1) - V_1(a_0 + h_2)}{(V_2 - V_1) - 2(h_2 - h_1)} \tag{4.3}$$

Analogous, the CMOD can be determined from these clip gauge readings:

$$CMOD = V_1 - \frac{h_1}{h_2 - h_1}V_2 \tag{4.4}$$

Both clip gauges have a precision[1] of ±1.0 µm, as required for the unloading compliance technique (see section 3.3.1.4 in Chapter 3). The accuracy of the height measurements for h_1 and h_2 is taken equal to the accuracy of the caliper used for measuring these distances (0.01 mm). Based on the accuracy of the measurement device, the accuracy of the initial crack depth a_0 is also taken to 0.01 mm. Subsequently, the precision of the CTOD measurements can be evaluated at increasing CTOD levels (Figure 4.3.a). This precision is in the µm-range. In absolute terms, the error increases with an increase of the CTOD level. In relative terms, the measurement error is largest at the early loading stages. For a CTOD level of 0.10 mm, commonly considered for stress based defect assessments [4.16], the precision is 1.75% (Figure 4.3.b). However, for strain based assessments, higher CTOD levels are typically reached [4.17], resulting in an error below 1%.

The presence of the drill holes and screws used for the attachment of the knife blocks potentially influences the crack behaviour. The drill holes are not allowed to be located outside a zone contained by an angle of 90° starting from the crack tip [4.9]. To evaluate the influence hereof, the deformation fields surrounding the crack are studied for both shallow ($a_0/W = 0.2$) and deeply ($a_0/W = 0.6$) notched homogeneous specimens based on full field deformation measurements (Chapter 6). Shown in Figure 4.4 is the strain in longitudinal direction at the specimen's surface. In addition, two dotted lines originating from the crack tip under 45° are plotted and the screw positions are indicated. As expected, negligible deformation is observed within these 45° lines. For the deeply notched specimen, the deformation free zone is even more widespread. A similar trend was observed at higher load levels. Furthermore, the deformation pattern shows no irregularities that could indicate any disturbing effect of the screws. It is therefore concluded that the considered double clip gauge method has no influence on the specimen deformation and can be considered for further use.

[1] As defined in Appendix C

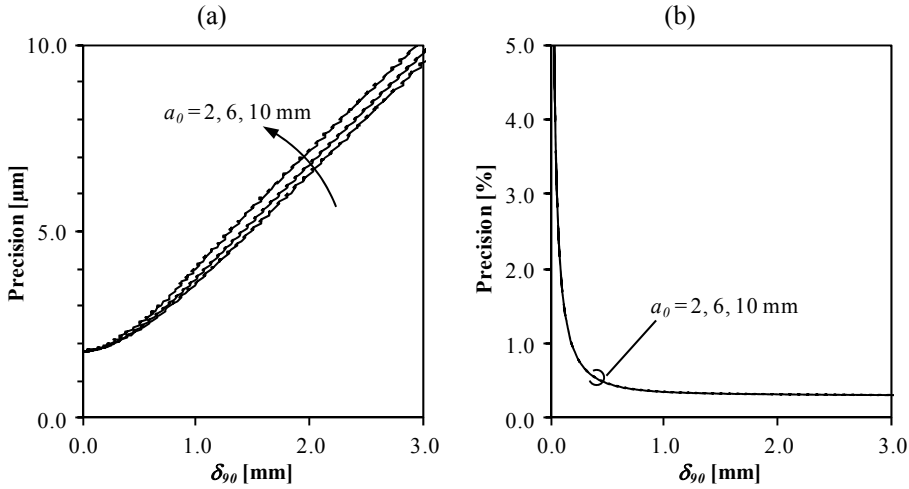

Figure 4.3. Evaluation of precision for SENT specimen with varying initial crack depths in absolute terms (a) and relative (b)

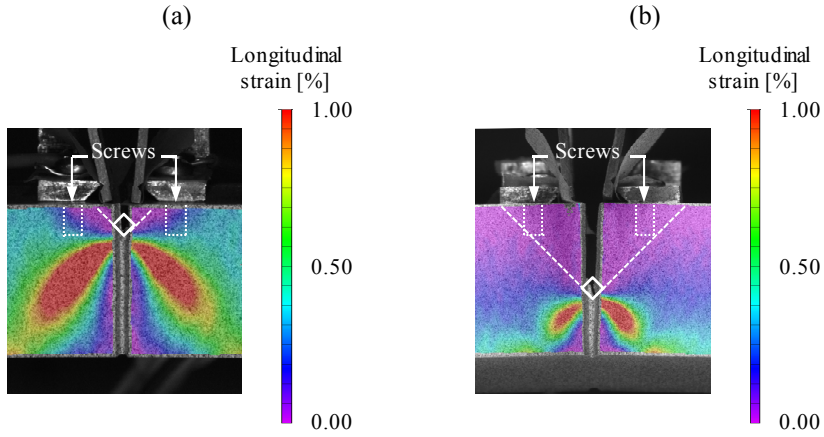

Figure 4.4. Deformation pattern around crack tip in SENT specimens ($B = W = 15$ mm) with shallow ($a_0/W = 0.2$) (a) and deep ($a_0/W = 0.6$) notch (b) at equal CTOD load level ($\delta_{90} = 0.2$ mm)

4.4.2. δ_5 method

The digital image correlation technique, discussed in full detail in Chapter 6, is also considered for the measurement of δ_5. During a test, pictures are taken of the specimen's surface, perpendicular to the crack mouth. From the full field deformation measurements, the displacements of two points located 2.5 mm at each side of the crack tip are used for the evaluation of δ_5 (Figure 4.1).

To evaluate the precision of this DIC-based method, the predicted distance between two points initially located 5.0 mm apart is calculated for multiple images of the undeformed specimen. From a total of 12 independent measurements, a standard deviation of 0.62 µm was calculated (measured extremes: $\delta_{5;min}$ - $\delta_{5;max}$ = 1.98 µm). It is therefore concluded that the presented method is precise enough for evaluating the CTOD, which is typically in the range of (tenths of) millimeters.

One might argue that the local deformations around the crack tip potentially influence the δ_5 measurements. However, when evaluating the strain field (Figure 4.5), it is clear that deformation is mainly localized at 45° shear bands originating from the crack tip. This figure furthermore indicates that even after significant ductile crack extension (i.e. approx. 1.7 mm), the strain in the zone of interest is limited.

These observations apply both for welded and homogeneous specimens, which is well in agreement with the findings of Koçak [4.18]. He has shown that the δ_5 method does not require any adjustments to compensate for the potential influence of neighboring (strength mismatched) materials.

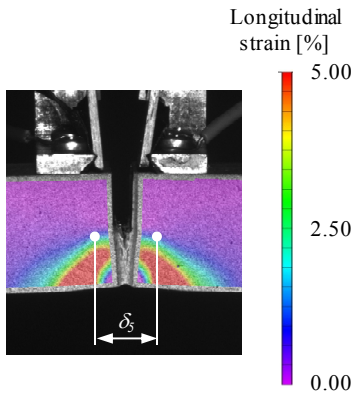

Figure 4.5. Example case illustrating longitudinal strain field and location of the tracked points for δ_5 method in test W01

4.5. Test results

4.5.1. SENT testing

Both the δ_5 and δ_{90} methods are applied to a series of SENT tests as described in section 4.3, resulting in two resistance curves for each specimen. The DCPD method is applied to quantify the amount of ductile crack extension. To facilitate the comparison, both CTOD definitions are evaluated at initiation and at 1.0 mm of ductile crack extension. Figure 4.6.a indicates an overall satisfying correspondence between both. However it is noted that the δ_{90} method tends to predict higher CTOD values relative to the δ_5 method. This difference is inherent to both definitions. Whereas the δ_5 definition makes use of the opening at the initial crack tip, the δ_{90} measurement is taken at a certain height above the initial crack tip. As some rotation of the specimen is observed, δ_{90} increases relative to δ_5. This effect furthermore results in increasing absolute errors at increasing CTOD levels, since the CTOD is evaluated towards the crack mouth in this case (Figure 4.6.b).

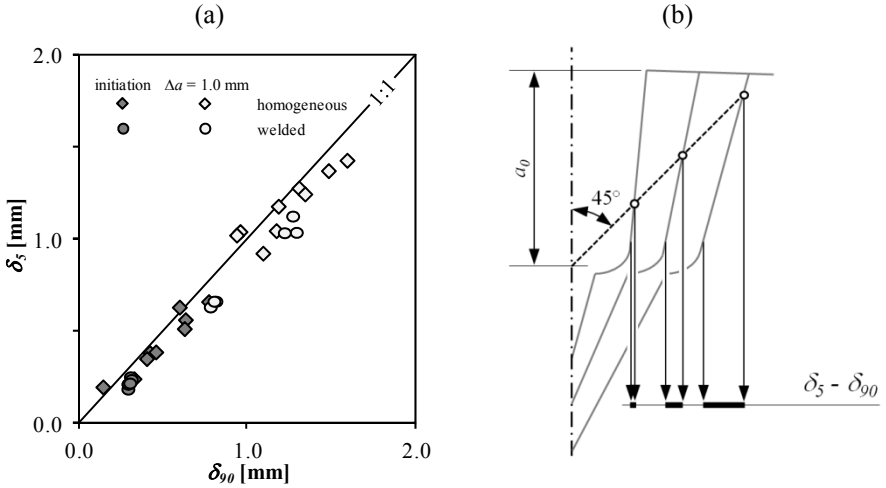

Figure 4.6. Comparison of CTOD definitions in SENT tests: δ_{90} versus δ_5 (a) and illustration of difference between δ_{90} and δ_5 for varying load levels (b)

4.5.2.MWP testing

Since the δ_5 method cannot be considered in MWP testing, the CTOD measured using the double clip gauge method is compared to the one measured from a macrograph extracted post-mortem at the middle of the crack. For δ_{90}, the value obtained after complete unloading is considered. Regarding the CTOD from the macrograph, the final opening is measured as shown in Figure 4.7.a and the initial opening (0.50 mm) is subtracted.

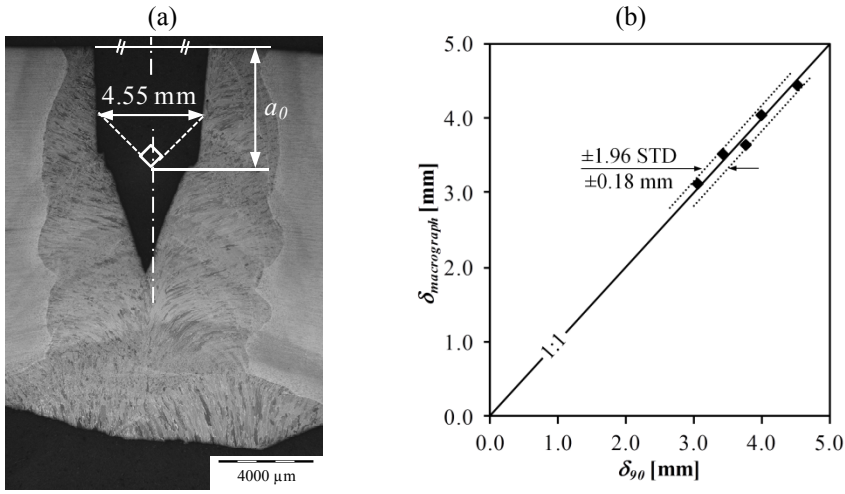

Figure 4.7. Evaluation of CTOD from macrograph for specimen WP5 (a) and comparison with double clip gauge measurement after unloading of the specimen (b)

The results for all considered MWP tests are shown in Figure 4.7.b. In general an excellent correspondence between both measurements is observed. By considering the CTOD values obtained from the macrographs ($\delta_{macrograph}$), which are assumed to represent the actual values, the accuracy of the double clip gauge method is evaluated[2]. Therefore, the standard deviation (*STD*) is evaluated based on the experimental data shown above (N = batch size = 5) via the following formula.

$$STD = \sqrt{\frac{1}{N}\sum_{i=1}^{N}\left(\delta_{macrograph} - \delta_{90}\right)^2} \tag{4.5}$$

Based on the calculated standard deviation, and furthermore assuming a normal error distribution, a 95% confidence interval is determined. This results in an accuracy of ±0.18 mm for the double clip gauge method.

$$\delta_{90} = \delta_{macrograph} \pm 1.96 STD = \delta_{macrograph} \pm 0.18 mm \tag{4.6}$$

The obtained accuracy appears rather low. It should however be noted that the CTOD values used for the evaluation of the accuracy are obtained at failure. Their average value equals 3.83 mm, which implies that the relative error does not exceed ±5%. Further research is however advised for applications focusing at lower load levels.

[2] For a definition of the accuracy, the reader is referred to Appendix C

4.6. Conclusions

For the evaluation of the crack tip loading in SENT and CWP specimens, the CTOD is preferred over the *J*-integral. For the evaluation of the CTOD, two methods have been considered for SENT testing, namely the double clip gauge method and the δ_5 method. Both methods indicated a nice correspondence, in particular at crack initiation. For increasing load levels, the double clip gauge method yields slightly higher CTOD values. The δ_5 method is however not applicable for MWP testing, since the crack tip region is not visually accessible. As a result, the CTOD values reported in all other chapters are based on the double clip gauge method[3].

To evaluate the accuracy of this double clip gauge method, the calculated values have been compared to macrographs extracted after completion of the tests. For a series of MWP tests, the error did not exceed 5% of the measured signal at the end of the test.

[3] As a result, the crack tip opening displacement is not referred to as δ_{90}. Instead, the more general term CTOD is used in the other chapters.

4.7. Bibliography

[4.1] Anderson, T. L., 1995, "Fracture Mechanics: Fundamentals and Applications", CRC press, Texas.

[4.2] Shih, C. F., 1981, "Relationships between the J-Integral and the Crack Opening Displacement for Stationary and Extending Cracks", Journal of Mechanics and Physics of Solids, 29, pp. 305-326.

[4.3] Rice, J. R., Paris, P. C., and Merkle, J. G., 1973, "Some Further Results of J-Integral Analysis and Estimates", ASTM STP 536, American Society of Testing and Materials, pp. 231-245.

[4.4] Shen, G., Gianetto, J. A., and Tyson, W. R., 2009, "Measurement of J-R Curves Using Single Specimen Technique on Clamped SE(T) Specimens", International Offshore and Polar Engineering Conference, Osaka, Japan, pp. 92-99.

[4.5] Lei, Y., and Neale, B. K., 1997, "J-Integral Function for a Centre-Cracked Tensile Specimen", International Journal of Pressure Vessels and Piping, 71, pp. 129-138.

[4.6] Rice, J. R., 1968, "A Path Independent Integral and the Approximate Analysis of Strain Concentration by Notches and Cracks", Journal of Applied Mechanics, 35, pp. 379-386.

[4.7] Frediani, A., 1984, "Experimental Measurement of the J-Integral", Engineering Fracture Mechanics, 19, pp. 1105-1137.

[4.8] Becker, T. H., Mostafavi, M., Tait, R. B., and Marrow, T. J., 2012, "An Approach to Calculate the J-Integral by Digital Image Correlation Displacement Field Measurement", Fatigue and Fracture Of Engineering Materials and Structures, 35, pp. 971-984.

[4.9] British Standards Institution, 1991, BS 7448-1: Fracture Mechanics Toughness Tests. Method for Determination of Kic, Critical CTOD and Critical J Values of Metallic Materials.

[4.10] Tang, H., Minnaar, K., Kibey, S., Macia, M. L., Gioielli, P., and Fairchild, D. P., 2010, "Development of the SENT Test for Strain-Based Design of Welded Pipelines", International Pipeline Conference, Calgary, Alberta, Canada, paper n° IPC2010-31590.

[4.11] Moore, P. L., and Pisarski, H. G., 2012, "Validation of Methods to Determine CTOD from SENT Specimens", International Offshore and Polar Engineering Conference, Rhodes, Greece, pp. 577-582.

[4.12] Fagerholt, E., Ostby, E., Borvik, T., and Hopperstad, O. S., 2012, "Investigation of Fracture in Small-Scale SENT Tests of a Welded X80 Pipeline Steel Using Digital Image Correlation with Node Splitting", Engineering Fracture Mechanics, 96, pp. 276-293.

[4.13] Cicero, S., F., G.-S., and Álvarez, J. A., 2008, "Structural Integrity Assessment of Components Subjected to Low Constraint Conditions", Engineering Fracture Mechanics, 75, pp. 3038-3059.

[4.14] Manzione, P., and Perez Ipiña, J., 1991, "Sensitivity Analysis of the Double Clip Gauge Method", Fatigue and Fracture Of Engineering Materials and Structures, 14, pp. 887-869.

[4.15] Schwalbe, K.-H., Heerens, J., Zerbst, U., Pisarski, H. G., and Koçak, M., 2002, "EFAM GTP 02 - the GKSS Test Procedure for Determining the Fracture Behaviour of Materials", GKSS-Forshungszentrum Geesthacht GmbH, Geesthacht.

[4.16] Canadian Standards Association, 2011, Z662 - 11: Oil and Gas Pipeline Systems.

[4.17] Wang, Y. Y., Liu, M., Song, Y., Petersen, R., Stephens, M., and Gordon, R., 2011, "Second Generation Models for Strain-Based Design", Pipeline Research Council International, Houston, Texas, United States.

[4.18] Koçak, M., 2010, "Structural Integrity of Welded Structures: Process - Property - Performance (3p) Relationship", International Conference of the International Institute of Welding, Istanbul, Turkey, pp. 3-19.

Chapter 5

–

Tearing Resistance: Sources of Variation

5.1. Introduction

In the preceding chapters, a methodology was established to accurately evaluate a material's tearing resistance. It is however widely acknowledged that, in particular for welds, this tearing resistance is not a single material parameter, though is influenced by a variety of factors (e.g. constraint, heterogeneity, …) [5.1-3].

To improve the understanding of some of these factors, a variety of SENT and MWP tests are carried out. The primary aim is to quantify:

- the scatter between similar tests (section 5.3)
- the influence of relative initial crack depth (section 5.4)
- the heterogeneity of welds: influence of notch orientation (section 5.5)
- the heterogeneity of welds: influence of o'clock position (section 5.6)
- the influence of the test specimen geometry (section 5.7)

Based on the above studies, a testing procedure is proposed that aims at being generally applicable with a limited degree of conservatism.

5.2. Materials and specimens

The results presented in this chapter are based on all tests described in the previous chapters. Reference is made to Appendix A for a description of the specifications for the SENT and MWP specimens considered in this chapter. It should be emphasized that a wide range of steel grades (API 5L X65 to X80), strength mismatch levels ($0\% \leq MM_{FS} \leq 33\%$), crack sizes ($0.2 \leq a_0 / W \leq 0.6$), … are considered.

5.3. Scatter

5.3.1.Method

The tested materials, in particular the weld metals, are not homogeneous by nature. As a result, the obtained tearing resistance is expected to vary between theoretically identical test specimens (e.g. identical notch position and initial crack size). To capture this effect, the ASTM E1820 procedure requires at least three valid test results [5.4]. As a result, most of the SENT tests in this dissertation are executed three times, grouped in a so-called configuration. The different specimens are extracted adjacent to each other.

For each configuration, a curve fit is made based on the data points from the (three) tests that are located between the 0.15 mm and 1.50 mm offset lines as illustrated in Figure 5.1.a. In accordance to the ASTM E1820 standard, an exponential curve with two fitting parameters (δ_1 and δ_2) is considered.

$$CTOD = \delta_1 (\Delta a)^{\delta_2} \tag{5.1}$$

In combination with this curve fit, a scatter band is calculated (Figure 5.1.b). The width of this scatter band represents the situation for which 95% of the data points between both offset lines are included. This scatter band has a constant width as a function of the crack extension, 2 x δ_s. This width is seen as a characteristic for the scatter and/or accuracy of the measured tearing resistance. The boundaries of the resistance curve can thus be written as:

$$CTOD = \delta_1 (\Delta a)^{\delta_2} \pm \delta_s \tag{5.2}$$

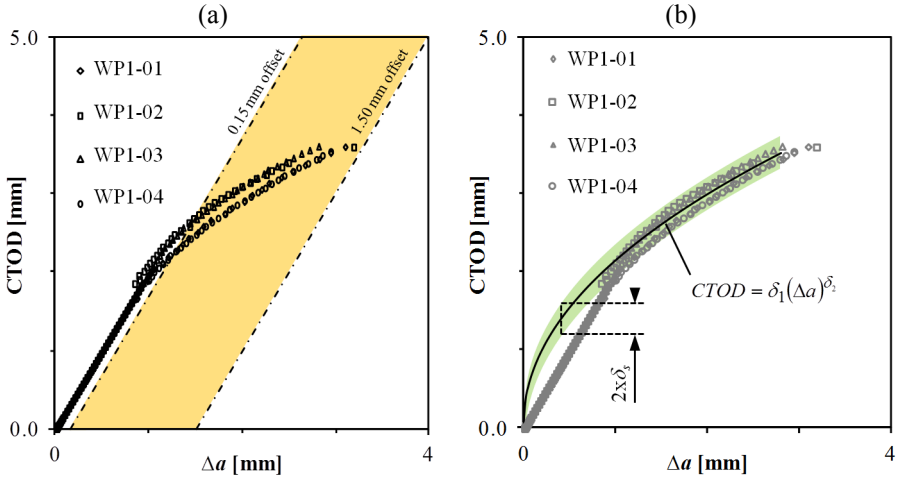

Figure 5.1. Data points considered to determine tearing resistance curve for SENT specimens WP1-01 till WP1-04 (a) and fitted curve in combination with scatter band (b)

5.3.2.Results

The scatter of the measured tearing resistance is evaluated for all configurations tested in the framework of this dissertation. Figure 5.2 shows the results for both the unloading compliance and potential drop methods. It is concluded that, on average, both methods result in a similar scatter; δ_s equals 0.15 mm for the potential drop method and 0.16 mm for the unloading compliance method. It might be argued that base metal specimens are of a more homogeneous nature and hence less prone to scatter of the material properties. However, the scatter for these tests, which are indicated by the solid symbols in Figure 5.2, is not considerably different compared to the scatter observed in the tests on welded specimens (open symbols).

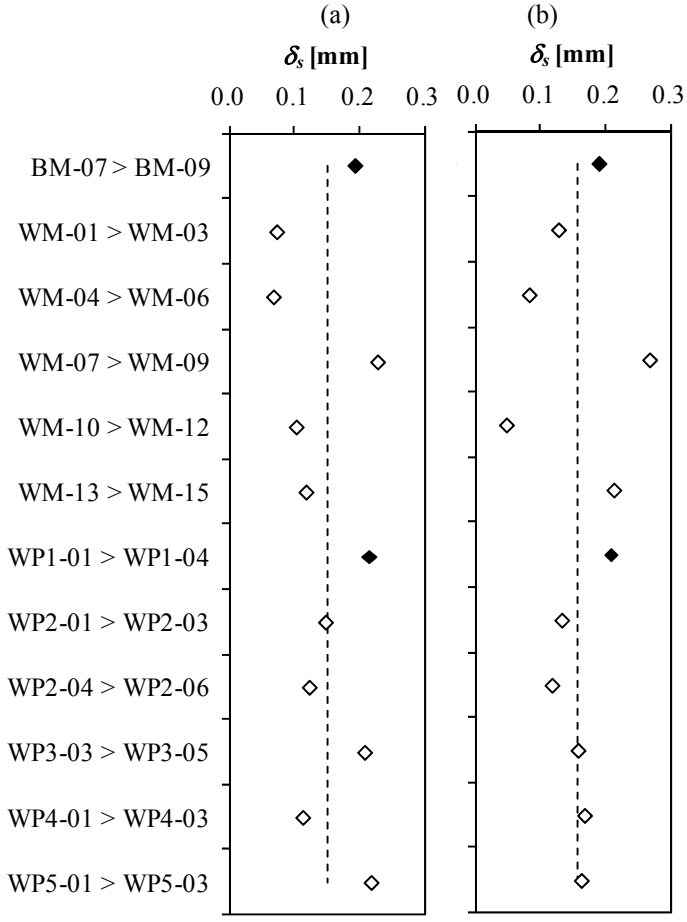

Figure 5.2. Scatter in CTOD (δ_s) for tests on SENT specimens using unloading compliance (UC) (a) and potential drop (PD) (b) method.

5.4. Influence of relative crack depth

5.4.1.Method

To study the effect of the relative crack depth, a total of six specimens are extracted from the same grade API-5L X80 base metal. Three different initial crack depths are machined in these specimens, resulting in relative initial crack depths (a_0 / W) of 0.2, 0.4 and 0.6.

5.4.2.Results

The tearing resistance is obtained by means of both the unloading compliance and potential drop methods in combination with the double clip gauge method. As the obtained results are similar for both crack extension measurement methods, only the results from the potential drop method are discussed below.

From the resulting experimental data, a clear decrease of the tearing resistance with increasing initial crack depth is observed (Figure 5.3). This difference is attributed to an increase of the crack tip constraint for deeper initial notches, an effect that is well described in literature [5.5, 6].

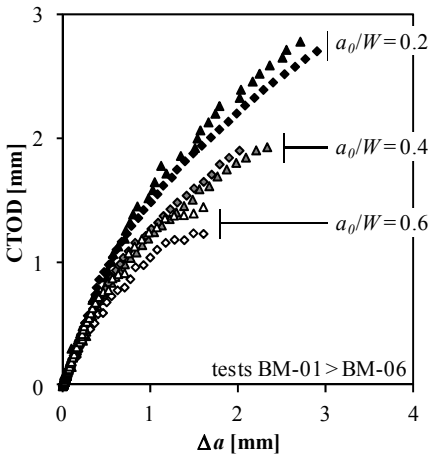

Figure 5.3. Influence of relative crack depth on tearing resistance obtained through SENT testing of homogeneous base metal.

5.5. Influence of notch orientation

5.5.1.Method

Welds are known to be of a strongly heterogeneous nature [5.7, 8]. The present section aims at evaluating the tearing resistance of a weld, considering varying notch orientations. In standards, recommendations regarding the preferred notch orientation are not always consistent. For example, API 1104 recommends the use of through thickness notches whereas DNV prescribes the use of inner or outer diameter notches [5.9-11]. To gain insight in this issue, nine specimens have been tested with notches applied from the outer diameter ("*OD-config*"), inner diameter ("*ID-config*") and in the through thickness ("*TT-config*") direction (Figure 5.4).

All specimens are extracted from an overmatched GMAW weld (MM_{FS} = + 20%). The weld macrograph displays a typical columnar dendritic grain structure, in particular near the weld cap (Figure 5.5.a). All specimens have identical cross sectional dimensions ($W = B = 15$ mm). The relative initial crack depth, a_0 / W, equals 0.40.

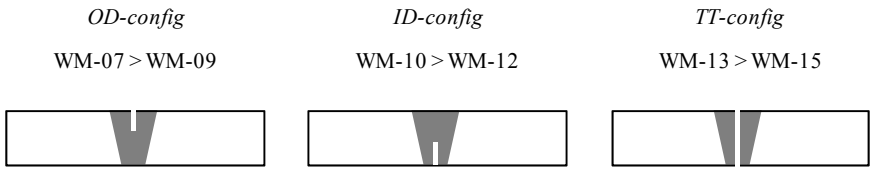

Figure 5.4. Schematic of notch orientation for specimens WM-07 till WM-15, all specimens have an initial relative crack depth equal to 0.40.

In an attempt to characterize the material heterogeneity, a hardness map of the entire weld is evaluated. To this extent, Vickers indentations with a load of 0.5 kg ($HV_{0.5}$) are performed approximately every 0.2 mm. The use of a softer wire for the welding of the root pass is reflected by a lower hardness in this area (Figure 5.5.b). The hardness map additionally displays a lower hardness in the heat affected zone, commonly referred to as softening. This might be attributed to grain growth of the base metal during the heat cycles imposed by the welding process [5.12].

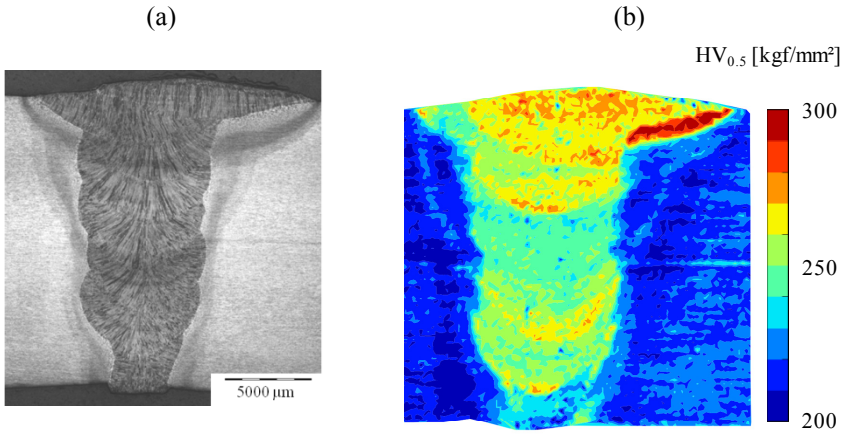

Figure 5.5. Macrograph (a) and hardness map obtained using Vickers indentations (5 kg) (b) for weld tested in SENT tests WM-07 till WM-15

5.5.2.Results

For each of the three configurations, the average tearing resistance and corresponding scatter is evaluated. The tearing resistance clearly depends on the notch orientation; it is significantly lower for the through-thickness notch (Figure 5.6). In addition, the tearing resistance for the specimens with an inner diameter notch is slightly higher compared to the specimens with an outer diameter notch. This difference does however not markedly exceed the scatter.

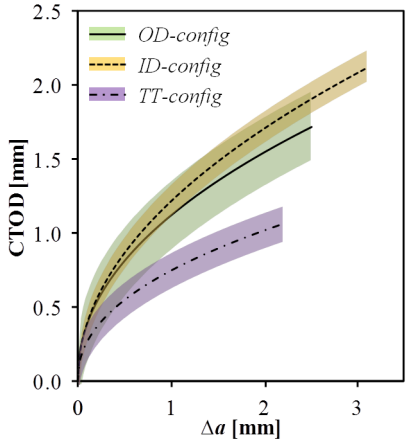

Figure 5.6. Obtained tearing resistance curves for SENT specimens from the same weld but with varying notch orientations.

Differences between the tearing resistances for the different configurations are expected, given the inhomogeneous nature of weldments. In an attempt to clarify the observed trend, the fracture surface of a specimen with a through-thickness notch is examined. In contrast to the inner and outer diameter notched configurations, a strongly non-uniform crack extension is observed, which invalidates the obtained tearing resistance curve[1]. The root pass clearly exhibits a higher tearing resistance as the crack has advanced more at the cap side (Figure 5.7).

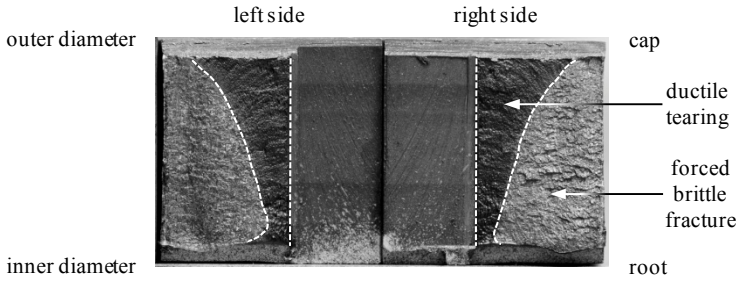

Figure 5.7. Fracture surface for through thickness oriented notch (specimen WM-15)

The observed difference is attributed to a number of factors:

- The welding wire for the root pass differs from the filler passes. The weld metal in the root is softer compared to the cap, which is likely to result in a higher tearing resistance.
- Towards the root of the weld, the weld beads are subjected to a number of post weld heat cycles from the subsequent welding passes. This causes a grain refined metal at the root side of the weld, which has the potential to result in a higher tearing resistance [5.13, 14].

These factors are also reflected by the slightly higher tearing resistance for the inner diameter configuration relative to the outer diameter configuration. The difference is however limited, which is a result of the relatively high initial crack depth. As a result, part of the crack extension takes place in the same weld bead for both configurations. It is expected that a more pronounced difference would be observed for a smaller initial crack depth.

[1] ASTM E1820 describes the crack front straightness requirement for SENB specimens as: each measured crack extension should not differ by more than 0.05 *B* from the average value. This implies a difference of max. 0.75 mm for these tests.

5.6. Influence of o'clock position

5.6.1.Method

A potential source of weld metal heterogeneity is the o'clock position, given the difference in welding position [5.15]. To that extent, a series of 11 specimens are tested, extracted from a different o'clock position (Figure 5.8).

The specimens are extracted from a grade API-5L X70 pipe with a slightly overmatching weld. This GMAW weld was realized in the 5G vertical up position.

(a)

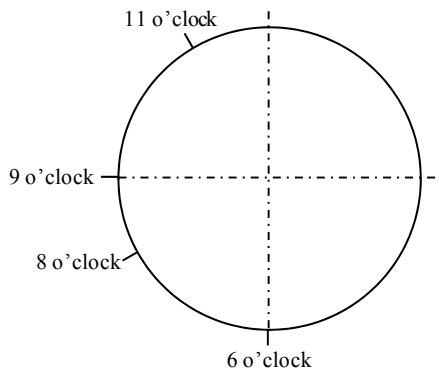

(b)

o'clock position	specimens
6	WP2-04
	WP2-05
	WP2-06
8	WP2-01
	WP2-02
	WP2-03
9	WP3-03
	WP3-04
	WP3-05
11	WP3-01
	WP3-02

Figure 5.8. Overview of extraction position for SENT specimens, sampling different o'clock positions.

In addition to the SENT specimens, tensile test specimens are extracted from different o'clock positions (7 o'clock and 10 o'clock). The base metal tensile properties show a large variation between both pipes, as discussed in Chapter 6. However, the variation with the o'clock position within the same pipe is limited. In Figure 5.9.a two tensile strain curves extracted at different o'clock positions are plotted for each pipe. For the weld metal, a more pronounced effect of the o'clock position is observed. Between the two positions tested, a 24 MPa (4%) difference in tensile strength is observed (Figure 5.9.b).

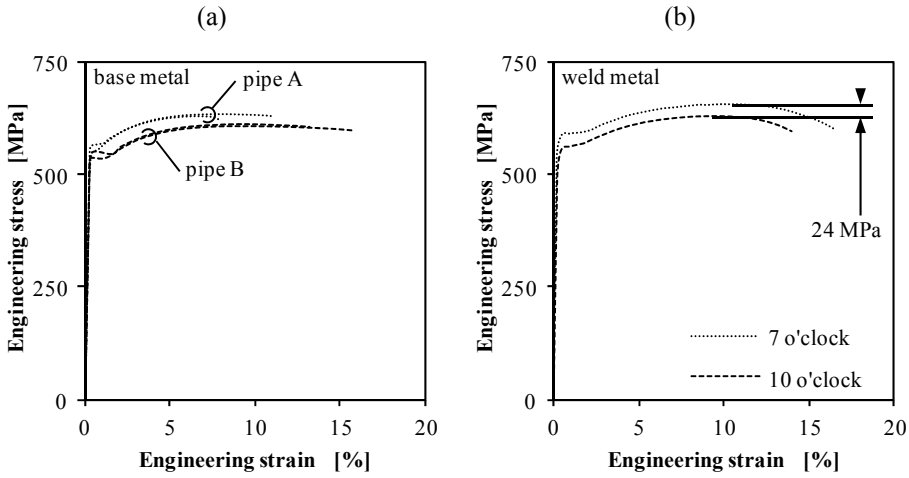

Figure 5.9. Heterogeneity of base (a) and weld (b) metal stress strain properties as a function of the o'clock position.

5.6.2.Results

For each configuration separately, the tearing resistance curve and corresponding scatter band are determined. In addition, a global fit and global scatter band is determined considering all specimens extracted from this weld. In the latter case, the scatter was 0.18 mm for the unloading compliance method and 0.16 mm for the potential drop method. These values are in close agreement with the scatter determined from all tests performed in the framework of this dissertation, as presented in section 5.3. This suggests that the o'clock position has no pronounced/measurable influence on the tearing resistance. This is also observed graphically in Figure 5.10, where the global scatter band and individually fitted curves are plotted.

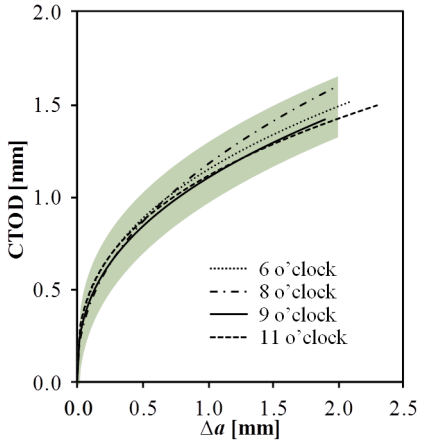

Figure 5.10. Scatter band obtained from all test specimens with curve fitted tearing resistance curves for individual o'clock positions

5.7. Influence of test specimen geometry

5.7.1.Method

The specimen geometry and loading condition are known to have a pronounced influence on the tearing resistance. Several comparisons are discussed in literature, e.g. between SENT and SENB specimens [5.16, 17]. The difference in constraint between CWP and SENT specimens is however not well described in literature. Some results indicate that the tearing resistance in CWP specimens is lower, whilst others report that SENT specimens have a higher constraint [5.17-19] and consequently lower tearing resistance. However, a correspondence has been reported between the constraint in:

- SENT specimens and (pressurized) pipes [5.20, 21]
- CWP and (pressurized) pipes (Chapter 7)

Therefore, the tearing resistance curves obtained from SENT and CWP specimens are expected to coincide.

In an attempt to clarify this issue, a total of five MWP tests are performed. For each MWP test, (at least) three SENT specimens are tested with a similar relative initial crack depth and defect location (Table 5.1). These SENT specimens are extracted adjacent to the MWP specimen, minimizing the potential influence of material heterogeneity (see cutting plan Chapter 2).

Table 5.1. Overview of MWP specimens with corresponding SENT specimens

MWP test	[-]	WP-1	WP-2	WP-3	WP-4	WP-5
SENT test	[-]	WP1-01 WP1-02 WP1-03 WP1-04	WP2-01 WP2-02 WP2-03 WP2-04 WP2-05 WP2-06	WP3-01 WP3-02 WP3-03 WP3-04 WP3-05	WP4-01 WP4-02 WP4-03	WP5-01 WP5-02 WP5-03
$a_0 / W = a_0 / t$	[-]	0.21	0.28	0.28	0.30	0.30

5.7.2.Results

For both specimen types, the resistance curves are determined based on the potential drop method for the crack extension; the double clip gauge method is used for the CTOD measurements. For the SENT specimens, the scatter bands are plotted, for the MWP specimen the actual test results are shown (Figure 5.11). A higher tearing resistance is observed for the MWP specimen compared to the SENT specimens.

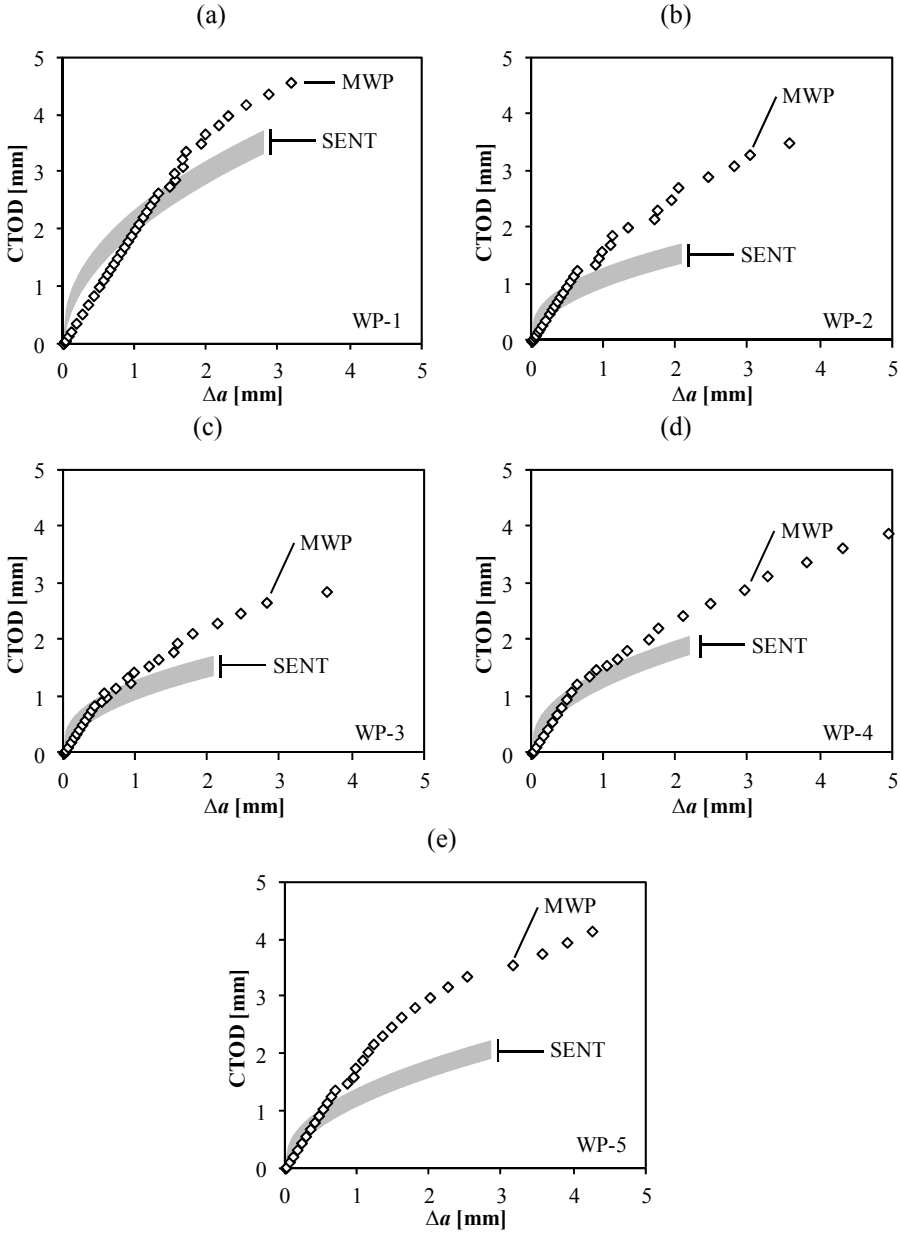

Figure 5.11. Comparison between tearing resistance curve obtained from SENT and MWP tests for specimens WP-1 (a), WP-2 (b), WP-3 (c), WP-4 (d) and WP-5 (e)

5.8. Discussion

Toughness testing of girth welds has always been and will probably remain a most delicate issue. By performing a large number (45) of SENT tests, insight has been gained in factors that (do not) affect the tearing resistance. This section aims at presenting a generally applicable testing approach.

The notch orientation and relative initial crack depth displayed a pronounced influence on the tearing resistance. First, the notch orientation is discussed. As already announced in section 5.5.1, the requirements of the different standards regarding the notch orientations are contrasting. Based on the current data set, the API 1104 requirement, i.e. notches should be applied in the through thickness direction, is most conservative. This observation is however based on a single weld, results in literature indicated that other trends might as well be observed [5.22, 23]. In addition, this approach should not be recommended because:

- This notch position tends to result in an invalid resistance curve since the crack extension is strongly non-uniform.
- The physical relevance is limited, as weld defects are most likely oriented in the circumferential direction.

Preference should thus be given to outer or inner diameter defects. These indicated a more uniform ductile crack extension and match the requirements of e.g. the DNV-OS-F101. The question however remains which of these notch positions should be selected to obtain a (reasonably) conservative assessment. To clarify this issue, the following is suggested:

- *hardness map*: the hardness map provides insight in the weld metal heterogeneity. In the present study, the non-uniform crack extension of the through-thickness notched specimens might be related to the hardness profile. The hardest zones indicated a lower tearing resistance in contrast to the zones with a lower hardness.
- *indicative specimen*: using a single test specimen that contains a through thickness notch potentially reveals the location of the zone(s) with the lowest/highest tearing resistance based on the crack front shape. Note however that the aim of this test is clearly not to obtain a resistance curve.

In combination with the selection of the notch orientation, the selection of the notch depth is crucial. A constraint difference results in a lower tearing resistance for deeper initial cracks. Therefore, results from specimens with varying initial defect depths are required for defect assessment procedures. One might argue that it is conservative to test only these specimens whose initial crack depth matches the maximum defect depths that are to be assessed. For example, a maximum crack depth of 5.0 mm can be selected, similar to the upper limit of the defects assessed using the EPRG Tier 2 guidelines [5.24]. However, the influence of weld metal heterogeneity on the tearing resistance curve potentially dominates the constraint effect related to the difference in initial crack depth. Hence, the conservativeness of this approach cannot be assured. It is therefore suggested to test specimens with varying crack depths, ranging between the defect depths that are to be assessed. Taking the recommended update of the EPRG Tier 2 guidelines [5.24] as guidance, this would imply testing specimens with 3.0, 4.0 and 5.0 mm deep cracks.

In contrast to the notch orientation and initial crack depth, no dependency was observed on the specimen's o'clock position. Despite a clear variability of the tensile properties with the o'clock position was observed, no distinction could be made between the tearing resistance curves. It can therefore be concluded that the fracture toughness specimens can be extracted from a random o'clock position. Note however that this conclusion relates to a single study, further validation is advised.

An important additional issue is the need for repetition of the tests. The current study does not indicate remarkable differences in scatter between welded and non-welded specimens. This scatter is in the same order of magnitude as the accuracy of the CTOD measurements, as determined from a series of MWP tests in section 4.5.2. These observations suggest that the observed scatter is primarily related to the limitations of the measurement methods. As such, an averaged resistance curve can for these tests be advised as input for defect assessment procedures, rather than a lower bound curve. Note however that sub-scale specimens are more susceptible to scatter in material properties, which is of particular relevance for welds. Since a sub-scale specimen only samples a limited amount of material, the likelihood of capturing locally deteriorated material properties decreases. This potentially results in an unconservative or overly conservative assessment, which is traditionally mastered by requesting a number of repetitions for the sub-scale test [5.25]. Notwithstanding the scatter in the tested specimens has been attributed to the limitations of the measurement methods, it is therefore recommended to test series of (at least) three identical specimens, as also advised for SENB / CT testing by ASTM E1820. It is furthermore noted that the average scatter observed in the current study is similar to results obtained in other testing laboratories for homogeneous base metal [5.26]. For the nine laboratories participating in a round robin study[2], an average scatter of ±0.16 mm was observed, when comparing the CTOD fracture toughness at 1.0 mm of crack extension for specimens from the same laboratory. This round robin study however revealed that the scatter for the entire data set (thus containing the results from all participating labs) is significantly higher and therefore unmistakably deserves recommendation for future research.

[2] In the framework of the current PhD project, Soete Laboratory has contributed to a round robin test program. Several SENT tests have been carried out on homogeneous (non-welded) material. This round robin study was organized by Dr. W.R. (Bill) Tyson of the Canadian CANMET MTL laboratory.

Eventually, the relationship between SENT and MWP specimens was studied, indicating that the MWP results are less stringent. Fairchild et al. have argued that the observed relationship might result from an overestimation of the tearing resistance in MWP specimens [5.27]. This could be attributed to an underestimation of the ductile crack extension for specimens that show a tilted (i.e. not in the plane of the original notch) crack extension. However, for the tested specimens no such crack extension was observed. Hence, the observed trend is explained from a constraint point of view, based on the following two trends:

- *the relative crack depth*: it is observed from finite element constraint calculations (both using *JQ*-theory and using damage mechanics) that the constraint in a SENT specimen closely matches the pipe's constraint for extremely shallow notched specimens ($a_0 / W = 0.1$). With increasing notch depth however, the SENT specimens become more conservative [5.20, 21]. As the relative crack depths investigated in this dissertation are higher than 0.1, it is believed that this contributes to the observed conservatism in SENT testing.
- *the presence of side grooves*: due to the presence of side grooves, the constraint is locally increased. Accordingly, crack growth is enhanced and the tearing resistance lowered [5.28].

It is thus concluded that the constraint is higher in the SENT specimens compared to the MWP specimens. This indicates the potential of the wide plate test. Defect assessments that have been based on tearing resistance curves obtained from SENT specimens in combination with analytical formulae contain a certain degree of conservatism. As a result, defects that appear (slightly) unconservative from such assessment might be re-assessed using wide plate tests (in combination with a pressure correction function – Chapter 8). Such assessment procedure is potentially less conservative.

5.9. Conclusions

From the study of tearing resistance curves obtained from both SENT and MWP specimens in welded and non-welded configurations, the following is concluded.

The scatter of the tearing resistance curves obtained from testing homogeneous, i.e. non-welded, and welded specimens does not differ significantly. Based on an extensive comparison, whereby the tearing resistance was evaluated for series of three (theoretically) identical specimens, it appears that the scatter between the different resistance curves is about ±0.15 mm and ±0.16 mm in terms of CTOD for the potential drop and unloading compliance method respectively.

The tearing resistance appears to be largely affected by the relative crack depth and notch location. As such, a single specimen geometry, which yields a conservative though relevant estimate of the tearing resistance, cannot be defined for all welds. From the observations in this chapter, it is suggested to perform a two step evaluation. A first screening phase consists of either determining a hardness map of the weld or testing of a single through-thickness notched specimen. A second phase then consists of a series of test specimens (e.g. three per configuration to capture scatter effects) with defect depths ranging between those considered in the defect assessment procedure. By doing so, the potential dominance of the weld metal heterogeneity over the constraint effect linked with the difference in initial defect depth is covered.

The constraint in SENT specimens is higher than is the case for MWP specimens. Hence, the defect assessment using SENT specimens is likely to be more restrictive. It is therefore advisable to consider wide plate testing in case defects are rejected using analytical flaw assessment procedures relying on SENT data.

5.10. Bibliography

[5.1] Cravero, S., and Ruggieri, C., 2005, "Correlation of Fracture Behavior in High Pressure Pipelines with Axial Flaws Using Constraint Designed Test Specimens - Part I: Plane Strain Analysis", Engineering Fracture Mechanics, 72, pp. 1344-1360.

[5.2] Gubeljak, N., Legat, J., and Koçak, M., 2002, "Effect of Fracture Path on the Toughness of Weld Metal", International Journal of Fracture, 115, pp. 343-359.

[5.3] Koçak, M., 2010, "Structural Integrity of Welded Structures: Process - Property - Performance (3p) Relationship", International Conference of the International Institute of Welding, Istanbul, Turkey, pp. 3-19.

[5.4] American Society of Testing and Materials, 2011, E1820 - Standard Test Method for Measurement of Fracture Toughness.

[5.5] Wang, E., Zhou, W., Shen, G., and Duan, D.-M., 2012, "An Experimental Study on J(CTOD)-R Curves of Single Edge Tension Specimens for X80 Steel", International Pipeline Conference, Calgary, Alberta, Canada, paper n° IPC2012-90323.

[5.6] Thaulow, C., Ostby, E., Nyhus, B., Zhang, Z. L., and Skallerud, B., 2004, "Constraint Correction of High Strength Steel - Selection of Test Specimens and Application of Direct Calculations", Engineering Fracture Mechanics, 71, pp. 2417-2433.

[5.7] Ostby, E., Sandvik, A., Levold, E., Nyhus, B., and Thaulow, C., 2009, "The Effects of Weld Metal Mismatch and Crack Position on the Strain Capacity in SENT Specimens in an X65 Material", International Offshore and Polar Engineering Conference, Osaka, Japan, pp. 162-168.

[5.8] Zhang, J. X., and Shi, Y. W., 1997, "The Effect of Welding Mechanical Heterogeneity on Fracture Toughness Feature of Base Metal", International Journal of Pressure Vessels and Piping, 72, pp. 199-202.

[5.9] 2010, API 1104: Welding of Pipelines and Related Facilities.

[5.10] Det Norske Veritas, 2006, RP-F108: Fracture Control for Pipeline Installation Methods Introducing Cyclic Plastic Strain.

[5.11] Det Norske Veritas, 2012, OS-F101: Submarine Pipeline Systems.

[5.12] Hashemi, S. H., Mohammadyani, D., Pouranvari, M., and Mousavizadeh, S. M., 2009, "On the Relation of Microstructure and Impact Toughness Characteristics of DSAW Steel of Grade API X70", Fatigue and Fracture Of Engineering Materials and Structures, 32, pp. 33-40.

[5.13] Calcagnotto, M., Ponge, D., and Rabe, D., 2010, "Effect of Grain Refinement to 1μm on Strength and Toughness of Dual Phase Steels", Materials Science and Engineering A, 527, pp. 7832-7840.

[5.14] Shin, S. Y., Hwang, B., Lee, S., Kim, N. J., and Ahn, S. S., 2007, "Correlation of Microstructure and Charpy Impact Properties in API X70 and X80 Line-Pipe Steels", Materials Science and Engineering A, 458, pp. 281-289.

[5.15] Sarafan, S., Ghaini, F. M., and Rahimi, E., 2012, "Effects of Welding Direction and Position on Susceptibility to Weld Metal Transverse Cracking in

Welding High-Strength Pipeline Steel with Cellulosic Electrodes", Welding Journal, 91, pp. 182S-185S.

[5.16] Mathias, L. L. S., Donato, G. H. B., and Ruggieri, C., 2012, "Applicability of SE(T) and SE(B) Fracture Specimens in Crack Growth Measurements of Pipeline Girth Welds", Pressure vessels and piping conference, Toronto, Ontario, Canada, paper n° PVP2012-78656.

[5.17] Cheng, W., Tang, H., Gioielli, P. C., Minnaar, K., and Macia, M. L., 2009, "Test Methods for Characterization of Strain Capacity: Comparison of R-Curves from SENT/CWP/FS Tests", Pipeline Technology Conference, Ostend, Belgium, paper n° Ostend2009-040.

[5.18] Wang, Y. Y., Liu, M., Song, Y., Petersen, R., Stephens, M., and Gordon, R., 2011, "Second Generation Models for Strain-Based Design", Pipeline Research Council International, Houston, Texas, United States.

[5.19] Wang, Y. Y., Liu, M., Zhang, F., Horsley, D., and Nanney, S., 2012, "Multi-Tier Tensile Strain Models for Strain-Based Design - Part 1: Fundamental Basis", International Pipeline Conference, Calgary, Alberta, Canada, paper n° IPC2012-90690.

[5.20] Cravero, S., and Ruggieri, C., 2004, "Integrity Assessment of Pipelines Using SE(T) Specimens", International Pipeline Conference, Calgary, Alberta, Canada, paper n° IPC04-0033.

[5.21] Xu, J., Zhang, Z. L., Ostby, E., Nyhus, B., and Sun, D. B., 2010, "Constraint Effect on the Ductile Crack Growth Resistance of Circumferentially Cracked Pipes", Engineering Fracture Mechanics, 77, pp. 671-684.

[5.22] Fonzo, A., Melis, G., Di Vito, G., Mannucci, G., Darcis, P., Richard, G., Quintanilla, H., and Armengol, M., 2009, "Techniques for Fracture Toughness Testing of Offshore Pipelines", Offshore Mechanics and Arctic Engineering Conference, Honolulu, Hawaii, USA, paper n° OMAE2009-80135.

[5.23] Tang, H., Minnaar, K., Kibey, S., Macia, M. L., Gioielli, P., and Fairchild, D. P., 2010, "Development of the SENT Test for Strain-Based Design of Welded Pipelines", International Pipeline Conference, Calgary, Alberta, Canada, paper n° IPC2010-31590.

[5.24] Denys, R., Andrews, R., Zarea, M., and Knauf, G., 2010, "EPRG Tier 2 Guidelines for the Assessment of Defects in Transmission Pipeline Girth Welds", International Pipeline Conference, Calgary, Alberta, Canada, paper n° IPC2010-31640.

[5.25] Jutla, T., and Garwood, S. J., 1987, "Interpretation of Fracture Toughness Data", Metal Construction, 19, pp. 276-280.

[5.26] Tyson, W. R., and Gianetto, J. A., 2013, "Low-Constraint Toughness Testing: Results of a Round Robin on a Draft SE(T) Test Procedure", Pressure Vessels and Piping Conference, Paris, France, paper n° PVP2013-97299.

[5.27] Fairchild, D. P., Crawford, M. D., Cheng, W., Macia, M. L., Nissley, N. E., Ford, S. J., Lillig, D. B., and Sleigh, J., 2008, "Girth Welds for Strain-Based Design Pipelines", International Offshore and Polar Engineering Conference, Vancouver, Canada, pp. 48-56.

[5.28] Shen, G., Tyson, W. R., Gianetto, J. A., and Park, D.-Y., 2010, "Effect of Side Grooves on Compliance, J-Integral and Constraint of Clamped SE(T) Specimen", Pressure Vessels and Piping Conference, Bellevue, Washington, USA, paper n° PVP2010-25164.

Chapter 6

–

Evaluation of Deformation and Strain Patterns

6.1. Introduction

Both for the SENT and MWP tests, knowledge of the strain development and distribution potentially leads to a more precise evaluation of the failure mode. It is known that a variety of parameters influence the strain distribution, e.g. presence of cracks, (strength mismatched) welds, ... As a result, the strain distribution is highly non-uniform. Consequently, it is not a priori known where the largest strains will occur and how these will affect failure. To gain insight in the deformations and the resulting strain fields, a suitable measurement technique is first introduced, namely Digital Image Correlation (DIC). In section 6.3 a brief introduction to this technique is provided. This section also describes the application to SENT and MWP specimens, which are listed in section 6.2. Characteristic strain patterns are outlined in section 6.4 for both the SENT and MWP specimens. In the last section 6.5, the link between deformation and tearing is studied for a set of SENT specimens.

6.2. Materials and specimens

The strain and deformation fields in both SENT and MWP specimens are studied. Regarding the SENT specimens, most of the tests used in the previous chapters are analyzed using full field strain measurements, though hereafter only a selection of these tests are discussed in further detail (indicated in Appendix A). In addition, the deformation of one SENB specimen is studied and compared to the deformation of a corresponding SENT test (listed in Appendix A).

In addition to these SENT tests, a total of six MWP specimens are studied. The mechanical properties and all relevant geometrical properties are listed in Appendix A. For the welded specimens, the stress-strain data of both base metal plates are characterized separately, in order to evaluate potential heterogeneity. Remark that specimen WP-06 was adopted from earlier work [6.1].

6.3. Digital Image Correlation

6.3.1 Principle

To visualize the deformations and corresponding strains, the Digital Image Correlation technique analyzes subsequent images of the test specimen. On the specimen's surface, a random high contrast speckle pattern is applied [6.2]. As the specimen deforms, the speckle pattern also changes (displacement and distortion). To quantify the deformation, the picture is divided in a two-dimensional matrix of nodes. The distance between these nodes is controlled by the step size expressed in pixels. As such, the step size is a first factor affecting the spatial resolution. At each node, the grey-scale intensity is evaluated as a weighted average of a square box surrounding the node. The size of this box is determined by a parameter named subset size, again expressed in pixels. This is the second parameter that controls the spatial resolution, since it gives expression to the area over which the deformations are averaged. Accordingly, with increasing subset size, strain singularities are less accurately captured. Two subsequently taken images can thus be compared to each other based on their resulting grey-scale intensity matrix. By matching the grey-scale distribution between these two images, the deformation can be quantified (Figure 6.1). From these deformations, the strains are eventually derived.

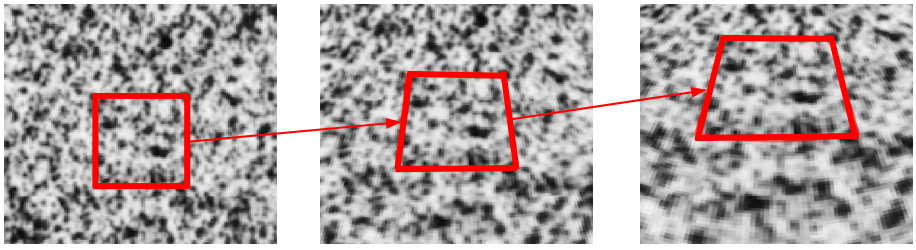

Figure 6.1. Comparison of subsets in subsequent images

As is clear from the above explanation, the subset size is a crucial parameter. A larger subset size will result in a more accurate correlation, whilst the spatial resolution will improve for a smaller subset. Since the preferred speckle size equals 3 x 3 pixels and a subset preferably contains three speckles [6.2], a subset size of 21 x 21 pixels is selected for all tests. The step size is set to five pixels. Both are in correspondence with literature and are believed to balance between accuracy and resolution [6.2, 3].

6.3.2 Procedure

To monitor the deforming specimen, a stand-alone system delivered by Limess GmbH is used [6.4]. This two-camera system allows 3D image correlation, since both cameras are slightly tilted relative to each other (Figure 6.2). Both monochrome cameras have a resolution of 2486 x 1985 pixels. Depending on the field of view, which in turn depends on the mounted lenses, an appropriate speckle size can thus be calculated.

- For SENT specimens, a characteristic field of view is 25 x 20 mm². Accordingly, the ideal speckle size of 3 x 3 pixels corresponds with a physical speckle size of 30 x 30 µm².
- For MWP specimens, the field of interest is larger, typically 900 x 300 mm². Ideally, the speckle size should therefore equal 1.1 x 1.1 mm².

In both cases, the speckle pattern is obtained by first applying a layer of highly elastic white paint onto the surface of the specimen. Subsequently, black speckles are sprayed on top of this layer.

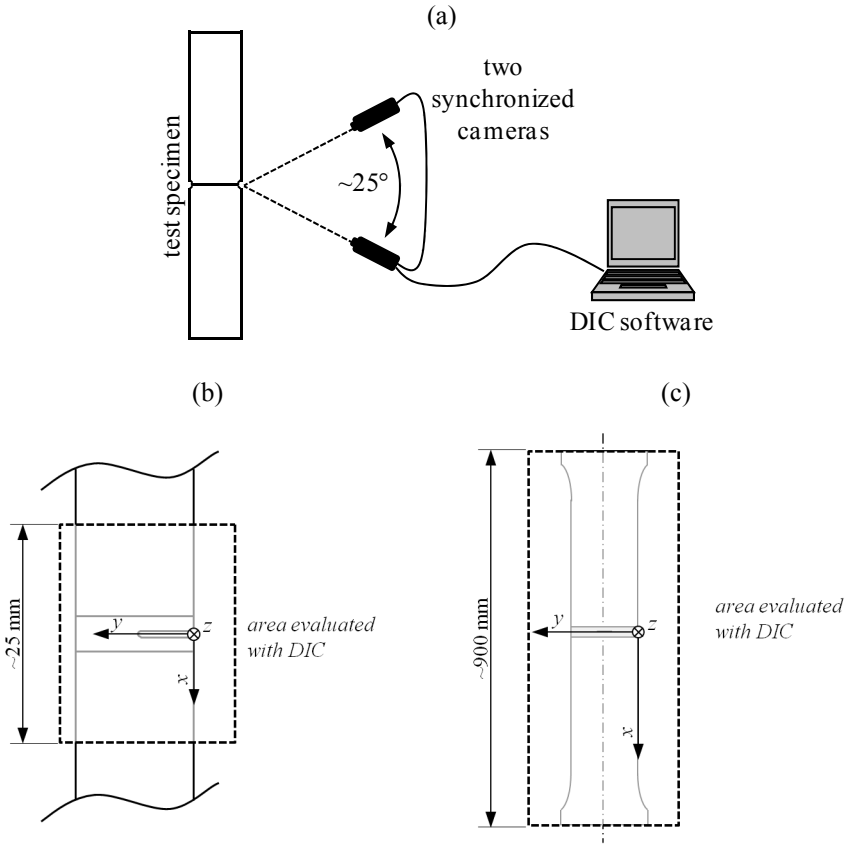

Figure 6.2. Schematic representation of DIC setup (a) and definition of *x*, *y* and *z*-directions for SENT (b) and MWP (c) specimens.

The displacements in *x*, *y* and *z*-direction, as defined in Figure 6.2.b and Figure 6.2.c for SENT and MWP specimens respectively, are determined through correlation of the digital images with specific software, namely VIC-3D [6.5]. It is noted at this point that, for both specimens, correlation lacks in the near vicinity of the crack. For the SENT specimens, only the areas above and below the side groove are analyzed. For the MWP specimen, the correlation is hindered by the presence of the mounting blocks for the double clip gauges.

6.3.3 Fracture mechanics applications

The DIC technique has been widely used to determine fracture parameters, e.g. *K* or *T*-stress, where linear elastic fracture mechanics theory applies [6.3, 6-8]. In contrast, only a limited number of articles are available considering elastic-plastic fracture mechanics analyses, which are primarily focusing on thin ductile sheet materials under mixed mode loading [6.9, 10]. Only recently, Fagerholt et al. [6.11] have also shown the possibilities of using DIC in SENT testing. Their primary aim was however to identify crack paths for plane-sided specimens with weldment, based on a node splitting technique. This contrasts the work in this dissertation; the SENT specimens are side-grooved to avoid crack tunneling [6.12]. Regarding the MWP specimen, the DIC technique has been used for the evaluation of the optimum specimen geometry by Hertelé et al. [6.13]. The results of their paper are adopted for selecting the dimensions of the MWP specimens in this dissertation (see also section 2.4.1.2 of Chapter 2).

6.4. Development of deformation fields

This paragraph aims at presenting characteristic deformation patterns for SENT and MWP specimens. To that extent, the deformation of homogeneous (i.e. non-welded) specimens is first studied. Following, particularities of welded specimens are discussed.

6.4.1 SENT testing

Focusing on homogeneous specimens, a characteristic strain evolution obtained using the DIC technique is shown in Figure 6.3, together with the corresponding load versus CMOD diagram. With increasing load, a zone of high plastic deformation originates from the crack tip. The following is observed:

- The region of high strain is concentrated in shear bands that are oriented 45° relative to the crack tip (as indicated by the dashed line), which corresponds well with the slip line theory [6.14].
- Although the stress concentration reaches a maximum value near the crack tip, the largest strains are observed at the specimen's surface opposite to the crack for this specimen. This is attributed to a lower triaxiality in this region compared to the material closer to the crack tip. Indeed, the deformation is not restrained by adjacent material.
- The maximum strain is not yet reached at the moment of crack initiation (T_3, determined using potential drop method); the strain continuously increases with applied displacement.

Additionally, the deformation pattern in a SENB specimen extracted from the same base metal is studied. Note first that the required forces are significantly lower for this configuration (Figure 6.4.a). The deformation pattern clearly develops in a different way as compared to the SENT specimen (Figure 6.4.b). A zone of tensile strain is developing from the crack tip, whilst a zone with compressive strain develops at the specimen's free surface opposite to the crack. As a result, the plasticity at the crack tip is not as widespread as is the case for the SENT specimen. This is not surprising given the higher constraint reported for SENB testing (section 2.2.2 of Chapter 2).

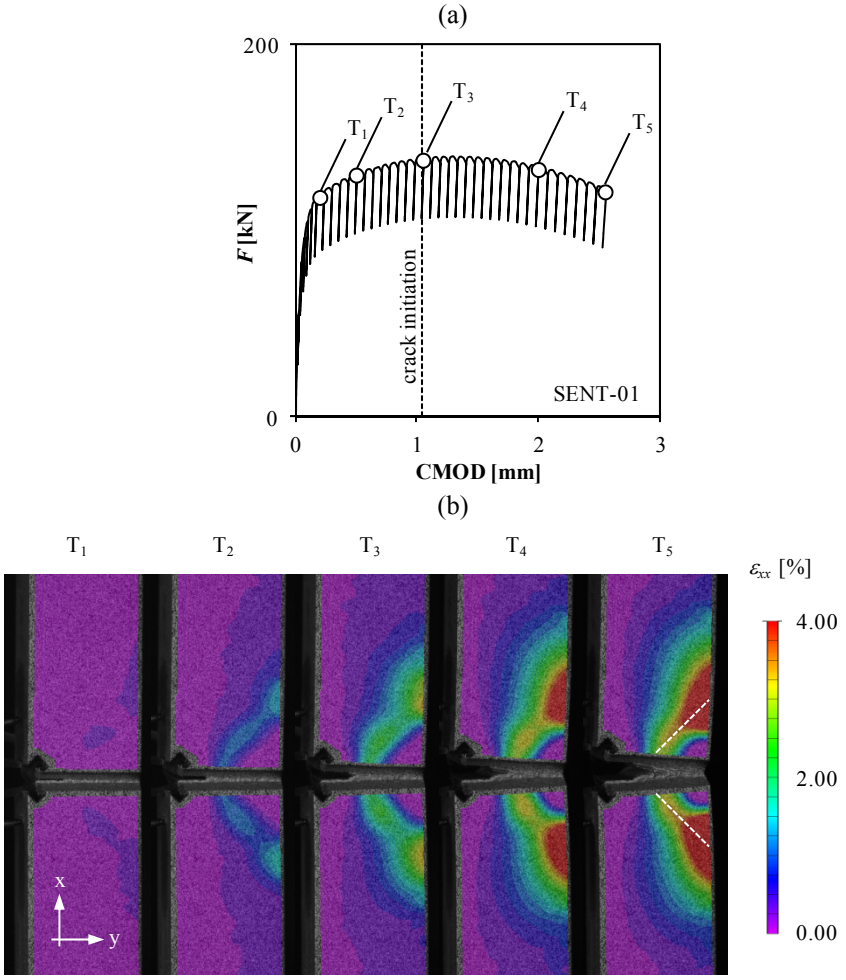

Figure 6.3. Load versus CMOD diagram for test on specimen SENT-01 with $a_0 / W = 0.25$ (a) and corresponding strain pattern upon loading (b).

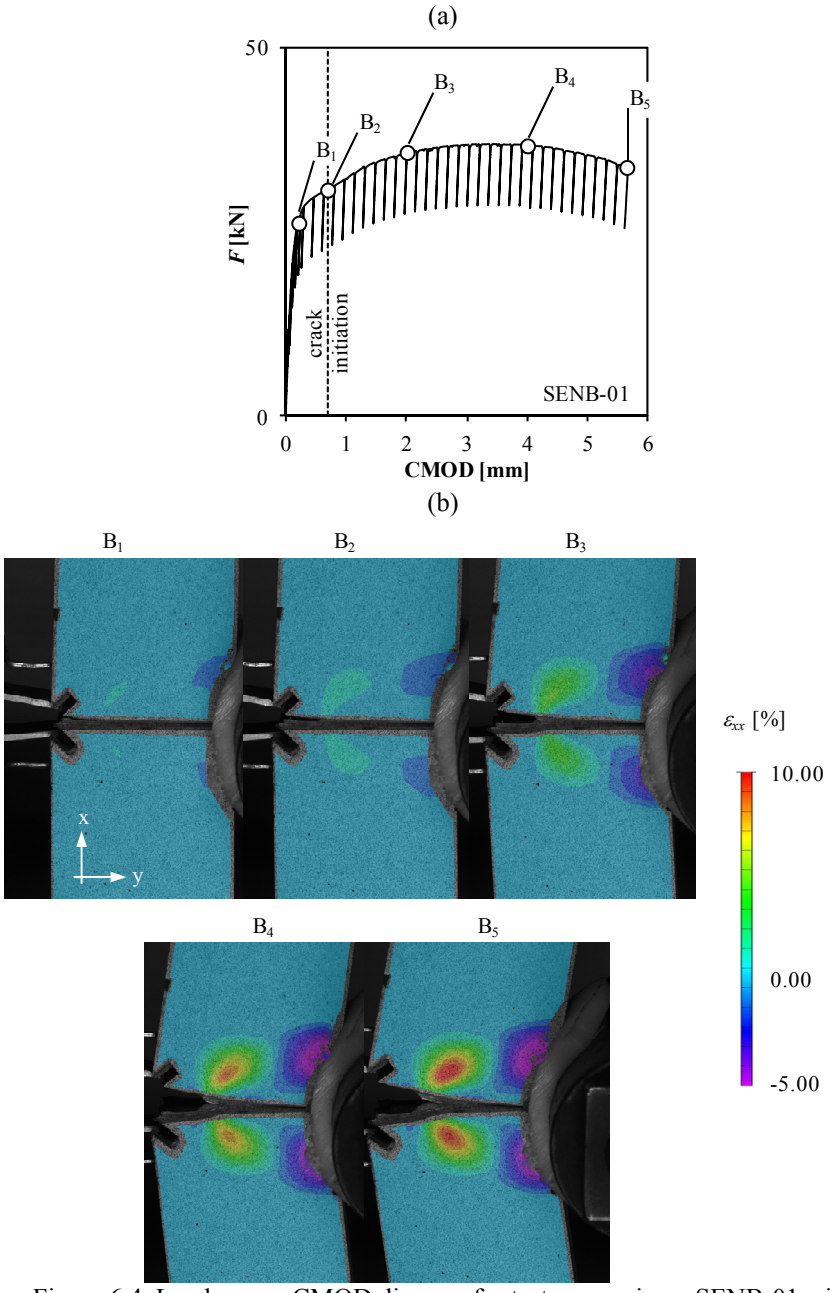

Figure 6.4. Load versus CMOD diagram for test on specimen SENB-01 with $a_0 / W = 0.25$ (a) and corresponding strain pattern upon loading (b).

For the base metal tests, strain fields developing symmetrically with respect to the crack tip are observed. Contrary, for weld metal tests large differences might be observed between the strain magnitudes in both base metals. This asymmetry is influenced by the presence of softer material in the vicinity of the crack tip. As such, the observed asymmetry is linked to:

- *overmatch*: in case the notch is located in stronger material, the strains will develop more easily in the nearby softer material. As a result, asymmetrical strain fields are rare for strength matching welds, unless significant softening is observed.
- *notch tip location*: although the notch tip is intended to be located at the weld metal center line, the actual notch tip might be located somewhat closer to one base material. Consequently, the strain will be directed towards the closest lower strength material.
- *heterogeneity*: the two pipes that are welded together seldom have the same strength properties; a difference between their strength is often observed. This results in a weaker and stronger pipe, whereby the weaker one has the tendency to take the majority of the deformation.

This asymmetry might be expected to influence the tearing resistance. However, no direct link was found between the asymmetry and the tearing resistance. As a representative example, the tearing resistance for specimens WM-10/11/12 is shown with their corresponding deformation pattern at the end of the test (Figure 6.5). All specimens are extracted from the same weld with theoretically identical initial notch position and size. However, specimen WM-10 shows a symmetrical strain pattern in contrast to specimens WM-11 and 12. Nevertheless, the obtained tearing resistance curves perfectly coincide for these tests.

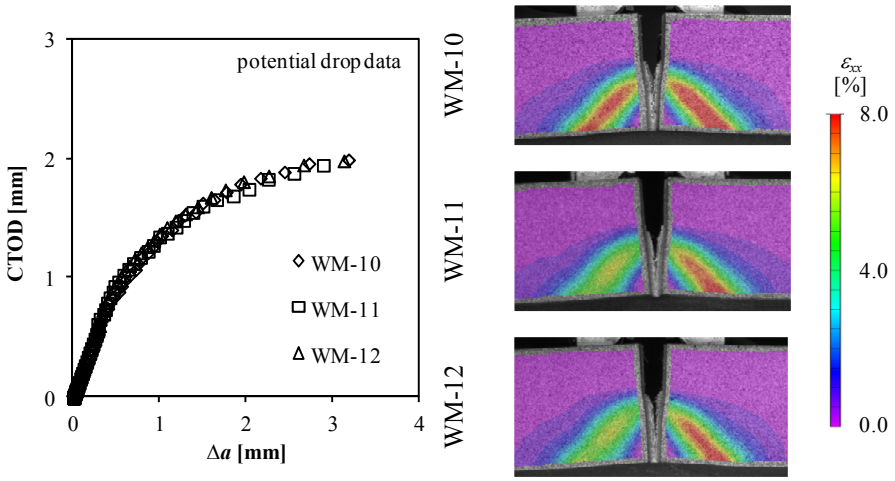

Figure 6.5. Comparison of tearing resistance curves for welded specimens with asymmetry in strain pattern

6.4.2 MWP testing

In the absence of brittle fracture, a wide plate specimen, when loaded in uniaxial tension, generally fails in either of the following ways:

- *Unstable ductile crack extension*: the specimen fails in the section containing the crack through unstable crack extension in the through-thickness direction.
- *Net section collapse*: the specimen fails in the section containing the crack whilst only a limited amount of ductile crack extension is observed. The failure is attributed to necking of the material.
- *Gross section (or global) collapse*: the specimen fails remote from the crack, through necking of the base metal.

Using the DIC technique, these failure modes are studied in this section. In addition, the use of the DIC technique allows replacing the traditional strain measurements via LVDT's with virtual strain measurements by tracking the displacement between two well-defined points. However, the position of these so-called virtual LVDT's remains crucial; a zone of homogeneous strain needs to be selected. For MWP specimens, a suitable location has been determined in the framework of the PhD by S. Hertelé [6.1]. A brief summary is provided in Figure 6.6. Remark that both remote strain measurements are performed in homogeneous regions, as initially aimed for.

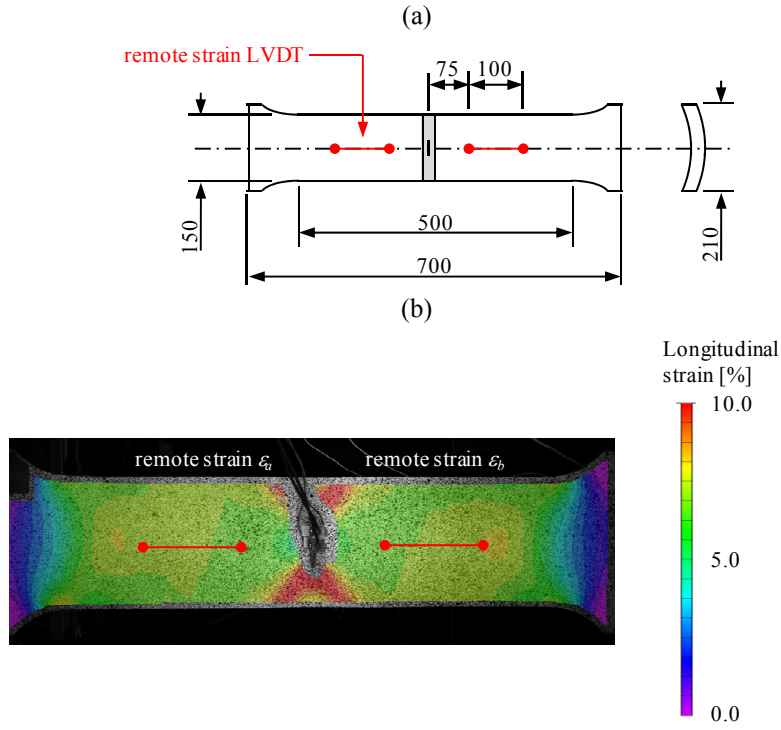

Figure 6.6. Schematic representation of LVDT locations for remote strain measurement (a) and example case illustrating homogeneity of strain fields in specimen WP-01 after completion of the test (b).

First, the focus is on homogeneous (i.e. non-welded) specimens. In the framework of this dissertation, only one such MWP specimen is tested. The base metal tensile test indicated a pronounced Lüders plateau (± 2.5 %). This is also observed during the MWP test. Figure 6.7 shows the stress-strain relationship for both tests. For the MWP specimen, the stress is obtained by dividing the applied force by the net section area. The strain is obtained from the virtual LVDT's, however only a single virtual LVDT is considered given the symmetry of the base metal properties at both sides of the notch. A nice correspondence is observed, though it is clear that the specimen did not fail through gross section collapse; the maximum strain in the wide plate specimen is lower than the material's uniform elongation. This is not surprising as the presence of the notch clearly introduces a stress concentration, which unmistakably provokes failure in this region for a homogeneous specimen.

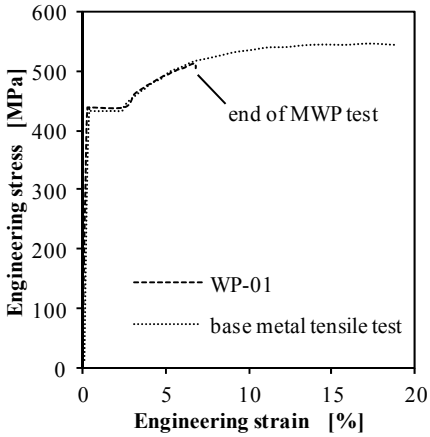

Figure 6.7. Tensile stress-strain relationship obtained during MWP test and base metal tensile test on specimen WP-01

Looking at the CMOD versus remote strain diagram (Figure 6.8), the presence of the Lüders plateau is also observed. In a first phase, between W_1 and W_2, the Lüders plateau develops around the crack. This results in a pronounced increase of the CMOD whilst the remote strain remains constant. This continues up to the moment the yield strength is exceeded in the base metal. As shown by W_3 and W_4, the Lüders plateau subsequently develops in the base metal. Remark that the Lüders strains do not develop symmetrically in both plates. An accidental weakest link causes one plate to deform prior to the other. Such weakest link might be a discontinuity in the specimens' geometry or local deterioration of the material properties. During this phase, no CMOD increase is observed since the applied load (force) only marginally increases. Accordingly, the crack driving force remains constant. Following this phase, the strain develops uniformly in both base metals (W_5), accompanied by a close to linear CMOD increase. Eventually, a rapid CMOD increase is observed whilst the strain reaches its maximum level; the tensile strain capacity (ε_{max}). At this point, a significant increase of the strain in the cracked section is observed (W_6).

These zones of high plastic strain around the crack are observed throughout the test (e.g. as clearly shown at moment W_2 and W_6 in Figure 6.8). They originate from the surface end of the crack and are directed towards the specimen's edges. The highest strains are localized in 45° shear bands, symmetrical around the crack. The DIC technique is thus capable of capturing these shear bands that have been described by the slip line theory [6.14]. However, the DIC technique does not allow to distinguish between net section collapse and unstable ductile crack extension. Both are characterized by an increase of the strain in the cracked section. Though, in case of net section collapse, no significant ductile crack extension is expected. Hence, crack growth data is required to distinguish these failure modes.

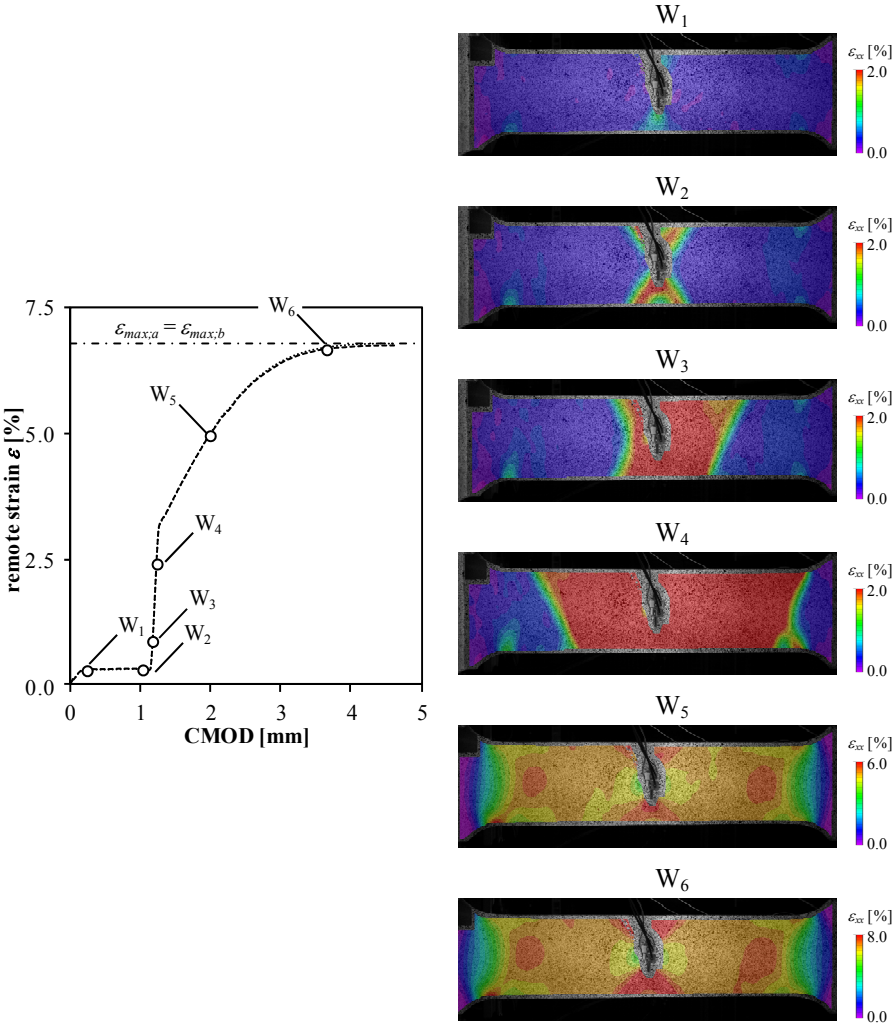

Figure 6.8. Strain evolution in specimen WP-01 during uniaxial tensile loading.

Second, the focus is on weld strength mismatched situations. Testing of specimens containing a weld potentially exhibits a number of particularities that could not be observed in homogeneous specimens. The following paragraphs provide a confirmation regarding some major phenomena based on the study of the deformation fields.

First, the presence of the weld potentially influences the crack driving force since the strength properties of this weld most probably differ from the surrounding base metal properties. In case of a stronger, overmatched weld metal the crack driving force is reduced [6.15-17]. If the weld metal's tearing resistance is sufficiently high, failure by necking in the pipe body is obtained rather than failure through ductile crack growth and subsequent net section collapse. This failure is referred to as gross section collapse.

By means of an example, the results of the test on specimen WP-06 are discussed. In this specimen the weld metal overmatches the base metal flow strength on average by 14.1%. This overmatch shields the defect from the applied displacement. This is reflected by a stabilization of the crack driving force, in terms of CMOD, beyond a critical level of the remote strain (Figure 6.9.a). This critical level corresponds to the uniform elongation of the base metal. Accordingly, necking of the base metal is observed (Figure 6.9.b). In accordance with the limited crack driving force, a limited ductile crack extension is observed (Figure 6.9.c). Accordingly, the failure is categorized as gross section collapse. The DIC measurements in this case additionally allow to experimentally study the deformation fields around the crack, illustrating that the typically observed shear lines (under 45° from the crack), are not present in the lower strength base plate. The deformation in this plate is entirely controlled by the gross section plasticity in this plate.

A second phenomenon that can be observed in welded specimens is a strength difference between the two base metal plates, commonly referred to as heterogeneity. As a result, the strain will not develop equally in both plates; deformation tends to concentrate in the lowest strength metal. Accordingly, the overall tensile strain capacity is lower than the maximum strain in the base metal. This overall strain capacity represents the amount of deformation taken by the entire segment, which can be approximated as the averaged remote strain:

$$\varepsilon_{\max;overall} = \frac{\varepsilon_{\max;a} + \varepsilon_{\max;b}}{2} \tag{6.1}$$

Within the framework of this dissertation, the highest level of heterogeneity was observed for specimen WP-02; a 26 MPa difference in terms of tensile strength (Figure 6.10.a). This is reflected by the remote strain versus CMOD plot; during the test the strain in the weakest plate (Material B) increases more rapidly (Figure 6.10.b). As a result, the final tensile strain capacity is significantly higher for this plate; the strain is twice as large as in the stronger plate (Material A). Looking back at the base metal stress-strain data, this difference is confirmed. At a stress level corresponding to the maximum force in the MWP test, strain levels corresponding to the ones measured with the remote (virtual) LVDT's are obtained. In conclusion, the rather limited 26 MPa difference in tensile strength significantly reduces the overall tensile strain capacity by 25% with respect to the maximum measured remote strain.

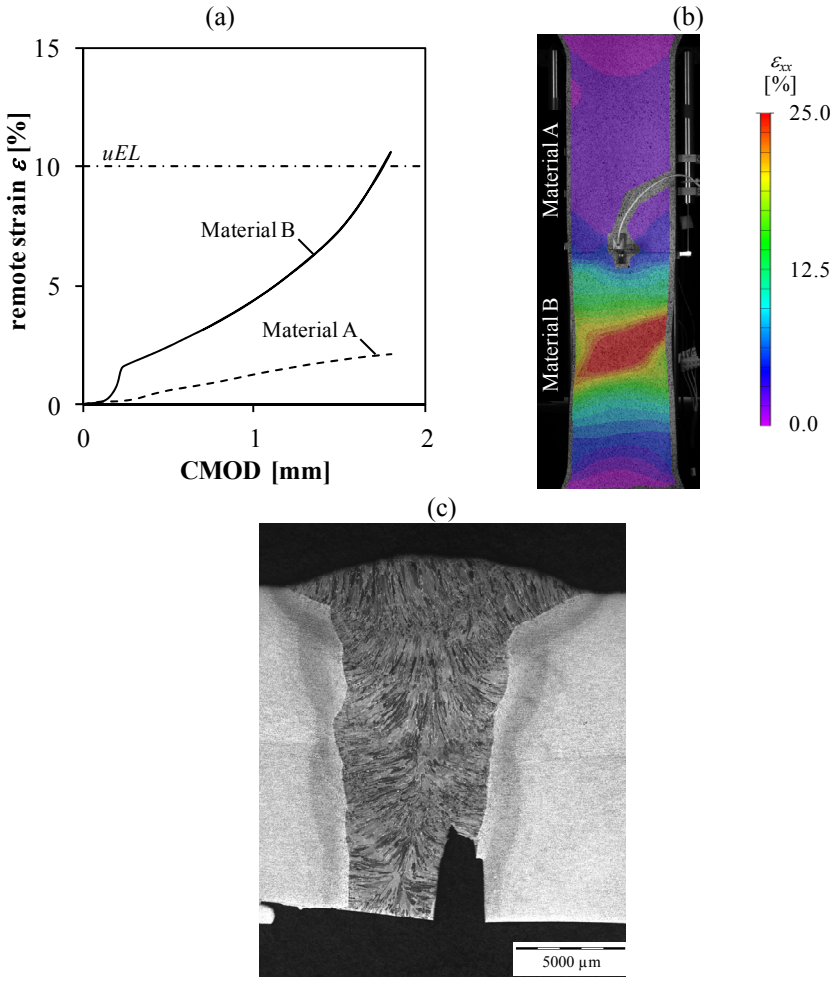

Figure 6.9. Evolution of crack driving force in terms of CMOD (a) and final strain distribution (b). Post-mortem macrograph of notch (c) for test WP-06.

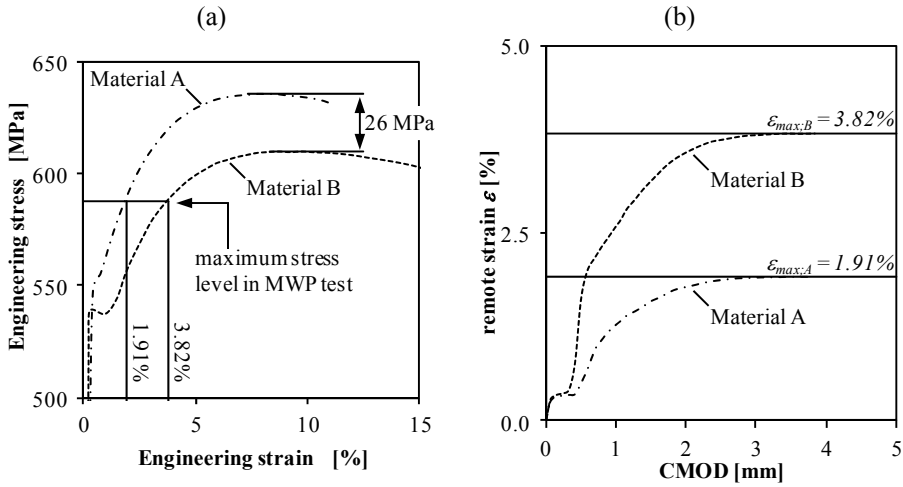

Figure 6.10. Base metal stress-strain data (a) and obtained remote strain versus CMOD relationship (b) for test WP-02

This difference in strain can be clearly observed in Figure 6.11.a. The DIC technique additionally allows studying the impact of material heterogeneity on the deformation fields around the crack tip. The normally observed shear lines originating from the crack towards the side edges of the specimen under 45°, have a tendency to concentrate in the weaker material. By means of comparison, the deformation in a more homogeneous specimen is also studied. From the base metal tests going with test WP-05, a negligible 5 MPa difference in tensile strength was observed between both base metals. Accordingly, the strain difference between both base metals is limited (Figure 6.11.b). In addition, the DIC measurements reveal that the strain field originating around the crack tip appears symmetrical.

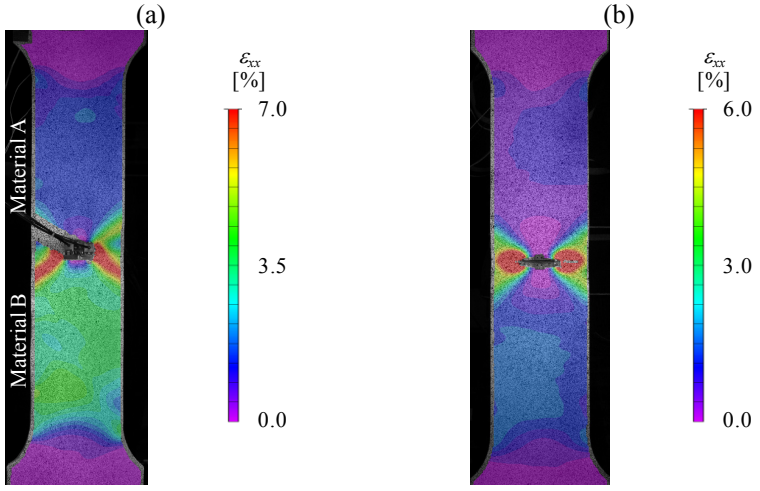

Figure 6.11. Strain distribution at the end of the test for heterogeneous specimen WP-02 (a) and specimen WP-05 with a negligible difference between both base metals' strength properties (b)

6.5. Tearing versus deformation

In this section attention is given to the deformation and strain patterns observed in SENT testing. From the deformations next to the side grooves, the amount of ductile crack extension is estimated and compared to the results of the potential drop method in section 6.5.1. Next, the relationship between the tearing resistance and the strain distribution is examined for both homogeneous and welded specimens in section 6.5.2.

6.5.1 Evaluation of ductile crack extension using DIC

6.5.1.1 Method

In this paragraph, the test results for three SENT specimens are examined, namely specimen BM-02, BM-03 and BM-05. These specimens are extracted from the same API-5L X80 material, though have different initial crack depths $a_0 / W = 0.2$, 0.4 and 0.6 respectively. In an attempt to monitor the ductile crack extension by means of full field measurements, the deformation near the side grooves is examined. More specifically, the deformation of a path located next to the side groove ($x = 2.0$ mm) is monitored by tracking the x and y displacements of 200 points. Figure 6.12.a shows this deformation for the specimen with initial crack size $a_0 / W = 0.4$ at constant increments of the CTOD. Remark that the difference between the deformed lines at load levels characterized by CTOD = 0.00 mm and 0.25 mm is significantly higher than the subsequent loading steps. This difference is attributed to rigid body movement due to minor movements in the test rig when first loaded. Regardless of the applied load, the deformation at the crack mouth ($y = 0$ mm) clearly progresses more rapidly than the deformation at the opposite side. Accordingly, two zones can be distinguished in the deformation pattern. In the first zone the deformation is controlled by the restraint of the remaining ligament (denoted as "Zone I" in Figure 6.12.b). In the second zone, the absence of any restraint controls the deformation (denoted as "Zone II" in Figure 6.12.b). A transient zone connects both zones, resulting in a continuous deformation gradient. The location of this transient zone is hypothesized to relate to the location of the actual crack tip. As a result, it could be possible to relate the crack tip blunting and amount of ductile crack extension to the location of this transient zone.

In an attempt to characterize the transient zone, a polynomial function is fitted through the 200 selected displacement points.

$$x(y) = c_m y^m + c_{m-1} y^{m-1} + \ldots + c_1 y + c_0 \tag{6.2}$$

In this case a polynomial of degree $m = 16$ was found to accurately describe the deformation. From this fitted curve, the first and second order derivatives are calculated and combined to determine the curvature (κ) as follows:

$$\kappa = \frac{\dfrac{d^2x}{dy^2}}{\left(1+\left(\dfrac{dx}{dy}\right)^2\right)^{3/2}} \tag{6.3}$$

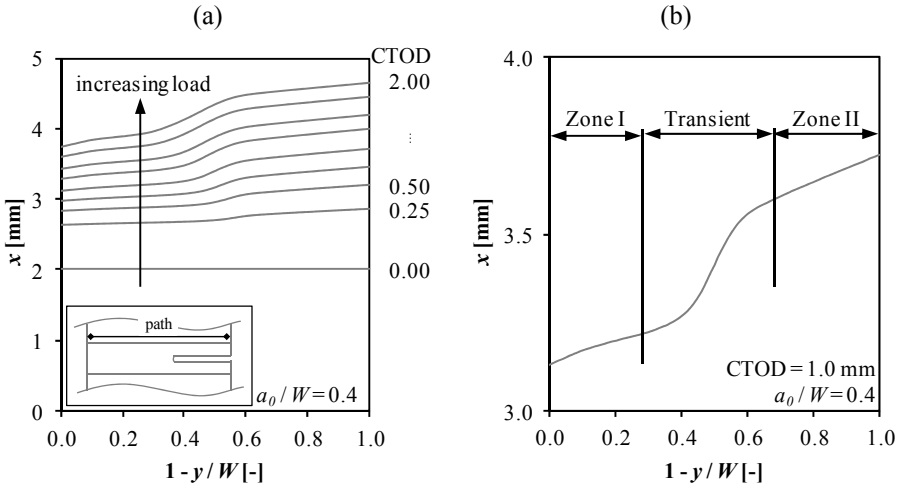

Figure 6.12. Deformation of path along side grooves at constant increments of computed CTOD (a) and detail of deformation pattern at CTOD = 1.0 mm (b).

Several points could be identified to characterize the position of this transient zone, e.g. the location of maximum bending ($dx/dy = 0$) or of maximum curvature. The latter is selected as it is located close to the zone where the deformation is mainly controlled by the restraint of the remaining ligament (Figure 6.13.a). Hence the shift of this point with increasing load levels is expected to relate (solely) to crack tip blunting and ductile crack extension. If for instance the point of minimum curvature is tracked, its position is no longer dominated by the crack tip location but is also influenced by the formation of a plastic wake, which originates as ductile crack extension proceeds. Accordingly, this point's position remains approximately constant during the test (Figure 6.13.b). In the remainder of this paragraph, only the position of maximum curvature is tracked throughout the test.

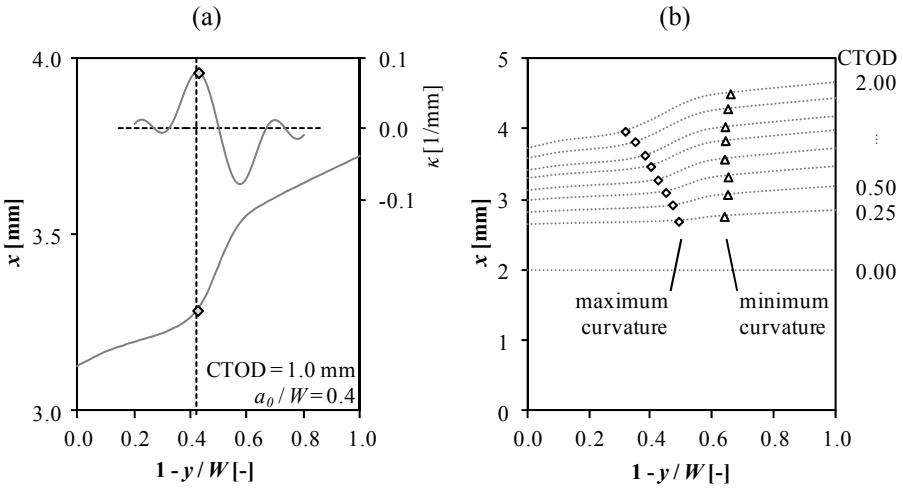

Figure 6.13. Determination of maximum curvature for one load level (a) and position of maximum and minimum curvatures throughout the test (b).

6.5.1.2 Comparison with potential drop data

To validate this approach, the obtained resistance curves are compared to the ones obtained using the potential drop technique. For the DIC curves (referred to as "DIC data" in Figure 6.14), significant scatter is present for low load levels, attributed to the inaccuracy of the DIC measurements. The predicted crack extension closely corresponds with the measured final crack extension, which was obtained through the nine points average method. Also plotted are the resistance curves obtained from the potential drop measurements (referred to as "PD data" in Figure 6.14). As both are plotted on top of each other, the correspondence between both becomes obvious, although it is noted that the scatter is higher for DIC data. In addition, the difference between both curves is not necessarily constant. These differences are not thoroughly understood and probably require further investigation. However, this is not expected to cause large problems as the overall trend between both curves is close to identical and will therefore result in comparable fitted curves. In addition, these curves indicate that the DIC method yields better results at the lowest relative crack depth. For deeply notched specimens ($a_0 / W = 0.6$) no meaningful DIC resistance curves are obtained; the obtained trend does not match with the resistance curve from the potential drop measurements. The reason for the decreasing correspondence with the reference curve from the PD measurements is to be found in other factors affecting the location of maximum curvature, i.e. interaction with the free surface. As shown in Figure 6.15 the deformation pattern does not contain the previously defined "Zone I" in case of deeply notched specimens; a zone with constant linear deformation lacks near the remaining ligament. This complicates the determination of the curvature and results in unrepresentative estimates of the crack extension data.

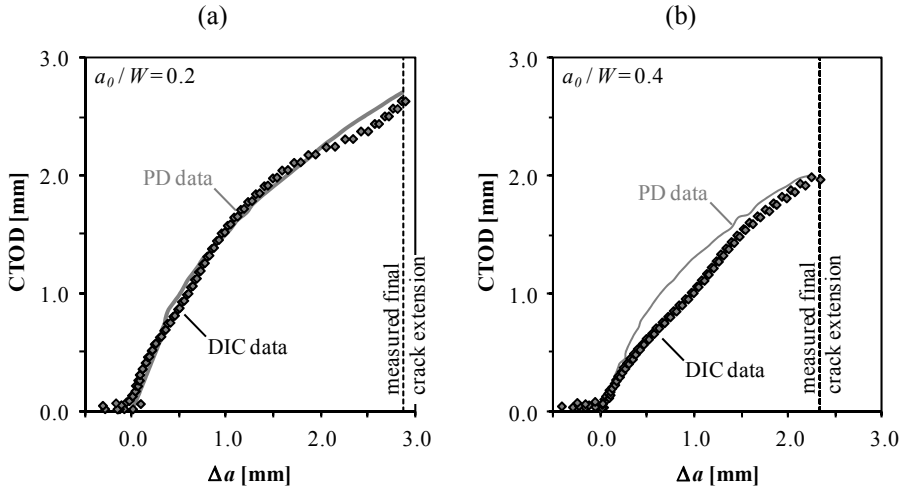

Figure 6.14. Resulting tearing resistance curves determined via DIC and PD for initial crack sizes $a_0/W = 0.2$ (a) and $a_0/W = 0.4$ (b) .

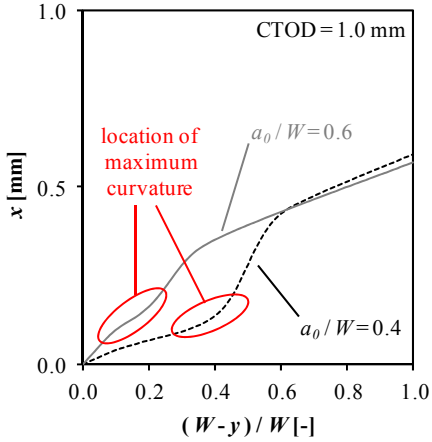

Figure 6.15. Difference in deformation profile for different initial crack depths.

6.5.2 Tearing resistance versus strain

As previously discussed, a material's tearing resistance strongly depends on the constraint. In literature, a variety of parameters have been considered to describe this constraint, e.g. the Q-parameter and the stress triaxiality h. The latter expresses the magnitude of the hydrostatic stress relative to the Von Mises equivalent stress. As is well known, hydrostatic stresses do not result in plastic deformation, in contrast to the Von Mises equivalent stresses. This implies that:

- a high constraint specimen (high triaxiality h) does not show as much plastic deformation as a low constraint specimen and,
- more generally, a specimen showing a high plastic deformation has a higher tearing resistance compared to a specimen showing less plastic deformation.

The above relates to the damage criterion described by Ishikawa et al. [6.18], who assumed that for a given material failure can be characterized by a critical equivalent plastic strain, depending on the stress triaxiality.

6.5.2.1 Method

The strain distribution for two sets of SENT specimens is investigated. These strain distributions are obtained from the full field digital image correlation measurements. To facilitate a quantitative comparison of the specimens, the maximum uniaxial longitudinal strain[1] is selected at a well defined moment during the test (e.g. crack initiation). Note however, that the side grooves caused a restriction of the area that could be analyzed.

For homogeneous, non-welded specimens, this maximum strain does not differ significantly at both sides of the crack. Accordingly, the overall maximum is considered. In contrast, the difference in maximum strain at both sides of the crack might be noteworthy in welded specimens. Therefore, the maximum strain is evaluated separately for "metal A" and "metal B", resulting in the maximum strains $\varepsilon_{max;A}$ and $\varepsilon_{max;B}$ respectively.

6.5.2.2 Observations for homogeneous specimens

The first set of specimens, extracted from the same grade API-5L X80 pipe metal, have different initial crack depths, ranging from $a_0 / W = 0.2$ to 0.6. These specimens are referred to as BM-01 till BM-09. As generally known and furthermore discussed in detail in Chapter 5, a higher initial crack depth results in a higher constraint [6.19-21]. Hence, the tearing resistance is expected to decrease with increasing initial crack depth. This is indeed observed for these specimens. Figure 6.16.a displays the fitted resistance curves for each tested crack depth.

In an attempt to compare the different strain distributions, the maximum strain is evaluated at two stages during the test, namely at crack initiation and at 1.5 mm of ductile crack extension. At both stages, a close to linear dependency is observed

[1] Finite element simulations demonstrated that the uniaxial longitudinal strain is almost identical (both in magnitude and distribution) to the equivalent plastic strain. The latter can however not be straightforwardly quantified using surface strain measurements.

between the strain magnitude and the relative crack depth (Figure 6.16.b). This linear trend is in line with the results published by Yang et al. [6.22], who recently reported a linear correlation between the initiation toughness and the area exceeding a critical equivalent plastic strain based on an extensive finite element study. Considering the increasing constraint for deeper initial cracks, it is thus concluded that a higher constraint indeed results in lower plastic strains around the crack.

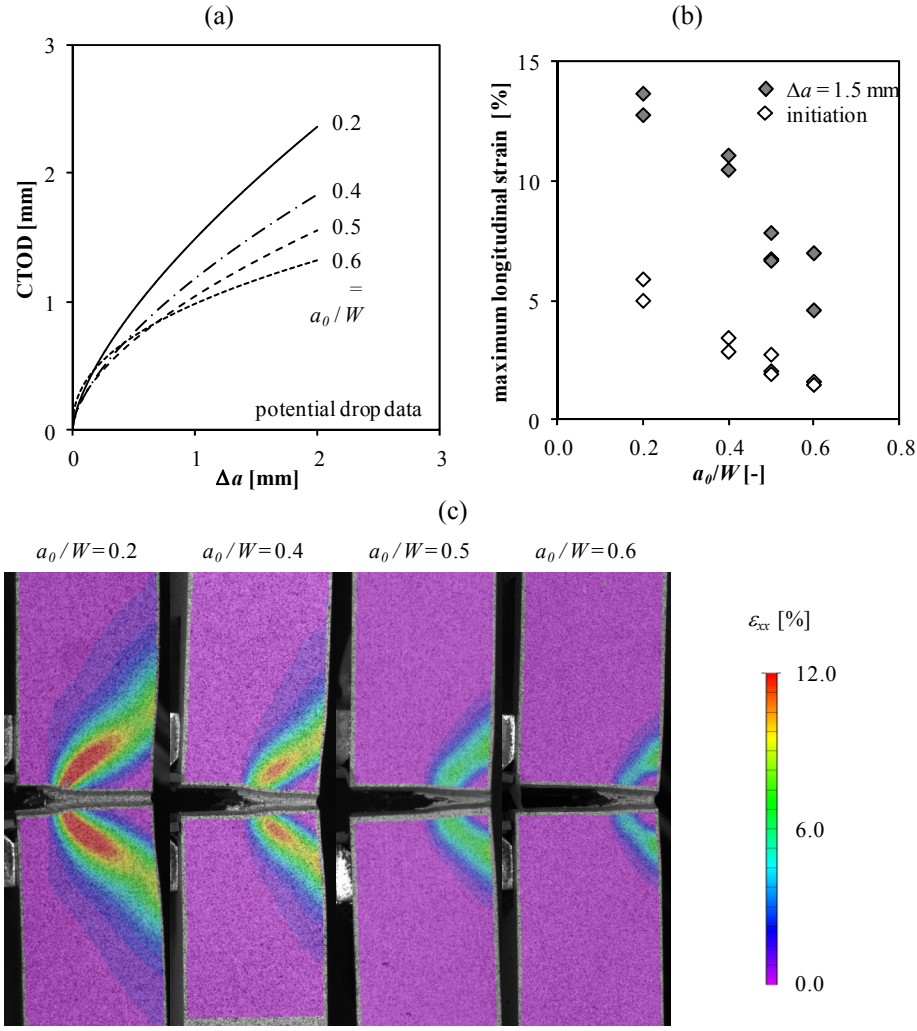

Figure 6.16. Influence of relative crack depth on tearing resistance curves (a), maximum strain at initiation and at fixed amount of crack extension (b) and full field strain distribution at 1.5 mm of crack extension (c)

The trend observed between the relative initial crack depth and maximum strain is furthermore illustrated by the full field strain distributions at a load level corresponding to 1.5 mm of crack extension (Figure 6.16.c). Although this comparison is of a more qualitative nature, it is clear that both the size and magnitude of the strains change with the initial crack depth. Relative to the maximum strain in the specimen, the strains tend to concentrate more around the surface opposite to the crack mouth for deeply notched specimens. In addition, a clear decrease of the maximum strain is observed from these plots.

6.5.2.3 Observations for welded specimens

A second set of specimens is extracted from an overmatched weld in a grade API-5L X80 pipe. Notches with an identical relative initial crack depth are located along the weld metal center line ($a_0 / W = 0.4$). The notch position differs; three specimens have a notch from the inner diameter side, three from the outer diameter and the last three have a notch located in the through-thickness direction. Given the heterogeneous nature of welds, a different tearing resistance is obtained depending on the notch position, as discussed in Chapter 6. However, the constraint in these specimens is not expected to differ drastically.

As outlined before, an asymmetrical strain distribution is often observed for weld strength mismatched SENT specimens. To account for this asymmetry, the average of both maximum strains (ε_{max}|average) and the maximum of both (ε_{max}|maximum) are evaluated for these specimens. This evaluation is carried out at crack initiation. This moment strongly relates to the tearing resistance; low initiation toughness corresponds to a lower tearing resistance. Again, a linear trend is observed between the initiation toughness and the maximum strain (Figure 6.17).

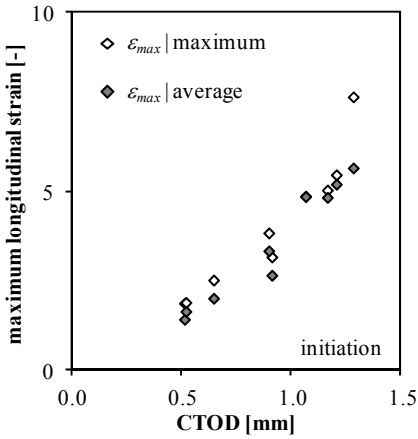

Figure 6.17. Relationship between CTOD at initiation and maximum strain for welded specimens WM-07 till WM-15

This linear trend is more pronounced if based on the average strain, which suggests that the tearing resistance is influenced by the deformation of both base metals rather than being controlled by a single one. Furthermore, the observed linear trend supports the idea that the occurring strain strongly relates to the material's toughness. It is therefore concluded that the occurring strain does not solely express the constraint, but, more generally, relates to the tearing resistance and hence the toughness of the material.

6.6. Conclusions

The DIC technique was successfully applied for both SENT and MWP specimens, notwithstanding the occurring strains are well in the plastic regime (strains beyond 20% were well captured, without delamination of the paint). From the resulting deformation and strain fields, the following major conclusions are drawn:

- The DIC technique is able to visualize the characteristic deformation patterns for the SENT and MWP specimens. The deformation pattern for the SENT specimens clearly shows high strain localization in two shear bands that have a 45° orientation relative to the crack and originate from the crack tip. The same type of deformation field is observed for MWP specimens, although these fields in that case start from the crack ends near the free surface.
- Although well known that weld metal strength mismatch and heterogeneity affect failure in SENT and MWP tests, the DIC technique additionally allows to qualitatively and quantitatively study their effect. In contrast to traditional (e.g. LVDT) measurements, this technique also allows examining the deformation pattern in the vicinity of the notch.
- Applications of the DIC technique for evaluating the crack extension in linear elastic fracture mechanics have been described in literature. In this chapter, a method has been introduced to estimate the amount of ductile crack extension in the elastic-plastic regime. The presented technique, which makes use of the deformation next to the side grooves, works fine for sufficiently ductile materials, preferably with a low initial crack depth. At current, preference is however given to the potential drop (or unloading compliance) method, since these are more generally applicable.
- Based on finite element simulations, a (linear) relationship between the equivalent plastic strain and constraint has been reported. This chapter provides experimental evidence for these findings. Based on two sets of SENT tests, respectively containing base metal and weld metal center line cracks, a linear correlation was observed between the initiation toughness and the maximum (surface) strain at initiation.

Note eventually that the application of the DIC technique additionally demonstrated advantages in SENT and MWP testing that have been discussed in other chapters. Recall for instance the δ_5 method for measuring the CTOD in SENT specimens (section 4.4.2) and the optimization of the pin locations for the DCPD measurements in MWP specimens (section 3.3.2.2).

6.7. Bibliography

[6.1] Hertelé, S., 2012, "Coupled Experimental-Numerical Framework for the Assessment of Strain Capacity of Flawed Girth Welds in Pipelines", Ph.D. thesis, Ghent University, Ghent, Belgium.

[6.2] Sutton, M. A., Orteu, J.-J., and Schreier, H. W., 2009, "Image Correlation for Shape, Motion and Deformation Measurements", Springer, New York.

[6.3] Yates, J. R., Zanganeh, M., and Tai, Y. H., 2009, "Quantifying Crack Tip Displacement Fields with DIC", Engineering Fracture Mechanics, 77, pp. 2063-2076.

[6.4] 2012, Limess Software Und Messtechnik GmbH, 24-08-2012, http://www.limess.com

[6.5] Correlated Solutions Inc., 24-08-2012, http://www.correlatedsolutions.com

[6.6] Pop, O., Meite, M., Dubois, F., and Absi, J., 2011, "Identification Algorithm for Fracture Parameters by Combining DIC and Fem Approaches", International Journal of Fracture, 170, pp. 101-114.

[6.7] Abanto-Bueno, J., and Lambros, J., 2002, "Investigation of Crack Growth in Functionally Graded Materials Using Digital Image Correlation", Engineering Fracture Mechanics, 69, pp. 1695-1711.

[6.8] Mekky, W., and Nicholson, P. S., 2006, "The Fracture Toughness of Ni/Al2o3 Laminates by Digital Image Correlation I: Experimental Crack Opening Displacement and R-Curves", Engineering Fracture Mechanics, 73, pp. 571-582.

[6.9] Sutton, M. A., Yan, J.-H., Deng, X., Cheng, C.-S., and Zavattieri, P., 2007, "Three-Dimensional Digital Image Correlation to Quantify Deformation and Crack-Opening Displacement in Ductile Aluminum under Mixed-Mode I/III Loading", Optical Engineering, 46, pp. 051003-1/17.

[6.10] Yan, J.-H., Sutton, M. A., Deng, X., Wei, Z., and Zavattieri, P., 2009, "Mixed-Mode Crack Growth in Ductile Thin-Sheet Materials under Combined in-Plane and out-of-Plane Loading", International Journal of Fracture, 160, pp. 169-188.

[6.11] Fagerholt, E., Ostby, E., Borvik, T., and Hopperstad, O. S., 2012, "Investigation of Fracture in Small-Scale SENT Tests of a Welded X80 Pipeline Steel Using Digital Image Correlation with Node Splitting", Engineering Fracture Mechanics, 96, pp. 276-293.

[6.12] Shen, G., Tyson, W. R., Gianetto, J. A., and Park, D.-Y., 2010, "Effect of Side Grooves on Compliance, J-Integral and Constraint of Clamped SE(T) Specimen", Pressure Vessels and Piping Conference, Bellevue, Washington, USA, paper n° PVP2010-25164.

[6.13] Hertelé, S., De Waele, W., Denys, R., and Verstraete, M., 2012, "Investigation of Strain Measurements in (Curved) Wide Plate Specimens Using Digital Image Correlation and Finite Element Analysis", Journal of Strain Analysis for Engineering Design, 47, pp. 276-288.

[6.14] Anderson, T. L., 1995, "Fracture Mechanics: Fundamentals and Applications", CRC press, Texas.

[6.15] Motohashi, H., and Hagiwara, N., 2007, "Analytical Study of Effects of Strength Matching on Strain Capacity", International Offshore and Polar Engineering Conference, Lisbon, Portugal, pp. 3101-3106.

[6.16] Hertelé, S., De Waele, W., Denys, R., Verstraete, M., and Horn, A., 2012, "Weld Strength Mismatch in Strain Based Flaw Assessment: Which Definition to Use?", Pressure Vessels and Piping Conference, Toronto, Canada, paper n° PVP2012-78306.

[6.17] Kan, W. C., Weir, M., Zhang, M. M., Lillig, D. B., Barbas, S. T., Macia, M. L., and Biery, N. E., 2008, "Strain Based Pipelines: Design Consideration Overview", International Offshore and Polar Engineering Conference, Vancouver, Canada, pp. 174-181.

[6.18] Ishikawa, N., Sueyoshi, H., and Igi, S., 2010, "Application of Damage Mechanics Modeling to Strain Based Design with Respect to Ductile Crack Initiation", International Pipeline Conference, Calgary, Alberta, Canada, paper n° IPC2010-31506.

[6.19] Wang, E., Zhou, W., Shen, G., and Duan, D.-M., 2012, "An Experimental Study on J(CTOD)-R Curves of Single Edge Tension Specimens for X80 Steel", International Pipeline Conference, Calgary, Alberta, Canada, paper n° IPC2012-90323.

[6.20] Thaulow, C., Ostby, E., Nyhus, B., Zhang, Z. L., and Skallerud, B., 2004, "Constraint Correction of High Strength Steel - Selection of Test Specimens and Application of Direct Calculations", Engineering Fracture Mechanics, 71, pp. 2417-2433.

[6.21] Cravero, S., and Ruggieri, C., 2005, "Correlation of Fracture Behavior in High Pressure Pipelines with Axial Flaws Using Constraint Designed Test Specimens - Part I: Plane Strain Analysis", Engineering Fracture Mechanics, 72, pp. 1344-1360.

[6.22] Yang, J., Wang, C. Z., Xuan, F. Z., and Tu, S. T., Unified Correlation of in-Plane and out-of-Plane Constraints with Fracture Toughness, via: http://onlinelibrary.wiley.com/doi/10.1111/ffe.12094/abstract accessed on: 19-08-2013.

Chapter 7

–

Comparison of Constraint in CWP Specimens and (Pressurized) Pipes

7.1. Introduction

The literature review presented in Chapter 2, indicated that the constraint ahead of the crack tip is strongly related to the tearing resistance. Since this tearing resistance potentially influences the failure mode, e.g. tangency approach discussed in Chapter 1, a constraint match is required between the intended application (i.e. full pipe under pressure) and the laboratory scale test specimen.

In literature, a multitude of papers deals with the comparison of constraint in SENT specimens to pipes. In contrast, the relationship between pipes and CWP specimens in terms of constraint is not well described in literature. The understanding of this relationship is however crucial for the evaluation of the tensile strain capacity obtained from both specimen types, as discussed in detail in Chapter 8.

To determine the constraint in (pressurized) pipes and CWP specimens, an evaluation of the stresses ahead of the crack tip is presented in this chapter. These evaluations are based on an extensive set of three dimensional finite element simulations. As discussed in detail in Chapter 2, preference is given to the following parameters to evaluate the constraint:

- *Q-parameter* The two-parameter *J-Q* framework developed by O'Dowd and Shih in the early 1990's is adopted [7.1, 2]. It is well accepted for situations with pronounced plasticity [7.3].
- *stress triaxiality parameter h* In addition, the stress triaxiality parameter *h*, defined as the ratio between the hydrostatic stress and the Von Mises equivalent stress, is evaluated ahead of the crack tip [7.4, 5].

The equivalence of the constraint parameters *Q* and *h* has been reported in literature [7.6, 7], though the stress triaxiality is assumed to have a higher physical relevance in case of ductile failure. The constraint analyses are first performed for homogeneous specimens. Subsequently, the influence of weld strength mismatch is considered, as strength overmatching welds are required for strain-based applications.

The remainder of this chapter is structured as follows; in section 7.2 a description of the test specimen geometries and finite element models is provided. Second, in section 7.3 an evaluation is made of the constraint evolution in (pressurized) pipes and CWP specimens. Conclusions are given in section 7.4.

7.2. Methodology

This section provides a description of the simulated test specimen geometries. Second, the developed finite element models and associated assumptions are outlined. The third and forth subsection elaborate on the material properties and the simulation of weld strength mismatched configurations respectively. Following, the test matrix is outlined. Finally, the details of the constraint calculations are provided.

7.2.1. Geometry of CWP specimens and pipes

The simulated pipe specimens are characterized by their outer diameter (D) and wall thickness (t) (Figure 7.1.a). Within the set of simulations performed, the wall thickness was fixed at 15 mm. The diameter is varied between 762 mm (30") and 1270 mm (50"). The length of the simulated pipe specimens equals four times their diameter, which suffices to yield results independent from the boundary conditions [7.8].

In practice, CWP specimens are extracted from pipes. Accordingly, these have a curvature defined by the pipe's diameter and have the same wall thickness. The total length of the CWP specimens equals 1200 mm, whereas the prismatic section is 900 mm long and 300 mm wide (Figure 7.1.b). All other geometrical properties are in agreement with the UGent Guidelines for CWP testing [7.9].

The specimens have constant depth surface breaking defects with an end-radius equal to the defect depth. The crack geometry is furthermore characterized by the defect depth (a) and defect arc length ($2c$). Unless otherwise specified, these defects are located at the weld metal centre along the pipe's inner diameter. The defect length is varied between 25 mm and 100 mm. The depth of the crack is varied between 3.0 and 6.0 mm, reflecting relative crack depths a/t between 0.20 and 0.40.

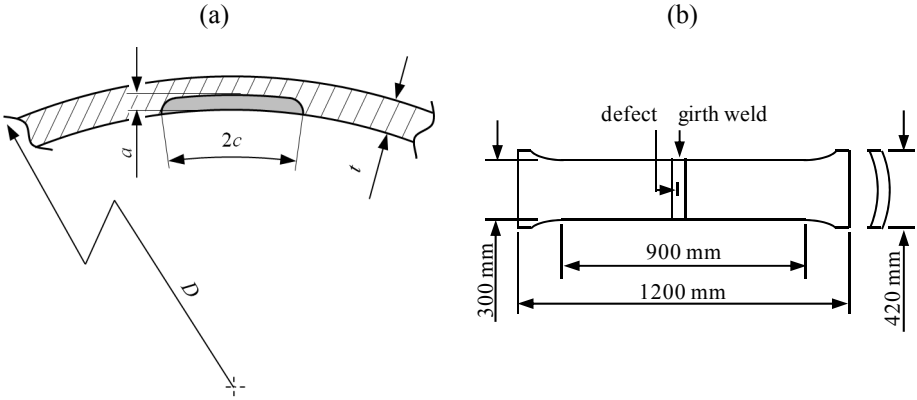

Figure 7.1. Definition of geometrical parameters: pipe (a) and CWP specimen (b)

7.2.2. Finite element models

Python scripts have been used to facilitate the parametric analysis of the above geometries through finite element simulations in ABAQUS™ v6.11. These scripts automatically generate, mesh, analyze and post-process the different geometries. For a detailed description of this scripting approach, the reader is referred to [7.10]. A main advantage hereof is the consistent mesh design, in particular around the crack tip. Regardless the dimensions of the crack and/or specimen, a gradually coarsening spider web mesh is created around the crack. This crack is, unless specified otherwise, located along the pipe's inner diameter. The crack is initially blunted with an initial root radius of 2.5 μm. This radius is small enough to accurately represent an infinitely sharp crack [7.11]. A typical mesh design is shown in Figure 7.2. Note that only half of the specimens are modeled, symmetry boundary conditions being applied along the length of the specimens. Based on linear brick elements with reduced integration (ABAQUS™ type C3D8R), the resulting models typically consist of 80 000 and 35 000 nodes for pipe and CWP specimens respectively.

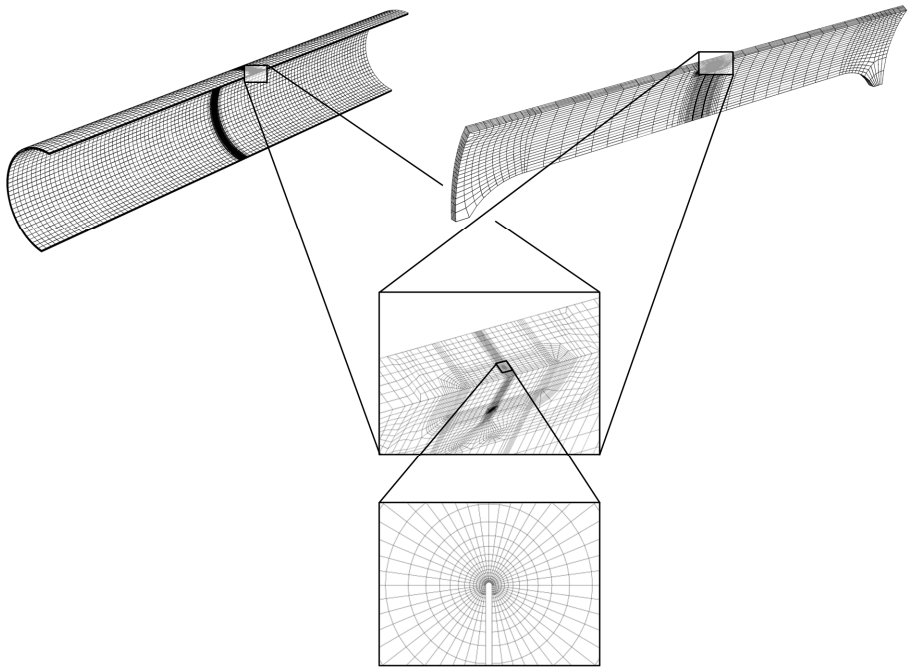

Figure 7.2. Characteristic mesh design for pipe specimens and CWP specimens.

Next to the symmetry boundary conditions, displacement boundary conditions are applied representing the axial straining for both pipe and CWP specimens. Clamped boundary conditions are simulated, since a pure uniaxial and longitudinal displacement is imposed, thus not allowing for any rotation. These displacements are transferred to the specimen through rigid bodies attached to the end of the specimen. In addition to the resulting axial load, the pipe specimens can be subjected to internal pressure. This pressure is applied at the inner diameter surface prior to the axial straining. For the simulated defects that are located at the inner diameter side, the internal pressure is also applied onto the crack faces and tip. Simulations with and without additional pressure have been performed for comparison. In case of

outer diameter defects, the internal pressure only acts on the pipe's inner diameter. Unless specifically mentioned, the considered pressure level (p) corresponds to a hoop stress (σ_{hoop}) equal to 80% of the pipe metal's actual yield strength.

The reference stress fields, required for the *J-Q* analyses (Chapter 2), are obtained from a Modified Boundary Layer (MBL) model with similar mesh design around the crack tip. These stress fields are evaluated at a fixed load level of $J = 50$ N/mm, defined by the load applied at the boundaries of the MBL model. This load level assures that the stress data are independent of the initial blunting [7.12].

7.2.3. Material properties and analysis approach

The analyses are completed using small strain assumptions. Although this is known to be an approximation, this approach has proven to yield a sufficiently accurate description of the crack tip stress fields [7.13]. In addition, this approach allows simulating weld metal strength overmatched configurations at high load levels in terms of *J*-integral, without observing a necking phenomenon in the lower strength base metal. Both for homogeneous and weld strength mismatched configurations, a non-linear elastic Ramberg-Osgood material model (i.e. deformation plasticity) is considered [7.14]. This model describes the true stress – true strain behaviour based on the strain hardening exponent n, Young's modulus E and 0.2% proof stress σ_0, which serves as the yield strength. Within the framework of this study, a yield strength of 420 MPa and Young's modulus of 206980 MPa are considered. The strain hardening exponent is varied between $n = 5$ and $n = 20$, representing yield-to-tensile (Y/T) ratios between 0.46 and 0.90 respectively.

$$\varepsilon = \frac{\sigma}{E} + 0.002\left(\frac{\sigma}{\sigma_0}\right)^n \tag{7.1}$$

At this point, the following two remarks should be made. First, it is noted that a Y/T-ratio of 0.46 is not realistic for pipeline applications; however this case is considered to cover a wide area of applicability. Second, the Ramberg-Osgood type of material is known to be less representative for contemporary pipeline steels [7.15, 16]. Nevertheless, this non-linear elastic material definition is selected as the ABAQUS™ implementation combines convergence of the simulations at high levels of plastic deformation with accurate *J*-integral calculations. The latter are based on the domain integral method implemented in Abaqus®. A total of twelve contours are considered. In case of welded specimens, it is noted that all contours are contained within the weld metal region.

7.2.4. Simulated weld properties

For the analysis of weld strength mismatched situations, the yield strength mismatch definition is adopted (Chapter 1), notwithstanding a definition based on the flow strength is preferred for strain based applications. As a result, within this chapter, the difference between weld and base metal solely originates from a difference in yield strength; the strain hardening exponents of weld and base metal are identical. Hence the yield strength mismatch levels can as well be interpreted as flow strength mismatch levels. Yield strength mismatch levels are varied between -20% (strength undermatching weld) and +50% (strength overmatching weld). Two types of welds have been selected based on the CSA recommendations for pipeline girth welding [7.17]. The first type represents a manual weld with a wide V-shaped bevel preparation. Its opening angle equals 30° (Figure 7.3.a). The second type represents a narrow gap automated weld with weld bevel opening angle equal to 10° (Figure 7.3.b). Both have a root opening of 5.0 mm. A weld cap reinforcement is also modeled. This semi circular geometrical reinforcement has a height of 1.0 mm for both weld types. It should be noted that only cracks located at the root weld metal centre line are considered.

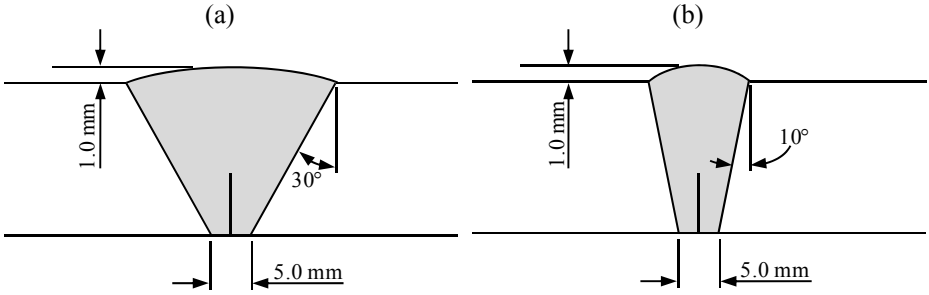

Figure 7.3. Investigated weld bevel geometries: wide V-shaped bevel (a) and narrow gap bevel (b)

7.2.5. Simulation matrix

Based on the different variables described in the previous sections, a test matrix has been composed for the presented constraint analysis. An overview of all simulated configurations is provided in Table 7.1, representing a total of 161 simulations.

Table 7.1. Overview of simulated configurations

pipe dimensions		defect dimensions		material properties		weld bevel profile		specimen type	
D	t	a	$2c$	n	MM_{YS}	narrow	wide	CWP	pipe σ_{hoop}/σ_0
[mm]	[mm]	[mm]	[mm]	[-]	[%]	[-]	[-]	[-]	[%]
762	15	3.0	25	10	-	-	-	x	0 - 100[1]
762	15	4.5	25	10	-	-	-	x	0; 80
762	15	6.0	25	10	-	-	-	x	0; 80
762	15	7.5	25	10	-	-	-	x	0; 80
762	15	3.0	50	10	-	-	-	x	0; 80
762	15	3.0	75	10	-	-	-	x	0; 80
762	15	3.0	100	10	-	-	-	x	0; 80
1016	15	3.0	25	10	-	-	-	x	0; 80
1270	15	3.0	25	10	-	-	-	x	0; 80
762	15	4.5	75	10	-	-	-	x	0; 80
1016	15	4.5	75	10	-	-	-	x	0; 80
1270	15	4.5	75	10	-	-	-	x	0; 80
762	15	3.0	25	5	-	-	-	x	0; 80
762	15	3.0	25	15	-	-	-	x	0; 80
762	15	3.0	25	20	-	-	-	x	0 - 100[1]
762	15	3.0	25	10	-20 - +50[2]	x	x	x	0
762	15	3.0	50	10	-20 - +50[2]	x	x	x	0
762	15	7.0	50	10	-20 - +50[2]	x	x	x	0

[1] Pressure levels representing relative hoop stresses between 0% and 100% have been simulated in steps of 10%.
[2] Mismatch level has been changed in steps of 10%.

7.2.6. Constraint calculations

For a detailed description of the calculation method used for the constraint parameters, the reader is referred to Chapter 2. In brief, the following definitions are considered:

$$Q = \frac{\sigma_{\theta\theta} - \sigma_{\theta\theta;ref}}{\sigma_0} \qquad \bar{r} = r/(J/\sigma_0) = 2 \qquad \theta = 90° \tag{7.2}$$

$$Q_m = \frac{\sigma_m - \sigma_{m;ref}}{\sigma_0} \qquad \bar{r} = r/(J/\sigma_0) = 2 \qquad \theta = 90° \tag{7.3}$$

$$\Delta Q = \frac{\left|Q_{\bar{r}=1} - Q_{\bar{r}=5}\right|}{4} \tag{7.4}$$

$$h = \frac{\sigma_m}{\sigma_e} \qquad \bar{r} = r/(J/\sigma_0) = 2 \qquad \theta = 90° \tag{7.5}$$

Recall that the angle θ is defined relative to the crack plane, perpendicular to this plane (Figure 7.4.a). Furthermore, both the middle of the crack ($\varphi = 0$, Figure 7.4.b) and the surface ends of the crack (approx. $\varphi = 90°$) are considered. The middle of the crack is known to exhibit the highest crack driving force for long and shallow defects and is therefore believed to govern fracture [7.18].

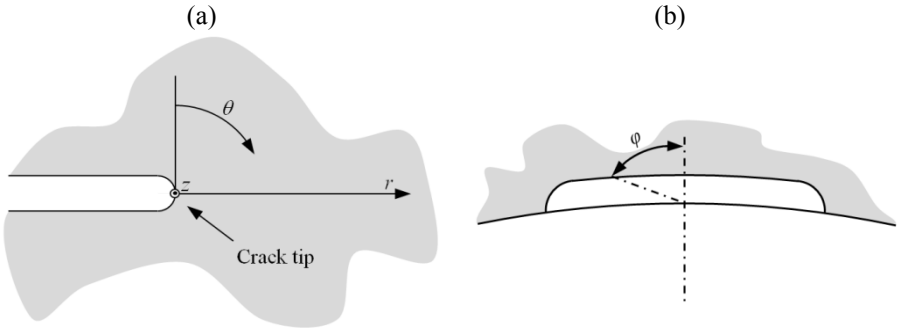

Figure 7.4. Definition of location relative to crack tip (a) and along crack front (b)

Within the remainder of this chapter, only Q-values will be reported unless significant differences between the different constraint parameters have been observed. Eventually, a comparison between the different constraint parameters is also presented.

7.3. Results and discussion

Within the following subsections the influence of different parameters (e.g. crack depth) on the evolution of the constraint ahead of the crack tip is discussed. These analyses are carried out on pressurized and unpressurized pipes and on CWP specimens. Representative results are shown for the sake of clarity, exceptions are explicitly highlighted. In all cases, the constraint is evaluated up to J / σ_0-values equal to two. For these values, remote plastic straining is guaranteed. By means of example, the evolution of J / σ_0 is shown as function of the uniform strain remote from the cracked ligament for a CWP and a pipe specimen (Figure 7.5).

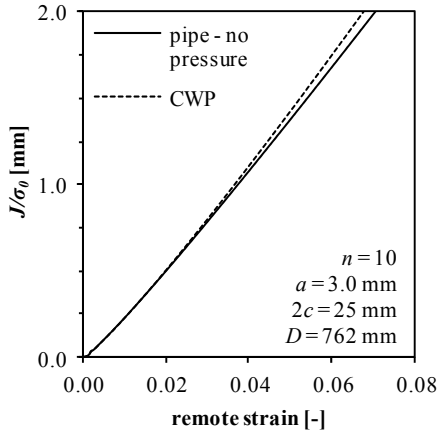

Figure 7.5. Example crack driving force curves for CWP and pipe specimens

7.3.1. Selection of reference stress field

The crack tip constraint is studied at both the middle of the crack and at the surface ends of the crack. For these locations, the validity of the *J-Q* theory is checked based on the magnitude of the ΔQ values. Two types of reference fields have been considered in this paper, namely the plane strain and plane stress fields obtained from MBL analyses. These fields differ both in magnitude and in shape (Figure 7.6). The plane stress reference field has a lower magnitude and appears flatter as function of the normalized distance ahead of the crack tip. Consequently, the plane strain solution represents a higher constraint condition.

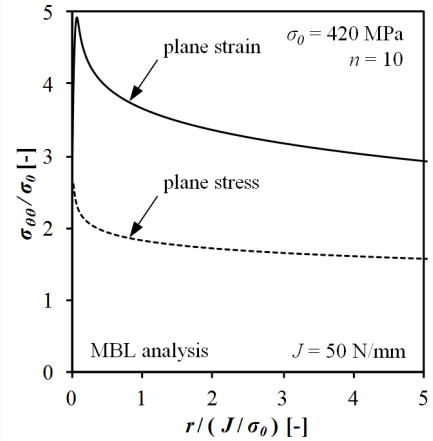

Figure 7.6. Plane stress and plane strain crack tip stress fields obtained from MBL analysis

First, the ΔQ values are calculated for the crack tip stress fields at the middle of the crack for pipe specimens ($\varphi = 0°$). Considering the plane stress crack tip stress field as a reference field, the ΔQ values clearly exceed the critical value of 0.1 for the validity of the *J*-*Q* calculations (Figure 7.7.a) [7.3, 19]. This implies that the actual crack tip stress fields are not parallel to the reference crack tip stress field. In contrast, when considering the plane strain solution for the reference stress field, the ΔQ values remain limited for almost all loading levels. Only at very low load levels, the ΔQ values exceed the critical value of 0.1, attributed to the initial crack tip blunting. Second, the crack tip stress fields at the surface ends of the crack are studied ($\varphi \approx 90°$). In this case, only the plane stress reference stress field results in ΔQ values below 0.1 (Figure 7.7.b). As a result, the $Q_{(m)}$ values reported in the remainder of this chapter are, unless explicitly specified otherwise, defined relative to the plane strain solution for the middle of the crack and the plane stress solution for the surface ends of the crack.

To accommodate a comparison of these locations, the constraint at both locations is calculated relative to the same reference stress field, i.e. the plane strain solution. As a result, the *J*-*Q* trajectory for the surface end of the crack is shifted compared to the situation using a plane stress solution (Figure 7.8.a). Relative to the constraint at the surface ends of the crack, the constraint at the middle of the crack is higher. This observation is additionally supported by the evolution of the triaxiality parameter (Figure 7.8.b). Similar observations have been made for all studied defects. Given the lower crack driving force at this location along the crack front, the occurrence of ductile crack extension in the circumferential direction is thus unlikely to occur for the simulated defects. This corresponds well with the experimental observations of uniaxially loaded part-through defects [7.20].

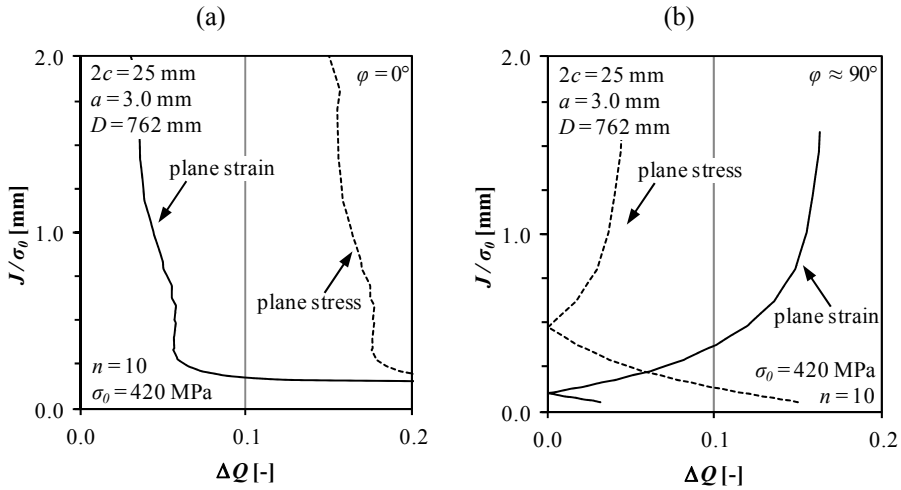

Figure 7.7. Calculated ΔQ values for plane strain and plane stress reference stress fields at middle of the crack (a) and at surface ends of the crack (b) for unpressurized pipe

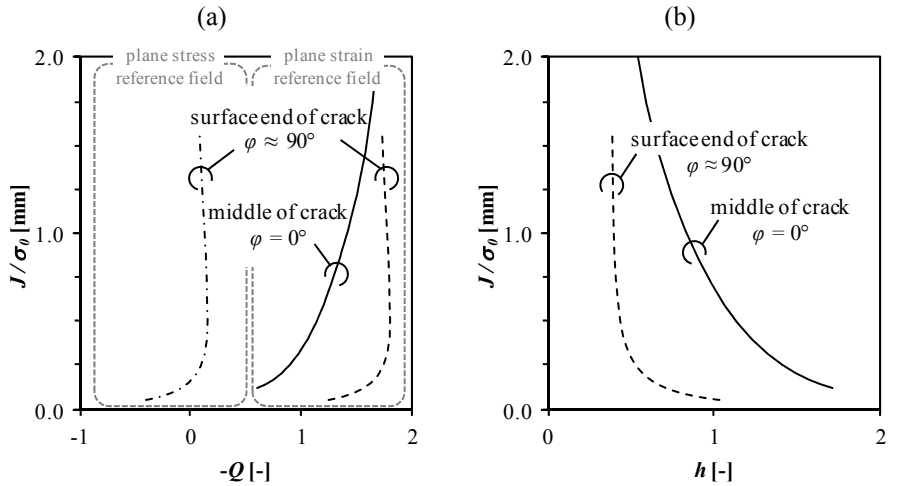

Figure 7.8. Constraint at surface ends of the crack and center of the crack based on Q-parameter and plane strain reference stress field (a) and triaxiality parameter h (b)

7.3.2. Influence of internal pressure

The internal pressure effect was studied for both the middle of the crack and the ends of the crack front near the free surface. First, the focus is on the middle of the crack. Looking at the resulting J-Q trajectories, no significant differences are observed between the various internal pressure levels (Figure 7.9.a); all show a similar loss of constraint upon the development of plasticity. Therefore it is concluded that, regarding the in-plane constraint, the degree of biaxiality in the loading situation has no influence.

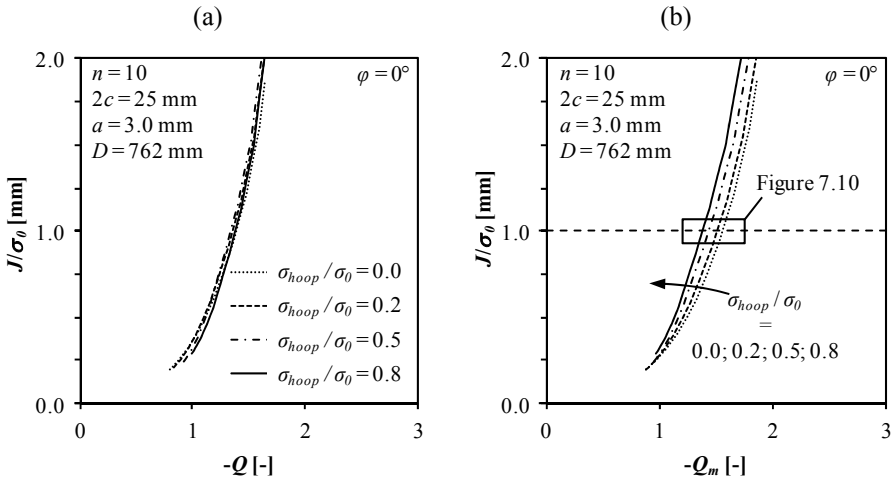

Figure 7.9. Resulting J-Q (a) and J-Q_m (b) trajectories for varying internal pressure levels

In contrast, when the out-of-plane constraint is more explicitly accounted for, e.g. by using the constraint parameter Q_m, a clear increase of the constraint is observed as the pressure level increases (Figure 7.9.b). In Figure 7.10 the different constraint parameters are evaluated at a fixed crack driving force level (i.e. $J / \sigma_0 = 1$) for varying internal pressure levels. Regardless the considered material, the constraint increase appears approximately linearly proportional to the internal pressure level when taking into account the out-of-plane constraint. These observations are in agreement with the results of Bass et al. [7.21], who also reported that the out-of-plane constraint is influenced by the biaxial loading level in contrast to the in-plane constraint.

Elaborating on the influence of the hoop stress, the influence of the flaw location is examined. Inner diameter defects differ from outer diameter defects as for the latter the pressure is not acting on the crack faces. No significant difference is observed between the (out-of-plane) constraint evolutions for both defect locations (Figure 7.11.a). This suggests that pressure acting on the crack faces does not influence the constraint. This is confirmed by comparing simulations for internal diameter cracks with and without pressure being applied on the crack faces (Figure 7.11.b). Accordingly, the influence of internal pressure relates to the hoop stress rather than additional longitudinal or radial stress components.

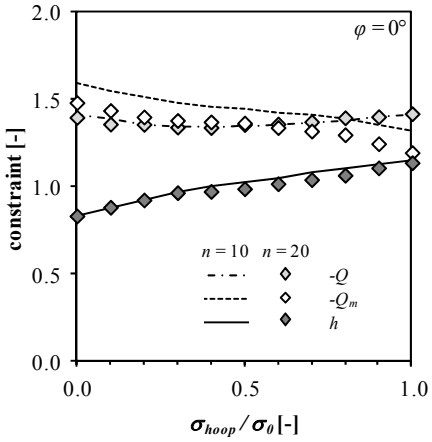

Figure 7.10. Influence of internal pressure on constraint parameters

Second, the constraint is studied at the surface ends of the crack. Here, the Q-parameter again shows a limited dependency on the internal pressure level. In contrast, the parameters that explicitly account for the out-of-plane constraint, Q_m and h, indicate an increase of the constraint with increase of the internal pressure level (Figure 7.12). The magnitude of this constraint increase is comparable to the one observed at the middle of the crack, hence no additional crack extension in the circumferential direction is expected based on these constraint considerations.

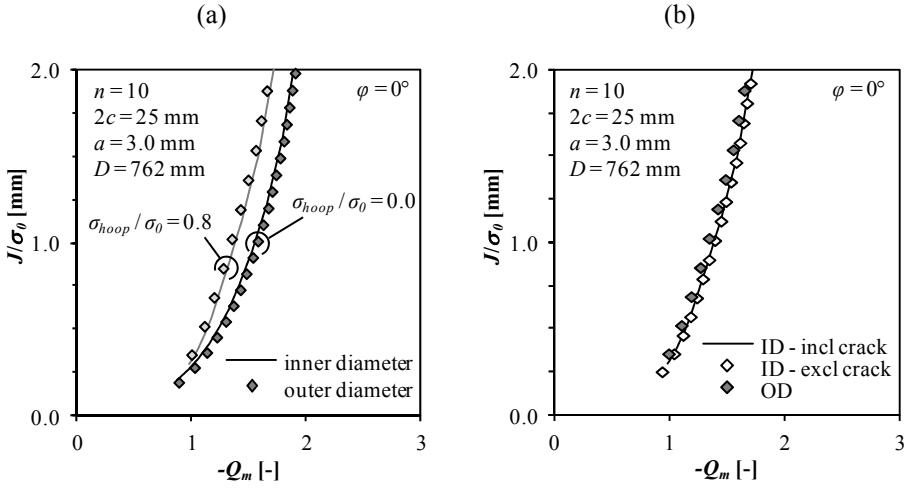

Figure 7.11. Influence of internal pressure on out-of-plane constraint:
comparison of defect location (a) and
influence of pressure applied to the crack faces (b)

Focusing on the current results, the observed effect can be explained by noting that, with increasing internal pressure, the hoop stresses increase. Hence, the out-of-plane stresses gain importance, resulting in higher Q_m and h values. Remark that this effect is not necessarily captured by Q, as this parameter only accounts for hoop stresses via the Poisson effect. This effect is of a secondary nature and may be within the accuracy range of the finite element calculations. Focusing on ductile fracture, the

Q_m and h parameters are however believed to be more relevant, in contrast to cleavage fracture where the in-plane constraint is of major importance [7.22]. Accordingly, the resistance curves of pressurized pipes are expected to be lower than those obtained from unpressurized pipes. However, based on available literature reports on both experimental and numerical work, only a minor decrease is observed in the *J*-*R* curve [7.23, 24]. This difference is most likely attributed to the limitations of the current modeling approach. The constraint level was not studied inside the large deformation zone just in front of the crack tip. The small strain assumption made does not allow investigating this feature. In addition, a potential minor difference can be neglected as scatter in the material properties is likely to influence the resistance curves more significantly [7.25].

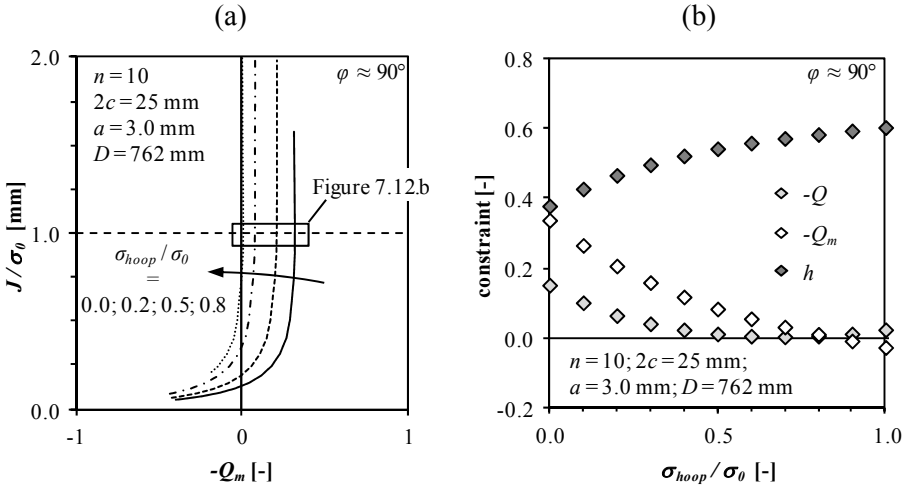

Figure 7.12. Influence of internal pressure on constraint parameters at surface ends of crack (a) and at middle of the crack (b)

7.3.3. Influence of curved wide plate geometry

Comparing the constraint evolutions in CWP specimens and unpressurized pipes at the middle of the crack, it is clear that both show a similar loss of constraint upon loading (Figure 7.13). This statement holds particularly for small defects (a x $2c$ = 3.0 x 25 mm²). With increasing defect dimensions, the difference between CWP and pipe specimens increases, regardless the considered constraint definition. Shown in Figure 7.13.a and b is the influence of the relative crack depth on the *J*-*Q* and *J*-*h* trajectory respectively. For shallow cracks (a/t = 0.2) the difference between pipe and CWP specimens is limited. In contrast, deep cracks (a/t = 0.4) indicate a higher constraint in the CWP specimens, in particular at lower load levels. Given the similarity between the trends described by the different constraint parameters, solely the *Q*-parameter will be considered in the remaining comparisons of pipe to CWP specimens. It is furthermore observed that the constraint increases for CWP specimens with increasing crack lengths (Figure 7.13.c). This contrasts with the unpressurized pipe specimens, which show no dependence of the constraint trajectories on crack length.

Another factor potentially influencing the constraint in the CWP specimen is the pipe diameter. It is observed that CWP specimens extracted from larger diameter pipes show an increased raise of the constraint during the early loading stages (Figure 7.13.d). In contrast, the constraint evolution in pipe specimens appears to be independent of diameter.

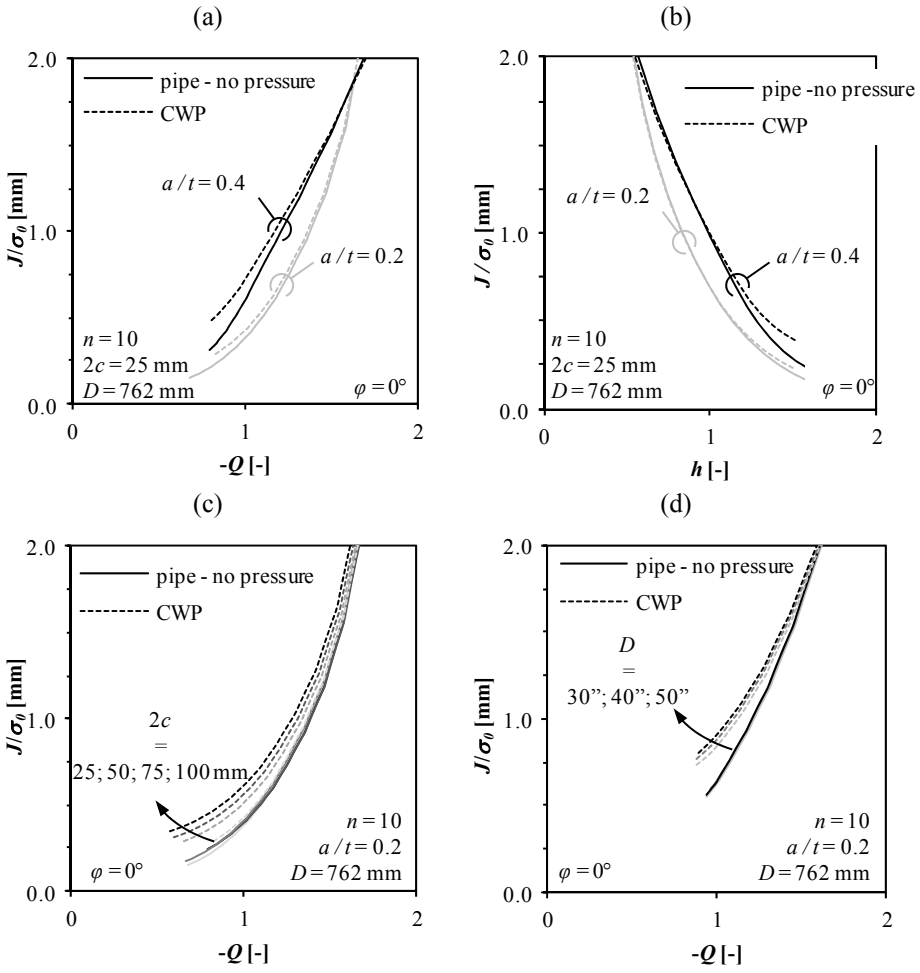

Figure 7.13. Influence of geometrical parameters on constraint in unpressurized pipe and CWP specimens: influence of relative crack depth on *J-Q* trajectory (a) and *J-h* trajectory (b) and influence of crack length (c) and pipe diameter (d) on *J-Q* trajectory

In an attempt to clarify the above observations, two effects are distinguished. First, local bending originates from a difference between the centre of the applied force and the centre of the resulting force in the cracked ligament [7.26]. Second, the presence of axial symmetry in pipe specimens increases the stiffness of the specimens and hence prevents bending.

The first effect is illustrated by examining the stress distribution in the remaining ligament ($b_0 = t - a_0$). Figure 7.14.a indicates that CWP specimens are more susceptible to bending than unpressurized pipe specimens with identical defect dimensions. This bending creates higher stresses near the crack tip and lower stresses at the back side of the crack (near $r/b_0 = 1$). Since the constraint calculations are based on the stress field's magnitude in the vicinity of the crack tip, the increased constraint in CWP specimens is attributed to an increased bending. This is first confirmed by Figure 7.14.b for CWP specimens. Remark a minor discontinuity in the stress field around $r/b_0 = 0.7$. This discontinuity is attributed to the transition between plastic and elastic deformation. On the other hand, the mesh was selected to obtain an accurate description of the stresses near the crack tip rather than the back side of the crack, resulting in a relatively coarse mesh in this region. The higher bending of the CWP specimens is secondly confirmed by higher ΔQ values for the CWP specimens relative to pipes (Figure 7.15).

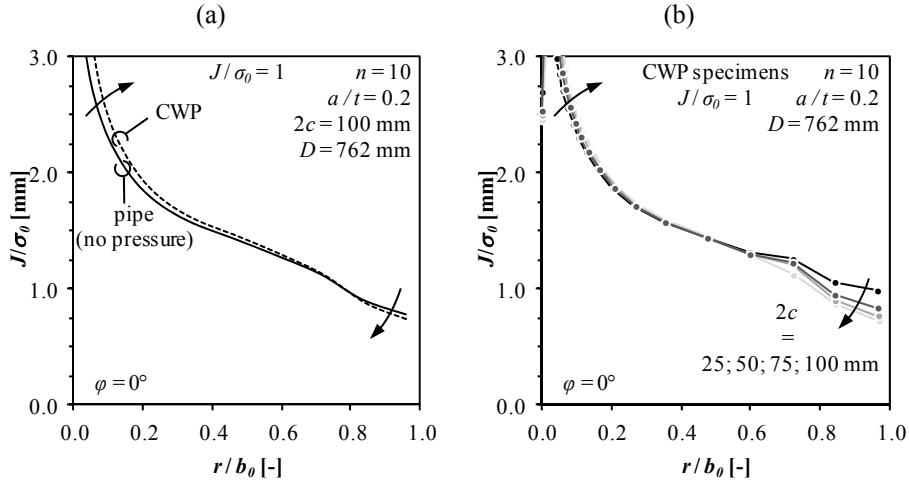

Figure 7.14. Stress profile in remaining ligament: comparison of CWP specimen to unpressurized pipe (a) and influence of defect length in CWP specimens (b)

The second effect mainly explains the observed influence of the pipe diameter. Regarding the unpressurized pipe specimens, the centre of the resulting force will, within the investigated range of defect sizes, never shift significantly from the pipe axis. Hence, the constraint trajectories remain relatively independent of the pipes' diameter. In contrast, the CWP specimens lack axial symmetry and are therefore likely to bend more. This bending effect is most pronounced for CWP specimens from large diameter pipes, as the absence of curvature decreases the bending stiffness. Consequently, the bending stresses increase and subsequently the constraint.

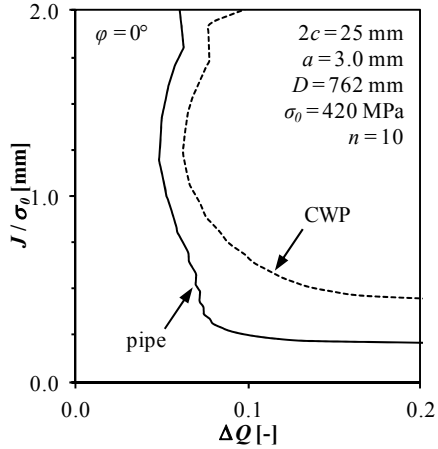

Figure 7.15. Calculated ΔQ values for pipe and CWP specimen with identical defect dimensions and material properties

In addition to the middle of the crack, the constraint is evaluated at the surface ends of the crack. Given the symmetry along the length axis of the specimens, both for the CWP and the pipe specimens, no difference in bending is present that, at the surface end of the crack, potentially results in a constraint difference between both specimens. Accordingly, it should not surprise that the constraint evolution at these points is very similar for pipe and CWP specimens. By means of example, the *J*-*Q* trajectories are plotted for specimens with varying initial defect depths (Figure 7.15.a) and defect lengths (Figure 7.16.b).

If the CWP test and full scale test were used for obtaining the tearing resistance, it is expected from the above observations and explanations that the resistance curve for the CWP specimen is lower than the one for the pipe specimen. This is in agreement with experimental data published by Cheng et al. [7.27]. Accordingly, it is concluded that CWP testing slightly underestimates the fracture toughness as compared to the full scale behaviour, especially for large defect sizes and/or large diameter pipes.

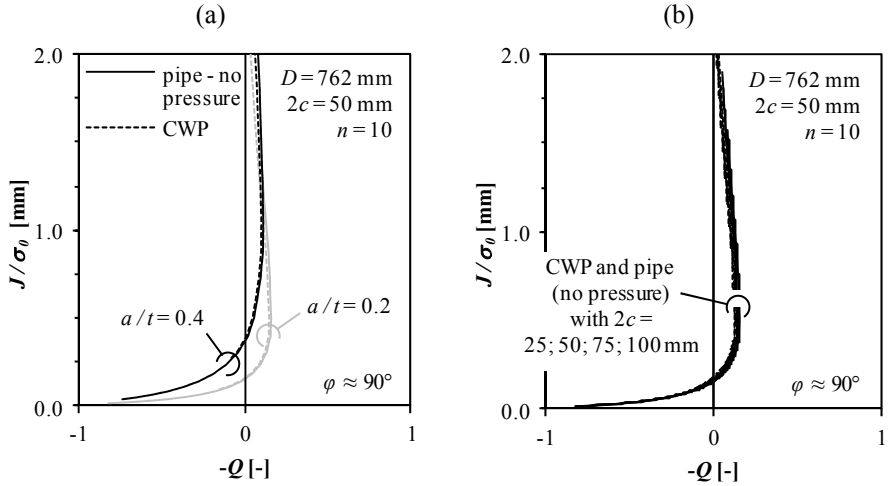

Figure 7.16. Influence of defect depth (a) and length (b) on constraint evolution at surface ends of a defect in pipe and CWP specimens

7.3.4. Influence of weld metal mismatch

The *J*-*Q* calculations for the weld metal strength mismatched configurations are based on a comparison with the MBL solutions of materials with similar yield strength as the material where the crack is located, i.e. the weld. A similar dependency of the constraint evolution on the mismatch level is observed for all constraint parameters, though only the *J*-*Q* trajectories are shown in this section. A higher mismatch level (overmatch) results in a decrease of the constraint, whereas a lower mismatch level (undermatch) increases the constraint (Figure 7.17.a). This is understood as, for higher strength weld metals, the plastic zone originating from the crack tip develops more easily in the adjacent softer base metal. This plastic deformation results in a relaxation of the stresses near the crack tip, hence the constraint lowers. In contrast, for undermatching welds limited plastic deformation takes place in the adjacent (high strength) base metal. Accordingly, the deformation is confined to the weld metal surrounding the crack tip and therefore the hydrostatic stresses increase relative to the strength matching (homogeneous) situation. This trend is in agreement with literature [7.28-30].

The above dependency is most pronounced at higher crack driving force levels. Although valid *Q*-calculations have not always been obtained at low crack driving force levels (ΔQ values exceeding 0.1), the *J*-*Q* curves are likely to merge at lower crack driving force levels. This observation is understood as the influence of weld metal strength mismatch only becomes relevant once the plastic zone, developing from the crack tip, reaches the fusion line and interacts with the adjacent base material [7.30].

Another relevant observation relates to the similarity between the constraint evolution in unpressurized pipe and CWP specimens (Figure 7.17.b). This allows concluding that, for a wide variety of strength mismatch conditions, the CWP specimens remain a slightly conservative alternative to full scale testing.

The weld width is expected to influence the constraint evolution. Focusing on strength overmatch situations, an increasing weld width will shield the crack tip stress fields from the adjacent lower strength material and it will take longer before the plastic zone reaches the fusion line. Accordingly, the beneficial effect going with strength overmatch is expected to decrease and to be postponed to higher crack driving force levels. Figure 7.18.a shows a comparison between a narrow and wide weld as defined in Figure 7.3. As expected, the wide weld shows less loss of constraint for increasing mismatch levels. This difference is highlighted by comparing the *Q*-values at a constant load level (Figure 7.18.b). The dependency of *Q* to strength mismatch is stronger for smaller welds.

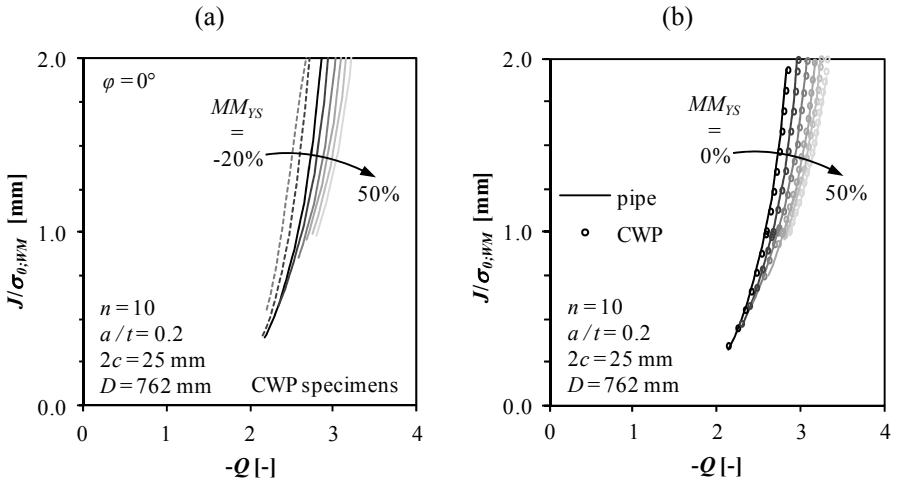

Figure 7.17. Influence of weld strength mismatch on constraint: influence of mismatch level (a) and comparison of CWP to pipe specimens (b)

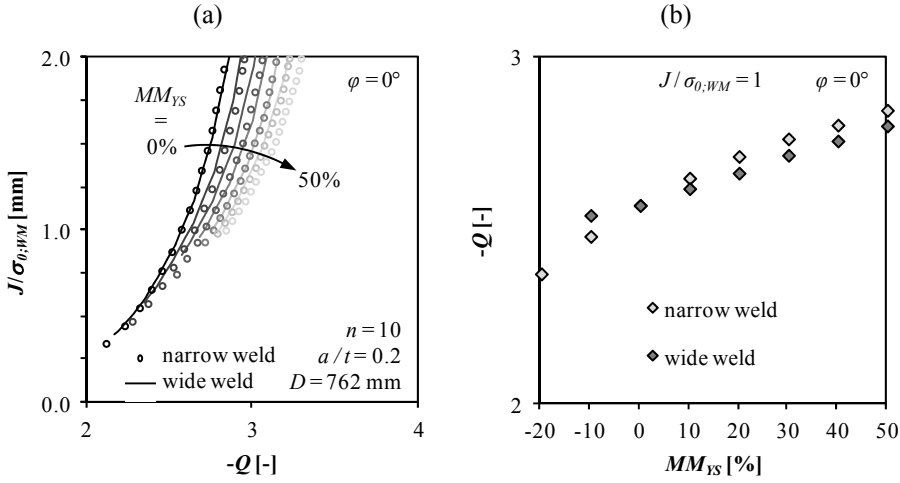

Figure 7.18. Influence of weld bevel geometry on *J*-*Q* trajectories: global overview (a) and detail at fixed load level $J / \sigma_{0;WM} = 1$ (b)

Bearing in mind that the constraint level relates to the tearing resistance, the following is concluded. Assuming homogeneous material properties of the tested specimens, an increase of the mismatch level yields a higher tearing resistance. In contrast, undermatching causes a decrease of the tearing resistance.

7.3.5. Comparison of constraint parameters

In the preceding sections, different parameters have been considered for the evaluation of the constraint ahead of the crack tip. In most cases, these parameters predict similar effects. It is therefore not surprising that these parameters can be uniquely related to each other. For the stress triaxiality parameter h and the parameter Q_m, this relationship is approximately independent of the considered specimen type (i.e. pipe or CWP specimen) and loading mode (i.e. with or without internal pressure). The relationship between both parameters however depends on the strain hardening properties of the materials (Figure 7.19.a). More specifically, the strain hardening coefficient n results in a shift of the correlation function. The slope of the correlation remains constant, implying that the constraint loss predicted by both parameters is similar. Moreover, the out-of-plane constraint is captured similarly by both the stress triaxiality h and the Q_m-parameter. Therefore, it is concluded that the observed dependency does not limit the application of either of both parameters in the framework of the presented comparisons as the main aim was to compare different specimen configurations and loading conditions, assuming identical material properties for the different specimens. Hence, the presented results in terms of h or Q_m can be extrapolated to materials with a different strain hardening behaviour.

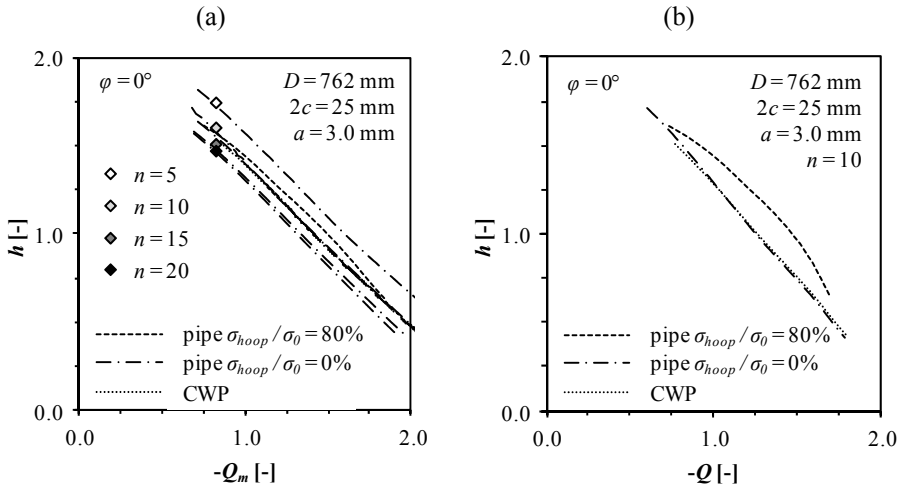

Figure 7.19. Relation between Q_m and h parameters (a) and Q and h parameters (b)

On the contrary, the relationship between the Q-parameter and the stress triaxiality depends on the loading condition, namely the internal pressure (Figure 7.19.b). This is not surprising as the Q-parameter was hardly influenced by the internal pressure level, in contrast to the stress triaxiality (§7.3.2). This difference is attributed to the out-of-plane constraint effects, which are not well captured in case of the Q-parameter. For some applications, this is of minor interest (e.g. cleavage fracture). However, within the current study ductile failure is of primary interest. As it is well known that the out-of-plane constraint influences the material's behaviour in this case, preference should therefore be given to a parameter that does account for the out-of-plane effects.

7.4. Conclusions

Based on an extensive set of finite element simulations, the crack tip stress fields and resulting *J-Q, J-*Q_m and *J-h* trajectories have been analyzed in (pressurized) pipe and CWP specimens. From these simulations it is concluded that:

- Internal pressure does not affect the in-plane constraint *Q*, only the out-of-plane constraint is slightly increased with increasing pressure level. However, to an extent that can be questioned to be relevant, as scatter from material testing is likely to influence the obtained tearing resistance approximately to the same extent.
- The constraint evolution in both homogeneous and weld strength mismatched configurations are comparable for pipe and CWP specimens. Although the CWP specimens remain slightly conservative.
- Weld strength mismatch influences the constraint evolution in pipe specimens. Overmatching welds show a higher loss of constraint than matching (homogeneous) and undermatching welds.
- To characterize the constraint in case ductile failure is studied, the Q_m and *h* parameter appear equivalent. Contrary, the *Q*-parameter underestimated the impact of the multi-axial loading conditions.

7.5. Bibliography

[7.1] O'Dowd, N. P., and Shih, C. F., 1991, "Family of Crack-Tip Fields Characterized by Triaxiality Parameter: Part I - Structure of Fields", Journal of Mechanics and Physics of Solids, 39, pp. 989-1015.

[7.2] O'Dowd, N. P., and Shih, C. F., 1992, "Family of Crack-Tip Fields Characterized by Triaxiality Parameter: Part II - Application", Journal of Mechanics and Physics of Solids, 40, pp. 939-963.

[7.3] Dodds, R. H., Shih, C. F., and Anderson, T. L., 1993, "Continuum and Micromechanics Treatment of Constraint in Fracture", Office of Nuclear Regulatory Research, Washington D.C.

[7.4] Cravero, S., Bravo, R. E., and Ernst, H. A., 2008, "Constraint Evaluation and Effects on J-R Resistance Curves for Pipes under Combined Load Conditions", International Offshore and Polar Engineering Conference, Vancouver, British Columbia, Canada, pp. 149-156.

[7.5] Henry, B. S., and Luxmoore, A. R., 1997, "The Stress Triaxiality Constraint and the Q-Value as a Ductile Fracture Parameter", Engineering Fracture Mechanics, 57, pp. 375-390.

[7.6] Hebel, J., Hohe, J., Friedmann, V., and Siegele, D., 2007, "Experimental and Numerical Analysis of in-Plane and out-of-Plane Crack Tip Constraint Characterization by Secondary Fracture Parameters", International Journal of Fracture, 146, pp. 173-188.

[7.7] Yuan, H., and Brocks, W., 1998, "Quantification of Constraint Effects in Elastic-Plastic Crack Front Fields", Journal of Mechanics and Physics of Solids, 46, pp. 219-241.

[7.8] Kibey, S. A., Lele, S. P., Tang, H., Macia, M. L., Fairchild, D. P., Cheng, W., Noecker, R., Wajutelewicz, P. J., Newbury, B., Kan, W. C., and Cook, M. F., 2011, "Full-Scale Test Observations for Measurement of Tensile Strain Capacity of Welded Pipelines", International Offshore and Polar Engineering Conference, Maui, Hawaii, USA, pp. 660-667.

[7.9] Denys, R., and Lefevre, A. A., 2009, "UGent Guidelines for Curved Wide Plate Testing", Pipeline Technology Conference, Ostend, Belgium, paper n° Ostend2009-110.

[7.10] Hertelé, S., De Waele, W., Denys, R., Verstraete, M., and Van Wittenberghe, J., 2012, "Parametric Finite Element Model for Large Scale Tension Tests on Flawed Pipeline Girth Welds", Advances in Engineering Software, 47, pp. 24-34.

[7.11] Cravero, S., and Ruggieri, C., 2005, "Correlation of Fracture Behavior in High Pressure Pipelines with Axial Flaws Using Constraint Designed Test Specimens - Part I: Plane-Strain Analyses", Engineering Fracture Mechanics, 72, pp. 1355-1360.

[7.12] Verstraete, M., De Waele, W., Hertelé, S., Van Minnebruggen, K., and Denys, R. M., 2012, "Constraint Analysis of Curved Wide Plate Specimens", European Conference on Fracture, Kazan, Russia, paper n° 1-9.

[7.13] English, S. A., and Arakere, N. K., 2011, "Effects of the Strain-Hardening Exponent on Two-Parameter Characterizations of Surface-Cracks under Large-Scale Yielding", International Journal of Plasticity, 27, pp. 920-939.

[7.14] Ramberg, W., and Osgood, W. R., 1943, "Description of Stress-Strain Curves by Three Parameters", National Advisory Committee for Aeronautics, Washington.

[7.15] Hertelé, S., De Waele, W., Denys, R., and Verstraete, M., 2012, "Full-Range Stress Strain Behaviour of Contemporary Pipeline Steels: Part I. Model Description", International Journal of Pressure Vessels and Piping, 92, pp. 34-40.

[7.16] Hertelé, S., De Waele, W., Denys, R. M., and Verstraete, M., 2012, "Full-Range Stress Strain Behaviour of Contemporary Pipeline Steels: Part II. Estimation of Model Parameters", International Journal of Pressure Vessels and Piping, 92, pp. 27-33.

[7.17] Canadian Standards Association, 2011, Z662 - 11: Oil and Gas Pipeline Systems.

[7.18] Brickstad, B., and Sattari-Far, I., 2000, "Crack Shape Developments for LBB Applications", Engineering Fracture Mechanics, 67, pp. 625-646.

[7.19] O'Dowd, N. P., and Shih, C. F., 1995, "Two-Parameter Fracture Mechanics: Theory and Applications", ASTM, Standard Technical Publication 1207.

[7.20] Denys, R., and Lefevre, A. A., 2009, "Failure Characterization of a Girth Weld with Surface-Breaking Flaw under Tensile Load", Pipeline Technology Conference, Ostend, Belgium, paper n° Ostend2009-111.

[7.21] Bass, B. R., Mcafee, W. J., Williams, P. T., and Pennell, W. E., 1999, "Fracture Assessment of Shallow-Flaw Cruciform Beams Tested under Uniaxial and Biaxial Loading Conditions", Nuclear Engineering and Design, 188, pp. 259-288.

[7.22] Neimitz, A., and Galkiewicz, J., 2006, "Fracture Toughness of Structural Components: Influence of Constraint", International Journal of Pressure Vessels and Piping, 83, pp. 42-54.

[7.23] Ostby, E., and Hellesvik, A. O., 2008, "Large-Scale Experimental Investigation of the Effect of Biaxial Loading on the Deformation Capacity of Pipes with Defects", International Journal of Pressure Vessels and Piping, 85, pp. 814-824.

[7.24] Tyson, W. R., Shen, G., and Roy, G., 2007, "Effect of Biaxial Stress on ECA of Pipelines under Strain-Based Design", International Offshore and Polar Engineering Conference, Lisbon, Portugal, pp. 3107-3113.

[7.25] Shen, G., and Tyson, W. R., 2009, "Evaluation of CTOD from J-Integral for SE(T) Specimens", Pipeline Technology Conference, Ostend, Belgium, paper n° Ostend2009-004.

[7.26] Hertelé, S., De Waele, W., and Denys, R. M., 2011, "Development of an Analytical Reference Stress Equation for Inner-Diameter Defected Curved Plates in Tension", International Journal of Pressure Vessels and Piping, pp. 256-261.

[7.27] Cheng, W., Tang, H., Gioielli, P. C., Minnaar, K., and Macia, M. L., 2009, "Test Methods for Characterization of Strain Capacity: Comparison of R-Curves from SENT/CWP/FS Tests", Pipeline Technology Conference, Ostend, Belgium, paper n° Ostend2009-040.

[7.28] Burstow, M. C., Howard, I. C., and Ainsworth, R. A., 1998, "The Effects of Material Strength Mismatching on Constraint at the Limit Load of Welded Three-Point Bend Specimens", International journal of fracture, 89, pp. 117-142.

[7.29] Boothman, D. P., Lee, M. M. K., and Luxmoore, A. R., 1999, "The Effects of Weld Mismatch on J-Integrals and Q-Values for Semi-Elliptical Surface Flaws", Engineering Fracture Mechanics, 64, pp. 433-458.

[7.30] Burstow, M. C., Howard, I. C., and Ainsworth, R. A., 1998, "The Influence of Constraint on Crack Tip Stress Fields in Strength Mismatched Welded Joints", Journal of Mechanics and Physics of Solids, 46, pp. 845-872.

Chapter 8

–

Tensile Strain Capacity of CWP Specimens versus (Pressurized) Pipes

8.1. Introduction

The use of CWP tests to evaluate the tensile strain capacity of pipes containing a circumferentially oriented defect was introduced in the first chapters. Recall that this type of test has been used since the early 1980's and its results formed the baseline for development of the EPRG Tier 2 guidelines [8.1]. The tensile strain capacity of a CWP specimen is implicitly assumed conservative with respect to that of a pipe without internal pressure. However, the presence of internal pressure is known to reduce the tensile strain capacity of pipe specimens drastically [8.2, 3]. A direct, analytical quantification of this tensile strain capacity reduction is currently inexistent for CWP specimens.

To address the above concern, this chapter aims at presenting analytical expressions that allow comparing the tensile strain capacity of:

- CWP specimens to unpressurized pipes (CWP versus up)
- pressurized with unpressurized pipes (pp versus up)
- pressurized pipes to CWP specimens (pp versus CWP)

As such, distinction is made between geometrical influences (CWP versus unpressurized pipes) and pressure effects (unpressurized versus pressurized pipes) before evaluating the actual relationship between CWP specimens and pressurized pipes. The latter is quantified by the *pressure correction function*. Given the large number of variables involved, preference is given to finite element simulations for this investigation. The details of this finite element approach and the analytical evaluation of the relative strain capacity are provided in section 8.2. Subsequently, the results of a study on homogeneous (i.e. non-welded) specimens are presented in section 8.3. Based on the outcome of this study, a second test matrix is composed, focusing on welded specimens and their specific particularities (e.g. strength mismatch and misalignment). The resulting conversion formulae and their application is discussed in section 8.4.

8.2. Correction function approach

This section first provides a description of the finite element models, followed in the second section by a comparison of the simulated crack driving force curves with data available in literature. Subsequently, the application of the tangency criterion for the evaluation of the tensile strain capacity is outlined. The relative strain capacity is introduced in the final section, along with the statistical framework used to identify the most significant parameters.

8.2.1. Finite element models

For the evaluation of the tensile strain capacity, finite element models (ABAQUS^{TM} version 6.11) of three different specimens are used, namely CWP specimens, unpressurized pipes and pressurized pipes. These finite element models are all based on the parametric Python script developed in the framework of the PhD dissertation of S. Hertelé [8.4]. As a result, the mesh design and the post processing of e.g. CTOD is identical for the different specimens. Recall that the same finite element models have been used in the previous chapter, though a mesh convergence study indicated a lower mesh density suffices for an accurate extraction of the CTOD and

remote strains in comparison to the mesh density needed for the extraction of the crack tip stress fields. For the CWP specimens, for instance, this resulted in a typical mesh of 13000 elements, in contrast to the 35000 elements for the constraint analyses.

Figure 8.1 presents a schematic overview of the simulated CWP specimens and pipes. For the CWP specimens, the geometry and instrumentation (i.e. location of the remote strain measurement, ε_{remote}) is adopted from the UGent guidelines for CWP testing [8.5]. For the pipe specimens, a length-to-diameter ratio of four was selected. In accordance to literature, this suffices to obtain crack driving force curves independent of the pipe's boundary conditions [8.6, 7]. The remote strains are derived from the relative displacement between two points located at distances D + 100 mm and D – 100 mm with respect to the location of the crack.

All specimens contain the same circumferential defect, which is – unless specifically mentioned - located along the inner diameter and has an initially blunted root radius of 0.075 mm. This defect has a constant depth (a) with semi-circular ends. The defect length ($2c$) is defined as the defect's arc length at the free surface. For welded specimens, the defect is located at the weld metal center line.

The imposed axial displacement is transferred to the specimens through rigid end blocks that are connected to the actual specimens via tie constraints. For the pressurized pipe specimens, the pressure is applied prior to the axial deformation. This is believed to represent actual loading conditions for onshore applications.

8.2.2. Influence of internal pressure – validation

The considered finite element approach was thoroughly validated for CWP specimens. The crack driving force was compared to both experimental and numerical data [8.4]. For pipe specimens, in contrast, no experimental validation was performed. Such validation requires a detailed description of the tested pipe (geometry, stress strain properties, tearing resistance, …). Unfortunately, no such descriptions have been found in literature. Therefore, the simulated crack driving force is compared to numerical data presented in literature [8.7]. In their paper, Jayadevan et al. report on finite element simulations for pipe specimens with steady cracks of varying sizes and with varying internal pressure levels. The dimensions of their pipe specimens correspond to the configurations presented in the previous section. The material's stress strain response is described by a Ramberg-Osgood relation, with a strain hardening exponent $n = 10$ and yield strength of 400 MPa. This material definition was modeled using an incremental plasticity approach, large strain effects have been accounted for.

For unpressurized pipes with varying crack depths, a nice correspondence is observed between the literature results and the simulations discussed in this chapter (Figure 8.2.a). Only for large defect depths and strain levels, deviations are observed. These differences are attributed to the high sensitivity of the results to the post-necking characteristics. A similar, excellent correspondence is observed for simulations of pressurized pipes with varying internal pressure levels (Figure 8.2.b).

Remark that the above confirms that internal pressure has indeed the potential to (drastically) increase the crack driving force and hence reduce the tensile strain capacity.

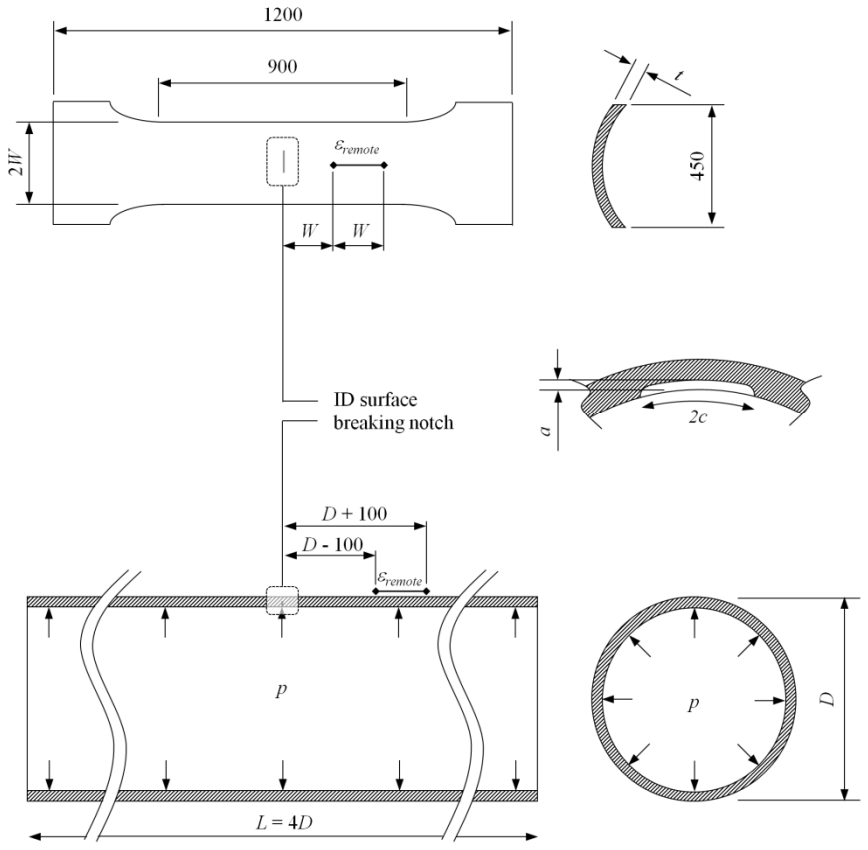

Figure 8.1. Schematic representation of CWP and pipe specimen geometry adopted for the finite element simulations, with indication of location for measurement of remote strain ε_{remote}

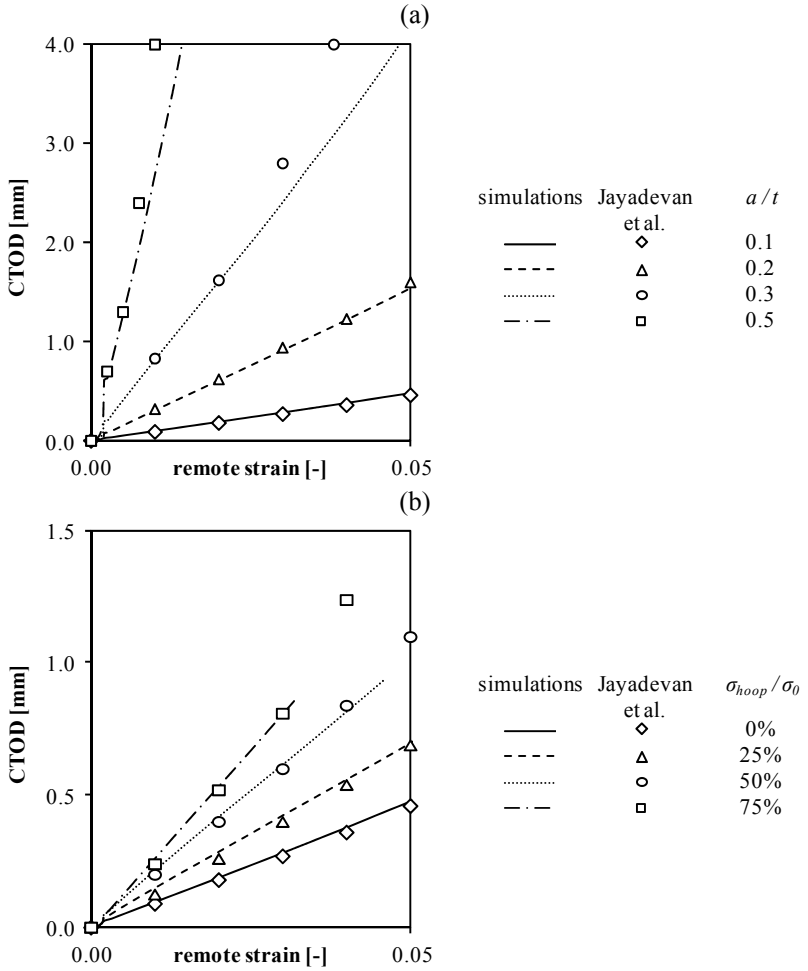

Figure 8.2. Comparison of simulated crack driving force with literature results for unpressurized pipes with varying initial crack depth (a) and for pipes with fixed relative crack depth ($a/t = 0.1$) and varying internal pressure level (b)

8.2.3. Evaluation of tensile strain capacity: tangency approach

To evaluate the tensile strain capacity, the following two failure modes are considered:

- *unstable ductile crack extension* This failure mode is determined by both the tearing resistance of the material and the crack driving force.
- *plastic collapse* The plastic collapse failure mode corresponds to a maximum in the load versus remote strain diagram. This failure mode comprises both net section and gross section (or global) collapse.

To evaluate the strain corresponding to the occurrence of unstable failure, the tangency approach presented in Chapter 1 is adopted. Therefore, the crack driving force curves for different crack depths are first obtained from finite element simulations (Figure 8.3.a). These simulations are performed for steady cracks with depths ranging from the initial crack depth (a_0) up to at least 2.0 mm extra, in steps of 0.5 mm. Following, these crack driving force curves, which present a relation between the CTOD and the remote strain for constant crack depths, are converted to crack driving force curves for constant remote strain levels (black curves in Figure 8.3.b). The latter express the CTOD as a function of the amount of ductile crack extension. The intersections of these curves with the tearing resistance curve (green curve in Figure 8.3.b), give expression to the evolution of the ductile crack extension as the remote strain level increases, $\varepsilon_{crack}(\Delta a)$. This function's maximum value is reached when the crack driving force becomes tangent to the material's tearing resistance, hence the term tangency approach (red dotted curve in Figure 8.3.b).

The maximum strain corresponding to plastic collapse is defined by the maximum of the force versus remote strain diagram for increasing defect depths (Figure 8.3.c). This again results in a critical strain level as function of the ductile crack extension $\varepsilon_{collapse}(\Delta a)$.

Based on these two critical strain functions, the maximum strain capacity ε_{max} is defined as:

- the intersection of the $\varepsilon_{crack}(\Delta a)$ and $\varepsilon_{collapse}(\Delta a)$ curves in case of failure through collapse or,
- the maximum value for $\varepsilon_{crack}(\Delta a)$ in case of failure through unstable ductile crack extension.

The first situation is illustrated for a material with a high tearing resistance (solid black line in Figure 8.3.d), the second for a material with a lower tearing resistance (solid green line in Figure 8.3.d). Note that this approach solely considers ductile crack extension in the through-thickness direction; the crack length remains constant.

(a)
simulated crack driving force curves for constant crack depths

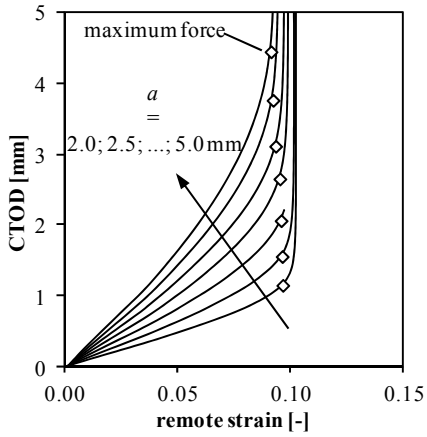

(b)
converted crack driving force curves for constant remote strain levels

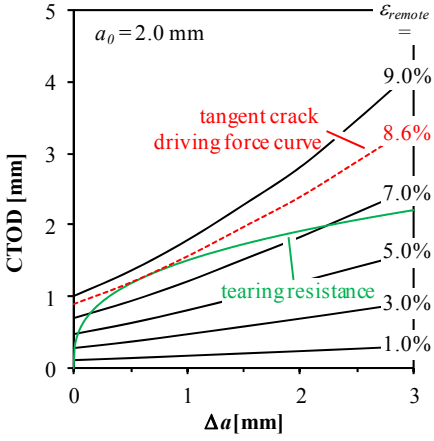

(c)
simulated load versus remote strain curves

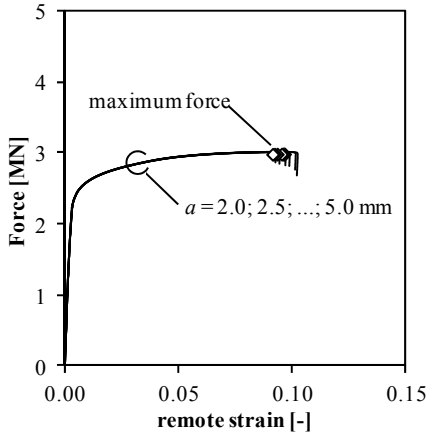

(d)
evaluation of proximity to collapse and fracture as function of remote strain and ductile crack extension

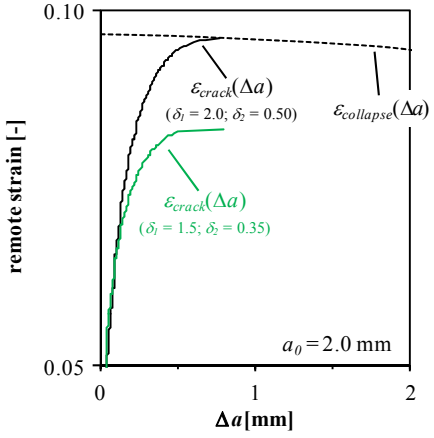

Figure 8.3. Illustration of the evaluation of tensile strain capacity using the tangency approach.

8.2.4. Evaluation of pressure correction function: statistical framework

The tensile strain capacities, as described in the previous section, simulated for two specimens (e.g. CWP and pipe) are compared. Therefore, the parameter $\zeta_{i,j}$ is introduced, expressing the strain capacity of specimen *i* relative to specimen *j*.

$$\zeta_{i,j} = \frac{\varepsilon_{\max,i}}{\varepsilon_{\max,j}} \tag{8.1}$$

This (relative) tensile strain capacity is evaluated for a large number of parameters, x_k, that are described in the following paragraphs (e.g. crack depth, mismatch, …). To study the effect of these parameters on the relative strain capacity, the following distinction is made:

- *single parameter*: the influence of one single parameter on $\zeta_{i,j}$. This parameter represents one of the parameters varied in the test matrix (e.g. relative initial defect depth a_0/t)
- *combined parameter*: the influence of the multiplication of two single parameters (e.g. $a_0/t \,.\, c/W$, representing the relative defect area)

The relative strain capacity is subsequently plotted as function of such single or combined parameters. To evaluate the influence of the studied parameter on the relative strain capacity $\zeta_{i,j}$, a statistical framework is set up, focusing on a linear correlation between the studied parameter(s) and the relative strain capacity. This framework is based on Student's *t*-test. This *t*-test compares the average relative strain capacity for all parameter values to the average relative strain capacity for each single parameter value. The use of this test is justifiable under the assumption of a normal distribution of the relative strain capacities for each parameter value and an equal variation for the different parameter values. In brief, the relative strain capacities are treated as follows [8.8]:

- The linear correlation between each parameter and the relative strain capacity is studied by determining the linear fitting coefficients $a_{1,k}$ and $a_{2,k}$ using the N (= total number of data points) simulated relative strain capacities:

$$\zeta_{i,j}\Big|_l = a_{1,k} + a_{2,k} x_{k,l} + \varepsilon_l \tag{8.2}$$

with:

$a_{1,k}$, $a_{2,k}$	fitting coefficients
$x_{k,l}$	value of the studied parameter
ε_l	random error
l	varying from 1 to N

- Under the null hypothesis, the parameter x_k has no influence on the relative strain capacity $\zeta_{i,j}$, implying that $a_{2,k}$ is expected to be zero. To adopt or reject this null hypothesis, the *t*-score is calculated as follows:

$$t-score = \frac{a_{2,k}\sqrt{N-2}}{\sqrt{\frac{\sum_{l=1}^{N}\left(\zeta_{i,j}\big|_l - a_1,k - a_{2,k}x_{k,l}\right)^2}{\sum_{l=1}^{N}\left(x_{k,l}-\overline{x_k}\right)^2}}} \tag{8.3}$$

with:

$x_{k,l}$ value of the studied parameter

$\overline{x_k}$ average value of the studied parameter for all simulations

- Using the calculated *t*-score, the significance (*p*-value) for rejecting the null hypothesis is eventually determined using tabulated values for the *t*-distribution.

As the most significant parameters are thereby identified, a linear correlation function is subsequently determined, using the selected single and combined parameters x_k.

$$\zeta_{i,j} = \hat{a}_1 + \hat{a}_2 \boldsymbol{X} = \hat{a}_1 + \hat{a}_2\left(c_0 + \sum_k c_k x_k\right) \tag{8.4}$$

The fitting coefficients $\hat{a}_1$, $\hat{a}_2$ and c_k are determined in such way that:

- for the considered ranges of all selected parameters the minimum and maximum value for $\boldsymbol{X}$ equal 0 and 1 respectively,
- higher $\boldsymbol{X}$-values represent a higher relative strain capacity ($\hat{a}_2 > 0$) and,
- the variability ψ around the linear correlation is at minimum.

This variability ψ is defined as the square root of the averaged sum over all points (N) of the squared difference between actual and predicted relative strain capacity:

$$\psi = \sqrt{\frac{1}{N}\sum_{l=1}^{N}\left(\zeta_{i,j}\big|_l - \hat{a}_1 - \hat{a}_2 X_l\right)^2} \tag{8.5}$$

Based on this variability, a 95% confidence interval is subsequently constructed. Therefore, the data is assumed to be distributed around the linear regression line from Eq.(8.4) following a *t*-distribution. This confidence interval is bounded by the following lines:

$$\zeta_{i,j} = \hat{a}_1 + \hat{a}_2 \boldsymbol{X} \pm 1.96\psi \tag{8.6}$$

In the above expression, the multiplication factor for the variability ψ originates from the assumed *t*-distribution in combination with the 95% confidence interval. This is schematically presented in Figure 8.4. Apart from the worked-out example presented in section 8.3.3.1, only a summary of the results of the statistical analyses is presented in this chapter. For the full details, the reader is referred to Appendix B.

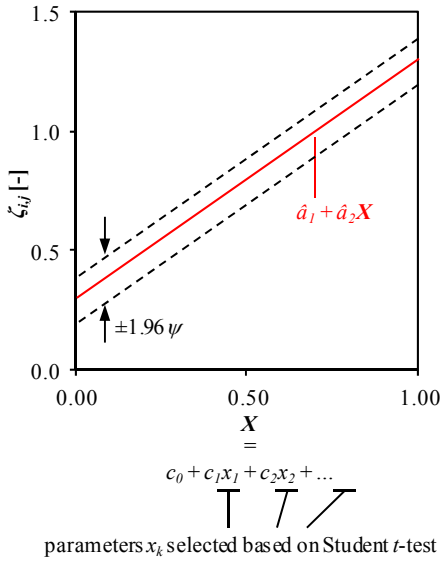

Figure 8.4. Schematic overview of statistical framework for the evaluation of relative strain capacity

8.3. Homogeneous specimens

A preliminary study is performed aiming at reducing the number of parameters and evaluating the proposed method. For this study, non-welded, hereafter referred to as homogeneous, specimens are considered. In the remainder of this section, an overview of the test matrix variables is first provided. Following, the influence of the reduced geometry (i.e. CWP versus unpressurized pipe) and internal pressure (i.e. pressurized versus unpressurized pipe) is discussed, eventually resulting in a comparison of CWP to pressurized pipe specimens.

8.3.1. Outline of test matrix

Pipe dimensions Given the limited influence of the pipe curvature on the crack driving force [8.9], a constant diameter value of 762 mm (30") is assumed. The wall thickness is also kept constant at 14 mm.

Defect size A uniform depth defect with semi-circular ending is considered, i.e. similar to the constraint analyses reported in the previous chapter. The defect dimensions are primarily selected based on the recently proposed revision of the EPRG Tier 2 guidelines [8.10, 11]. The initial defect depth, a_0, is varied between 2.0 and 5.0 mm, resulting in relative initial crack depths between 0.14 and 0.36. The defect length is varied between 25 and 100 mm, resulting in relative crack lengths c / W between 0.08 and 0.33. Note that the width of the wide plate specimens (300 mm) was used for the normalization of the crack length, also for the pipe specimens.

Internal pressure A case study indicated that a local minimum is observed for the tensile strain capacity as function of the internal pressure level, whereby the location of the minimum depends on the post-yield characteristics (Figure 8.5.a). Four different internal pressure levels are simulated, resulting in hoop stresses equal to 50, 60, 70 and 80 percent of the material's yield strength. These simulations are referred to as pp_{50}, pp_{60}, pp_{70} and pp_{80} respectively. Eventually, the minimum value of the simulated tensile strain capacities for these four pressure levels is selected for comparison of unpressurized pipes to CWP specimens.

Tearing resistance To define the material's tearing resistance, a generic form is assumed where the amount of ductile crack extension (Δa) is related to the CTOD by means of two fitting parameters δ_1 and δ_2 [8.12].

$$CTOD = \delta_1 (\Delta a)^{\delta_2} \tag{8.7}$$

Aiming to cover a broad spectrum of toughness levels, appropriate values for the two fitting parameters δ_1 and δ_2 are selected [8.13]. Plotted in Figure 8.5.b are the resulting resistance curves with the corresponding fitting parameters. The same resistance curves are assumed for both the CWP and pressurized pipe specimens. It is thereby implicitly assumed that the constraint does not differ significantly between both specimens, as shown in Chapter 2 and 7.

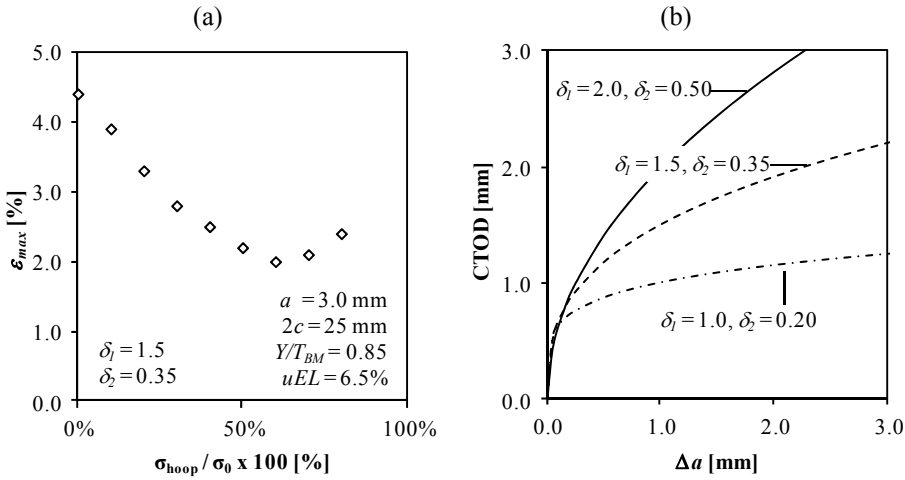

Figure 8.5. Influence of internal pressure on strain capacity (a) and considered tearing resistance curves (b).

Stress-strain properties The material's stress-strain properties are characterized by means of the Young's modulus E, the yield strength σ_0, the Y/T-ratio and the uniform elongation uEL. The first two are kept constant at 206900 MPa and 555 MPa respectively, representing an API-5L grade X80 material. To allow independent variation of the other parameters, the UGent stress-strain model is adopted [8.14]. In total, four different Y/T-ratios are selected, ranging from 0.80 to 0.95 in steps of 0.05. Subsequently, two realistic uEL levels are determined for each Y/T-ratio. This is based on a set of experimental data taken from literature [8.10, 15] (Figure 8.6.a). An overview of the selected material properties is provided in Table 8.1, and two example stress-strain curves are plotted in Figure 8.6.b.

All parameters are combined in a so-called full factorial test matrix, resulting in a total of 2304 simulated strain capacities. These in turn result in 384 relative strain capacities $\zeta_{i,j}$.

Table 8.1. Selected material properties for preliminary study

Y/T	***uEL***	***E***	σ_0	***Y/T***	***uEL***	***E***	σ_0
[-]	**[%]**	**[MPa]**	**[MPa]**	**[-]**	**[%]**	**[MPa]**	**[MPa]**
0.80	10.0	206900	555	0.90	4.8	206900	555
0.80	14.0	206900	555	0.90	8.8	206900	555
0.85	6.4	206900	555	0.95	3.2	206900	555
0.85	10.0	206900	555	0.95	7.3	206900	555

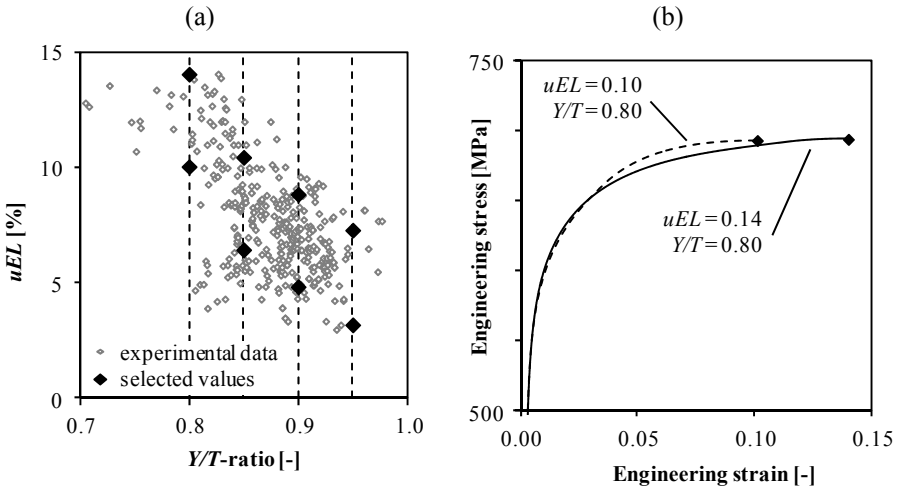

Figure 8.6. Selected uniform elongation levels going with *Y/T*-ratio. Experimental data taken from [8.10, 15] (a) and example stress-strain curves up to necking for material with low *Y/T*-ratio

8.3.2. Failure modes

In the absence of weld metal strength mismatch effects, failure through global collapse is excluded. The specimens will undeniably fail in the notched section, either through net section collapse (i.e. maximum force accompanied by rapid increase of the CTOD) or unstable crack extension (i.e. tangency criterion). The failure mode thereby depends on the crack driving force in combination with the assumed tearing resistance.

By means of example, the crack driving force curves are plotted for CWP, unpressurized pipe and pressurized pipe specimens with identical stress-strain properties and defect dimensions (Figure 8.7). This figure already indicates some general trends. First, the crack driving force for the unpressurized pipe is lower than for the CWP specimen. This is expected given the limited width of the CWP specimen compared to the pipe's circumference. However, the collapse strain, at maximum force, is almost identical. This is due to the limited size of the considered defects; for larger defects a more pronounced decrease of the collapse strain is observed for the CWP specimen. Second, the crack driving force for the pressurized pipe is larger than for the unpressurized case. This is in agreement with the observations reported in literature, as discussed in section 8.2.2. In addition, the internal pressure results in a remarkable decrease of the collapse strain for the net section collapse failure.

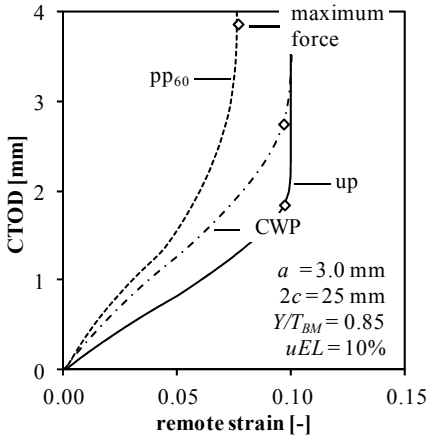

Figure 8.7. Example crack driving force curves for unpressurized pipe, pressurized pipe and CWP specimen. The moment of maximum force is indicated by the open diamond symbol.

8.3.3. CWP specimen versus unpressurized pipe

8.3.3.1. Results

To gain insight in the processing of the simulated relative strain data, the statistical analysis is worked out step by step (see also Figure 8.8 and Figure 8.9).

For this statistical analysis, two data sets are available (Figure 8.8.a). A first set, ξ, contains all single and combined parameters, x_k , involved in this study. A second set, ω, contains all simulated relative strain capacities $\zeta_{CWP;up}$ that are related to a unique combination of the parameter values x_k. In total, the set ω consists of $N = 384$ elements.

In a first step, the linear correlation between these parameters x_k and the relative strain capacity $\zeta_{CWP;up}$ is studied (Figure 8.8.b). Therefore, the correlation coefficients, $a_{1,k}$ and $a_{2,k}$, between $\zeta_{CWP;up}$ and the parameter x_k are first determined using a least squares fit (Eq.(8.2)). Using these correlation coefficients, the *t*-scores are determined in accordance to Eq.(8.3). Subsequently, the *p*-values are derived using tabulated values for the *t*-distribution.

As the significance levels for all parameters are known, the parameters for the final correlation function can now be selected (Figure 8.8.c). Almost every single and combined parameter appears significant (*p*-value < 0.01). Therefore, the following alternative selection criteria are considered in this dissertation:

- single parameters are selected if their significance level, *p*-value, is lower than 10^{-8}, and
- combined parameters are selected if their significance exceeds the significance level of both single parameters.

Based on these criteria, the following parameters are withheld:

- relative initial crack depth a_0 / t
- relative crack length c / W
- *Y/T*-ratio Y/T
- relative crack size $a_0 / t \cdot c / W$
- crack depth · *Y/T*-ratio $a_0 / t \cdot Y/T$
- crack length · *Y/T*-ratio $c / W \cdot Y/T$
- crack depth · tearing resistance $a_0 / t \cdot \delta_1$
- crack length · tearing resistance $c / W \cdot \delta_1$

(a)

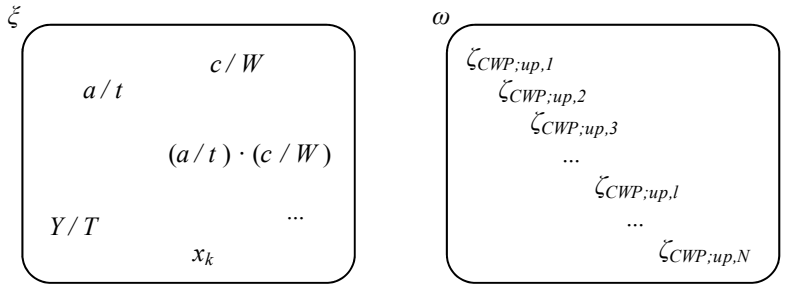

(b)

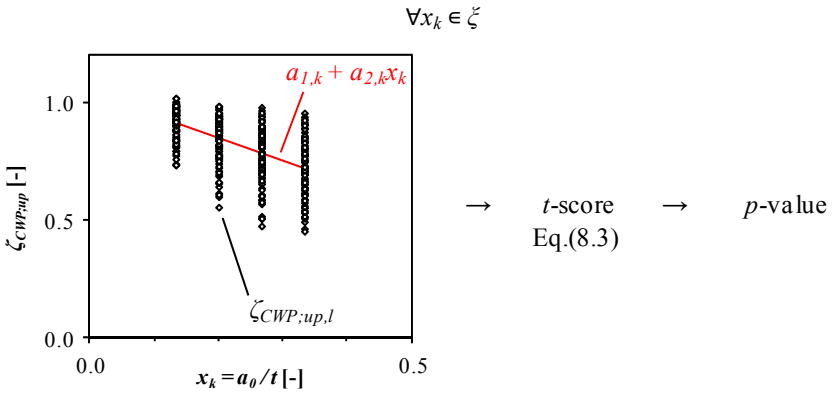

(c)

x_k	p-value	selection criteria	
a_0 / t	$1 \cdot 10^{-34}$	$< 10^{-8}$	✓
c / W	$3 \cdot 10^{-18}$	$< 10^{-8}$	✓
Y/T	$3 \cdot 10^{-29}$	$< 10^{-8}$	✓
uEL	$3 \cdot 10^{-8}$	$< 10^{-8}$	✗
δ_l	$2 \cdot 10^{-6}$	$< 10^{-8}$	✗
$(a_0 / t) \cdot (c / W)$	$2 \cdot 10^{-51}$	$< 10^{-34}$	✓
$a_0 / t \cdot Y/T$	$7 \cdot 10^{-51}$	$< 10^{-34}$	✓
$a_0 / t \cdot uEL$	$6 \cdot 10^{-1}$	$< 10^{-34}$	✗
...	...	...	

Figure 8.8. Illustration of first step in selection process of parameters: set of parameters and relative strain capacities (a), linear correlation of single parameter (b) and evaluation of significance levels (c)

As such, a subset of parameters is created that is used for the evaluation of the relative strain capacity. The function $\boldsymbol{X}$ is subsequently composed as a linear combination of the subset parameters. The fitting coefficients $\hat{a}_1$, $\hat{a}_2$ and c_k are obtained by minimizing the variability of the data points $\zeta_{CWP;up,l}$ around the linear trend that is described by Eq.(8.4) (Figure 8.9.a). The resulting fitting coefficients for this so-called statistical solution are listed in Table 8.2, as is the resulting variability, $\psi = 0.04$.

Besides this statistical solution, a so-called full solution was obtained by considering all (significant and non-significant) parameters for the evaluation of $\boldsymbol{X}$. For this full solution, the same variability was obtained (Figure 8.9.b). In contrast, when selecting only the relative initial crack depth and relative crack length as the parameters x_k used for the function $\boldsymbol{X}$, the variability clearly deteriorates ($\psi = 0.08$, Figure 8.9.c). These two cases add belief to the method of selecting the most influential parameters.

Table 8.2. Overview of fitting coefficients and resulting variability for comparison of the strain capacity of CWP specimen to this of unpressurized pipe

parameter		statistical solution
constant	c_0	0.872
a_0 / t	c_1	5.368
c / W	c_2	2.865
Y/T	c_3	0.298
$a_0 / t \cdot c / W$	c_4	-1.511
$a_0 / t \cdot Y/T$	c_5	-6.791
$c / W \cdot Y/T$	c_6	-3.724
$a_0 / t \cdot \delta_l$	c_7	-0.491
$c / W \cdot \delta_l$	c_8	-0.126
$\hat{a}_1$		0.439
$\hat{a}_2$		0.597
ψ		0.04

(a)

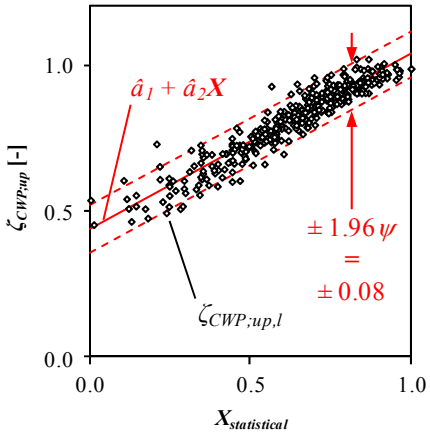

$$X_{statistical} = c_0 + \sum_k c_k x_k$$

with $x_k \in \xi \mid p\text{-value} < 10^{-8}$

(b)

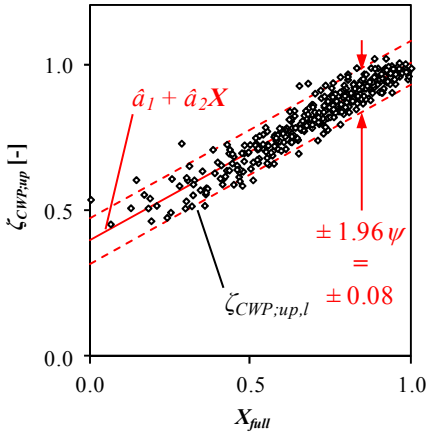

$$X_{full} = c_0 + \sum_k c_k x_k$$

with all x_k

(c)

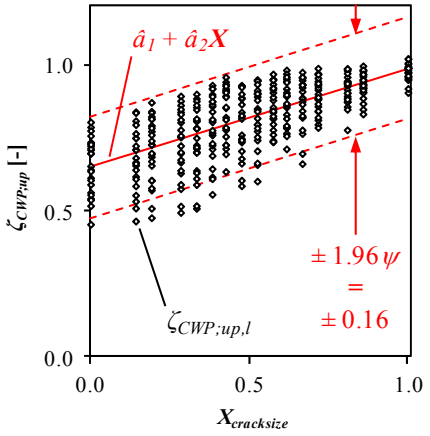

$$X_{cracksize} = c_0 + \sum_k c_k x_k$$

with $x_k \in \{a_0 / t\,,\, c / W\}$

Figure 8.9. Illustration of second step in selection process, with linear regression considering all parameters with p-value lower than 10^{-8} (a), all parameters (b) and only the relative crack depth and length (c)

8.3.3.2. Discussion

For all performed simulations the relative strain capacity $\zeta_{CWP;up}$ does not exceed unity. Looking more into detail to the results, it is observed that the relative strain capacity $\zeta_{CWP;up}$ decreases with increasing relative defect lengths. This is attributed to the limited width of the CWP specimens. As a result, the strain patterns originating from the crack, under approximately 45° in the transverse direction, interfere with the boundaries of the CWP specimen. Due to the absence of adjacent material at the specimen edge, the crack experiences a lower restraint and hence a higher crack driving force in CWP specimens compared to pipes. This effect is most pronounced for longer cracks; the zones with high strain values reach the specimen boundaries more easily. As a result, the CWP test result becomes more conservative with increasing crack lengths. In Figure 8.10.a the strain patterns for specimens with increasing crack lengths are illustrated, indeed showing that the high strain zones reach the specimen boundaries for longer cracks. Note that these specimens have identical material properties (Y/T = 0.80 and uEL = 14%) and the same defect depth (a = 3.0 mm).

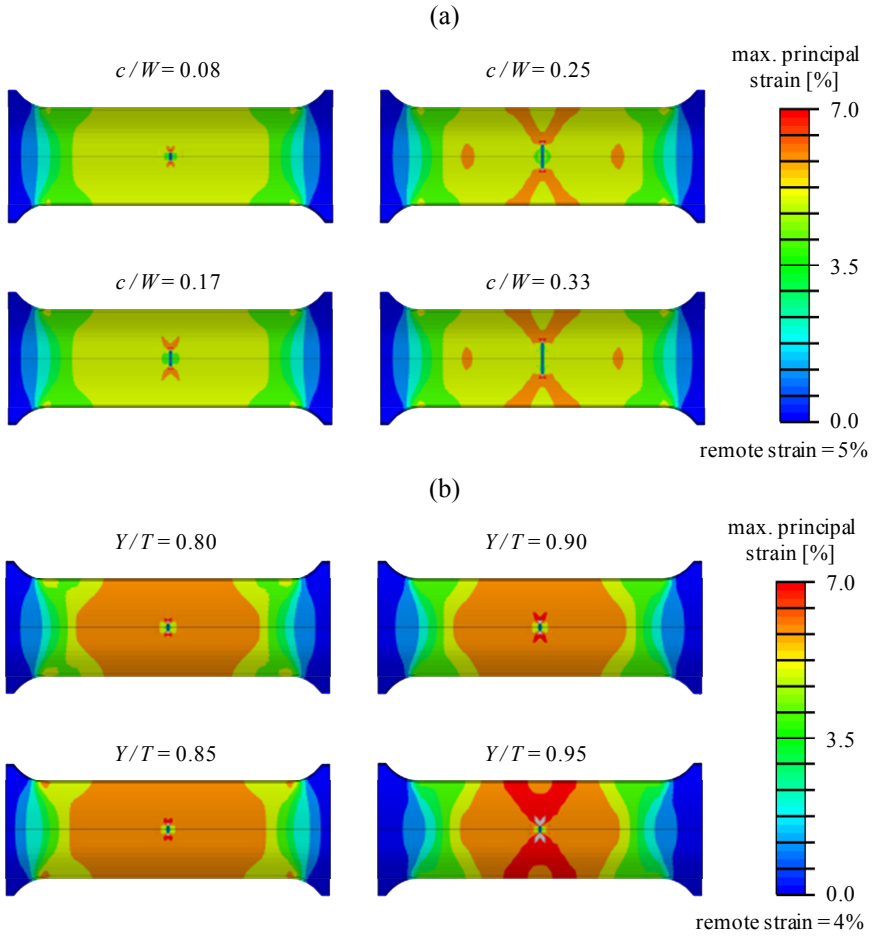

Figure 8.10. Influence of crack length (a) and Y/T-ratio (b) on the strain pattern for CWP specimens

An increase of the relative crack depth also results in a reduction of the relative strain capacity $\zeta_{CWP;up}$. An explanation for this effect is found in the absence of axial symmetry for the CWP specimen. This results in localized bending of the specimen due to an offset between the remotely applied force and the resultant force in the cracked section. This effect is most pronounced for deeper defects, which result in larger offsets. Recall that this effect also contributes to the minor constraint difference between CWP and pipe specimens (Chapter 7).

The influence of the *Y/T*-ratio is related to the size of the plastic zone around the crack tip, both at the free surface and at the middle of the crack. In both cases, it is clear that a limited strain hardening capacity of the material results in a more widespread plastic zone. This larger plastic zone is therefore, in case of the surface end of the crack, more likely to interact with the specimen edges and hence suffers from the loss of restraint (Figure 8.10.b). Looking at the middle of the crack, the deformation resulting from bending is most pronounced in case the remaining ligament deforms plastically. This is promoted by a low strain hardening capacity of the material.

The above also explains the significance of the interaction of the relative defect dimensions and the *Y/T*-ratio. First, the defect length gains significance for metals with a high *Y/T*-ratio. For these materials, the interaction with the specimen edges is clearly enhanced for longer cracks. In contrast, for shorter cracks the influence of the *Y/T*-ratio is slightly more limited, which is attributed to the larger area that is to be plasticized. Second, the effect of the defect depth is analogously most pronounced for high *Y/T*-ratios.

Another significant combined parameter is the relative defect size. For short cracks (i.e. $2c = 25$ mm), the decrease of the relative strain capacity $\zeta_{CWP;up}$ is less pronounced compared to long cracks (i.e. $2c = 100$ mm). This is attributed to an increase of the bending for longer defects, since the offset between the applied force and the resultant force in the cracked section increases.

Finally, the parameters illustrating the interaction between the tearing resistance and the relative crack depth and length are discussed. In both cases, the decrease of the relative strain capacity $\zeta_{CWP;up}$ is more pronounced for materials with a higher tearing resistance. This is attributed to the increased plastic deformation around the crack (e.g. 45° shear lines) for these materials. A larger plastic zone implies a higher likelihood for interaction with the specimen's boundaries and for the formation of a plastic hinge.

In conclusion, the qualitative impact of the main single parameters on the relative strain capacity is listed in Table 8.3.

Table 8.3. Qualitative impact of single parameters on strain capacity of CWP specimens relative to unpressurized pipes ($\zeta_{CWP;up}$)

	a_0/t	c/w	Y/T	uEL	δ_l
$\zeta_{CWP;up}$ increases for...	↓	↓	↓	-	↓

8.3.4. Unpressurized pipe versus pressurized pipe

8.3.4.1. Results

In contrast to the previous section, the results of the statistical analysis are briefly summarized. Three single parameters meet the significance requirements:

- relative initial crack depth a_0 / t
- relative crack length c / W
- *Y/T*-ratio Y/T

In contrast to the previous comparison, no combined parameters are withheld. The linear combination of these single effects again results in a statistical solution (Table 8.4). The variability for this solution, $\psi = 0.06$, is only slightly higher as compared to the full solution that takes into account all single and combined parameters ($\psi = 0.05$).

Table 8.4. Overview of fitting coefficients and resulting variability for comparison of the strain capacity of unpressurized pipe with pressurized pipe

parameter		statistical solution
constant	c_0	1.475
a_0 / t	c_1	2.709
c / W	c_2	-0.865
Y/T	c_3	-1.635
$\hat{a}_1$		0.300
$\hat{a}_2$		0.368
ψ		0.06

8.3.4.2. Discussion

For increasing relative initial crack depths, the relative strain capacity $\zeta_{pp;up}$ increases. This observation is in correspondence with the findings of Wang et al. [8.16]. In their paper, Wang et al. considered similar defect dimensions and material properties compared to the presented test matrix, hence this result should not surprise. However, Wang et al. only considered relative crack depth, whereas the *Y/T*-ratio and defect length also have a pronounced influence on the relative strain capacity $\zeta_{pp;up}$. It should however be noted that the relative crack depth has by far the most pronounced influence, as is clear from the weighing factors in Table 8.4.

The influence of the relative initial crack depth and of the relative crack length are not well understood. Although the following observations can be made:

- the effect of the relative initial crack depth is most pronounced for long defects and materials with a high *Y/T*-ratio. For short defects, i.e. c = 12.5 mm, no effect of the defect depth is observed.
- the observed effect is potentially influenced by the defect location. An additional qualitative study is performed to investigate the potential difference between defects located along the pipe's outer diameter instead of the inner diameter as assumed in this chapter. Illustrated in Figure 8.11 are the crack driving force curves for both small and large defects in pressurized and unpressurized pipes. For the unpressurized pipe, the defect location has a marginal impact on the crack driving force. In contrast, for pressurized pipes a clear increase of the CTOD is observed at a constant remote strain level for the lower initial crack depth (a = 2.0 mm). For the deeper cracks, a = 5.0 mm, no pronounced influence of the defect location is observed.

This points out the importance of the test matrix limitations and the fact that these should be accounted for when considering the use of the presented relative strain capacity equations.

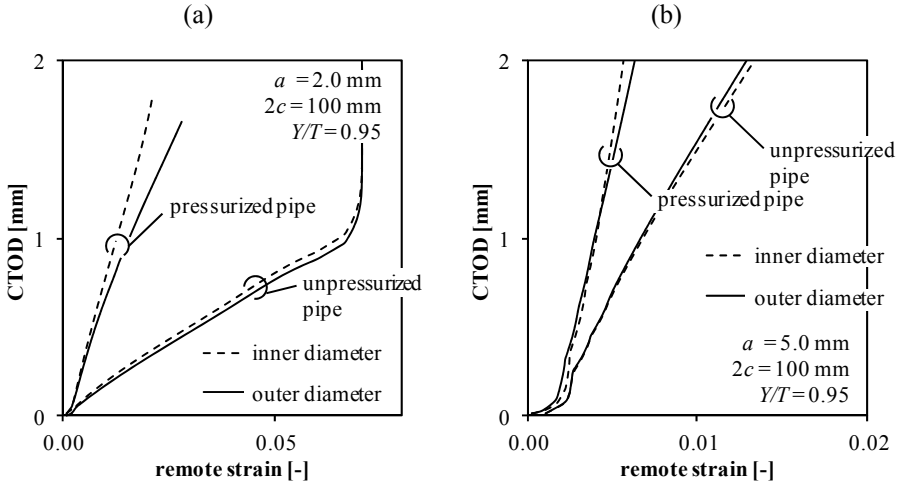

Figure 8.11. Influence of defect location (inner diameter versus outer diameter) on crack driving force curves for long defects with low (a) and high (b) initial crack depth.

For metals with a higher *Y/T*-ratio the relative strain capacity $\zeta_{pp;up}$ decreases. In all cases an increase of the plasticity in the vicinity of the crack tip is observed for pressurized pipes compared with unpressurized pipes (Figure 8.12). An increase of the *Y/T*-ratio is known to furthermore increase the plastic zone size. This effect is assumed to be more pronounced for pressurized pipes since in this case the zone with large (excessive) plastic deformation in front of the crack tip is larger.

In summary, the qualitative impact of all main parameters on the relative strain capacity $\zeta_{pp;up}$ is provided in Table 8.5.

Table 8.5. Qualitative impact of single parameters on relative strain capacity for pressurized and unpressurized pipes ($\zeta_{pp;up}$)

	a_0/t	c/w	Y/T	uEL	δ_1
$\zeta_{pp;up}$ increases for...	↑	↓	↓	-	-

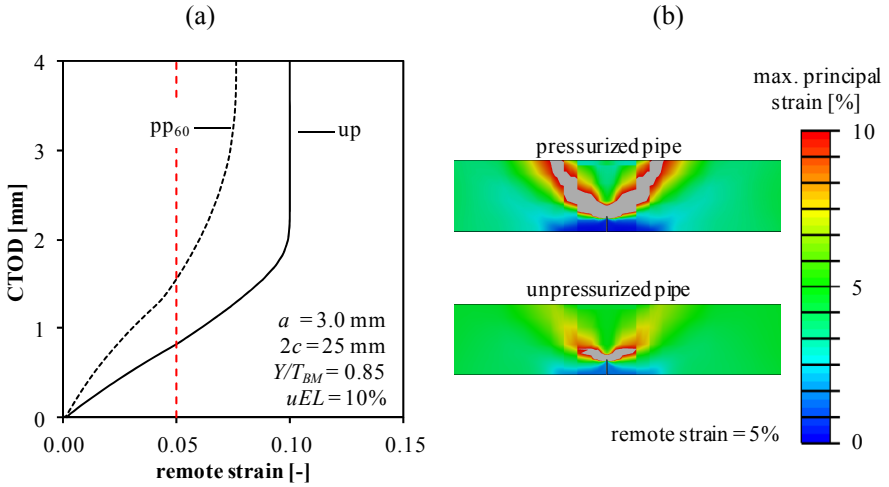

Figure 8.12. Difference in crack driving force between pressurized pipe and unpressurized pipe (a) and effect of internal pressure on strain patterns at crack tip region (b).

8.3.5. CWP specimen versus pressurized pipe

The strain capacity of the pressurized pipe relative to the CWP specimen can be interpreted as the ratio of:

- the strain capacity of the pressurized pipe relative to the unpressurized pipe
- and, the strain capacity of the CWP specimen relative to the unpressurized pipe.

In other words:

$$\zeta_{pp;CWP} = \frac{\varepsilon_{\max;pp}}{\varepsilon_{\max;CWP}} = \frac{\zeta_{pp;up}}{\zeta_{CWP;up}} \tag{8.8}$$

Consequently, the factors affecting both relative strain capacities $\zeta_{pp;up}$ and $\zeta_{CWP;up}$ separately, as discussed in the previous two sections, are expected to influence the relative strain capacity $\zeta_{pp;CWP}$. It should therefore not surprise that these parameters also turn out to be the most statistically relevant. The resulting fitting parameters for this statistical solution are listed in Table 8.6. Given the small magnitude of the weighing factors related to the tearing resistance, a second solution is additionally determined. This second one omits the tearing resistance and is referred to as the reduced solution. It is observed that the variability is identical for both solutions ($\psi = 0.05$). As a lower number of parameters clearly enhances the user-friendliness of these equations, preference is therefore given to this reduced solution.

Unfortunately, the impact of the single parameters on the relative strain capacity $\zeta_{pp;CWP}$ cannot always be straightforwardly derived from the impact these parameters have on the separated effects (i.e. $\zeta_{CWP;up}$ and $\zeta_{pp;up}$). This is because the maximization of the relative strain capacity $\zeta_{pp;CWP}$ implies that $\zeta_{pp;up}$ should be maximal and/or $\zeta_{CWP;up}$ should be minimal. This often results in a contradictory requirement for the parameter value, e.g. for the relative initial crack depth (Table 8.7).

In conclusion, the correlation between all simulations and the reduced solution is shown in Figure 8.13. Worth nothing at this point is that the strain capacity of the pressurized pipe is not always smaller than the one of the corresponding CWP specimen. For a limited number of cases, with deep and long cracks located in a material with high *Y/T*-ratio, the relative strain capacity exceeds unity.

Table 8.6. Overview of fitting coefficients and resulting variability for comparison of the strain capacity of pressurized pipe to CWP specimen

parameter		statistical solution	reduced solution
constant	c_0	3.008	3.098
a_0 / t	c_1	-7.583	-7.918
c / W	c_2	-8.354	-8.457
Y/T	c_3	-3.011	-3.122
$a_0 / t \cdot c / W$	c_4	11.836	12.249
$a_0 / t \cdot Y/T$	c_5	8.780	9.103
$c / W \cdot Y/T$	c_6	6.367	6.597
$a_0 / t \cdot \delta_1$	c_7	-0.036	-
$c / W \cdot \delta_1$	c_8	0.126	-
$\hat{a}_1$		0.272	0.287
$\hat{a}_2$		0.805	0.778
ψ		0.05	0.05

Table 8.7. Qualitative impact of single parameters on the relative strain capacity of pressurized pipes to CWP specimens ($\zeta_{pp;CWP}$)

	a_0/t	c/w	Y/T	uEL	δ_1
$\zeta_{CWP;up}$ maximal for...	↓	↑	↑	-	↑
$\zeta_{pp;up}$ minimal for...	↑	↓	↓	-	-
$\zeta_{pp;CWP}$ maximum for...	↑	↑	↑	-	(↑)

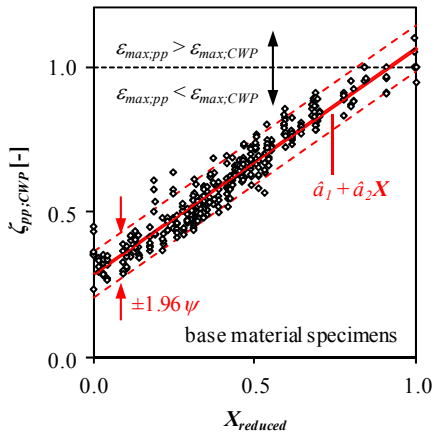

Figure 8.13. Simulated data plotted with reduced solution for evaluation of $\zeta_{pp;CWP}$

8.3.6. Summary

From all studied parameters, and within their studied range, the following parameters are seen to be most influential:

- relative initial crack depth
- relative crack length
- *Y/T*-ratio

The tearing resistance showed to have only a minor impact on the relative strain capacity. The material's uniform elongation has no influence on the relative strain capacity for the investigated cases. Hence, in the remainder of this work, a fixed uniform elongation will be selected for a given *Y*/*T*-ratio.

Furthermore, the presented methodology appears effective in selecting the parameters that reduce the variability around the presented linear correlations.

8.4. Welded specimens

The study of welded specimens involves the incorporation of two effects not previously considered, namely weld metal strength mismatch and misalignment. The first is expressed in terms of the material's flow strength, as discussed in Chapter 1.

8.4.1. Outline of test matrix

Pipe dimensions In correspondence to the previous series of simulations, the pipes are characterized by a diameter of 762 mm and wall thickness of 14 mm.

Defect size A uniform depth defect with semi-circular ends, that is located at the weld metal center line is considered. The defect depth is chosen identical to the simulations of the previous test matrix. Based on the application limits of the strain based defect assessment procedure presented by Fairchild et al. [8.17], the defect length is restricted to 25 and 50 mm.

Misalignment For misaligned specimens, a diameter reduction of the adjacent pipe is assumed, reflecting a uniform hi-lo misalignment between both pipe sections equal to 1.6 mm. This magnitude is selected as it represents a maximum allowable value in accordance to European and Canadian standards [8.18, 19].

Weld geometry A narrow gap weld with a root opening of 4.0 mm and half opening angle of 10° is modeled. In addition, a slight geometrical overmatch (cap height of 1.0 mm) is assumed for all simulations. A schematic representation of the studied weld geometry is provided in Figure 8.14.a&b for specimens without and with misalignment respectively.

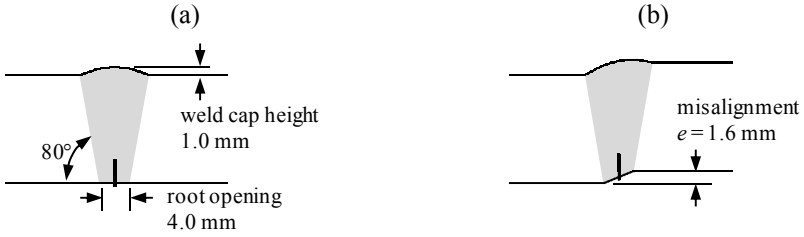

Figure 8.14. Detailed view of weld profile in specimen without (a) and with (b) misalignment.

Internal pressure Again several internal pressure levels are examined, though the number of cases was reduced. Only pressure levels corresponding to a hoop stress of 60 and 70 percent of the material's yield strength are examined. These pressure levels showed to be the most detrimental during the study on homogeneous specimens.

Tearing resistance Since the tearing resistance showed a questionable influence in the previous comparison, further attention is drawn to this effect. The studied tearing resistances are identical to the ones considered for the analysis of homogeneous specimens.

Base metal stress-strain properties The uniform elongation did not show to have a significant influence on the relative strain capacity, hence this parameter is omitted from the test matrix. A single uniform elongation is selected for each *Y/T*-ratio based

on the experimental data shown in Figure 8.6.a. The selected combinations are listed in Table 8.8. Since the *Y/T*-ratio showed a pronounced influence on the relative strain capacity, this parameter is again selected as a variable. However, to reduce the number of simulations, only three *Y/T*-ratios are studied; 0.80, 0.90 and 0.95. The material's stress-strain relationship is again described based on the UGent model [8.14].

Weld metal stress-strain properties For the weld metal, variation of the uniform elongation is also omitted and a single value is selected corresponding with each *Y/T*-ratio. The weld metal strength mismatch levels, expressed in terms of MM_{FS}, range between -9% and +38% (Figure 8.15).

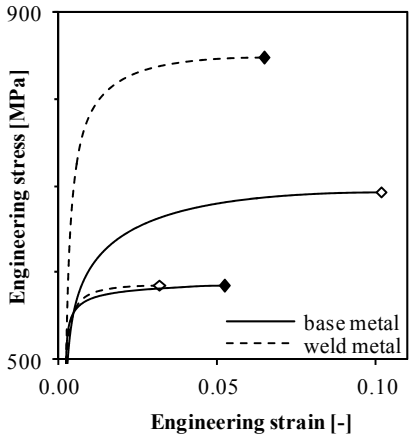

Figure 8.15. Stress-strain curves corresponding to largest flow stress overmatch (black symbols) and undermatch (open symbols).

Table 8.8. Selected stress-strain properties for base and weld metals

base metal		weld metal	
Y/T [-]	*uEL* [%]	*Y/T* [-]	*uEL* [%]
0.80	10.0	0.85	6.4
0.90	7.0	0.90	4.8
0.95	5.0	0.95	3.2

All parameters are again combined in a full factorial test matrix, resulting in 6736 simulated strain capacities. This corresponds to 1684 relative strain capacities. Note however that for the interpretation and application of these simulated data, the boundary conditions of this test matrix should be taken into account. It is for instance known that the weld shape potentially has a pronounced effect on the crack driving force curves [8.20].

8.4.2. Failure modes

In contrast to the previous study, failure through global collapse can now be expected for high weld metal strength overmatch levels. Looking at the crack driving force curves for a pressurized pipe, it is indeed observed that an increased overmatch decreases the crack driving force (Figure 8.16). Depending on the tearing resistance, the pipe will, at increasing strength overmatch levels, fail through global collapse. In this case, the strain continuously increases and the CTOD stabilizes. The tensile strain capacity is than defined at the moment of maximum force. For this series of simulations however, the moment of maximum force tends to coincide with the end of the simulation for the pressurized pipe specimens[1]. This is due to the multi-axial stress state in the base metal, which allows plastic deformation to a larger extent in comparison with a uniaxial tensile test. Hence, the simulations tend to underestimate the tensile strain capacity for the pressurized pipe specimens in case of global collapse. This should however not be overrated since:

- the tensile strain capacity that is assumed in this case always exceeds the uniform elongation of the material[2], since the biaxial loading increases the deformation capacity compared to the uniaxial case.
- an underestimation of the tensile strain capacity for the pressurized pipes results in a conservative assessment for the current problem. The final aim is to correlate the strain capacity of a CWP to the pressurized pipe. The CWP strain capacity serves as a starting point for the proposed conversion formula. The predicted tensile strain capacity of the pressurized pipes will thus be underestimated for the reasons mentioned above.

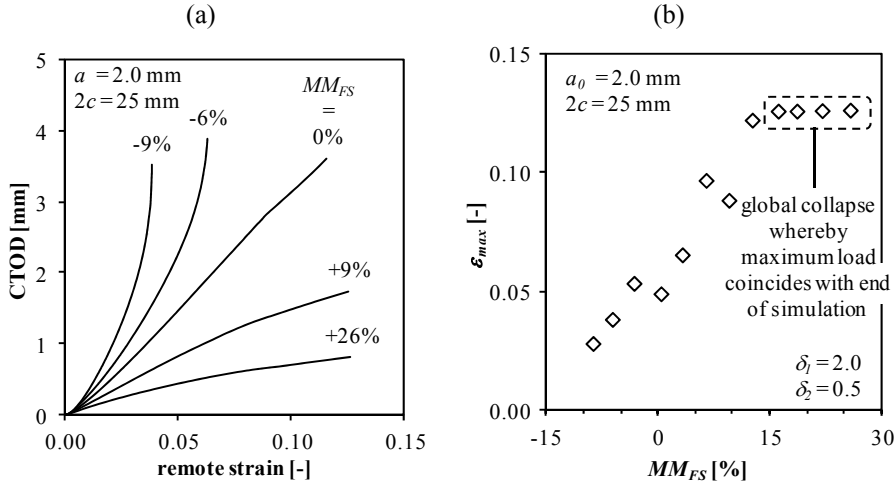

Figure 8.16. Crack driving force curves for varying flow stress mismatch levels (a) and resulting tensile strain capacity (b) for pressurized pipe (pp_{60})

[1] A larger axial displacement has been applied, resulting in a flat load-displacement diagram whereby the point of maximum force is rarely reached, even for remote strain levels twice the material's uniform elongation.

[2] It appears impractical to perform a strain based design aiming for a strain capacity exceeding the material's uniform elongation.

The above shortcoming of the simulations solely holds for the pressurized pipes. For the CWP and unpressurized pipe specimens, the point of maximum force can be clearly determined from the simulations. However, for the current geometry and material properties no characteristic crack driving force curves have been obtained where global collapse of the specimens can be expected. Although the crack driving force clearly decreases for increasing mismatch levels, no stabilization of the CTOD is observed beyond the point of maximum force (Figure 8.17.a). This is attributed to the small width of the weld. The strain distribution for a highly overmatched unpressurized pipe is shown in Figure 8.17.b. Focusing on the detailed strain distribution around the crack tip, the strength overmatch clearly reduces the strain in the weld. However, the high strains originating from the crack tip extend towards the base metal. This locally exhausts the base metal's ductility and hence explains the strain localization near the weld observed in the global view at a remote strain level of 13%.

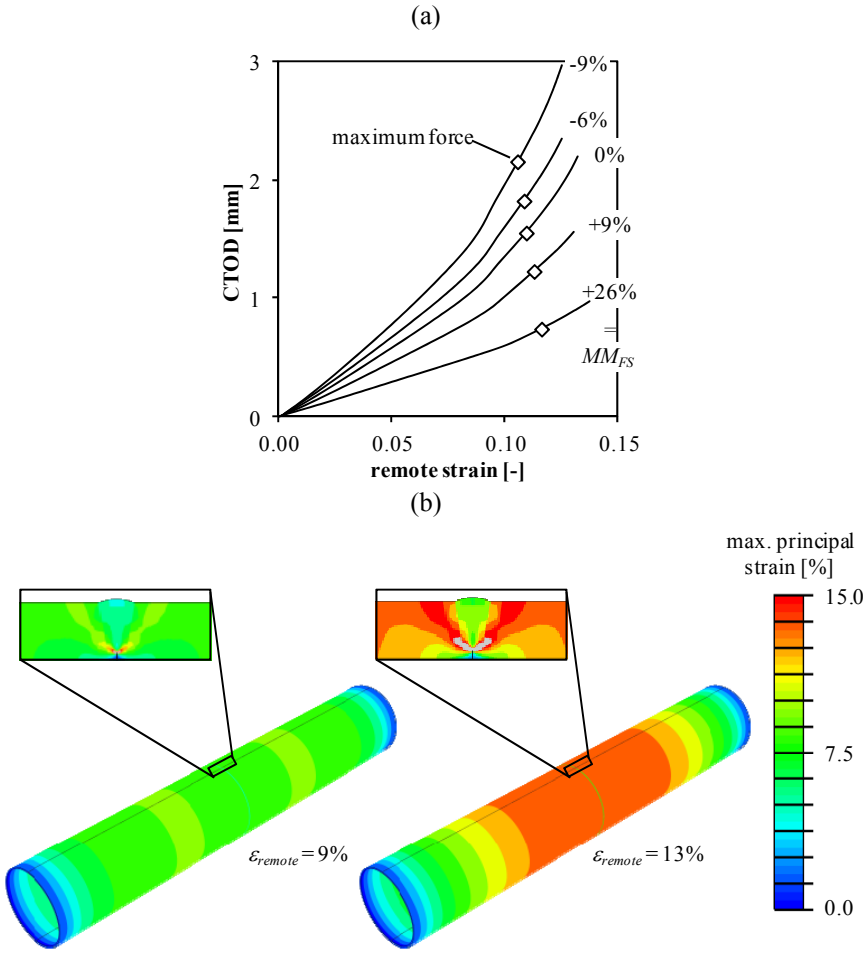

Figure 8.17. Crack driving force (a) and strain evolution (b) in unpressurized pipe

8.4.3. CWP specimen versus unpressurized pipe

8.4.3.1. Results

The following single parameters appear most significant from the statistical analysis when evaluating the strain capacity of the CWP specimens relative to the unpressurized pipes:

- relative crack depth a_0 / t
- relative crack length c / W
- mismatch level MM_{FS}

In addition, the following combined parameters appear more significant compared to their single parameters:

- crack size $a_0 / t \cdot c / W$
- crack depth · *Y/T*-ratio of weld metal $a_0 / t \cdot Y/T_{WM}$
- crack length · *Y/T*-ratio of weld metal $c / W \cdot Y/T_{WM}$
- *Y/T*-ratio of base metal · mismatch level $Y/T_{BM} \cdot MM_{FS}$

A linear combination of the above listed parameters is therefore considered for predicting the relative strain capacity $\zeta_{CWP;up}$. The fitting coefficients for this statistical solution $\boldsymbol{X}$ are listed in Table 8.9, resulting in a variability $\psi = 0.11$.

Table 8.9. Overview of fitting coefficients and resulting variability for comparison of the strain capacity of CWP specimen to unpressurized pipe

parameter		statistical solution
constant	c_0	0.569
a_0 / t	c_1	0.771
c / W	c_2	5.785
MM_{FS}	c_3	-0.014
$a_0 / t \cdot c / W$	c_4	-23.028
$a_0 / t \cdot Y/T_{WM}$	c_5	0.752
$c / W \cdot Y/T_{WM}$	c_6	-4.109
$Y/T_{BM} \cdot MM_{FS}$	c_7	0.023
$\hat{a}_1$		0.137
$\hat{a}_2$		1.245
ψ		0.11

8.4.3.2. Discussion

The influence of most parameters is similar to the one found for the study on homogeneous specimens. As such, an increase of the relative initial crack depth or relative crack length results in a decrease of $\zeta_{CWP;up}$. However, the *Y/T*-ratio (of weld and based metal) and tearing resistance parameter δ_I are no longer observed as an important single parameter. For the combined parameters, the *Y/T*-ratio of the weld metal appeared most significant in combination with the relative defect dimensions. The latter is understood as the crack tip plasticity develops first in the weld, hence it's *Y/T*-ratio is more important than the base metal stress-strain properties.

The influence of the weld metal strength mismatch is such that overmatching increases the relative strain capacity $\zeta_{CWP;up}$. The explanation is twofold. First, an increase of the overmatch will clearly promote global collapse. Second, the overmatching weld induces multi-axial stresses in the adjacent base metal; transverse deformation is restrained. For high strength overmatch levels, the weld behaves as a rigid body interconnecting the base metals. As a result, the deformation capacity of the material at the location of the remote strain measurements is increased, eventually beyond the material's uniform elongation determined from uniaxial tensile tests.

This effect is illustrated in Figure 8.18, where the crack driving force curves of the CWP specimens shift below the ones corresponding to the unpressurized pipe by increasing the mismatch level. This implies that the relative strain capacity, $\zeta_{CWP;up}$, might become larger than one for these cases.

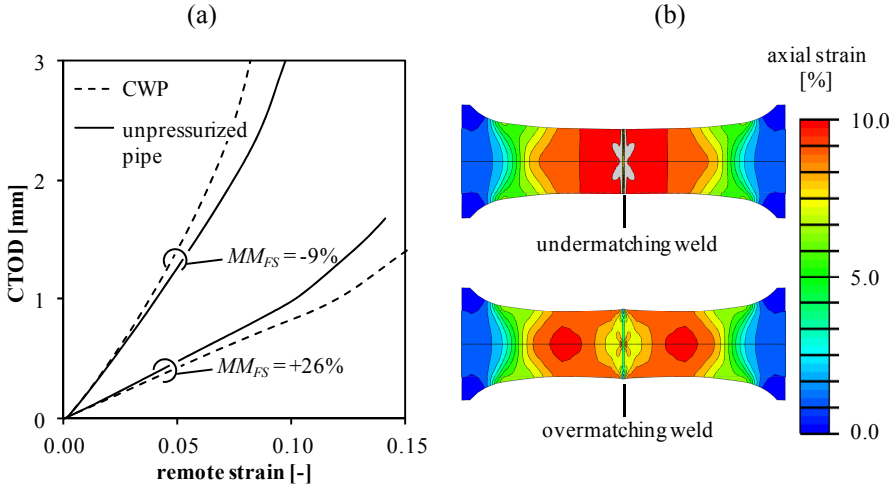

Figure 8.18. Crack driving force curves for CWP and unpressurized pipes with varying mismatch levels (a) and strain distribution of the corresponding CWP specimens with ten times magnified deformations (b)

Looking at the strain distribution, shown in Figure 8.18.b, the non-uniformity is reflected by strain hot-spots at the center of the base metal. These hot-spots are a result of the lateral restraint created by the overmatching weld, which results in shear bands originating from the weld near the specimen's edge towards the center of the specimen. At the location where both shear bands interact, a zone of large strain is formed.

Finally, the influence of the combined effect of the strength mismatch and the base metal's *Y/T*-ratio is discussed. For high Y/T_{BM} values, the effect of the weld metal strength mismatch is significantly more pronounced. In contrast, low Y/T_{BM} values show a less pronounced dependency on the mismatch level. This is again attributed to the strain distribution. Higher base metal *Y/T*-ratios promote the formation of strain hot-spots from the early loading stage onwards, since the shear bands originating from the specimen's edge extend over a wider area. For base metals with a pronounced strain hardening capacity, the interaction between the shear bands at the center of the specimen is less pronounced.

The qualitative impact of all investigated parameters on the strain capacity of CWP specimens relative to unpressurized pipes is listed in Table 8.10. Remark that the tearing resistance and misalignment did not show any influence on $\zeta_{CWP;up}$.

Table 8.10. Influence of single effects on strain capacity of CWP specimens relative to unpressurized pipes

	a_0/t	c/w	Y/T_{BM}	Y/T_{WM}	δ_1	MM_{FS}	e/t
$\zeta_{CWP;up}$ increases for...	↓	↓	↑	↓	-	↑	-

8.4.4. Unpressurized pipe versus pressurized pipe

8.4.4.1. Results

The relevance of the different single and combined parameters is first studied. The following single parameters impact the strain capacity of the pressurized pipe relative to the unpressurized pipe:

- relative initial crack depth a_0 / t
- relative crack length c / W
- mismatch level MM_{FS}
- misalignment e / t

The corresponding fitting coefficients are listed in Table 8.11. The obtained variability $\psi = 0.14$ is relatively high, though it is noted that only a minor decrease was observed when considering all single and combined parameters ($\psi = 0.13$).

Table 8.11. Overview of fitting coefficients and resulting variability for comparison of the strain capacity of pressurized pipes relative to unpressurized pipes

parameter		statistical solution
constant	c_0	1.100
a_0 / t	c_1	-0.534
c / W	c_2	-3.864
MM_{FS}	c_3	0.008
e / t	c_4	-0.123
$\hat{a}_1$		0.026
$\hat{a}_2$		1.012
ψ		0.14

8.4.4.2. Discussion

For shorter defects, the strain capacity of the pressurized pipes is closer to the unpressurized case. This trend is, somewhat surprising, opposite to the observed dependency in the preliminary analysis. This is however attributed to the reduction of the selected defect lengths used in the simulations, for two reasons:

- the observed effect of the initial crack depth was much more pronounced for longer defects, which are not part of the current test matrix
- for shorter defects, the occurrence of global collapse is more likely. In this case the pressurized pipe's strain capacity will approximate or even exceed the strain capacity of the unpressurized pipe as was discussed in section 8.4.2.

Regarding the relative crack length, an increase results in a decrease of the relative strain capacity $\zeta_{pp;up}$. This trend is similar to the preliminary analysis, though furthermore strengthened by the global collapse limit state, as global collapse is more likely for shorter defects. Similarly, the influence of the weld metal strength mismatch can be explained. The higher the mismatch level, the more likely becomes global collapse. Hence, the relative strain capacity increases for higher overmatch levels.

The effect of the misalignment is not surprising, since similar observations were reported in literature [8.9, 21]. The additional plasticity around the crack tip, which is induced by the misalignment, results in a pronounced deterioration of the flawed zone in combination with the already increased plasticity in this crack tip region for the pressurized pipes.

In conclusion, the quantitative effect of the relevant single parameters on the relative strain capacity is schematically presented in Table 8.12.

Table 8.12. Influence of single effects on strain capacity of pressurized pipes relative to unpressurized pipes

	a_0/t	c/w	Y/T_{BM}	Y/T_{WM}	δ_l	MM_{FS}	e/t
$\zeta_{pp;up}$ increases for...	↓	↓	-	-	-	↑	↓

Using the obtained relative strain capacity data for this set of welded specimens, a comparison is made to the pressure corrections presented in literature (see also section 1.3 in Chapter 1). Recall first that the ExxonMobil procedure, published by Fairchild et al. [8.22], uses an average relative strain capacity $\zeta_{up;pp}$ equal to 1.85. This value, represented by the green line in Figure 8.19, corresponds closely to the current set of simulated relative strain capacities, for which an average value of 1.92 is obtained. Second, the correction factor of the CRES-BP procedure is compared to the simulated data [8.16]. This correction factor aims at conservatively predicting the strain capacity of unpressurized pipes based on the strain capacity of the pressurized ones. The correction factor is function of the relative crack depth. Using this correction factor, presented by the red line in Figure 8.19, yields conservative estimates in most studied cases, though leaves an enormous variability for the simulated data. This variability potentially induces a high degree of conservatism.

More importantly is however that this correction factor yields potentially unconservative estimates of the strain capacity for unpressurized pipes, in particular for shallow notches ($a_0 / t = 0.14$). This is potentially attributed to the failure through global collapse, particularly observed for these cases. As discussed in section 8.4.2, this results in strain capacities exceeding the material's uniform elongation for pressurized pipes, in contrast to the unpressurized ones. It is however unclear if these cases have been accounted for in the CRES-BP formulation or not, although this could logically be expected since specimens with strength mismatch levels up to 30% in terms of tensile strength and similar crack sizes as used in this work have been studied.

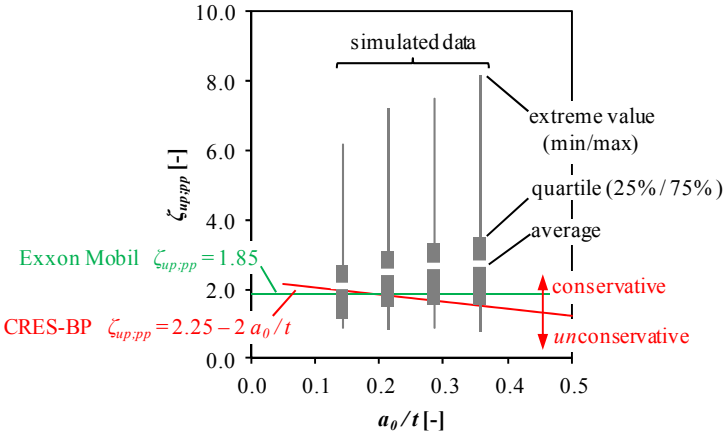

Figure 8.19. Comparison between simulated relative strain capacity $\zeta_{up;pp}$ and correction factor presented in literature
(CRES-BP and Exxon Mobil procedure [8.16, 22])

8.4.5. CWP specimen versus pressurized pipe

The correlation between the tensile strain capacity of CWP specimens and pressurized pipe specimens represents the actual pressure correction function. This relative strain capacity can be interpreted as the ratio between $\zeta_{pp;up}$ and $\zeta_{CWP;up}$. Hence, it is expected that the influence of a single parameter on $\zeta_{pp;CWP}$ can be derived from the minimization and/or maximization of $\zeta_{CWP;up}$ and $\zeta_{pp;up}$ respectively (Table 8.13). This particularly holds when the parameter only indicates a significant contribution to either $\zeta_{pp;up}$ or $\zeta_{CWP;up}$. This for instance applies to the influence of misalignment, whose influence on $\zeta_{pp;CWP}$ can be adopted from $\zeta_{pp;up}$. The influence of the weld metal's Y/T-ratio however contrasts the expectations. This is attributed to a dominating dependency of $\zeta_{pp;up}$ to this parameter, notwithstanding this parameter was not selected (significance slightly higher than 10^{-8} for $\zeta_{pp;up}$). Note also that for these parameters that significantly affect both $\zeta_{pp;up}$ and $\zeta_{CWP;up}$, the minimization/maximization rule results in contrasting requirements in the present study. Hence, their final dependency depends on the dominance of the parameter for either $\zeta_{pp;up}$ or $\zeta_{CWP;up}$.

Table 8.13. Influence of single effects on strain capacity of pressurized pipes relative to CWP specimens

	a_0/t	c/w	Y/T_{BM}	Y/T_{WM}	δ_l	MM_{FS}	e/t
$\zeta_{pp;up}$ maximum for...	↓	↓	-	-	-	↑	↓
$\zeta_{CWP;up}$ minimum for...	↑	↑	↓	↑	-	↓	-
$\zeta_{pp;CWP}$ increases for...	↑	↓	↓	↓	-	↑	↓

The linear fit parameters and resulting variability are provided in Table 8.14. An overview of this linear trend and the simulated data is plotted in Figure 8.21.a. Remark first that the CWP test strain capacity is not necessarily lower than the one of the pressurized pipe; several values for the relative strain capacity $\zeta_{pp;CWP}$ are obtained beyond unity. Second, the reported anomaly described in section 8.4.2 is studied. In that section, it was stated that the tensile strain capacity for pressurized pipes that fail through collapse is underestimated, since the maximum in the load-displacement curve cannot be reached. The moment of maximum force coincides with the end of the simulation. Nevertheless, the failure is categorized as plastic collapse for these specimens (in addition to these cases where plastic collapse is correctly predicted). Subsequently, distinction can be made between the relative strain capacities that are categorized as plastic collapse and those that are not (Figure 8.20). Since the data points that are related to plastic collapse are approximately uniformly spread through the cloud of data points, no significant influence of this anomaly on the pressure correction function is expected.

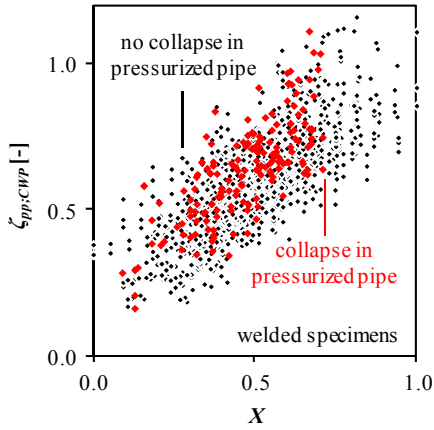

Figure 8.20. Evaluation of relative strain capacity $\zeta_{pp;CWP}$ for all simulated cases, with indication of data points representing prediction of collapse for the pressurized pipe (red)

Table 8.14. Overview of fitting coefficients and resulting variability for comparison of CWP specimen to pressurized pipe

parameter		statistical solution
constant	c_0	0.629
a_0 / t	c_1	1.053
c / W	c_2	-1.379
MM_{FS}	c_3	0.069
e / t	c_4	-0.119
$a_0 / t \cdot c / W$	c_5	6.236
$a_0 / t \cdot Y/T_{WM}$	c_6	-0.854
$c / W \cdot Y/T_{WM}$	c_7	-1.799
$Y/T_{BM} \cdot MM_{FS}$	c_8	-0.071
$\hat{a}_1$		0.271
$\hat{a}_2$		0.701
ψ		0.11

Third, the variability is relatively high, $\psi = 0.11$, resulting in a 95% confidence interval of ± 0.22 with respect to the relative strain capacity $\zeta_{pp;CWP}$. This potentially results in a large underestimation of the tensile strain capacity for the pressurized pipes, based on the outcome of a CWP test. This particularly holds for situations corresponding to small $\boldsymbol{X}$ values. For sake of completeness, the nominal error is calculated based on the following relationships:

$$\zeta_{pp;CWP}\Big|_{avg} = \hat{a}_1 + \hat{a}_2 X \tag{8.9}$$

$$\zeta_{pp;CWP}\big|_{\min} = \hat{a}_1 + \hat{a}_2 X - 1.96\psi \tag{8.10}$$

$$error = \frac{\left|\zeta_{pp;CWP}\big|_{avg} - \zeta_{pp;CWP}\big|_{\min}\right|}{\zeta_{pp;CWP}\big|_{avg}} \tag{8.11}$$

This error is presented in Figure 8.21.b. On average, an underestimation of 40% is observed, with extremes for small ***X***-values up to 80%. To eliminate these extreme values, an additional lower bound limit is added to the pressure correction function. This lower bound takes into account that not a single simulated relative strain capacity was lower than 0.16. This results in the following corrected pressure correction function:

$$\zeta_{pp;CWP}\big|_{corrected} = \max\left(\hat{a}_1 + \hat{a}_2 X - 1.96\psi; 0.16\right) \tag{8.12}$$

This corrected function is shown in Figure 8.21.b, which additionally illustrates that the maximum error does not exceed 57%. The average error however remains relatively high, 37%. Accordingly, it is recognized that this high scatter and corresponding error might hamper the application of the pressure correction function. As a result, the following two-level assessment is proposed:

- *Level 1: analytical assessment* For the first level, the use of the presented pressure correction function (Eq.(8.12)) is advised. This results in a quick evaluation of the tensile strain capacity for the pressurized pipe, though inhibits a variable degree of conservatism.
- *Level 2: finite element assessment* For the second level, the pressure correction function is determined using a well focused finite element study, that considers project specific geometrical and material properties. As such, the scatter that is observed in the current study can be reduced.

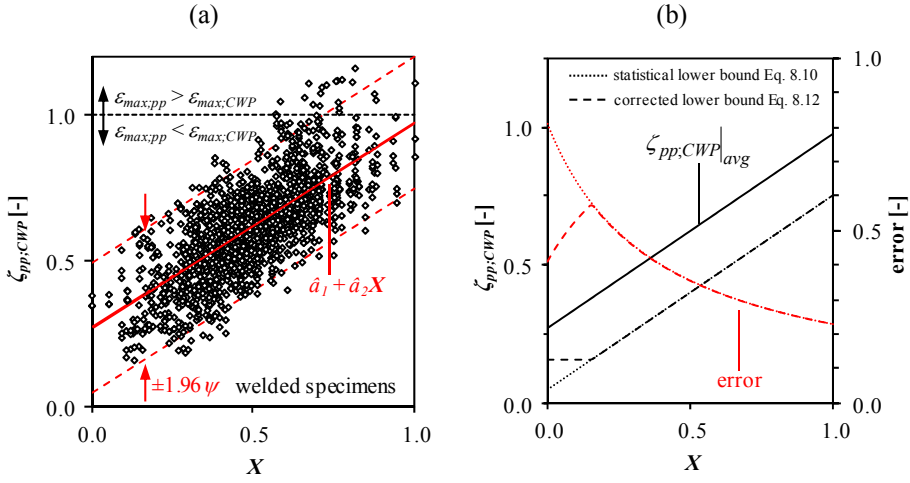

Figure 8.21. Simulated data plotted with proposed solution for evaluation of $\zeta_{pp;CWP}$ (a) and potential underestimation error based on statistical 95% confidence interval (b)

8.4.6. Summary

The presented study, aiming to clarify the strain capacity of pressurized pipes relative to CWP specimens, indicated that the following parameters have a pronounced impact:

- weld metal strength mismatch
- misalignment
- defect dimensions (length and depth)
- strain hardening capacity of both the weld and base metal (Y/T_{BM} and Y/T_{WM})

In contrast, the material's tearing resistance has no pronounced influence on the relative strain capacity. Based on a linear combination of these parameters that have a pronounced impact, and also considering some combined effects, a pressure correction function has been proposed. It is however noted that, given the large scatter of the simulated data with respect to this correction function, the conservatism involved in such analysis might be significant. Therefore, a second assessment level is added. For this second level approach, a project specific pressure correction function is derived based on finite element simulations of representative cases.

It is finally noted that application of the presented equation(s) is strictly limited to the studied configurations. Recall that, for instance, the weld geometry and defect location (inner versus outer diameter) might have a pronounced impact.

8.5. Conclusions

Based on an extensive set of finite element simulations for both welded and non-welded specimens, it is concluded that the following parameters primarily affect the strain capacity of pressurized pipes relative to CWP specimens:

- weld metal strength mismatch
- misalignment
- defect dimensions (length and depth)
- strain hardening capacity of both the weld and base metal (Y/T_{BM} and Y/T_{WM})

In contrast, the uniform elongation and tearing resistance indicated a rather negligible influence on this relative strain capacity.

These studies eventually led to the formulation of a two-level approach for the evaluation of the relative strain capacity $\zeta_{pp;CWP}$. For the first level, an analytical correction function is presented that allows estimating the strain capacity for pressurized pipes based on the outcome of a CWP test (Eq.(8.13)&(8.14)). The values for the fitting coefficients in the expression below are provided in Table 8.15.

$$\zeta_{pp;CWP} = \max\left(\hat{a}_1 + \hat{a}_2 X - 1.96\psi; 0.16\right) \tag{8.13}$$

$$X = c_0 + c_1\frac{a_0}{t} + c_2\frac{c}{W} + c_3 MM_{FS} + c_4\frac{e}{t} + c_5\frac{a_0}{t}\frac{c}{W} + c_6\frac{a_0}{t}Y/T_{WM} + c_7\frac{c}{W}Y/T_{WM} + c_8 Y/T_{BM} MM_{FS} \tag{8.14}$$

Table 8.15. Fitting coefficients for pressure correction function $\zeta_{pp;CWP}$

c_0	c_1	c_2	c_3	c_4	c_5	c_6	c_7	c_8
0.629	1.053	-1.379	0.069	-0.119	6.236	-0.854	-1.799	-0.071

$\hat{a}_1$	$\hat{a}_2$	ψ
0.271	0.701	0.11

However, the application of this pressure correction function should be restricted to situations confined within the boundaries of the test matrix used to derive this equation. In addition, this analytical expression introduces conservativeness in the assessment. To overcome these shortcomings, a second assessment level is added. A project specific pressure correction function can be established based on finite element simulations. To develop this correction function, the framework presented in this chapter can be applied.

8.6. Bibliography

[8.1] Knauf, G., and Hopkins, P., 1996, "The EPRG Guidelines on the Assessment of Defects in Transmission Pipeline Girth Welds", 3R International, 35, pp. 620-624.

[8.2] Ostby, E., and Hellesvik, A. O., 2008, "Large-Scale Experimental Investigation of the Effect of Biaxial Loading on the Deformation Capacity of Pipes with Defects", International Journal of Pressure Vessels and Piping, 85, pp. 814-824.

[8.3] Gordon, J. R., Zettlemoyer, N., and Mohr, W. C., 2007, "Crack Driving Force in Pipelines Subjected to Large Strain and Biaxial Stress Conditions", International Offshore and Polar Engineering Conference, Lisbon, Portugal, pp. 3129-3140.

[8.4] Hertelé, S., 2012, "Coupled Experimental-Numerical Framework for the Assessment of Strain Capacity of Flawed Girth Welds in Pipelines", Ph.D. thesis, Ghent University, Ghent, Belgium.

[8.5] Denys, R., and Lefevre, A. A., 2009, "UGent Guidelines for Curved Wide Plate Testing", Pipeline Technology Conference, Ostend, Belgium, paper n° Ostend2009-110.

[8.6] Kibey, S. A., Lele, S. P., Tang, H., Macia, M. L., Fairchild, D. P., Cheng, W., Noecker, R., Wajutelewicz, P. J., Newbury, B., Kan, W. C., and Cook, M. F., 2011, "Full-Scale Test Observations for Measurement of Tensile Strain Capacity of Welded Pipelines", International Offshore and Polar Engineering Conference, Maui, Hawaii, USA, pp. 660-667.

[8.7] Jayadevan, K. R., Ostby, E., and Thaulow, C., 2004, "Fracture Response of Pipelines Subjected to Large Plastic Deformation under Tension", International Journal of Pressure Vessels and Piping, 81, pp. 771-783.

[8.8] Wilcox, R. R., 2010, "Fundamentals of Modern Statistical Methods: Substantially Improving Power and Accuracy", Springer, Los Angeles.

[8.9] Kibey, S. A., Minnaar, K., Issa, J. A., and Gioielli, P. C., 2008, "Effect of Misalignment on the Tensile Strain Capacity of Welded Pipelines", International Offshore and Polar Engineering Conference, Vancouver, Canada, pp. 90-95.

[8.10] Denys, R. M., and De Waele, W., 2009, "Comparison of API 1104 - Appendix a Option 1 and EPRG-Tier 2 Defect Acceptance Limits", Pipeline Technology Conference, Ostend, Belgium, paper n° Ostend2009-113.

[8.11] Denys, R., Andrews, R., Zarea, M., and Knauf, G., 2010, "EPRG Tier 2 Guidelines for the Assessment of Defects in Transmission Pipeline Girth Welds", International Pipeline Conference, Calgary, Alberta, Canada, paper n° IPC2010-31640.

[8.12] American Society of Testing and Materials, 2011, E1820 - Standard Test Method for Measurement of Fracture Toughness.

[8.13] Fairchild, D. P., Macia, M. L., Kibey, S., Wang, X., Krishnan, V. R., Bardi, F., Tang, H., and Cheng, W., 2011, "A Multi-Tiered Procedure for Engineering Critical Assessment of Strain-Based Pipelines", International Offshore and Polar Engineering Conference, Maui, HI, United States, pp. 698-705.

[8.14] Hertelé, S., De Waele, W., and Denys, R., 2011, "A Generic Stress-Strain Model for Metallic Materials with Two-Stage Strain Hardening Behaviour", International Journal of Non-Linear Mechanics, 46, pp. 519-531.

[8.15] Denys, R. M., Hertelé, S., De Waele, W., and Lefevre, A. A., 2009, "Estimate of Uniform Elongation (uEL) Capacity of Pipeline Steels from Yield Strength", Pipeline Technology Conference, Ostend, Belgium, paper n° Ostend2009-108.

[8.16] Liu, M., Wang, Y. Y., Song, Y., Horsley, D., and Nanney, S., 2012, "Multi-Tier Tensile Strain Models for Strain-Based Design - Part 2: Development and Formulation of Tensile Strain Capacity Models", International Pipeline Conference, Calgary, Alberta, Canada, paper n° IPC2012-90659.

[8.17] Wang, S., Kibey, S., Minnaar, K., Macia, M., Fairchild, D. P., Kan, W. C., Ford, S. J., and Newburry, B., 2011, "Strain-Based Design - Advances in Prediction Methods of Tensile Strain Capacity", International Journal of Offshore and Polar Engineering, 21, pp. 1-7.

[8.18] European Committee for Standardization, 2010, EN 12732: Gas Supply Systems. Welding Steel Pipework. Functional Requirements.

[8.19] Canadian Standards Association, 2011, Z662 - 11: Oil and Gas Pipeline Systems.

[8.20] Lin, G., Meng, X.-G., Cornec, A., and Schwalbe, K. H., 1999, "The Effect of Strength Mismatch on Mechanical Performance of Weld Joints", International Journal of Fracture, 96, pp. 37-54.

[8.21] Kan, W. C., Weir, M., Zhang, M. M., Lillig, D. B., Barbas, S. T., Macia, M. L., and Biery, N. E., 2008, "Strain Based Pipelines: Design Consideration Overview", International Offshore and Polar Engineering Conference, Vancouver, Canada, pp. 174-181.

[8.22] Fairchild, D. P., Kibey, S., Tang, H., Krishnan, V. R., Macia, M. L., Cheng, W., and Wang, X., 2012, "Continued Advancements Regarding Capacity Prediction of Strain-Based Pipelines", International Pipeline Conference, Calgary, Alberta, Canada, paper n° IPC2012-90471.

Chapter 9

–

Conclusions and Outlook for Future Research

9.1. General conclusions

Several procedures have recently been developed for the assessment of girth weld defects under so-called strain based conditions. A literature review of these assessment procedures, presented in Chapter 1, identified the following research needs:

- selection of suitable laboratory scale test specimen and establishing a methodology for the evaluation of the tearing resistance, and
- quantification of the influence of internal pressure on the tensile strain capacity, allowing to relate the tensile strain capacity of pressurized pipes to curved wide plate (CWP) specimens.

To address these challenges, this work adopts a mixed experimental-numerical research methodology, described in section 9.1.1. An overview of the main research results is presented in 9.1.2.

9.1.1.Methodology

9.1.1.1. Experimental

Effort has been made to evaluate the tearing resistance using laboratory scale test specimens. The literature study presented in Chapter 2 revealed that SENT specimens are most suitable for this purpose, since their constraint approximates the constraint in (pressurized) pipes in a conservative way.

For the evaluation of the tearing resistance, an accurate evaluation of the ductile crack extension and CTOD is required. Both have been experimentally evaluated for a series of SENT specimens in the framework of this dissertation.

To measure the ductile crack extension, the unloading compliance (UC) and direct current potential drop (DCPD) methods have been studied. Both methods are standardized for SENB and CT testing. However, no specific procedures are available for SENT testing. In this dissertation, a methodology, described in full detail in Chapter 3, has been established for both measurement methods. This allowed first to evaluate the accuracy of these methods, but also to compare the crack growth measurement methods. As such, the equivalence of the UC and DCPD methods has been demonstrated. The obtained accuracy and the scatter of the resulting tearing resistance curves are similar for both crack growth measurement methods.

To evaluate the crack tip opening displacement, the double clip gauge and δ_5 methods have been studied in Chapter 4 of this dissertation. Both methods yield similar CTOD values. Although, for increasing toughness levels, the δ_5 method results in a slight underestimation with respect to the CTOD values obtained using the double clip gauge method. This difference is attributed to a minor difference in the CTOD definitions corresponding to both methods.

To further investigate the relation between crack extension and deformation around the crack in SENT specimens, full field deformation measurements have been performed during the experiments. These measurements not only allowed to evaluate the CTOD (through the previously discussed δ_5 method), though also enabled the identification of characteristic deformation patterns. As such,

non-symmetrical deformation patterns have been identified for welded specimens, though these did not affect the tearing resistance (Chapter 6).

To demonstrate the robustness of the presented measurement methods, and also to improve the comparability of the experimental data, some of the presented test methods have also been applied to medium wide plate (MWP) tests. As such, it has been demonstrated that the double clip gauge method and direct current potential drop method allow evaluating the ductile tearing resistance in both SENT and MWP specimens. In addition, full field strain measurements have shown benefits regarding the evaluation of mismatch and heterogeneity effects on the strain distribution in MWP specimens.

9.1.1.2. Numerical

The quantification of the strain capacity of pressurized pipes relative to this of CWP specimens is based on finite element simulations. This is related to the need for high test capacities, the potential heterogeneity (in particular for welded specimens) and the large number of parameters involved. To evaluate the tensile strain capacity, the tangency approach has been adopted. Note that this approach also forms the baseline for multiple strain based defect assessment procedures [9.1-5]. This approach requires knowledge of the tearing resistance and crack driving force. In this dissertation, the latter is obtained from finite element simulations; the tearing resistance is a required input parameter.

The tearing resistance strongly depends on the constraint. To evaluate the constraint, the Q-parameter, Q_m-parameter and triaxiality parameter h have been considered in this dissertation (Chapter 2). All three are based on the analysis of the crack tip stress fields, obtained from detailed finite element studies. These finite element studies have indicated that the Q-parameter has a lower ability to describe the out-of-plane constraint effects, in contrast to the other parameters (Chapter 7). This out-of-plane constraint is particularly relevant when ductile failure is studied. Hence, preference should be given to the Q_m-parameter and stress triaxiality parameter h for a comparison of the constraint in pressurized pipes and CWP specimens.

9.1.1.3. Combined experimental-numerical

In addition, finite element simulations have also been considered to improve the interpretation of experimental test results. More specifically, the use of elastic-plastic finite element simulations provided an improved understanding of the experimentally observed compliance evolution. In addition, coupled thermal-electric simulations have proven to be a valuable tool for the calculation of the crack extension based on the experimentally measured potential drop data.

9.1.2.Main results

9.1.2.1. Evaluation of ductile tearing resistance

Using the validated test methods for the evaluation of the ductile crack extension and CTOD, effort has been made to establish guidelines for the evaluation of the tearing resistance using SENT specimens (Chapter 5).

The experiments have indicated that the notch orientation and relative crack depth (potentially) have a pronounced impact on the tearing resistance of (welded) specimens. The influence of the notch depth is attributed to a constraint difference. The weld metal heterogeneity results in a sensitivity to the notch orientation (outer diameter, inner diameter and through thickness defects have been studied).

In contrast, the extraction position of the test specimen along the weld's circumference (o'clock position) did not indicate any significant influence on the tearing resistance for the tested weld. Based on these observations, and aiming for a limitedly conservative assessment, the following recommendations have been formulated regarding the evaluation of the tearing resistance, as input for defect assessment procedures:

- *selection of notch orientation*: the use of through thickness notched specimens for the evaluation of the tearing resistance is discouraged since these do not represent the actually assessed defects. However, the use of through thickness notched specimens potentially reveals the zones that have the lowest tearing resistance based on the crack front shape. Alternatively, hardness mapping of the weldment allows assessing its heterogeneity.
- *relative notch depth*: the relative notch depth is preferably varied between the crack depths that need to be assessed. Selecting only these notch depths that result in the highest constraint, i.e. deepest notches, is not necessarily conservative as the weld metal heterogeneity potentially dominates the constraint effect. Hence, lower resistance curves might be observed for more shallow notches, despite the lower constraint.

In addition, it is recommended to test multiple specimens with identical notch depth, orientation, … Although not explicitly observed in the current study, material heterogeneity potentially results in locally deteriorated material properties. Using laboratory scale test specimens, these potentially result in an erroneous estimation of the tearing resistance. To that extent, the ASTM E1820 recommendations for SENB testing could be adopted, which state that each test should be repeated at least three times [9.6].

For a number of SENT specimens, the tearing resistance has been evaluated against MWP specimens extracted adjacent to these SENT specimens. Based on the results of five MWP tests, it has been concluded that the constraint in SENT specimens is higher compared to MWP specimens. Given the constraint match between wide plate specimens and (pressurized) pipes, as noted in section 9.1.2.2, this suggests that a defect assessment that is based on SENT tests is potentially more conservative compared to an assessment that is based on wide plate test results.

9.1.2.2. Quantification of relative strain capacity

The quantification process, as indicated in section 9.1.1.2, consists of a constraint evaluation followed by a comparison of the tensile strain capacities, based on simulations of CWP tests and axial tension tests on (pressurized) pipes.

First, the constraint difference between (pressurized) pipes and CWP specimens has been investigated using the Q, Q_m and h parameters (Chapter 7). This investigation revealed that, relative to unpressurized pipes, the crack tip constraint in CWP specimens is slightly higher. The difference between both is influenced by the defect size and pipe curvature. For increasing crack sizes, the constraint marginally increases in CWP specimens relative to unpressurized pipes. Similarly, an increase of the constraint has been observed in CWP specimens extracted from pipe with a higher diameter. In contrast, the constraint in pipes is not affected by the pipe diameter. Focusing on the internal pressure effect, a slight increase of the out-of-plane constraint has been observed. This constraint change is independent of the defect location (inner or outer diameter). Based on these observations, a marginal difference in tearing resistance is expected for CWP specimens and (pressurized) pipes. In combination with results published in literature, the tearing resistance curve used for the evaluation of the strain capacity of (pressurized) pipes and CWP specimens has however been assumed identical.

The latter is an important observation for the second step in the quantification process. This second step comprises the evaluation of the (relative) strain capacity between pressurized pipes and CWP specimens using the tangency approach (Chapter 9). To that extent, distinction has been made between geometrical effects (CWP versus unpressurized pipe) and pressure effects (pressurized versus unpressurized pipe). For each effect, the parameters that most importantly contribute to the difference in strain capacity have been identified. As regards the comparison of CWP specimens to unpressurized pipe specimens, the crack size and mismatch level are the most dominant parameters. For the comparison of unpressurized with pressurized pipe specimens, the presence of weld metal misalignment additionally controls the relative strain capacity. These parameters also primarily influenced the relative strain capacity of pressurized pipes to CWP specimens. No significant influence of the material's uniform elongation and the tearing resistance on the relative strain capacity has been observed.

Eventually, this study has led to the formulation of a two-level pressure correction approach. For the first level, an analytical pressure correction function has been proposed that allows assessing the tensile strain capacity of pressurized pipes from CWP test data. This correction function was derived as lower bound to an extensive series of simulation results and therefore induces a relatively high degree of conservatism. It is important to mention that application of this analytical equation is, in terms of (weld) geometry and material properties, restricted to the simulated configurations. As a result, a second assessment level has been introduced that allows evaluating a project-specific pressure correction function. To that extent, the methodology presented in this dissertation, i.e. based on finite element simulations in combination with the tangency approach, has been advised.

In conclusion, the pressure correction approach can be combined with the analytical UGent strain based design equation, presented in section 1.2.3. This allows to conservatively estimate the tensile strain capacity of pressurized pipes.

9.2. Outlook for future research

9.2.1.Extension and evaluation of SENT guidelines

Effort has been made within this dissertation to establish testing methodologies for the evaluation of the tearing resistance using SENT specimens. Using these validated methodologies, the presented guidelines should be more extensively validated, since these are currently based on observations from a limited number of weldments.

Another extension of the evaluation of these guidelines is to study the tearing resistance for HAZ defects. This inhibits a number of particularities related to:

- orientation and heterogeneity: similar to the studies performed on weld metal center line defects, these should also be considered in addition to the variability due to the heterogeneous nature of the materials.
- crack extension path: for all tested weld metal center line cracks, crack extension has been observed along the crack plane (i.e. perpendicular to the loading direction). However, given the weld geometry and the heterogeneous material properties, it is likely that the crack path deviates from this plane for HAZ defects.

9.2.2.Numerical-experimental constraint evaluation

In this dissertation, the study of the crack tip constraint provided insight in the potential difference between specimen types. To address this issue, finite element simulations have primarily been considered. It remains however crucial to evaluate the observed finite element results and to quantify the observed trends in terms of tearing resistance.

To that extent, the development of a new constraint framework is advised. This framework preferably allows to evaluate the constraint both experimentally and numerically. The use of (surface) strains is therefore suggested, as these can both be simulated and measured experimentally. The results from the full field deformation measurements presented in Chapter 6 are a potential first step towards the development of such framework. Recall that, for a series of welded and non-welded specimens, a linear relationship has been reported between the maximum elastic-plastic surface strains and the (initiation) toughness. If these observations can be generalized and compared to simulations, thereby carefully assessing out-of-plane effects, constraint evaluations potentially become less abstract and more easily interpretable/applicable in practice.

9.2.3.Extension towards multiple/embedded defects

Within this dissertation, only single, surface breaking defects with constant depth have been studied. Such studies imply a number of simplifications compared to defects observed in the field. In practice defects are irregularly shaped, sometimes embedded or multiple defects appear in the same girth weld. Studying the effect of multiple defects and evaluating the relationship between embedded and surface breaking defects therefore deserves attention.

Regarding the study of embedded defects, Østby et al. [9.7] have recently reported that the conversion formulae, available in standards (e.g. DNV-RP-F108 [9.8]), are potentially unconservative under strain based conditions.

The presence of multiple defects along the pipes circumference comprises two facets.

- It is unclear whether these strain based criteria can be interpreted as a defect tolerance per 300 mm arc length. This is common practice for stress based workmanship criteria [9.9, 10]. Hence, it is recommended to study the tensile strain capacity of (pressurized) pipes containing multiple defects along their circumference.
- Multiple (small) defects might as well be present in each other's vicinity. In this case, it is advisable to evaluate whether these can be treated as individual defects or will be extending towards each other. The latter would clearly result in a deterioration of the tensile strain capacity.

9.3. Bibliography

[9.1] Det Norske Veritas, 2012, OS-F101: Submarine Pipeline Systems.

[9.2] Fairchild, D. P., Macia, M. L., Kibey, S., Wang, X., Krishnan, V. R., Bardi, F., Tang, H., and Cheng, W., 2011, "A Multi-Tiered Procedure for Engineering Critical Assessment of Strain-Based Pipelines", International Offshore and Polar Engineering Conference, Maui, HI, United States, pp. 698-705.

[9.3] Wang, Y. Y., Liu, M., Zhang, F., Horsley, D., and Nanney, S., 2012, "Multi-Tier Tensile Strain Models for Strain-Based Design - Part 1: Fundamental Basis", International Pipeline Conference, Calgary, Alberta, Canada, paper n° IPC2012-90690.

[9.4] Liu, M., Wang, Y. Y., Song, Y., Horsley, D., and Nanney, S., 2012, "Multi-Tier Tensile Strain Models for Strain-Based Design - Part 2: Development and Formulation of Tensile Strain Capacity Models", International Pipeline Conference, Calgary, Alberta, Canada, paper n° IPC2012-90659.

[9.5] Liu, M., Wang, Y. Y., Horsley, D., and Nanney, S., 2012, "Multi-Tier Tensile Strain Models for Strain-Based Design - Part 3: Model Evaluation Agains Experimental Data", International Pipeline Conference, Calgary, Alberta, Canada, paper n° IPC2012-90660.

[9.6] American Society of Testing and Materials, 2011, E1820 - Standard Test Method for Measurement of Fracture Toughness.

[9.7] Ostby, E., Nyhus, B., and Thaulow, C., 2011, "Small-Scale Testing of the Effect of Embedded Defect Position in the Thickness Direction of an X65 UOE Pipe", International Offshore and Polar Engineering Conference, Maui - USA, pp. 593-599.

[9.8] Det Norske Veritas, 2006, RP-F108: Fracture Control for Pipeline Installation Methods Introducing Cyclic Plastic Strain.

[9.9] 2010, API 1104: Welding of Pipelines and Related Facilities.

[9.10] Knauf, G., and Hopkins, P., 1996, "The EPRG Guidelines on the Assessment of Defects in Transmission Pipeline Girth Welds", 3R International, 35, pp. 620-624.

Appendix A

–

Experimental Work:

Overview of Test Specimens

A.1. Introduction

This appendix presents an overview of all fracture mechanics test specimens that are tested in the framework of this dissertation. Distinction is made between:

- small scale test specimens, i.e. SENT and SENB, and
- medium wide plate (MWP) test specimens.

For each specimen, the respective chapter(s) is (are) listed in which the test results are considered. For an exact description of the geometry of these test specimens, the reader is referred to the section "Research approach" in Chapter 2.

A.2. Small scale test specimens

Two types of small scale test specimens are considered in the framework of this dissertation. Although the majority concerns SENT testing, the result of a single SENB test is also considered (Table A.1). The SENT specimens are divided in homogeneous and welded specimens, listed in Table A.2 and Table A.3 respectively. Note that the last columns of each table contain a reference to the chapters in which the results of the respective specimens are considered.

Table A.1. Homogeneous SENB specimen

Specimen	B [mm]	W [mm]	a_0/W [-]	API-5L Grade	Y/T [-]	Chapter			
						3	4	5	6
SENB-01	14.0	28.0	0.25	X60	0.75				•

Table A.2. Overview of homogeneous SENT specimens

Specimen	B [mm]	W [mm]	a_0/W [-]	API-5L Grade	Y/T [-]	Chapter			
						3	4	5	6
BM-01	15.0	15.0	0.20	X80	0.86	•	•	•	•
BM-02	15.0	15.0	0.20	X80	0.86	•	•	•	•
BM-03	15.0	15.0	0.40	X80	0.86	•	•	•	•
BM-04	15.0	15.0	0.40	X80	0.86	•	•	•	•
BM-05	15.0	15.0	0.60	X80	0.86	•	•	•	•
BM-06	15.0	15.0	0.60	X80	0.86	•	•	•	•
BM-07	15.0	15.0	0.50	X80	0.86	•	•	•	•
BM-08	15.0	15.0	0.50	X80	0.86	•	•	•	•
BM-09	15.0	15.0	0.50	X80	0.86	•	•	•	•
SENT-01	28.0	14.0	0.25	X60	0.75				•
WP1-01	14.0	14.0	0.21	X65	0.82	•		•	
WP1-02	14.0	14.0	0.21	X65	0.82	•		•	
WP1-03	14.0	14.0	0.21	X65	0.82	•		•	
WP1-04	14.0	14.0	0.21	X65	0.82	•		•	

Table A.3. Overview of welded SENT specimens

Specimen	$W = B$ [mm]	a_0/W [-]	API-5L Grade	Y/T_{BM} [-]	Y/T_{WM} [-]	Notch	Welding Process	MM_{FS} [%]	Chapter 3	4	5	6
WM-01									•	•	•	
WM-02	12.5	0.50	X80	0.91	0.83	WMC root	SMAW	+1	•	•	•	
WM-03									•	•	•	
WM-04									•	•	•	
WM-05	12.5	0.50	X80	0.91	0.93	WMC root	GMAW	+33	•	•	•	
WM-06									•	•	•	
WM-07									•		•	•
WM-08	15.0	0.40	X80	0.86	0.93	WMC cap	GMAW	+20	•		•	•
WM-09									•		•	•
WM-10									•		•	•
WM-11	15.0	0.40	X80	0.86	0.93	WMC root	GMAW	+20	•		•	•
WM-12									•		•	•
WM-13									•		•	•
WM-14	15.0	0.40	X80	0.86	0.93	WMC TT[1]	GMAW	+20	•		•	•
WM-15									•		•	•
WP2-01									•		•	
WP2-02									•		•	
WP2-03	11.5	0.28	X70	0.90	0.91	WMC root	GMAW	+6	•		•	
WP2-04									•		•	
WP2-05									•		•	
WP2-06									•		•	
WP3-01									•		•	
WP3-02									•		•	
WP3-03	11.5	0.28	X70	0.92	0.89	WMC root	GMAW	+0	•		•	
WP3-04									•		•	
WP3-05									•		•	
WP4-01									•		•	
WP4-02	14.0	0.30	X80	0.89	0.94	WMC root	GMAW	+8	•		•	
WP4-03									•		•	
WP5-01									•		•	
WP5-02	14.0	0.30	X80	0.91	0.94	WMC root	GMAW	+0	•		•	
WP5-03									•		•	

[1] through thickness direction

A.3. Medium wide plate test specimens

The medium wide plate specimens considered in this dissertation are listed in Table A.4. Note that the name of the MWP specimens correlates to the name of some SENT specimens. These specimens are extracted adjacent to each other, as discussed in the section dealing with sampling position in Chapter 2 (e.g. the SENT specimen WP1-01 is extracted adjacent to MWP specimen WP-1).

Table A.4. Overview of MWP specimens

Specimen			WP-1	WP-2	WP-3	WP-4	WP-5	WP-6
a_0		[mm]	3.00	4.00	4.00	5.25	5.25	3.00
$2c$		[mm]	60	40	40	50	50	40
D		[mm]	flat	1219	1219	1219	1219	1219
t		[mm]	15.0	13.7	13.7	17.0	17.0	13.7
a_0/t		[-]	0.20	0.29	0.29	0.31	0.31	0.22
Notch		[-]	-	WMC root	WMC root	WMC root	WMC root	HAZ root
API-5L Grade		[-]	X65	X70	X70	X80	X80	X70
BM_A	$R_{p;0.2}$	[MPa]	450	559	570	555	586	572
	R_m	[MPa]	549	635	633	675	672	653
BM_B	$R_{p;0.2}$	[MPa]	-	557	569	564	581	550
	R_m	[MPa]	-	609	618	675	676	616
WM	$R_{p;0.2}$	[MPa]	-	597	563	666	625	659
	R_m	[MPa]	-	657	633	710	667	705
average mismatch	MM_{YS}	[%]	-	+ 6	- 2	+ 11	+ 2	+ 18
	MM_{FS}	[%]	-	+ 6	0	+ 8	0	+ 14
	MM_{TS}	[%]	-	+ 6	+ 1	+ 5	- 1	+ 11
Chapter	3		•	•	•	•	•	
	4		•	•	•	•	•	
	5		•	•	•	•	•	
	6		•	•	•	•	•	•

Appendix B

–

Statistical Analysis of Relative Strain Capacity

B.1. Introduction

This appendix provides more details regarding the statistical analysis going with the evaluation of the relative strain capacity between:

- CWP specimens and unpressurized pipes
- Pressurized and unpressurized pipes
- Pressurized pipes and CWP specimens

These results are summarized and discussed in Chapter 8.

B.2. Homogeneous specimens

B.2.1. Test matrix

All combinations of the material and geometrical properties listed in Table B.1 are simulated for the following specimens:

- CWP
- Pipe – no pressure (also referred to as: *up*)
- Pipe – $\sigma_{hoop} / \sigma_0 = 50\%$ (also referred to as: pp_{50})
- Pipe – $\sigma_{hoop} / \sigma_0 = 60\%$ (also referred to as: pp_{60})
- Pipe – $\sigma_{hoop} / \sigma_0 = 70\%$ (also referred to as: pp_{70})
- Pipe – $\sigma_{hoop} / \sigma_0 = 80\%$ (also referred to as: pp_{80})

This results in a total of 2304 simulated strain capacities and 384 relative strain capacities.

Table B.1. Considered properties for test matrix for the study of homogeneous specimens

c [mm]	a_0 [mm]	D [mm]	t [mm]	σ_0 [MPa]	post-yield characteristics (Y/T; uEL) ([-]; [%])	tearing resistance (δ_1; δ_2) ([-]; [-])
12.5	2.0	762	14	555	(0.80; 10.0)	(1.0; 0.20)
25.0	3.0				(0.80; 14.0)	(1.5; 0.35)
37.5	4.0				(0.85; 6.4)	(2.0; 0.50)
50.0	5.0				(0.85; 10.0)	
					(0.90; 4.8)	
					(0.90; 8.8)	
					(0.95; 3.2)	
					(0.95; 7.3)	

B.2.2. CWP versus unpressurized pipe

For all single and combined parameters, their statistical significance is studied in accordance with the statistical framework presented in Chapter 8 (Student's *t*-test). An overview of the obtained significance levels (*p*-levels) is provided in Table B.2.

The influence of the selected (most significant) parameters on the relative strain capacity is schematically provided in Table B.3.

Table B.2. Significance levels for all single and combined parameters involved in analysis of the relative strain capacity $\zeta_{CWP;up}$ of homogeneous specimens

single parameter	significance	combined parameter	significance
a_0/t	1×10^{-34}	$(a_0 \cdot c) / (t \cdot W)$	2×10^{-51}
c/W	3×10^{-18}	$a_0/t \cdot Y/T$	7×10^{-51}
Y/T	3×10^{-29}	$a_0/t \cdot uEL$	6×10^{-1}
uEL	3×10^{-8}	$a_0/t \cdot \delta_l$	1×10^{-40}
δ_l	2×10^{-6}		
		$c/W \cdot Y/T$	2×10^{-25}
		$c/W \cdot uEL$	6×10^{-1}
		$c/W \cdot \delta_l$	1×10^{-24}
		$Y/T \cdot uEL$	5×10^{-14}
		$Y/T \cdot \delta_l$	7×10^{-13}
		$uEL \cdot \delta_l$	6×10^{-5}

Table B.3. Visualization of the influence of parameters selected for preliminary test matrix regarding the relative strain capacity $\zeta_{CWP;up}$

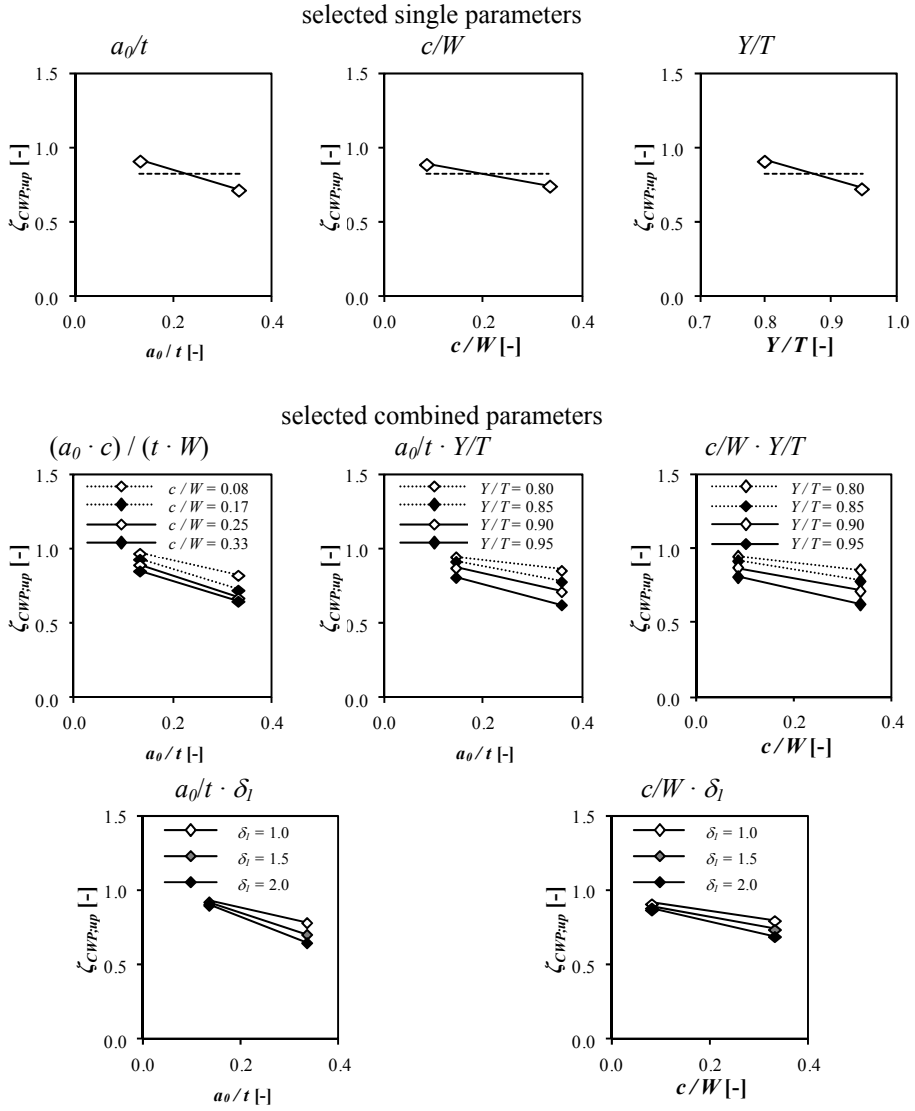

B.2.3. Pressurized versus unpressurized pipe

For the comparison of the strain capacity of the pressurized with the unpressurized pipes, the significance levels are listed below in Table B.4. Only three, single factors are withheld as being significant, their impact on the relative strain capacity $\zeta_{pp;up}$ is shown in Table B.5.

Table B.4. Significance levels for all single and combined parameters involved in analysis of the relative strain capacity $\zeta_{pp;up}$ of homogeneous specimens

single parameter	significance	combined parameter	significance
a_0/t	2×10^{-52}	$(a_0 \cdot c) / (t \cdot W)$	2×10^{-7}
c/W	6×10^{-8}	$a_0/t \cdot Y/T$	8×10^{-40}
Y/T	3×10^{-9}	$a_0/t \cdot uEL$	4×10^{-31}
uEL	1×10^{-3}	$a_0/t \cdot \delta_l$	7×10^{-14}
δ_l	5×10^{-3}		
		$c/W \cdot Y/T$	2×10^{-9}
		$c/W \cdot uEL$	2×10^{-2}
		$c/W \cdot \delta_l$	2×10^{-8}
		$Y/T \cdot uEL$	8×10^{-3}
		$Y/T \cdot \delta_l$	3×10^{-5}
		$uEL \cdot \delta_l$	2×10^{-1}

Table B.5. Visualization of the influence of selected parameters on the relative strain capacity $\zeta_{pp;up}$

selected single parameters

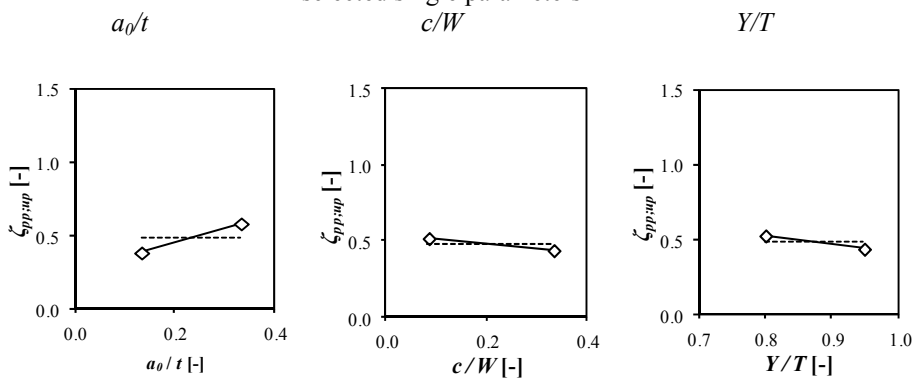

B.2.4. Pressurized pipe versus CWP

The significance levels for the different parameters, regarding the comparison of the strain capacity of pressurized pipes of CWP specimens, are provided in Table B.6. These significance levels are merely considered for the evaluation of the selection method, which makes use of these parameters that have shown a significant influence in either of the two previous sections.

Table B.6. Significance levels for all single and combined parameters involved in analysis of the relative strain capacity $\zeta_{pp;CWP}$ of homogeneous specimens

single parameter	significance	combined parameter	significance
a_0/t	4×10^{-107}	$(a_0 \cdot c) / (t \cdot W)$	4×10^{-43}
c/W	1×10^{-5}	$a_0/t \cdot Y/T$	5×10^{-113}
Y/T	5×10^{-8}	$a_0/t \cdot uEL$	3×10^{-17}
uEL	3×10^{-2}	$a_0/t \cdot \delta_l$	1×10^{-47}
δ_l	4×10^{-1}		
		$c/W \cdot Y/T$	6×10^{-5}
		$c/W \cdot uEL$	3×10^{-2}
		$c/W \cdot \delta_l$	1×10^{-5}
		$Y/T \cdot uEL$	3×10^{-1}
		$Y/T \cdot \delta_l$	2×10^{-1}
		$uEL \cdot \delta_l$	2×10^{-1}

B.3. Welded specimens

B.3.1. Test matrix

All combinations of the geometrical and material properties listed in Table B.7 and Table B.8 are simulated for the following specimens:

- CWP
- Pipe – no pressure (also referred to as: up)
- Pipe – $\sigma_{hoop} / \sigma_0 = 60\%$ (also referred to as: pp_{60})
- Pipe – $\sigma_{hoop} / \sigma_0 = 70\%$ (also referred to as: pp_{70})

This results in a total of 6912 simulated strain capacities and 1728 relative strain capacities.

Table B.7. Considered geometrical properties for test matrix of welded specimens

c [mm]	a_0 [mm]	D [mm]	t [mm]	σ_0 [MPa]	e [mm]
12.5	2.0	762	14	555	0.0
25.0	3.0				1.6
	4.0				
	5.0				

Table B.8. Considered material properties for test matrix of welded specimens

σ_0 [MPa]	MM_{YS} [%]	weld metal post-yield characteristics (Y/T_{BM}; uEL_{BM}) ([-], [%])	base metal post-yield characteristics (Y/T_{BM}; uEL_{BM}) ([-], [%])	tearing resistance (δ_1; δ_2) ([-]; [-])
555	0	(0.85; 6.4)	(0.80; 10.0)	(1.0; 0.20)
	10	(0.90; 4.8)	(0.90; 7.0)	(1.5; 0.35)
	20	(0.95; 3.2)	(0.95; 5.0)	(2.0; 0.50)
	30			

B.3.2. CWP versus unpressurized pipe

For the evaluation of the relative strain capacity of CWP specimens to unpressurized pipes, the significance levels are listed in Table B.9. The influence of the most significant single and combined parameters is illustrated in Table B.10.

Table B.9. Significance levels for all single and combined parameters involved in the analysis of the relative strain capacity $\zeta_{CWP;up}$ of welded specimens

single parameter	significance	combined parameter	significance
a_0/t	5×10^{-95}	$(a_0 \cdot c) / (t \cdot W)$	0
c/W	6×10^{-181}	$a_0/t \cdot Y/T_{BM}$	2×10^{-82}
Y/T_{BM}	4×10^{-8}	$a_0/t \cdot Y/T_{WM}$	2×10^{-100}
Y/T_{WM}	2×10^{-8}	$a_0/t \cdot \delta_l$	4×10^{-52}
δ_l	1×10^{-1}	$a_0/t \cdot MM_{FS}$	1×10^{-8}
MM_{FS}	3×10^{-55}	$a_0/t \cdot e/t$	2×10^{-25}
e/t	9×10^{-8}		
		$c/W \cdot Y/T_{BM}$	2×10^{-152}
		$c/W \cdot Y/T_{WM}$	2×10^{-190}
		$c/W \cdot \delta_l$	1×10^{-90}
		$c/W \cdot MM_{FS}$	1×10^{-6}
		$c/W \cdot e/t$	5×10^{-18}
		$Y/T_{BM} \cdot Y/T_{WM}$	1×10^{-1}
		$Y/T_{BM} \cdot \delta_l$	8×10^{-2}
		$Y/T_{BM} \cdot MM_{FS}$	2×10^{-57}
		$Y/T_{BM} \cdot e/t$	3×10^{-7}
		$Y/T_{WM} \cdot \delta_l$	4×10^{-1}
		$Y/T_{WM} \cdot MM_{FS}$	7×10^{-54}
		$Y/T_{WM} \cdot e/t$	3×10^{-8}
		$\delta_l \cdot MM_{FS}$	8×10^{-53}
		$\delta_l \cdot e/t$	1×10^{-7}
		$MM_{FS} \cdot e/t$	9×10^{-5}

Table B.10. Visualization of the influence of parameters selected for analysis of welded specimens regarding the relative strain capacity $\zeta_{CWP;up}$

selected single parameters

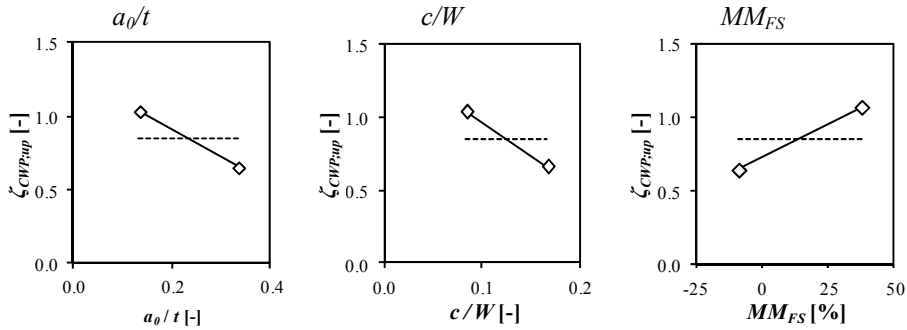

selected combined parameters

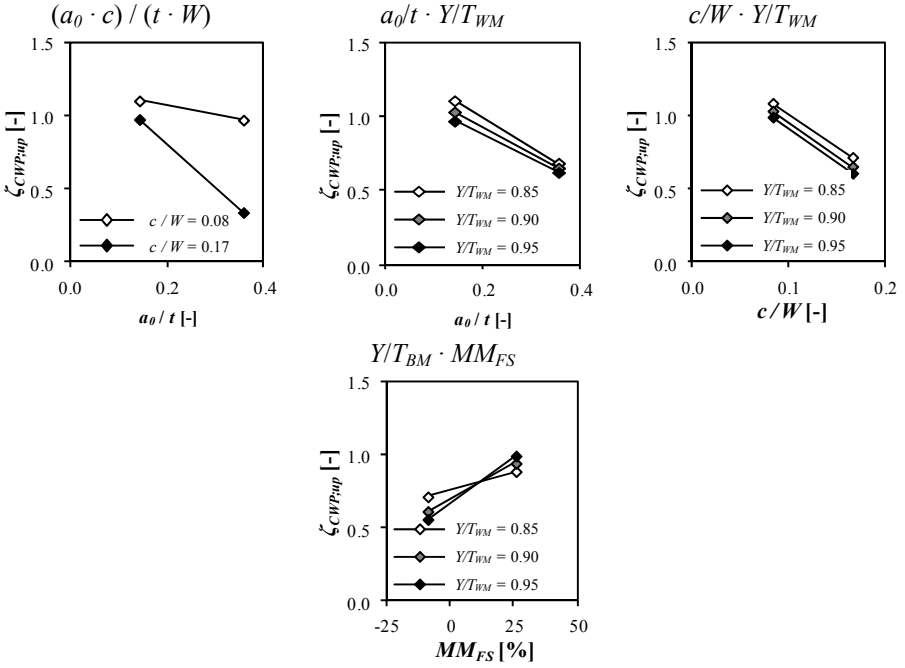

B.3.3. Unpressurized versus pressurized pipe

With respect to the relative strain capacity of pressurized pipes relative to unpressurized pipes, the significance level for all parameters is provided in Table B.11. The impact of the most significant ones is visualized in Table B.12.

Table B.11. Significance levels for all single and combined parameters involved in the analysis of the relative strain capacity $\zeta_{pp;up}$ of welded specimens

single parameter	significance	combined parameter	significance
a_0/t	3×10^{-12}	$(a_0 \cdot c) / (t \cdot W)$	7×10^{-163}
c/W	7×10^{-186}	$a_0/t \cdot Y/T_{BM}$	9×10^{-11}
Y/T_{BM}	5×10^{-3}	$a_0/t \cdot Y/T_{WM}$	4×10^{-11}
Y/T_{WM}	4×10^{-8}	$a_0/t \cdot \delta_l$	2×10^{-2}
δ_l	2×10^{-8}	$a_0/t \cdot MM_{FS}$	1×10^{-23}
MM_{FS}	2×10^{-55}	$a_0/t \cdot e/t$	1×10^{-60}
e/t	4×10^{-60}		
		$c/W \cdot Y/T_{BM}$	2×10^{-165}
		$c/W \cdot Y/T_{WM}$	8×10^{-184}
		$c/W \cdot \delta_l$	5×10^{-63}
		$c/W \cdot MM_{FS}$	4×10^{-4}
		$c/W \cdot e/t$	2×10^{-4}
		$Y/T_{BM} \cdot Y/T_{WM}$	6×10^{-1}
		$Y/T_{BM} \cdot \delta_l$	2×10^{-10}
		$Y/T_{BM} \cdot MM_{FS}$	4×10^{-53}
		$Y/T_{BM} \cdot e/t$	3×10^{-60}
		$Y/T_{WM} \cdot \delta_l$	4×10^{-6}
		$Y/T_{WM} \cdot MM_{FS}$	1×10^{-45}
		$Y/T_{WM} \cdot e/t$	2×10^{-51}
		$\delta_l \cdot MM_{FS}$	5×10^{-53}
		$\delta_l \cdot e/t$	1×10^{-41}
		$MM_{FS} \cdot e/t$	1×10^{-3}

Table B.12. Visualization of the influence of parameters selected for analysis of welded specimens regarding the relative strain capacity $\zeta_{pp;up}$

selected single parameters

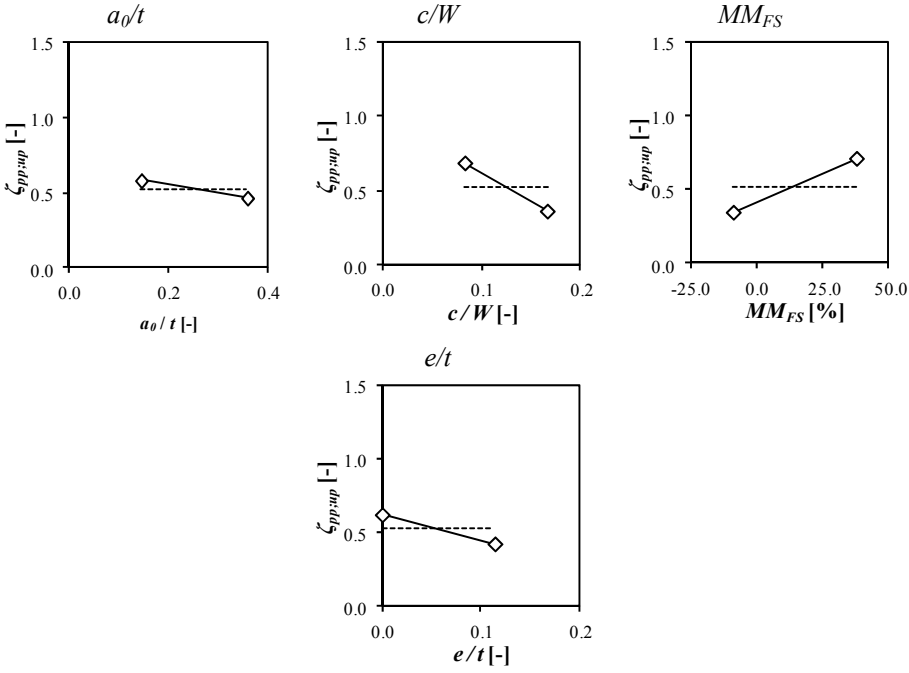

B.3.4. CWP versus pressurized pipe

The significance levels for the different parameters, regarding the comparison of the strain capacity of pressurized pipes to CWP specimens, are listed in Table B.13.

Table B.13. Significance levels for all single and combined parameters involved in the analysis of the relative strain capacity $\zeta_{pp;CWP}$ of welded specimens

single parameter	significance	combined parameter	significance
a_0/t	2×10^{-60}	$(a_0 \cdot c) / (t \cdot W)$	4×10^{-6}
c/W	2×10^{-27}	$a_0/t \cdot Y/T_{BM}$	2×10^{-54}
Y/T_{BM}	8×10^{-2}	$a_0/t \cdot Y/T_{WM}$	6×10^{-58}
Y/T_{WM}	4×10^{-2}	$a_0/t \cdot \delta_l$	2×10^{-53}
δ_l	6×10^{-4}	$a_0/t \cdot MM_{FS}$	2×10^{-18}
MM_{FS}	1×10^{-19}	$a_0/t \cdot e/t$	8×10^{-52}
e/t	4×10^{-115}		
		$c/W \cdot Y/T_{BM}$	5×10^{-28}
		$c/W \cdot Y/T_{WM}$	1×10^{-27}
		$c/W \cdot \delta_l$	5×10^{-2}
		$c/W \cdot MM_{FS}$	9×10^{-1}
		$c/W \cdot e/t$	5×10^{-71}
		$Y/T_{BM} \cdot Y/T_{WM}$	1×10^{-2}
		$Y/T_{BM} \cdot \delta_l$	1×10^{-2}
		$Y/T_{BM} \cdot MM_{FS}$	1×10^{-7}
		$Y/T_{BM} \cdot e/t$	2×10^{-119}
		$Y/T_{WM} \cdot \delta_l$	1×10^{-2}
		$Y/T_{WM} \cdot MM_{FS}$	5×10^{-10}
		$Y/T_{WM} \cdot e/t$	6×10^{-116}
		$\delta_l \cdot MM_{FS}$	2×10^{-17}
		$\delta_l \cdot e/t$	4×10^{-67}
		$MM_{FS} \cdot e/t$	3×10^{-26}

Appendix C

–

Accuracy and Precision

C.1. Definition

When evaluating the experimental methods (e.g. for the measurement of ductile crack extension) presented in this dissertation, distinction is made between the accuracy and the precision of these methods. For a correct understanding, both terms require a clear definition. The definition considered in this dissertation is taken from ISO 5725 - Accuracy of Measurement Methods and Results.

First, the precision is defined as the repeatability or reproducibility of a measurement. In other words, the precision quantifies the difference between subsequent measurements of the same quantity.

Second, the accuracy is used in this dissertation. The accuracy is defined as the closeness of the measurement value to the actual (true) value (reference value in Figure C.1). Remark that this accuracy is the result of both the trueness and the precision.

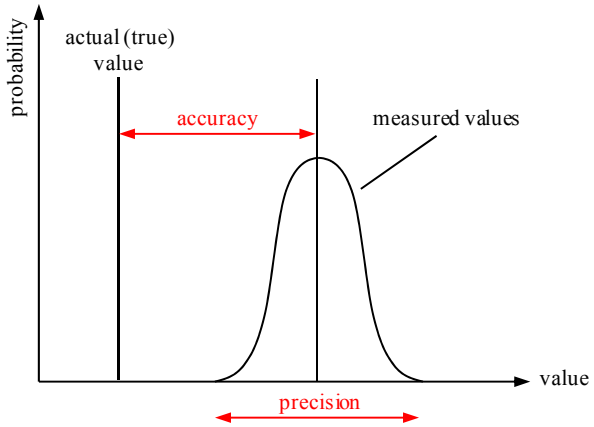

Figure C.1. Graphical illustration of the definitions of accuracy and precision as considered in this dissertation

Appendix D

–

Modified Boundary Layer (MBL) Model

D.1. Introduction

D.1.1. General

Since the 1920s researchers try to understand the failure behaviour of cracked structures. It has quickly been understood that the shape and magnitude of the stress fields ahead of the crack tip influence this behaviour. Consequently, theoretical concepts have been developed to describe the stress fields ahead of the crack tip. At first, materials have been studied in which hardly any plasticity developed in the vicinity of the crack tip. These studies have resulted in the linear elastic fracture mechanics (LEFM) theory. Within this theoretical concept, the crack tip stress fields are described by an analytical expression developed by Williams in the late 1950s [D.1].

$$\sigma_{ij} = \frac{K_I}{\sqrt{2\pi r}} f_{ij}(\theta) + \begin{bmatrix} T & 0 & 0 \\ 0 & 0 & 0 \\ 0 & 0 & \upsilon T \end{bmatrix} + \ldots \tag{D.1}$$

In this so-called Williams expansion, the first term was believed to be dominant over the others. As a result, LEFM theory only considers K_I, defining the magnitude of the first term, to describe the crack tip stress fields. Unfortunately, this theory breaks down when the material ahead of the crack tip deforms plastically. To overcome this shortcoming, the elastic-plastic fracture mechanics (EPFM) theory has been developed by Hutchinson, Rice and Rosengren (HRR) [D.2]. They described the crack tip stress fields by means of the following equation, known as the HRR-solution:

$$\sigma_{ij} = \sigma_0 \left(\frac{EJ}{\alpha \sigma_0^2 I_n r} \right)^{1/n+1} \tilde{\sigma}_{ij}(n, \theta) \tag{D.2}$$

The above description works well for situations where the plasticity is limited to a small zone in the vicinity of the crack tip, alternatively termed as small scale yielding conditions. Under these conditions, both the shape and magnitude of the crack tip stress field remain geometry independent. In contrast, when fully contained yielding conditions are examined, it is no longer possible to accurately describe the crack tip stress fields by means of a single parameter. Under these conditions the material's fracture toughness depends on the specimen's geometry and the loading condition [D.3, 4]. This dependence is alternatively termed as the constraint condition. Consequently, fracture toughness results, in terms of critical J or K_I values, are no longer directly transferable between a laboratory scale specimen and a large structure.

D.1.2. Constraint parameters

In an attempt to clarify the influence of different constraint conditions, several new theoretical concepts have been developed. At first, the LEFM theory has been extended, also considering the second term in the Williams expansion. This term's magnitude is defined by the level of the *T*-stress. As such, a two parameter theoretical concept was developed, known as the *K*-*T* theory [D.5-7]. However, as already stated in the previous section, this theory is only applicable for situations that lack plasticity in the vicinity of the crack tip.

Nowadays, the most suitable theory for investigating fully contained yielding conditions is an extension of the *J*-integral concept. This extension has been developed in the early 1990s by O'Dowd & Shih and describes the constraint effects by means of the *Q*-parameter [D.8, 9]. This parameter has been defined by the following relationship:

$$\sigma_{ij} = (\sigma_{ij})_{\mathrm{HRR}} + Q\ \sigma_0\ \delta_{ij} \tag{D.3}$$

It is clear that the leading term is still the HRR-solution, setting the size scale of the crack tip stress field. Additionally, the *Q*-parameter defines the magnitude of a uniform hydrostatic shift in the crack tip stress field. This shift will lead to a lowered stress level for negative *Q*-values, representing low constraint conditions. In contrast, an increased stress level (positive *Q*) will be observed for high constraint conditions. O'Dowd & Shih have shown that the expression in Eq.(D.3) is valid for distances r ahead of the crack tip between J/σ_0 and $5\,J/\sigma_0$. As a result, the *Q*-parameter is most often evaluated at a distance $r = 2\,J/\sigma_0$. In that case, a simple modification of Eq.(D.3) defines the *Q*-parameter:

$$Q = \frac{\sigma_{\theta\theta} - \sigma_{\theta\theta;MBL}}{\sigma_0} \qquad \tilde{r} = r/\left(J/\sigma_0\right) = 2 \qquad \theta = 90° \tag{D.4}$$

This initial definition, provided by O'Dowd & Shih, is based on the HRR solution as the reference field. However, nowadays applications rather use the small scale yielding (SSY) reference stress field to calculate the *Q*-parameter.

$$\sigma_{ij} = (\sigma_{ij})_{\mathrm{SSY;T=0}} + Q\ \sigma_0\ \delta_{ij} \tag{D.5}$$

This field is used because of its good correspondence with the HRR-field in terms of shape and magnitude. Furthermore, the SSY field can be more easily calculated, based on a modified boundary layer (MBL) analysis. This analysis requires a MBL model, of which the development and a validation are presented in this appendix.

The remainder of this appendix is organized as follows. First, some more detailed theoretical background is provided in section D.2. Afterwards, an analytical and numerical validation is provided in section D.3. Finally, section D.4 describes a comparison between the *T*-stress and *Q*-parameter based on the validated model.

D.2. The Modified Boundary Layer model

D.2.1. General

A modified boundary layer model aims to generate a high constraint stress field in the vicinity of the crack tip, representing small scale yielding conditions (see §D.1.2). These conditions require a situation of plain strain. In addition, the stress field around the crack tip should be dominated by the $1/\sqrt{r}$ singularity in accordance to the LEFM theory. This stress field can be obtained from the finite element simulations of a circular body around the crack tip, schematically represented in Figure D.1.

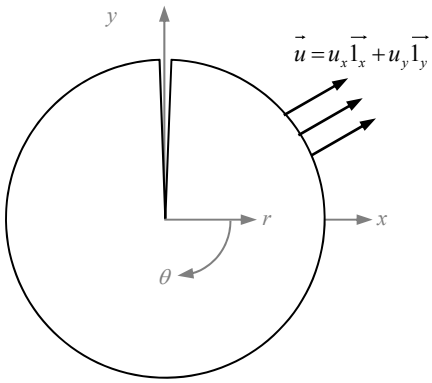

Figure D.1.Schematic representation of Modified Boundary Layer model

A displacement of the elastic mode I singular field is imposed on the boundaries of this body. This displacement field is defined by the following equations:

$$u_x = K_I \frac{1+\upsilon}{E}\sqrt{\frac{r}{2\pi}}\sin\left(\frac{\theta}{2}\right)\left(3-4\upsilon-\cos(\theta)\right) \tag{D.6}$$

$$u_y = -K_I \frac{1+\upsilon}{E}\sqrt{\frac{r}{2\pi}}\cos\left(\frac{\theta}{2}\right)\left(3-4\upsilon-\cos(\theta)\right) \tag{D.7}$$

The magnitude of the above displacement fields is controlled by K_I. However, since LEFM theory applies, K_I can also be expressed in terms of J. For plane strain conditions, the following relationship applies:

$$J = \frac{K_I^2\left(1-\upsilon^2\right)}{E} \tag{D.8}$$

Apart from the plane strain conditions described so far, the MBL model can also be used to study the effect of other constraint conditions on the magnitude of the crack tip stress field. These constraint conditions are created by applying different T-stress levels on the boundary of the MBL FE model:

$$u_{x,T} = -T\frac{\upsilon(1+\upsilon)}{E} r\sin(\theta) \tag{D.9}$$

$$u_{y,T} = -T\frac{1-\upsilon^2}{E} r\cos(\theta) \tag{D.10}$$

D.2.2. Finite element model

A parametric Python® script was developed to generate the model and the input file needed for the Abaqus® processor. This model will be used to study the constraint effects for cracks obtained after fatigue pre-cracking. Hence, an infinitely sharp crack should be modelled. Unfortunately, the corresponding mesh configuration will neither be able to withstand large deformations nor will such mesh yield realistic stress distributions. Consequently, an initially blunted crack is modelled with a notch tip radius (r_0) of 2.5 μm. This radius can be assumed to represent an infinitely sharp crack [D.10, 11]. Furthermore, the outer radius is 10^6 times the notch tip radius, which is in good correspondence with reported MBL models [D.10, 12, 13]. This large outer radius prevents the interaction of plasticity effects with the applied linear elastic boundary conditions.

In order to obtain the required plane strain boundary conditions, the developed FE model is a 2D model that consists of plane strain linear elements with reduced integration (Abaqus® type CPE4R). In addition, a gradually coarsening mesh is used to minimize the number of elements. This mesh consists of 210 rings of 80 elements around the circumference (Figure D.2.a). Furthermore, the radial size of the smallest elements is equal to r_0 / 10 (Figure D.2.b) to accurately describe the stress field near the crack tip. The final mesh contains 16638 elements.

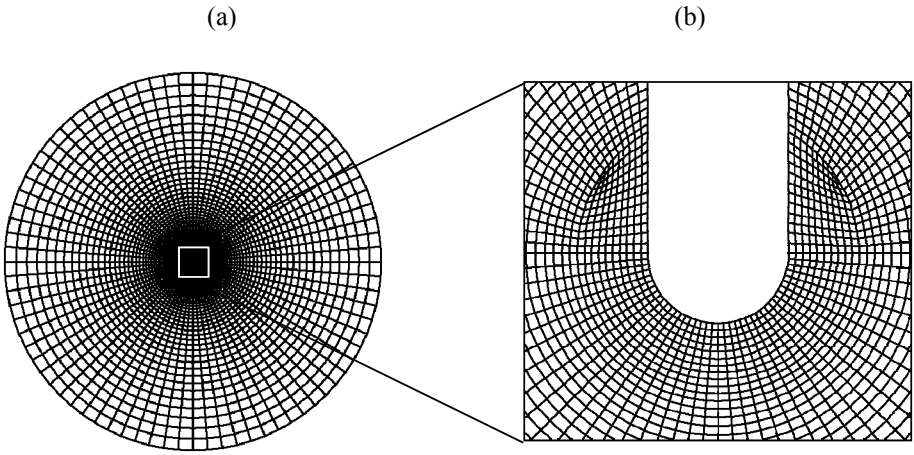

Figure D.2. Mesh configuration of MBL model: global view (a)
and detailed view of the crack tip (b)

D.2.3. Evaluation of boundary conditions and applied load

On the outer boundary of the model, the displacement fields described by Eq.(D.6) and Eq.(D.7) are applied. These fields are defined by means of continuously varying functions in terms of r and θ. In this case, r equals the outer radius of the MBL model and the angle is varied between $\theta = 0$ and $\theta = 2\pi$. To evaluate the accuracy of the applied boundary conditions, the resulting displacement fields are compared to the theoretical displacement fields (Figure D.3). An excellent correspondence is observed.

Considering this correspondence, the calculated load level should correspond to the applied load level. Therefore, a comparison is made between the applied and calculated J-value. A J-level of 1000 N/mm is applied. A limited difference of 3% is noted. However, a comparable difference has also been reported in literature [D.14]. Therefore, this correspondence is considered satisfying.

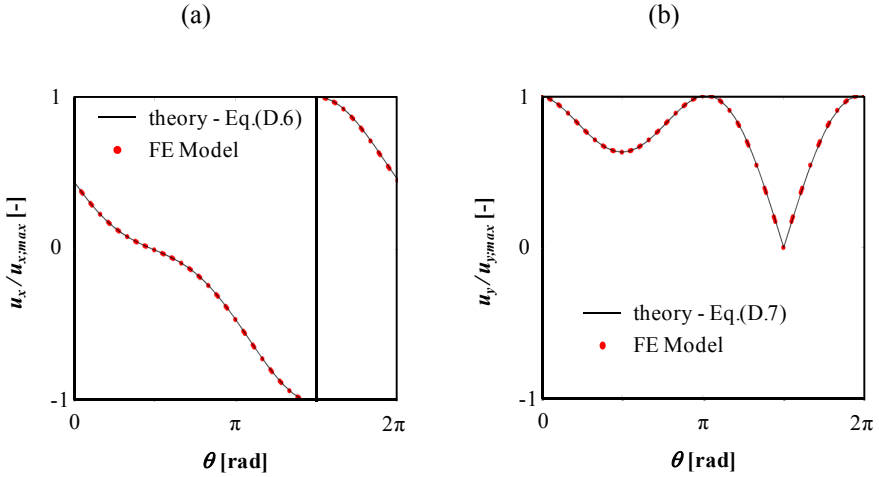

Figure D.3. Applied displacement boundary conditions in x-direction (a) and y-direction (b)

D.3. Validation of crack tip stress fields

D.3.1. Linear elastic validation

At first the MBL FE model is validated for a linear elastic material, corresponding to LEFM theory. In such case, the shape of the crack tip stress field should match the theoretical shape described by the Williams expansion (Eq.(D.1)). For an applied T-stress level equal to zero, this equation reduces to the expression below for the crack tip opening stress, σ_{xx}, ahead of the crack tip:

$$\sigma_{xx} = \frac{K_I}{\sqrt{2\pi r}} \tag{D.11}$$

This theoretical distribution is plotted in Figure D.4, also presenting the stress distribution obtained from the FE model. An excellent correspondence is observed between both distributions.

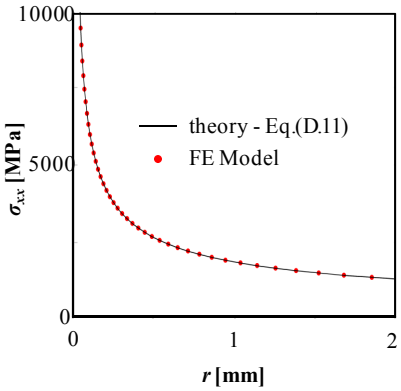

Figure D.4. Linear elastic validation of MBL crack tip stress fields (at $\theta = \pi/2$)

D.3.2. Elastic-plastic validation

For a second validation, the plasticity effects around the crack tip are taken into account. Unfortunately, no theoretical solution exists for these SSY crack tip stress fields. Therefore, the results from the MBL FE model are compared to the results obtained from a literature review [D.8, 15]. For this validation a Ramberg-Osgood stress-strain relationship is assumed:

$$\varepsilon = \frac{\sigma}{E} + \alpha\left(\frac{\sigma}{\sigma_0}\right)^{n-1}\frac{\sigma}{E} \tag{D.12}$$

For the validation, the following values are considered: Young's modulus $E = 200$ GPa, yield strength $\sigma_0 = 400$ MPa, $\alpha = 1$ and strain hardening exponent $n = 10$. Furthermore, small strain conditions are assumed (NlGeom has been set off in Abaqus®).

The crack tip stress field was studied for an applied load level $J = 1000$ N/mm and a root radius of 2.5 µm. The resulting stress field σ_{xx} is plotted in Figure D.5. Comparing this stress field with the results from literature, a fairly good correspondence is achieved. Therefore, the MBL FE model is considered to correctly predict the crack tip stress fields.

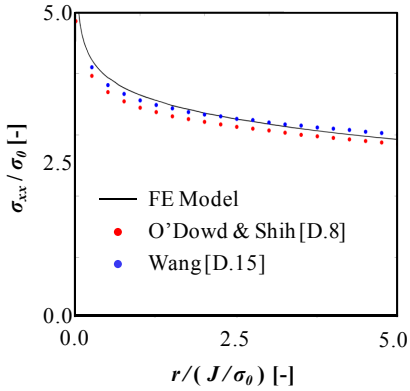

Figure D.5. Elastic-plastic validation of MBL crack tip stress fields (at $\theta = \pi/2$)

D.4. Constraint

As already briefly described in §D.2.1, the MBL FE model is a useful tool to investigate the influence of different constraint conditions in terms of *T*-stress. This section first investigates the exact influence of the *T*-stress on the magnitude and shape of the crack tip stress fields. Second, the *Q*-parameter is calculated for each of the studied *T*-stress levels. These calculations lead to a relationship between the *T*-stress and *Q*-parameter.

D.4.1. Influence of *T*-parameter on crack tip stress field

Based on Eq.(D.9) and Eq.(D.10) an extra displacement can be applied on the outer boundary of the MBL model. This will generate different constraint conditions in the vicinity of the crack tip, most likely resulting in a shift of the crack tip stress field. This shift is expected towards higher stress levels for high constraint conditions (positive *T*-stresses). In contrast, lower stress levels are expected for so-called low constraint conditions (negative *T*-stresses). Indeed, as indicated by Figure D.6, a positive *T*-stress results in a higher stress σ_{xx}, whereas a negative *T*-stress results in a lower stress σ_{xx}.

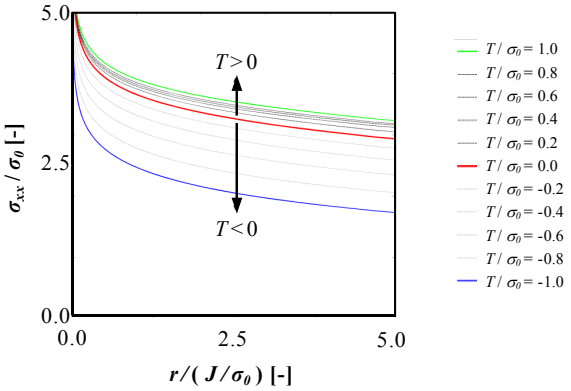

Figure D.6. Influence of *T*-stress on the stress level ahead of the crack tip (at $\theta = \pi/2$)

D.4.2. Relationship between *T*-stress and *Q*-parameter

From the above crack tip stress fields, the Q-parameter is calculated for different *T*-stress levels. Consequently, a relationship between these two constraint parameters is obtained. This relationship is displayed in Figure D.7. When the results from the MBL FE model are compared to results published in literature [D.15], an excellent correspondence is achieved. Only for the smallest investigated *T*-stress level a minor difference is observed.

From the obtained relationship it can be concluded that positive *T*-stress levels result in limited constraint conditions if expressed by the *Q*-parameter. In contrast, negative *T*-stress levels tend to strongly influence the *Q*-parameter. These results are in correspondence with the results of O'Dowd & Shih [D.9].

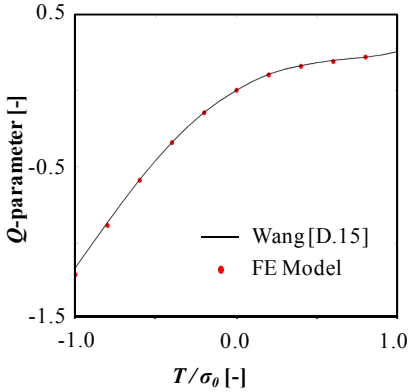

Figure D.7. Relationship between *T*-stress and *Q*-parameter obtained from MBL analysis

D.5. Conclusions

A finite element model was presented to calculate the magnitude of the crack tip stress fields in a MBL model under different constraint conditions. The following conclusions were drawn:

- The relationship between the Q-parameter and T-stress was investigated, showing a weak influence of the T-stress on the Q-parameter for positive T-stresses. In contrast, negative T-stress resulted in pronounced negative Q-values.
- For elastic-plastic conditions the obtained stress field showed an excellent correspondence to the stress fields published by other researchers.
- For linear elastic conditions, the crack tip stress fields corresponded to the analytical crack tip stress field.
- A limited difference was observed between the applied load level in terms of J and the calculated load level.

D.6. Bibliography

[D.1] Williams, M. L., 1957, "On the Stress Distribution at the Base of a Stationary Crack", Journal of Applied Mechanics, 24, pp. 109-114.

[D.2] Anderson, T. L., 1995, "Fracture Mechanics: Fundamentals and Applications", CRC press, Texas.

[D.3] Xu, J., Zhang, Z. L., Ostby, E., Nyhus, B., and Sun, D. B., 2009, "Effects of Embedded Defects in Pipelines Subjected to Plastic Strains During Operation", International Journal of Pressure Vessels and Piping, 86, pp. 787-797.

[D.4] Thaulow, C., Ostby, E., Nyhus, B., Zhang, Z. L., and Skallerud, B., 2004, "Constraint Correction of High Strength Steel - Selection of Test Specimens and Applications of Direct Calculations", Engineering Fracture Mechanics, 71, pp. 2417-2433.

[D.5] Du, Z. Z., and Hancock, J. W., 1991, "The Effect of Non-Singular Stresses on Crack-Tip Constraint", Journal of Mechanics and Physics of solids, 39, pp. 555-567.

[D.6] Al-Ani, A. M., and Hancock, J. W., 1991, "J-Dominance of Short Crack in Tension and Bending", Journal of Mechanics and Physics of solids, 39, pp. 23-43.

[D.7] Betegon, C., and Hancock, J. W., 1991, "Two-Parameter Characterization of Elastic-Plastic Crack Tip Fields", ASME Journal of applied mechanics, 58, pp. 104-113.

[D.8] O'Dowd, N. P., and Shih, C. F., 1991, "Family of Crack-Tip Fields Characterized by a Triaxiality Parameter - Part I. Structure of Fields", Journal of Mechanics and Physics of solids, 99, pp. 989-1015.

[D.9] O'Dowd, N. P., and Shih, C. F., 1992, "Family of Crack-Tip Fields Characterized by a Triaxiality Parameter - Part II. Fracture Applications", Journal of Mechanics and Physics of solids, 40, pp. 939-963.

[D.10] Cravero, S., and Ruggieri, C., 2003, "A Two-Parameter Framework to Describe the Effect of Constraint Loss on Cleavage Fracture and Implications for Failure Assessments of Cracked Components", Journal of Brazilian Society of Mechanical Sciences and Engineering, 15, pp. 403-412.

[D.11] Ranestad, O., Zhang, Z. L., and Thaulow, C., 1999, "Quantification of Geometry and Material Mismatch Constraint in Steel Weldments with Fusion Line Cracks", International Journal of Fracture, 99, pp. 211-237.

[D.12] Horn, A. J., 2010, "Development of an Engineering Assessment Procedure for Predicting Cleavage Fracture from Non-Sharp Defects Using the Failure Assessment Diagram", Ph.D. dissertation, University of Manchester, Manchester.

[D.13] Sherry, A. H., Wilkes, M. A., Beardsmore, D. W., and Lidbury, D. P. G., 2005, "Material Constraint Parameters for the Assessment of Shallow Defects in Structural Components - Part I: Parameter Solutions", Engineering Fracture Mechanics, 72, pp. 2373-2395.

[D.14] Zhang, Z. L., Hauge, M., and Thaulow, C., 1997, "The Effect of T-Stress on the near Tip Stress Field on an Elastic-Plastic Interface Crack", International Conference on Fracture, Sydney, Australia, pp. 2643-2650.

[D.15] Wang, X., 2009, "Two-Parameter Characterization of Elastic-Plastic Crack Front Fields: Surface Cracked Plates under Tensile Loading", Engineering Fracture Mechanics, 76, pp. 958-982.

Publications

A1 – Peer reviewed journal publications included in Science Citation Index

Hertelé, S., De Waele, W., Denys, R. and **Verstraete, M.**, 2013, "Sensitivity of plastic response of defective pipeline girth welds to the stress-strain behaviour of base and weld metal", Journal of Offshore Mechanics and Arctic Engineering – Transactions of the ASME, 135(1).

Hertelé, S., **Verstraete, M.**, Denys, R. and De Waele, W., 2013, "Global collapse and J integral analysis for inner-diameter defected curved plates in tension", International Journal of Pressure Vessels and Piping.

Verstraete, M., Denys, R., Van Minnebruggen, K., Hertelé, S. and De Waele, W., 2013, "Determination of CTOD resistance curves in side-grooved Single‑Edge Notched Tensile specimens using full field deformation measurements", Engineering Fracture Mechanics.

Hertelé, S., De Waele, W., Denys, R. and **Verstraete, M.**, 2012, "Full-range stress-strain behaviour of contemporary pipeline steels : Part I : model description", International Journal of Pressure Vessels and Piping, 92, pp. 34-40.

Hertelé, S., De Waele, W., Denys, R. and **Verstraete, M.**, 2012, "Full-range stress-strain behaviour of contemporary pipeline steels : part II : estimation of model parameters", International Journal of Pressure Vessels and Piping, 92, pp. 27-33.

Van Wittenberghe, J., De Baets, P., De Waele, W., Ost, W., **Verstraete, M.** and Hertelé, S., 2012, "Resonant bending fatigue test setup for pipes with optical displacement measuring system", Journal of Offshore Mechanics and Arctic Engineering-Transactions of the ASME, 134(3).

Hertelé, S., De Waele, W., Denys, R. and **Verstraete, M.**, 2012, "Investigation of strain measurements in (curved) wide plate specimens using digital image correlation and finite element analysis", Journal of Strain Analysis for Engineering Design, 47(5), pp. 276-288.

Hertelé, S., De Waele, W., Denys, R., **Verstraete, M.** and Van Wittenberghe, J., 2012, "Parametric finite element model for large scale tension tests on flawed pipeline girth welds", Advances in Engineering Software, 47(1), pp. 24-34.

A2 – Peer reviewed journal publications

Verstraete, M., De Waele, W., Hertelé, S., Denys, R., Van Puyvelde, D. and Van Minnebruggen, K., 2011, "Measurement of ductile crack extension in laboratory scale fracture mechanics testing", Mechanical Engineering Letters, 5, pp. 104-114.

Hertelé, S., De Waele, W., Denys, R. and **Verstraete, M.**, 2011, "Analytical validation of crack driving force calculations for defects in plates and pipes under tension", Mechanical Engineering Letters, 5, pp. 81-88.

C/P – Conference proceedings

Verstraete, M., Hertelé, S., Van Minnebruggen, K., Denys, R. and De Waele, W., 2013, "UGent guidelines for SENT testing", Pipeline Technology Conference, Ostend, Belgium, paper n° S08-03.

Verstraete, M., Van Minnebruggen, K., Hertelé, S., Denys, R. and De Waele, W., 2013, "Determination of tearing resistance in SENT and CWP specimens using direct current potential drop measurements", Pipeline Technology Conference, Ostend, Belgium, paper n° S08-04.

Hertelé, S., **Verstraete, M.**, Van Minnebruggen, K., Denys, R. and De Waele, W., "Applications of digital image correlation in girth weld testing", Pipeline Technology Conference, Ostend, Belgium, paper n° S03-02.

Hertelé, S., Van Minnebruggen, K., **Verstraete, M.**, Denys, R. and De Waele, W., "Effects of line pipe steel heterogeneity on tensile strain capacity", Pipeline Technology Conference, Ostend, Belgium, paper n° S13-03.

Van Minnebruggen, K., **Verstraete, M.**, Hertelé, S., Van Wittenberghe, J., Thibaux, P., Denys, R. and De Waele, W., 2013, "Finite element analysis of crack driving force and mode mixity for spiral pipe seam weld flaws", Pipeline Technology Conference, Ostend, Belgium, paper n° S15-03.

Van Minnebruggen, K., Hertelé, S., **Verstraete, M.**, Van Wittenberghe, J., Thibaux, P., Denys, R. and De Waele, W., 2013, "Development of a finite element model for spiral welded pipes loaded in tension", Pipeline Technology Conference, Ostend, Belgium, paper n° S15-04.

Verstraete, M., Hertelé, S., Van Minnebruggen, K., Denys, R. and De Waele, W., 2013, "Considerations in selecting laboratory scale test specimens for evaluation of fracture toughness", Sustainable Construction and Design, Ghent, Belgium.

Hertelé, S., Denys, R., Van Minnebruggen, K., **Verstraete, M.** and De Waele, W., 2013, "Combined numerical-experimental framework for strain based design and flaw assessment of girth welds", Sustainable Construction and Design, Ghent, Belgium.

Hertelé, S., **Verstraete, M.**, Van Minnebruggen, K., Denys, R. and De Waele, W., 2012, "Curved wide plate testing with advanced instrumentation and interpretation", International Pipeline Conference, Calgary, Alberta, Canada, paper n° IPC2012-90591.

Verstraete, M., De Waele, W., Denys, R. and Hertelé, S., 2012, "Pressure correction factor for strain capacity predictions based on curved wide plate testing", International Pipeline Conference, Calgary, Alberta, Canada, paper n° IPC2012-90592.

Verstraete, M., De Waele, W., Denys, R. and Hertelé, S, 2012, "Comparison of pipeline girth weld defect acceptance at the onset of yielding according to CSA Z662 and EPRG guidelines", International Pipeline Conference, Calgary, Alberta, Canada, paper n° IPC2012-90593.

Hertelé, S., De Waele, W., Denys, R., **Verstraete, M.**, Van Minnebruggen, K. and Horn, A., 2012, "Weld strength mismatch in strain based flaw assessment : which definition to use?", Pressure Vessels and Piping Conference, Toronto, Canada, paper n° PVP2012-78306.

Hertelé, S., De Waele, W., Denys, R. and **Verstraete, M.**, 2012, "Justification of the mapping approach for finite element modelling of ductile tearing" Sustainable Construction and Design, Ghent, Belgium.

Cauwelier, M., Maelfait, J., **Verstraete, M.**, Hertelé, S., Van Minnebruggen, K. and De Waele, W., 2012, "Validation of a finite element model for fracture mechanics specimens" Sustainable Construction and Design, Ghent, Belgium.

Beddeleem, J., De Waele, W., Hertelé, S., **Verstraete, M.** and Van Minnebruggen, K., 2012, "Characterization of mechanical properties in weld metal using inverse modeling" Sustainable Construction and Design, Ghent, Belgium.

Verstraete, M., Hertelé, S., De Waele, W. and Denys, R., 2012, "Influence and evaluation of constraint on fracture toughness in pipeline research", Sustainable Construction and Design, Ghent, Belgium.

Verstraete, M., Hertelé, S., De Waele, W., Denys, R. and Van Minnebruggen, K., 2012, "Measurement of ductile crack extension in single edge notch tensile specimens", International Conference on Experimental Mechanics, Porto, Portugal.

Verstraete, M., De Waele, W., Hertelé, S., Van Minnebruggen, K. and Denys, R., 2012, "Constraint analysis of curved wide plate specimens", European Conference on Fracture, Kazan, Russia, paper n° 289.

Van Minnebruggen, K., Van Puyvelde, D., De Waele, W., **Verstraete, M.**, Hertelé, S. and Denys, R., 2011, "Implementation of an unloading compliance procedure for measurement of crack growth in pipeline steel", Sustainable Construction and Design, Ghent, Belgium.

Verstraete, M., De Waele, W. and Hertelé, S., 2011, "Development and validation of a high constraint modified boundary layer finite element model", Sustainable Construction and Design, Ghent, Belgium.
De Keyser, Karel, Van Acker, F., Hertelé, S., **Verstraete, M.**, De Waele, W. and Denys, R., 2011, "Validation of a wide plate finite element model using digital image correlation", Sustainable Construction and Design, Ghent, Belgium.

Hertelé, S., De Waele, W., Denys, R. and **Verstraete, M.**, 2011, "Sensitivity of plastic response of defective pipeline girth welds to the stress-strain behavior of base and weld metal", International Conference on Ocean, Offshore and Arctic Engineering, Rotterdam, the Netherlands, paper n° OMAE2011-49239.

Verstraete, M., Hertelé, S., De Waele, W. and Wellekens, J.-B., 2011, "Investigation of strains in a transverse weld tensile test specimen through digital image correlation", Photomechanics, Brussels, Belgium.

Hertelé, S., De Waele, W., Denys, R. and **Verstraete, M.**, 2011, "Design of a (mini) wide plate specimen for strain-based weld integrity assessment", Sustainable Construction and Design, Ghent, Belgium.

Verstraete, M., De Waele, W., Hertelé, S. and Denys, R., 2011, "Evaluation of strength mismatch by FE Analysis and DIC measurements on cross weld tensile specimens". International Offshore and Polar Engineering Conference, Maui, Hawaii, USA, pp. 607-614.

Hertelé, S., De Waele, W., Denys, R. and **Verstraete, M.**, 2011, "Modelling crack driving force in plates and pipes under tension : a comparison with literature", Synergy Conference, Gödöllö, Hungary.

Verstraete, M., De Waele, W., Denys, R. and Hertelé, S., 2011, "Evaluatie van de vervormingscapaciteit van lasverbindingen", BIL/NIL Lassymposium, Antwerp, Belgium.

Hertelé, S., De Waele, W., Denys, R. and **Verstraete, M.**, 2011, "Gekoppeld experimenteel-numeriek onderzoek naar de vervormingscapaciteit van pijpsecties met omtrekslasfout", BIL/NIL Lassymposium, Antwerp, Belgium.

Denys, R., Hertelé, S., **Verstraete, M.** and De Waele, W., 2011, "Strain capacity prediction for strain-based pipeline designs", International seminar on Welding of High Strength Pipeline Steels, Araxá, Brazil.

Denys, Rudi, Hertelé, S. and **Verstraete, M.**, 2010, "Strain capacity of weak and strong girth welds in axially loaded pipelines", International Pipeline Technology Conference 2010, Beijing, China.

Hertelé, S., De Waele, W., Denys, R., Van Wittenberghe, J. and **Verstraete, M.**, 2010, "Limit load and reference stress for curved wide plates", International Pipeline Conference, Calgary, Alberta, Canada, paper n° IPC2010-31290.

Hertelé, S., De Waele, W., Denys, R., Van Wittenberghe, J. and **Verstraete, M.**, 2010, "Investigation of pipe strain measurements in a curved wide plate specimen", International Pipeline Conference, Calgary, Alberta, Canada, paper n° IPC2010-31292.

Van Wittenberghe, J., De Baets, P., De Waele, W., Ost, W., **Verstraete, M.** and Hertelé, S., 2010, "Pipe resonant bending fatigue test setup with optical measuring system", International Pipeline Conference, Calgary, Alberta, Canada, paper n° IPC2010-31115.

Denys, R., Hertelé, S. and **Verstraete, M.**, 2010, "Longitudinal strain capacity of GMAW welded high niobium (HTP) grade X80 steel pipes", International seminar on Application of High Strength Line Pipe 2010, Xi'an, China.

Hertelé, S., De Waele, W., Denys, R., Abdel Wahab, M. and **Verstraete, M.**, 2010, "Inherent possibilities and limitations of finite element modelling of defective girth welds", Sustainable Construction and Design, Ghent, Belgium.

Faes, Koenraad, Maas, F., De Waele, W., De Baets, P., **Verstraete, M.**, Delbaere, D. and Van Der Donckt, E., 2010, "Weldability of micro-alloyed high-strength pipeline steels using a new friction welding variant", IIW International Congress, Sofia, Bulgaria.

Wellekens, J.-B., De Waele, W., Denys, R., Hertelé, S. and **Verstraete, M.**, 2010, "Interpretation of stress-strain curve in pipeline research" , Sustainable Construction and Design, Ghent, Belgium.

Verstraete, M., De Waele, W., Hertelé, S. and Denys, R., 2010, "Evaluation of pipe bending reference stress equations", Sustainable Construction and Design, Ghent, Belgium.